University of Alberta

RELIABILITY-BASED MANAGEMENT OF FATIGUE FAILURES

by

Georg Josi

A thesis submitted to the Faculty of Graduate Studies and Research
in partial fulfillment of the requirements for the degree of

Doctor of Philosophy
in
Structural Engineering

Department of Civil and Environmental Engineering

Spring 2010
Edmonton, Alberta

Examining Committee

Gilbert Grondin, Civil and Environmental Engineering

Vivek Bindiganavile, Civil and Environmental Engineering

Samer Adeeb, Civil and Environmental Engineering

Jozef Szymanski, Civil and Environmental Engineering

Walied Moussa, Mechanical Engineering

Amit Kanvinde, Civil and Environmental Engineering, University of California, Davis

Dedicated with love to my grandmother, Elisa Blatter-Joder, who passed away on October 6, 2006, for being a great inspiration and a role model. You will always have a special place in my heart.

Mit Liebi mim Grosi, Elisa Blatter-Joder, wo am 6. Oktober 2006 verstorbe isch, gwidmet. Du bisch für üs aui äs grosses Vorbiud gsi u wirsch immer ä spezieue Platz i mim Härz ha.

ABSTRACT

Fatigue assessments have been carried out predominantly with quasi-deterministic approaches, such as the use of S–N curves. However, both the loading and the resistance of fatigue prone components are subjected to significant uncertainties. Consequently, a prediction of the remaining fatigue life based on deterministic load and resistance models can lead to unreliable results. This work presents a general reliability-based approach to predict fatigue life of steel components. The approach incorporates prediction of fatigue crack initiation, modeled with a strain-based correlation approach, and propagation, modeled using a linear elastic fracture mechanics approach, and is applicable to new, cracked or repaired structural components.

Based on the analysis of existing test results and additional crack initiation and propagation tests on weld metal, the relevant probabilistic fatigue material properties of grade 350WT steel and a matching weld metal were established. An experimental program was carried out on welded details tested either in the as-welded, stress-relieved, conventionally peened, or ultrasonically peened condition. It was demonstrated that ultrasonic peening is superior to the other investigated post weld treatment methods. Using finite element analyses, the results of the tests were deterministically predicted for several different initial conditions, including initial flaw and crack sizes and locations, as well as different levels of residual stresses. A model incorporating an initial flaw and accounting for crack closure and the threshold stress intensity factor range was retained.

A probabilistic analysis using Monte Carlo Simulation was carried out to calibrate the relevant parameters. A general reliability-based approach, which includes both the loading and resistance sides of the limit state function was proposed and applied to three practical examples: prediction of test results from two test programs and the prediction of the remaining fatigue life of a cracked component as a function of the safety index. These three applications demonstrated that accurate fatigue life predictions targeting a predefined safety index are achieved.

ACKNOWLEDGEMENTS

I would like to express my sincere gratitude to everyone who, by their support, encouragement, help, or remarks have contributed to the fulfillment of this work.

I would like to acknowledge the financial assistance of the Natural Sciences and Engineering Research Council of Canada and Syncrude Canada Ltd. Personal financial assistance in the form of scholarships from Cohos Evamy Intagratedesign (Structural Engineering Scholarship), the CISC Alberta Region (Geoffrey L. Kulak Scholarship), Alberta Ingenuity, the Faculty of Graduate Studies (Mary Louise Imrie Award), and the Graduate Student Association are greatly appreciated. Without these funds, the completion of my thesis would have been impossible.

I would like to thank Dr. Gilbert Y. Grondin for giving me the opportunity to do my Ph.D. studies here at the University of Alberta. He was not only great in supervising my thesis, but also in making sure that the necessary funds for this research project were always available. Equal thanks go to Dr. Geoffrey L. Kulak, who was always a reliable source of wisdom and made sure that we comfortably settled here in Edmonton, to Dr. Khaled Obaia of Syncrude Canada Ltd for keeping the research advancing in the right direction, and to Dr. Scott Walbridge of the University of Waterloo for introducing me to reliability concepts in fatigue.

The assistance of the technicians in the I.F. Morrison Laboratory of the Department of Civil Engineering—Sean, Greg, Michael, and Richard—the Department of Chemical and Materials Engineering—Clark, you are the best (welder)—and at Syncrude Research—Steffen and Tim—is acknowledged with thanks. Joe, it was great to work with you. You deserve a lot of credit for the endless hours you spent in the lab and on the computer for me. Thank you very much.

Thanks to Jeff, Alfred, Christophe, Marc, Bruce and especially the Pfaeffli Family (Housi, Marianne, Lucille, Kobi, David, and Bernhard) for making us feel at home again here in Alberta. A very special thank you to the entire hockey crew—Shawn, Dean, Billy, Al, Mike, Kyle, Damon, Perry and (again) Alfred to name a few—to adopt one of those soft Europeans on your squad. Every skate was a lot of fun and a welcome distraction from research life.

In addition, I would like to extend a cordial thank you to my family in Switzerland. My parents' foresight to provide me with nothing but the best education has allowed me to tackle many challenges. I will be eternally grateful for all the opportunities this has provided me with.

Last, but not least, I would like to extend my sincere gratitude and love to you, Monika. You sacrificed so much to help me fulfill my ambitions. A thank you is not enough to express what you have done for me…

TABLE OF CONTENTS

LIST OF TABLES

LIST OF FIGURES

LIST OF ABBREVIATIONS AND SYMBOLS

Abbreviations

AASHTO	American Association of State Highway and Transportation Officials
ANSI	American National Standards Institute
ASCE	American Society of Civil Engineers
ASM	American Society for Metals
ASME	American Society of Mechanical Engineers
ASTM	American Society for Testing and Materials
AWS	American Welding Society
BS	British Standard
BSI	British Standards Institution
CAFL	Constant Amplitude Fatigue Limit
CAMI	Coated Abrasive Manufacturers Institute
CEN	European Committee for Standardization
CDF	Cumulative Distribution Function
CNC	Computer Numerical Control
COV	Coefficient Of Variation
CSA	Canadian Standards Association
C(T)	Compact Tension (specimen)
CVN	Charpy V-Notch
DCEP	Direct Current Electrode Positive
DNV	Det Norske Veritas
DVS	Deutscher Verbund für Schweisstechnik
EC	Eurocode
ECCS	European Convention for Constructional Steelwork
EDM	Electrical Discharge Machining
EDX	Energy Dispersive X-Ray
EN	European Standard
FCAW	Flux Cored Arc Welding
FORM	First Order Reliability Method
FOSM	First Order Second Moment
HAZ	Heat Affected Zone
HPS	High Performance Steel
IABSE	International Association for Bridge and Structural Engineering

IIW	International Institute of Welding
JCSS	Joint Committee on Structural Safety
LEFM	Linear Elastic Fracture Mechanics
LN	Lognormal distribution
LVDT	Linear Variable Differential Transformer
MCS	Monte Carlo Simulation
M(T)	Middle Tension (specimen)
NBCC	National Building Code of Canada
pdf	probability density function
SAE	Society of Automotive Engineers
SEM	Scanning Electron Microscope
SE(T)	Single-Edge Tension (specimen)
SIA	Swiss Society of Engineers and Architects
SIF	Stress Intensity Factor
SWT	Smith, Watson, and Topper (relationship)
VAFL	Variable Amplitude Fatigue Limit

cp	conventionally peened
np	non-peened
nt	non-treated
up	ultrasonically peened

Symbols

A	fatigue life constant; coefficient
A_r	area at rupture (in a monotonic tension test)
A_0	constant
A_1	constant
A_{max}	coefficient to determine β_G corresponding to maximum load
A_{min}	coefficient to determine β_G corresponding to minimum load
A_{res}	coefficient to determine β_G corresponding to residual stresses
B	width; coefficient; constant
C	crack growth constant; coefficient
D	coefficient; damage
E	modulus of elasticity
ER	expansion ratio (ratio of pin to hole diameter)

E_1	electrical energy per unit length of the largest weld pass at the toe
F_{av}	correction factor to determine average strain amplitude in crack initiation tests
$F_{\max}$	correction factor to determine maximum strain amplitude in crack initiation tests
F_{sr}	fatigue resistance
F_{srt}	stress range at CAFL
$F_U(u)$	CDF of u
F_y	nominal yield strength
$F_Z(z)$	CDF of z
$G(\mathbf{Z})$	limit state function
H	height; length
$K_{eff,\max}$	effective maximum stress intensity factor (accounting for residual stresses)
$K_{eff,\min}$	effective minimum stress intensity factor (accounting for residual stresses)
K_l	stress intensity factors for long cracks
$K_{\max}$	maximum stress intensity factor
$K_{\min}$	minimum stress intensity factor
K_{op}	crack opening stress intensity factor
K_{pl}	crack closure stress intensity factor
K_{res}	stress intensity factor due to residual stresses
K_s	stress intensity factors for short cracks
K'	cyclic strength coefficient
L	length
N	number of cycles
N_R	remaining fatigue life in reliability analysis
N_S	accepted number of cycles to failure in reliability analysis
N_{actual}	actual number of truck passages
N_c	expected number of truck passages
N_{day}	expected number of stress cycles per day
N_{design}	design number of truck passages; design number of cycles to failure
N_e	number of cycles to failure due to $\Delta\sigma_e$
N_{init}	crack initiation life
N_{mean}	mean number of cycles to failure
N_{meas}	measured number of truck passages

$N_{predicted}$	predicted number of cycles to failure
N_{prop}	stable crack propagation life
N_{total}	total fatigue life ($N_{total} = N_{init} + N_{prop}$)
$N(t)$	number of estimated loading sequences per time unit
$P(\bullet)$	probability of occurrence of event "$\bullet$"
$P_{\max}$	maximum load
$P_{\min}$	minimum load
R	stress, strain or load ratio; resistance
RA	Reduction in area at rupture
R_{eff}	effective stress ratio (accounting for residual stresses)
R_n	nominal resistance
SCF	stress concentration factor
S	load effect (solicitation)
S_n	nominal load effect (solicitation)
T	time (peening intensity); thickness
T_r	remaining fatigue life
U	ratio to account for crack closure effect
Var_{weld}	variability coefficient for welding residual stresses
W	width
$\mathbf{X}$	normalized vector of the design variables
$\mathbf{Z}$	vector of the design variables

a	crack size
a_{av}	average crack size (in crack propagation model)
a_0	initial crack size (in crack propagation model)
a_f	final crack size (in crack propagation model)
a_{init}	initial flaw/crack size
a_{trans}	transitional crack size
a/c	crack aspect ratio
$(a/c)_{init}$	initial crack aspect ratio
b	fatigue strength exponent
c	crack size (major axis of elliptical crack); fatigue ductility exponent
d_i	fatigue damage due to a stress range $\Delta\sigma_i$
da/dN	crack growth rate
f_{sr}	calculated stress range (CSA)
k_t	elastic stress concentration factor for a short crack

m	crack growth exponent; slope of AASHTO fatigue curves
n_i	individual load sequence
n'	cyclic strain hardening exponent
p_f	probability of failure
r^2	coefficient of determination (in a regression analysis)
s_C	standard deviation of crack growth constant C
t	thickness
u	random number
x	normalized design variable
z	design variable
z_r	repair depth
ΔK	stress intensity factor range
ΔK_{eff}	effective stress intensity factor range (accounting for crack closure)
ΔK_{th}	threshold stress intensity factor range
Δa	crack extension
$\Delta\varepsilon$	strain range
$\Delta\varepsilon/2$	strain amplitude
$(\Delta\varepsilon/2)_{av}$	average applied strain amplitude in a crack initiation test
$(\Delta\varepsilon/2)_{nom}$	nominally applied strain amplitude in a crack initiation test
$\Delta\varepsilon_{el}/2$	elastic strain amplitude
$\Delta\varepsilon_{pl}/2$	plastic strain amplitude
$\Delta\sigma$	stress range
$\Delta\sigma_D$	constant amplitude fatigue limit
$\Delta\sigma_{E2}$	equivalent stress range at two million cycles (Eurocode)
$\Delta\sigma_{app}$	applied stress range
$\Delta\sigma_c$	fatigue strength at two million cycles (ECCS curves)
$\Delta\sigma_{c,d}$	design fatigue resistance at two million cycles (Eurocode)
$\Delta\sigma_e$	equivalent stress range
$\Delta\sigma_{fat,th}$	theoretical stress range due fatigue load
$\Delta\sigma_g$	gross section stress range
$\Delta\sigma_{init}$	theoretical stress range at initiation site
$\Delta\sigma(Q_{fat})$	calculated stress range (Eurocode)
Φ_0	elliptical integral
α	sample mean

α_F	load factor for fatigue
$\vec{\alpha}$	direction cosine vector
β	safety index; stress intensity correction factor; sample standard deviation
β_{50}	safety index for a reference period of 50 years
β_E	crack shape correction factor
β_{ESW}	product of β_E, β_S, and β_W
β_G	stress gradient correction factor
β_S	free surface correction factor
β_W	finite width (or thickness) correction factor
ε	parameter of lognormal distribution (expressing the variance)
ε_{ext}	strain due to external load
$\varepsilon_{\max}$	maximum strain
$\varepsilon_{\min}$	minimum strain
ε_r	strain at rupture
ε_{res}	residual strain
ε_{SH}	strain at onset of strain hardening
ε_{tot}	total strain ($\varepsilon_{tot} = \varepsilon_{res} + \varepsilon_{ext}$)
ε_u	strain at the ultimate strength
ε'_f	fatigue ductility coefficient
ϕ	resistance factor
ϕ_F	resistance factor for fatigue
γ	load factor; fatigue constant of a detail
λ	reduction factor for fatigue loading (Eurocode); parameter of lognormal distribution (expressing the expected value); parameter of the Exponential distribution
μ	mean value
μ_R	mean value of the resistance
μ_S	mean value of the load effect (solicitation)
μ_X	mean value of normalized limit state function
$\mu_{\mathbf{Z}}$	mean value of the limit state function
η	adjustment coefficient for fatigue load
θ	parameter in Weibull distribution
σ	stress; standard deviation
σ_R	standard deviation of the resistance
σ_S	standard deviation of the load effect (solicitation)

$\sigma_{\mathbf{Z}}$	standard deviation of the limit state function
σ_X	standard deviation of normalized limit state function
$\sigma_{fat,\max}$	maximum stress due to fatigue load
$\sigma_{fat,\min}$	minimum stress due to fatigue load
σ_i	magnitude of the stress field at some distance away from the crack tip
$\sigma_{\max}$	maximum stress
$\sigma_{\max,app}$	maximum applied stress
$\sigma_{\max,0}$	maximum stress neglecting residual stresses
$\sigma_{\min}$	minimum stress
$\sigma_{\min,app}$	minimum applied stress
σ_n	nominal stress
σ_{op}	crack opening stress
σ_{peak}	peak stress (stress concentration)
σ_{res}	residual stress
σ_{us}	static ultimate strength
σ_y	yield strength
σ_{ys}	static yield strength
$\sigma_f^{'}$	fatigue strength coefficient
τ	parameter in Weibull distribution
υ	Poisson's ratio

1. INTRODUCTION

1.1 Motivation

Fatigue of steel structures such as bridges, mining equipment, or offshore structures, results in important overall economic losses, either from costs of repair or loss of use of the structure or equipment [Fisher 1984]. Furthermore, the unanticipated nature of many failures, especially of mobile components such as mining or earth moving equipment, can cause serious safety hazards.

The fatigue performance of steel structures is a function of several factors such as loading and service conditions, material properties, the geometrical configuration of the component subjected to cyclic loading, and initial imperfections. Because these factors show considerable variability, the life cycle assessment of these structures and the management of their repair can only be done effectively through reliability-based approaches.

Due to the large variability usually observed in fatigue test results, the fatigue resistance of structural details is best determined through testing. However, fatigue testing is time consuming and expensive. Furthermore, it is often impractical, or sometimes impossible, to test full size equipment or structural components. Therefore, alternative means to testing are often required, such as analytical prediction models.

Several investigations based on probabilistic approaches for fatigue life predictions have been conducted over the past few years, especially in the offshore and nuclear power production industries [Sundararajan 1995]. These investigations account for variability in loads and resistance, but are generally based on the assumption that pre-existing fatigue cracks are present and thus focus only on the propagation stage of the fatigue cracks. However, many structural components contain flaws that do not have a sharp tip and a significant portion of the fatigue life is spent initiating a crack. Therefore, the crack initiation stage of the fatigue life needs to be included in a reliability-based approach.

1.2 Objectives and Scope

A collaborative research program between the University of Alberta and an industrial partner was initiated in the summer of 2001. The main objective of the program is to improve the management of the repair of fatigue cracks in heavy mining equipment. Cracks are a common occurrence in oil sand mining equipment and frequent repairs have to be carried out. Unfortunately, little or no scientific data are available to compare the efficiency of the different applied repair methods (cost, time, and expected service life of the repairs). The following steps were identified as critical to improve the management of fatigue crack repairs in mining equipment:

1. Collect in-situ data to characterize the loading;

2. Define the fatigue material properties for grade 350WT steel, which is commonly used in structural components of mining equipment;
3. Develop a deterministic approach to predict the fatigue life of components and structures from crack initiation to final fracture;
4. Investigate the efficiency of different fatigue crack repair methods;
5. Develop a general reliability-based approach to predict the remaining fatigue life of cracked or repaired components.

The first step, in-situ data collection, was performed on a large excavator during a short operating period during summer conditions [Yin et al. 2006], but still needs to be extended to other equipment and operating conditions. Fatigue material properties of the base metal have been established through testing [Yin et al. 2006, Wang 2010]. However, no data on the weld metal have been included in the material characterization tests. Deterministic approaches to predict fatigue resistance under constant amplitude loading were validated in an earlier research project at the University of Alberta [Chen et al. 2005]. An investigation of the effectiveness of the fatigue crack repair method of stop hole drilling with and without cold expansion of the hole is underway [Wang 2010]. The study presented in the following chapters deals primarily with welded details. The repair method of crack gouging and rewelding with and without subsequent ultrasonic peening is investigated in detail. A general reliability-based approach based on one of the deterministic approaches proposed by Chen et al. [2005] and extended to include initial imperfections and residual stresses is developed. Although the research program primarily focuses on heavy mining equipment, the approach is applicable to any steel structure subjected to cyclic loading, whether new, in-service (cracked or uncracked), or repaired. Although the approach is validated for constant amplitude fatigue loading conditions, a procedure to account for variability of loading is proposed. No in-situ measurements were carried out in the work presented in the following. Some other important aspects in fatigue life prediction, such as overloads, multiple crack interaction, or corrosion, are also beyond the scope of this study.

1.3 Methodology

Since fatigue testing of large scale components is time-consuming and expensive, small scale tests in conjunction with analytical methods are an attractive alternative to predict the fatigue performance of large scale components. The following methodology is applied in the present study:

- Definition of fatigue material properties for the base and weld metals;
- Laboratory testing of small scale welded butt joint specimens and of large scale flat plates containing a gouged and rewelded crack repair;
- Deterministic prediction of the test results using fracture mechanics approaches;

- Development of a probabilistic prediction model applied to the tested specimens;
- Calibration of the parameters used in the probabilistic model;
- Development of a general reliability-based approach to manage fatigue cracks.

The approach is defined in a general way to allow its adoption to any structural engineering application, with new or repaired components. In addition to fracture mechanics considerations, the efficiency of weld improvement methods is incorporated into the reliability analysis. Emphasis is placed on ultrasonic peening as a promising post weld treatment method.

1.4 Organization of the Thesis

The thesis consists of nine chapters, including the *Introduction*, and five appendices. The organization of the thesis is summarized in Figure 1.1.

Background information on fatigue crack initiation, crack propagation, fatigue repair methods, post weld treatment, and reliability theory in structural engineering and fatigue applications are presented in Chapter 2. Based on the conclusions from Chapter 2, a literature review of four fatigue related topics relevant to the research presented in this work, namely, the material properties, initial flaws in welds (size and shape), residual stresses, and post weld treatment through ultrasonic peening, is presented in Chapter 3.

In Chapter 4, the fatigue material properties defined from crack initiation and propagation tests on grade CSA G40.21-350WT steel are analysed to obtain statistical distributions of each parameter. Furthermore, tests on weld metal matching G40.21-350WT steel were carried out and the results are statistically analysed.

The details and results of an experimental program are presented in Chapter 5. Small scale welded butt joint coupons were tested under constant amplitude cyclic loading to investigate the performance of untreated, stress-relieved, conventionally peened, and ultrasonically peened specimens. Larger scale specimens containing a welded repair were investigated. Most of these specimens are untreated. The effect of ultrasonic peening was examined on three out of fourteen specimens.

In Chapter 6, a deterministic prediction of the small scale test results is made based on the background information presented in Chapter 2, the literature review (Chapter 3), and the fatigue material properties (Chapter 4). The dashed link in Figure 1.1 between Chapters 5 and 6 indicates that some information from the experimental program was used for the deterministic predictions. Finite element models are developed to obtain strains and stresses in the presence of an initial flaw. Different combinations of

parameters (initial flaw size and location, residual stress fields, four different sub-models in the crack propagation stage) are investigated.

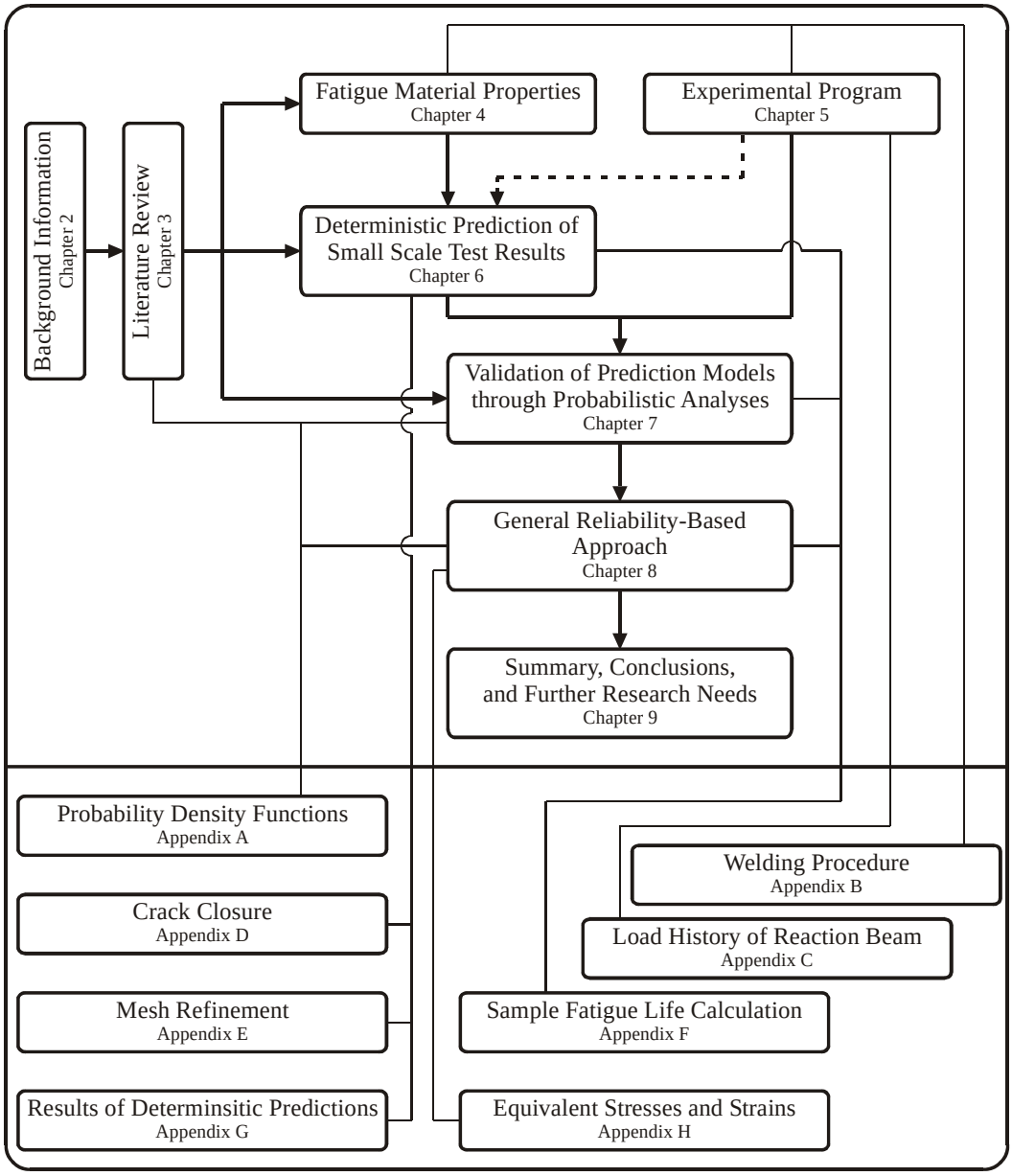

Figure 1.1 *– Organization of the thesis.*

In Chapter 7 the most appropriate of the approaches presented in Chapter 6 is selected and Monte Carlo Simulations (MCS) are conducted to obtain a probabilistic distribution of the predicted fatigue life for the small scale tests. MCS are also used to investigate the importance of each random variable. The most influential parameters are calibrated in order to obtain a better fit between the probabilistic predictions and the test results.

Based on the preceding work, a general reliability-based approach is proposed in Chapter 8. The approach is applied to three examples, two being predictions of test results and one being a prediction of the remaining fatigue life of a cracked excavator boom. The first two examples use constant amplitude loading from laboratory tests, whereas the latter uses in-situ measurements to characterise the loading.

Chapter 9 presents a summary, conclusions and recommendations for future work from the present study.

Additional information that was deemed too detailed to include in the body of the thesis is presented in appendix. Each appendix shown in Figure 1.1 is linked with a line to the chapter(s) where its content is used.

2. BACKGROUND

2.1 Introduction

The key concepts governing the work presented in this report are outlined in this chapter. First, relevant concepts of fatigue including the three stages of fatigue cracking – initiation, stable, and unstable propagation – are presented in Section 2.2. Different fatigue crack repair methods are summarized in Section 2.3, with emphasis on welded repairs. Finally, the issues of reliability in structural engineering applications and of the probabilistic analyses of the fatigue behaviour of welded structures are addressed in Section 2.4.

2.2 Fatigue

2.2.1 General

Repeated application of stress can initiate and cause the propagation of micro-cracks in materials. These cracks can grow to macroscopic proportions with the continued application of cyclic stress. This is the process known as fatigue. Unless otherwise noted, the term “fatigue” is intended to apply to mechanical and high-cycle fatigue. Mechanical fatigue is a result of the fluctuation of externally applied stresses, specifically without influence from environmental or time-dependent effects. In this work the term high-cycle fatigue refers to initiation and propagation of cracks under stresses that are less than the yield strength of the material, which results in fatigue lives that generally exceed 200,000 load cycles. The aim of this section is to give a brief introduction to the theory of fatigue.

2.2.2 Parameters Influencing Fatigue Life

The fatigue life of a member or structural detail is simply the number of stress cycles that can be sustained before failure. Some of the parameters that potentially influence the fatigue life of a structural detail are [Smith & Hirt 1989]:

- applied load spectrum;
- geometry and fabrication of the detail;
- material characteristics; and
- environmental effects.

All four parameters are addressed in the present work. Although for most applications in this work the load spectrum is well defined (from load controlled fatigue tests), a general approach to incorporate the uncertainty in fatigue loading of in-service structures is proposed in Chapter 8. The geometry and fabrication of the detail will be discussed in detail in this report. The fatigue relevant material characteristics of steels commonly used in heavy mining equipment and bridges have been investigated at the University of

Alberta [Chen et al. 2005, Yin et al. 2006, Wang 2010] and the results from these studies will be used. Fatigue properties of the weld metal will be determined experimentally in the present work (cf. Chapter 4). Although corrosion is an important factor in some applications, service temperature is the only environmental factor considered in this study.

Load Spectrum

Through a stress analysis, the load spectrum can be transformed into a stress spectrum, which is defined by the stress range ($\Delta\sigma = \sigma_{max} - \sigma_{min}$), the mean stress, and the stress sequence that a structural detail is subjected to. Fatigue tests on many different welded details have shown that $\Delta\sigma$ is the most important load-related parameter that governs the fatigue life of a detail [Gurney 1979b, Maddox 1991].

For welded details, it has been found that other stress parameters such as mean stress, which is commonly expressed through the stress ratio, $R = \sigma_{min} / \sigma_{max}$, have a negligible effect on fatigue resistance [Fisher et al. 1997]. The dependence of fatigue life solely on the stress range is largely a reflection of the presence of high tensile residual stresses, coupled with high stress concentration, at some locations of the welded detail. Post weld improvement methods, such as ultrasonic peening, aim to significantly reduce the tensile residual stresses and may even eliminate surface stress raisers such as weld profile imperfections and flaws. In such cases it is recognized that the mean stress has an effect on the fatigue resistance [Walbridge 2005].

Geometry and Fabrication of the Detail

At locations where both stress concentrations and tensile residual stresses are high, the detail will be particularly susceptible to fatigue cracking. The magnitude of stress concentration and tensile residual stresses is dictated by the geometry and fabrication of the detail. Due to the discontinuity caused by the presence of a weld and its shape, stress concentrations are created, cf. Figure 2.1. In addition, the weld surface is not smooth and may contain crack-like flaws, which further increase the stress concentration. The magnitude of the stress concentration due to the discontinuity depends on the detail geometry and needs to be addressed in the design process. The magnitude of the stress concentration due to flaws depends on the fabrication process and craftsmanship.

Welding invariably produces residual stresses. During the weld heating and cooling processes the weld material and the base material in the heat affected zone are restrained from expansion and contraction by the surrounding base material. Therefore, high residual stresses are introduced in the cooling stage.[1] The residual stress distribution varies both in the transverse and through-thickness directions of a welded structure and

[1] Transverse and longitudinal residual stresses are introduced. Only the generally more detrimental transverse residual stresses (i.e., parallel to the applied load) are considered here.

depends on factors such as the detail under consideration (size and shape) and the welding process and procedure.

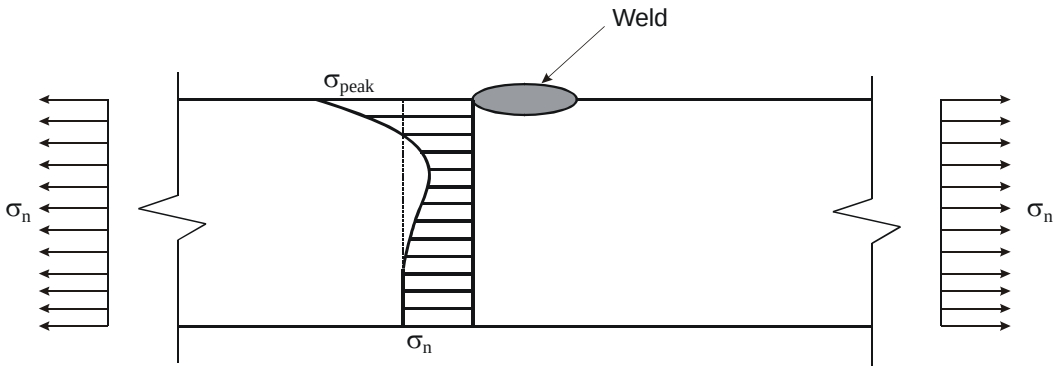

Figure 2.1 *– Stress concentration, σ_{peak}, caused by a weld bed due to shape discontinuity in a plate subjected to a uniform tension pressure, σ_n.*

Large plate dimensions are often used in heavy mining equipment and bridges and the so-called size effect needs to be considered for such components. According to Stephens et al. [2001] thicker, un-notched specimens under bending stresses show a reduction in fatigue resistance of up to 30% compared to similar thin specimens (< 10 mm). This is attributed to the steeper stress gradient present in small plate thicknesses, which reduces the volume of material subjected to the high stresses. Under axial stresses no reduction in fatigue strength due to the size effect is expected as the stresses in an un-notched specimen are uniformly distributed across the entire section. However, it must be noted that because of this uniform stress distribution, the axially loaded specimens show a fatigue limit reduction of up to 25% compared to the bending fatigue limit of specimens subjected to the same maximum stress [Stephens et al. 2001]. Welded details, which always contain flaws, also show a size effect. The probability of having a flaw of size large enough to be detrimental to the fatigue life increases with component size [Maddox 1991]. Therefore, a large welded component is more likely to have a severe crack initiation site and thus a shorter fatigue life than a small component with the same geometry and subjected to the same stresses.

Material Characteristics

Tests on non-welded specimens have shown that material characteristics—or more precisely the microstructure of metals—can influence the fatigue life of a member [Stephens et al. 2001]. In structural engineering applications, where most commonly low alloy steels are used, it is generally accepted that the material properties, particularly the tensile strength, does not affect the fatigue performance [Fisher et al. 1997]. However, investigations carried out at the University of Alberta [Chen et al. 2005, Yin et al. 2006, Wang 2010] yielded fatigue material properties that result in longer fatigue lives for high

performance steel (HPS) compared to common bridge steel (Grade 350WT), which has a lower tensile strength than HPS. In contrast to these findings, Garbatov & Guedes Soares [2004] suggest that the fatigue resistance decreases with an increase in tensile strength. In an application example they demonstrate that the fatigue life is 10 times longer for a detail consisting of 270 MPa actual yield strength compared to the same detail subjected to the same loading, but consisting of 400 MPa actual yield strength steel. No reason for the lower fatigue resistance of higher strength steels is given. An analysis of the University of Alberta data, supplemented by additional data collected in this research, will examine the effect of material characteristics (see Chapter 4).

Conversely, it is undisputed that the failure criterion (yielding of remaining cross-section or brittle fracture) is influenced by the material characteristics of the steel [Barsom & Rolfe 1999].

Service Temperature

It has been shown that service temperatures as low as -50°C do not significantly affect the fatigue behaviour of steel [Suresh 1998; Stephens et al. 2001; Kitsunai & Yoshihisa 1991]. Suresh [1998] and Stephens et al. [2001] suggest that the fatigue strength at low temperatures is slightly increased compared to room temperature fatigue strength due to the slight increase in tensile strength observed at low temperature. However, if brittle fracture is the governing failure criterion, low temperatures will decrease the fatigue life of the structure and may offset the beneficial increase in fatigue strength. For temperatures that significantly exceed the service temperatures of heavy mining equipment and bridges (> 300°C), the fatigue strength is reduced due to creep phenomena [Suresh 1998; Stephens et al. 2001].

For the expected range of operating temperatures of civil engineering structures, where -50°C < T < +50°C, the fatigue behaviour is not adversely affected by the service temperature. Therefore, the influence of service temperature on the fatigue strength is not further considered herein, with, of course, the exception when brittle fracture is the governing failure criterion.

2.2.3 Fatigue Design Methods

Two basic approaches for the fatigue design of members and elements have been commonly used in civil engineering applications. These are based on extensive physical testing and analytical studies. The two approaches are [Fisher *et al.* 1997]:

- Use of experimentally determined relationships between stress range and fatigue life ($\Delta\sigma - N$ curves);
- application of fracture mechanics principles.

Because of its ease of application, $\Delta\sigma - N$ curves are often preferred to the fracture mechanics approach. However, explaining the failure mechanism under fatigue loading

can not be done by the use of $\Delta\sigma - N$. Consequently, the work carried out here primarily applies fracture mechanics principles. However, comparisons of test and analytical results to $\Delta\sigma - N$ curves is done throughout this report and thus the $\Delta\sigma - N$ approach is described in the following as well.

Δσ – N Approach

$\Delta\sigma - N$ curves, which usually show the independent variable, $\Delta\sigma$, on the ordinate and the dependent variable , N, on the abscissa, have been established for a large number of structural details, mainly through testing of full-scale welded details. The test results are divided into various categories, reflecting the severity of stress raisers in the tested details. This approach of dividing details into fatigue categories is commonly used for the design of civil engineering structures.

Although based on the same test results and concepts, two different sets of fatigue curves are used in design: the $\Delta\sigma - N$ curves in the American Association of State Highway and Transportation Officials (AASHTO) Specification [AASHTO 2007] and the $\Delta\sigma - N$ curves in the European Convention for Constructional Steelwork (ECCS) Recommendations [ECCS 1985]. The AASHTO curves, which are also used in the Canadian Highway Bridge Design Code CAN/CSA S6-06 [CSA 2006], are illustrated in Figure 2.2. The different curves are designated as categories A to E , representing the fatigue strengths from the highest to the lowest, respectively. Each curve is uniquely defined by its fatigue life constant, A, and all curves have the same slope, $m = 3$. Similar information in the ECCS recommendations, not shown here, is designated by a detail category number, which represents the reference fatigue strength at two million cycles, $\Delta\sigma_c$.

Both constant amplitude and variable amplitude fatigue tests have indicated that the fatigue life of steel structures tends to be infinite if all the applied stress ranges are less than a threshold value, $\Delta\sigma_D$. This is called the constant amplitude fatigue limit (CAFL) and is represented by the horizontal portions of the $\Delta\sigma - N$ curves in Figure 2.2. As long as all stress ranges applied to a detail are lower than the CAFL for that detail, no fatigue damage is expected to take place. However, this approach can lead to an overestimate of the fatigue life when just a few cycles exceed the CAFL, resulting in a deterioration of the structure and a reduction of $\Delta\sigma_D$ [Kunz 1992]. This is taken into account in recent standards such as CSA–S16–01 [CSA 2001] and Eurocode 3 [CEN 2005] where a fatigue curve with a slope of $m = 5$ is used below the CAFL. Although the concept of a CAFL is used in most structural engineering standards, there is experimental evidence that a fatigue limit does not exist for many engineering materials, including steel [Rice et al. 1988, Bathias 1999, Tanaka & Akiniwa 2002].

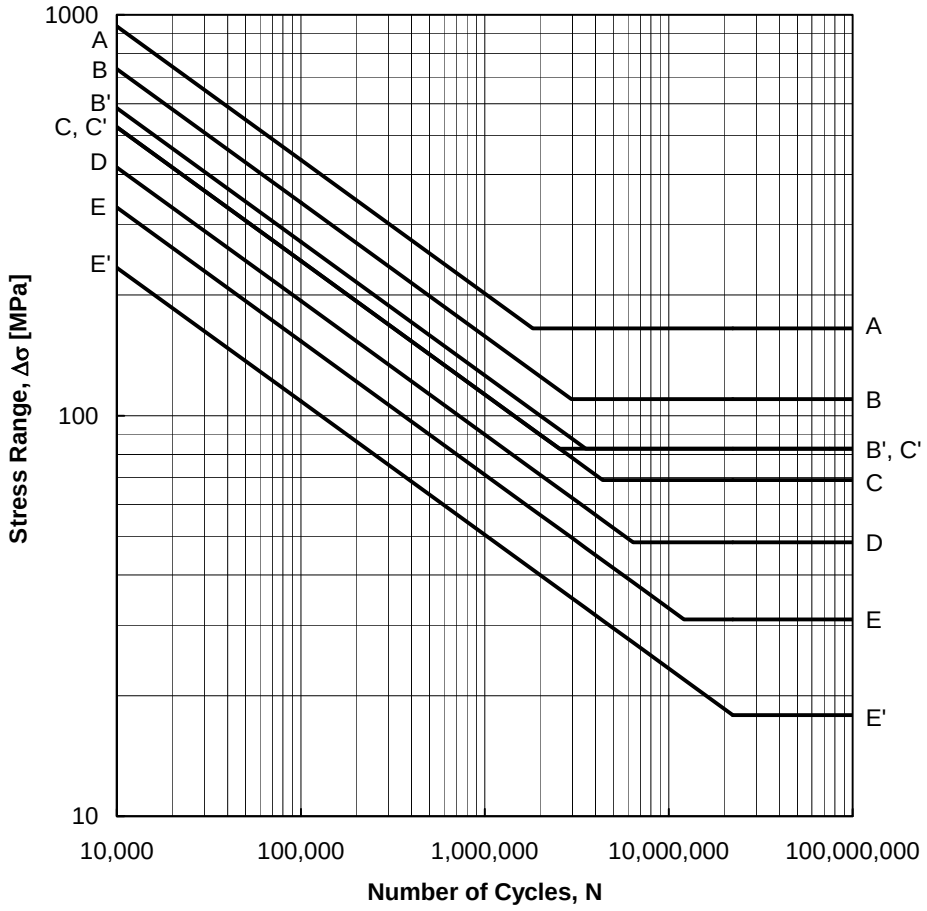

Figure 2.2 *– $\Delta\sigma - N$ curves according to AASHTO [2007].*

Common practice has been to obtain $\Delta\sigma - N$ curves from fatigue tests on full-scale details subjected to constant amplitude load cycles until failure of the specimen. A regression analysis of fatigue test results is conducted to obtain a design $\Delta\sigma - N$ diagram, which is taken as the mean minus two standard deviations from the mean [Klippstein 1987]. This procedure for defining the fatigue strength of a detail has several shortcomings:

- There is no consistent definition of failure (number of cycles to first detection of a crack, specific length of a crack, multiple detection of multiple cracks, etc.) and therefore the number of cycles to failure, N, is somewhat arbitrary.
- Unless the test results upon which the curves are based are rigorously investigated (initial flaw or crack sizes, actual stress concentration, crack growth behaviour), little information about crack initiation and propagation characteristics can be deduced from the $\Delta\sigma - N$ curves.
- If a crack is detected in a component, only vague predictions of the remaining fatigue life can be determined from $\Delta\sigma - N$ curves. This is

mainly due to the lack of information available prior to the crack detection (initial flaw or crack size and especially loading history).

- No distinction between crack initiation and crack propagation life is possible.
- The test data were fitted to curves having a predefined slope of 3 on a log-log scale. However, it is well established that some details follow slopes that are smaller than 3 [Stephens et al. 2001].
- Actual $\Delta\sigma - N$ curves, even on a log-log plot, are non-linear and not, as assumed in the regression analysis, straight lines [Wirsching 1995].
- By subtracting two standard errors of the estimate from the mean regression curve, a detail may be said to have the fatigue strength of a given category if not more than roughly 2.5% of the fatigue test data fall below the defined curve [Albrecht & Rubeiz 1990]. In other words a simplified confidence interval of approximately 95% is obtained. However, subtracting two standard deviations from the mean does not yield a constant probability of failure. Due to a non-constant standard deviation of $\log N$ for different stress ranges, $\Delta\sigma$, the true confidence limit is a curved surface [Nelson 1984]. Therefore, only a coarse reliability analysis can be carried out using $\Delta\sigma - N$ curves.

It has to be understood that the $\Delta\sigma - N$ curve approach is very rational for the design of new and for a first assessment of existing structures [Fisher et al. 1997]. However, more detailed analyses are often necessary, e.g. when a crack is detected in a structure and the remaining life needs to be estimated or when test data are not available for a certain detail (especially for large scale components that can not be readily tested). In such cases fracture mechanics often yields more reliable results than an assessment based on $\Delta\sigma - N$ curves. In particular, a fracture mechanics approach does not need to take into account the prior history of the investigated component.

2.2.4 Fracture Mechanics[1]

Fracture mechanics can be defined as an engineering discipline that quantifies the conditions under which a structure, or part thereof, fails due to the growth of a crack, a [Harris 1995]. It is a branch of continuum mechanics dealing with the stress field around a crack tip. In structural steel components cracks usually occur at locations containing high stress concentrations, high residual tensile stresses, initial flaws or some combination of these factors. These cracks might be present after fabrication or may have to initiate during the life of the structure. They grow in a stable manner under the application of cyclic loading until the crack size becomes sufficiently large to cause

[1] The term Fracture Mechanics is used here to describe the entire growth of a crack, i.e., its initiation and propagation. Only the crack opening mode (Mode I) is considered in the present work. This mode is predominantly present in structures containing a crack [Broek 1989].

unstable crack propagation. Accordingly, three stages of crack growth can be distinguished, as is shown in Figure 2.3:

A. Crack initiation stage
B. Stable crack propagation stage
C. Unstable crack propagation stage

During the crack initiation and stable crack propagation stages further damage can be avoided by either reducing the loading or by performing repairs. However, once the unstable crack propagation stage is reached the structural element can hardly be salvaged. In other words failure will take place.

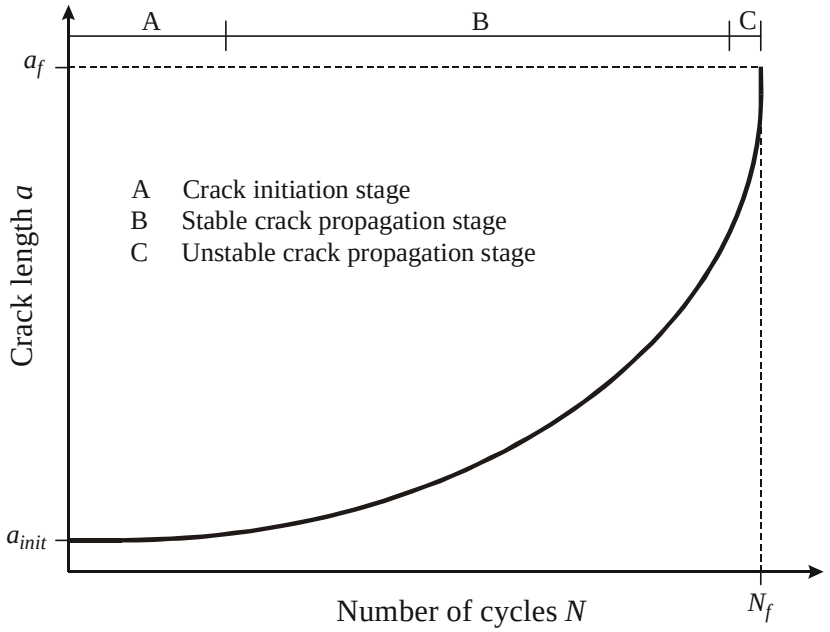

Figure 2.3 *– Schematic illustration of crack growth.*

Research on fracture mechanics started as early as in 1920 when Griffith [1920] investigated the fracture behaviour of glass. However, it was not until the Liberty ships, built during World War II with all welded steel hulls, showed signs of brittle fracture that significant research on fracture mechanics of metals really started. In the 1950's a breakthrough paper on stable and unstable crack growth in high strength steel and aluminium alloys was published by Irwin [1956]. At about the same time Forsyth [1952] observed in aluminium and aluminium-silver alloys that the mechanisms of failure at high and low stresses were fundamentally different. The crack initiation mechanism was first observed in aluminium-copper alloys by Forsyth [1953]. In spite of these significant advancements in fracture mechanics, it continued to receive little attention in structural engineering applications because of the straightforward use of $\Delta\sigma - N$ curves. However, the economic need to accurately predict the remaining fatigue life and to define adequate

inspection intervals of in-service structures has triggered interest in this field in the last 25 years [Pense et al. 1984, Maarschalkerwaart 1989, Brühwiler & Kunz 1993, Lovejoy 2003]. More background on fracture mechanics can be found in several comprehensive books, such as Broek [1989], Barsom & Rolfe [1999], or Anderson [2005].

The total fatigue life of a structural component is made up of the sum of the crack initiation life and the stable crack propagation life. As shown in the $\Delta\sigma - N$ plot of Figure 2.4, for small effective stress ranges most of the fatigue life is consumed by the initiation of a crack, whereas for high effective stress ranges the stable crack propagation stage becomes the governing phase.

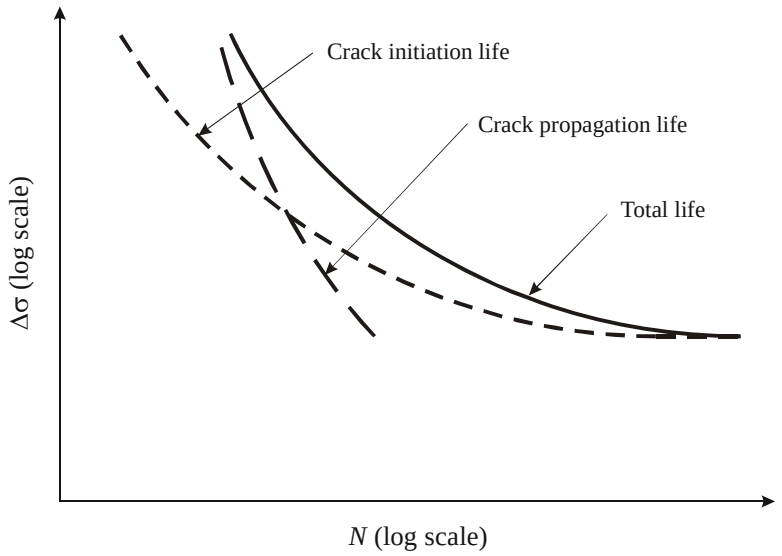

***Figure 2.4** – Schematic $\Delta\sigma - N$ curve divided into crack initiation and propagation.*

The term effective stress range is used here to describe actual stresses at the detail of interest. The effective stress range therefore accounts for stress concentration and residual stresses. Because of the presence of geometric imperfections, flaws, and tensile residual stresses, the actual stresses in welded details are high. It is therefore generally agreed that the crack initiation stage is negligible for welded components. However, the following three points need to be considered in determining whether this statement is true:

- The transition between crack initiation and stable crack propagation is not uniquely defined. At extremes, an engineer may define the transition as the nucleation of very small flaws along persistent slip bands, while others may define the transition as the stage at which a crack can be visually detected. Of course, between this wide range of viewpoints lies a broad band of other possible definitions.

- If post weld treatment, such as weld toe peening, is used, the high tensile residual stresses at the critical locations are substantially reduced or even eliminated.
- If the remaining fatigue life of a structure is determined with a reliability based approach, the crack initiation life should be incorporated in the investigation in order to achieve a more realistic estimate.

Crack initiation life can be determined using so-called empirical correlation approaches. The stable crack propagation life is best calculated using a linear elastic fracture mechanics (LEFM) approach. Before presenting these two approaches in greater detail, it is appropriate to discuss the transition between crack initiation and crack propagation and to outline some conventions regarding the definition of crack size.

Transition between Crack Initiation and Crack Propagation

Figure 2.5 shows that the crack initiation phase determined from a test includes the physical crack initiation (formation of slip bands and intrusions/extrusions) as well as the first part of the physical crack propagation stage (microcrack propagation). This reflects the difficulty in observing the crack initiation stage. The technical crack propagation stage only comprises the macrocrack propagation and final fracture. This observation is of great significance for the technical definition of the transition between the two phases (approaches for this definition are presented later in this section).

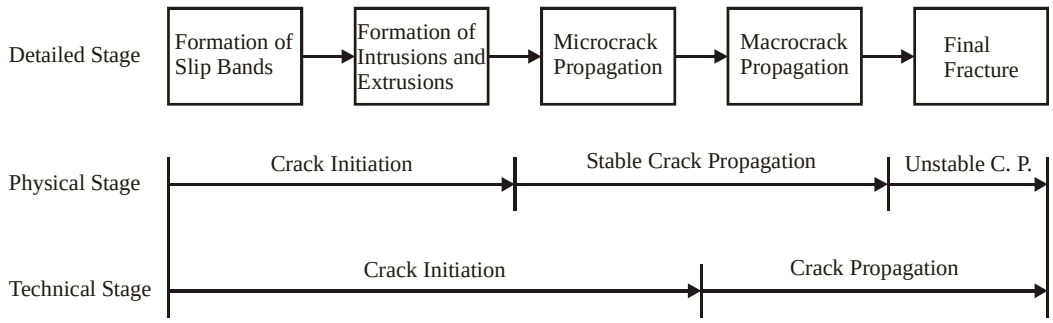

Figure 2.5 *– Physical and technical crack initiation and propagation phases.*

Definition of Crack Size

Cracks can be grouped into through-thickness cracks (Figure 2.6 a) and b)) and part-through-thickness cracks, such as embedded cracks and surface cracks (Figure 2.6 c) and d)). For a through-thickness crack the crack dimension is designated as $2a$ when two crack tips exist and a when there is only one crack tip (edge crack). Part-through-thickness cracks are usually modeled with an elliptical crack tip and the crack size is therefore defined by the major axis, c , and the minor axis, a . For an embedded crack, c

and a are equal to half the crack length and depth, respectively. For a semi-elliptical surface crack, c is equal to half the crack length and a is equal to the full crack depth.

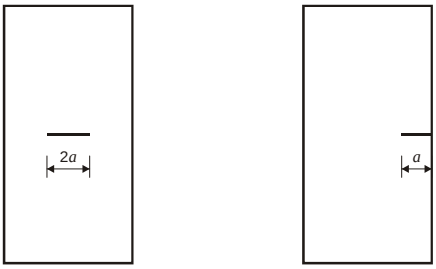

a) center through-thickness crack *b) edge through-thickness crack*

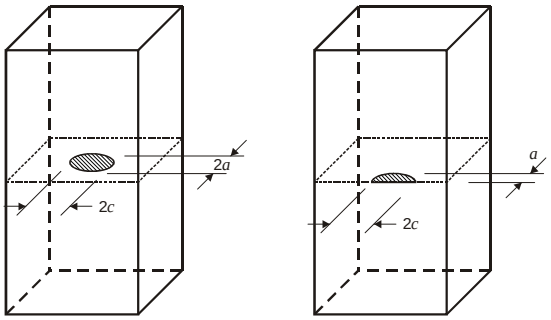

c) embedded elliptical crack *d) semi-elliptical surface crack*

***Figure 2.6** – Definition of crack size.*

Fatigue Crack Initiation

The formation of persistent slip bands as observed by Forsyth [1953] is at the origin of fatigue crack initiation. Under cyclic loading these persistent slip bands emerge to the surface, forming microscopic size intrusions and extrusions, which act as stress concentrations initiating a crack. To determine the crack initiation life empirical correlation approaches can be used. In these approaches damage parameters are correlated to fatigue test results. The following three methods of empirical correlation approaches are usually distinguished:

- stress-based method
- strain-based method
- energy-based method

[Chen et al. 2005] showed that in the presence of localized high stresses, which is usually the case in welded details, the strain-based method gives more accurate results than the stress-based method. For many applications the strain-based and energy-based methods yield similar results, although energy based approaches are superior for complex strain

fields. However, the energy-based method requires more complex and time consuming computations and is therefore not as well suited for a probabilistic analysis as the strain-based method. Therefore, only the strain-based method is used here and briefly outlined in the following. For more information on this method as well as the stress-based and energy-based methods, the reader is referred to Ellyin [1997], Suresh [1998], Dowling [1999] or Stephens et al. [2001].

Strain-Based Method

Initially developed in the late 1950s and early 1960s for low cycle fatigue of ductile materials, the strain-based method also applies for low to high cycle fatigue where small plastic strains exist [Stephens et al. 2001]. The method accounts for localized plastic deformations in regions where fatigue cracks initiate. It assumes that the material in highly strained areas, where cracks will form, behaves similarly to material in a smooth specimen under cyclic strain controlled loading with the same strain [Morrow & Socie 1981]. Knowing the localized strains – e.g. through measurements or an inelastic finite element analysis – the fatigue crack initiation life can be calculated using the un-notched strain-life properties of the material. Since the predicted crack initiation life is not very sensitive to the exact strain [Dowling 1982], the strain-based method is an effective tool for the prediction of crack initiation life.

The strain-based method uses a strain amplitude, $\Delta\varepsilon/2$, versus crack initiation life curve (strain-life curve), as shown in Figure 2.7. The total strain amplitude is resolved into elastic and plastic strain components that can be approximated by straight lines on a log-log scale. At a given number of initiation cycles, N_{init}, the total strain amplitude is the sum of the elastic and plastic strain amplitudes, resulting in the following expression for completely reversed strain cycles ($R = \varepsilon_{\min}/\varepsilon_{\max} = -1$):

$$\frac{\Delta\varepsilon}{2} = \frac{\Delta\varepsilon_{el}}{2} + \frac{\Delta\varepsilon_{pl}}{2} = \frac{\sigma_f'}{E}\left(N_{init}\right)^b + \varepsilon_f'\left(N_{init}\right)^c \tag{2.1}$$

where
$\Delta\varepsilon/2$: total strain amplitude (= half the total strain range)
$\Delta\varepsilon_{el}/2$: elastic strain amplitude
$\Delta\varepsilon_{pl}/2$: plastic strain amplitude
σ_f' : fatigue strength coefficient
E : modulus of elasticity
b : fatigue strength exponent
ε_f' : fatigue ductility coefficient
c : fatigue ductility exponent

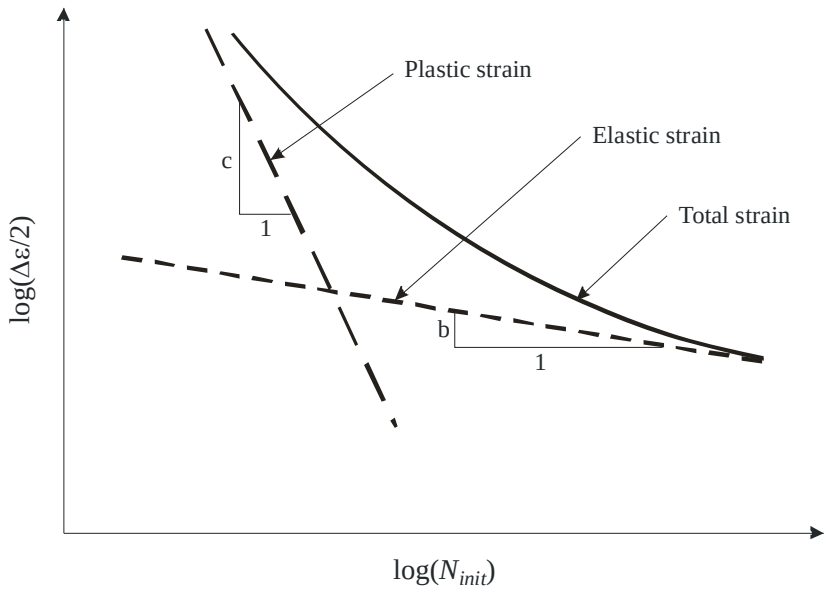

***Figure 2.7** – Schematic strain-life curve showing total, elastic and plastic strain components.*

The elastic component of equation (2.1) can be rewritten as:

$$\frac{\Delta\varepsilon_{el}}{2}E = \frac{\Delta\sigma}{2} = \sigma_f^{'}\left(N_{init}\right)^b \tag{2.2}$$

which is Basquin's equation [Basquin 1910]. The plastic component of equation (2.1) is called the Coffin-Manson relationship [Tavernelli & Coffin 1962].

As mentioned earlier, the total strain amplitude in a structural component, $\Delta\varepsilon/2$, is determined either by strain measurements at the detail or from an inelastic finite element analysis of the detail. The fatigue material properties $\sigma_f^{'}$, b, $\varepsilon_f^{'}$, and c are commonly established from regression analysis for the elastic and the plastic strain components of $\Delta\varepsilon/2-N$ test results on smooth specimens. These specimens are usually subjected to strain-controlled cyclic loading, i.e., the test is conducted under controlled constant amplitude strain. The elastic and plastic strain components are obtained from readings of stabilized cyclic stress–strain hysteresis loops, as illustrated in Figure 2.8. A hysteresis loop typically stabilizes after less than 1,000 cycles [Chen et al. 2005].

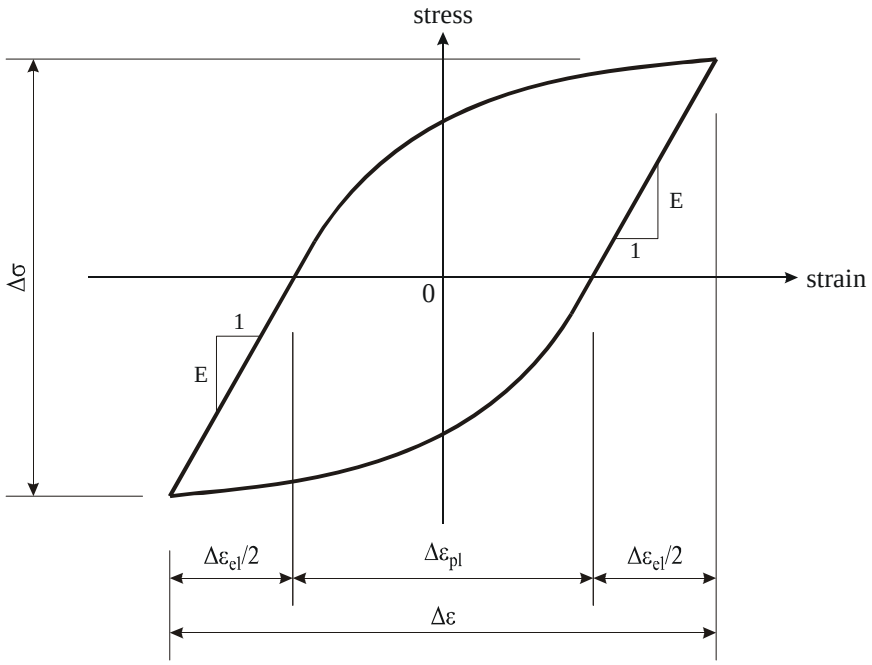

Figure 2.8 *– Stabilized cyclic stress–strain hysteresis loop.*

The modulus of elasticity, E , is obtained from the initial unloading portion in tension or in compression of the stabilized hysteresis loop. Alternatively, E can be determined from a cyclic stress–strain curve, as illustrated in Figure 2.9. The cyclic stress–strain curve is established by connecting the peaks of stabilized hysteresis loops from tests with different strain amplitudes. If the cyclic stress–strain curve lies above the monotonic curve, as is the case for the illustrative example shown in Figure 2.9, the material is said to show cyclic hardening behaviour. Conversely, if the cyclic stress–strain curve lies below the monotonic curve, the material is said to show cyclic softening behaviour.

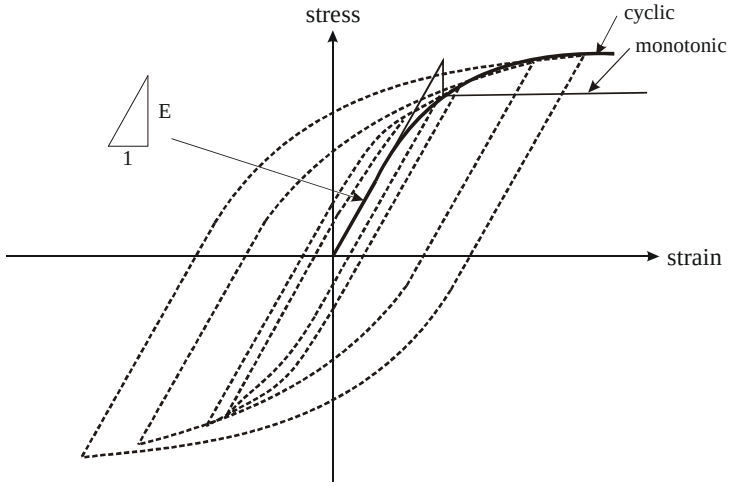

Figure 2.9 *– Cyclic stress–strain curve obtained from stabilized hysteresis loops.*

The cyclic stress–strain curve is usually described using the Ramberg-Osgood equation:

$$\varepsilon = \frac{\sigma}{E} + \left(\frac{\sigma}{K'}\right)^{1/n'} \tag{2.3}$$

where K' and n' are the cyclic strength coefficient and cyclic strain hardening exponent, respectively. In a finite element model, equation (2.3) should be used in place of the monotonic stress–strain relationship to determine the state of strain at the critical location of crack initiation.

If the modulus of elasticity, E, of the monotonic and cyclic stress–strain curves are assumed to be the same, which is a reasonable assumption for most practical purposes, the elastic and plastic strain components can be directly obtained from the following relationships [Stephens et al. 2001]:

$$\begin{aligned} \frac{\Delta\varepsilon_{el}}{2} &= \frac{\Delta\sigma}{2E} \\ \frac{\Delta\varepsilon_{pl}}{2} &= \frac{\Delta\varepsilon}{2} - \frac{\Delta\varepsilon_{el}}{2} \end{aligned} \tag{2.4}$$

where E is obtained from a monotonic tension coupon test.

The crack initiation life, N_{init}, for a given detail can be computed from the cyclic material properties and the calculated local strain amplitude by solving equation (2.1). It should be noted that for very long fatigue lives ($N_{init} > 10^7$), the $\Delta\varepsilon/2 - N$ curves tend to be very shallow and might even become horizontal for materials with a fatigue limit. Therefore, fatigue life predictions at low strain amplitudes are rather approximate, resulting in estimates that may vary by more than an order of magnitude [Morrow & Socie 1981].

Equation (2.1) is valid for completely reversed strain cycles ($R = \varepsilon_{\min}/\varepsilon_{\max} = -1$). In most civil engineering applications R is greater than –1, often surpassing zero. This is even more pronounced near welds, where high tensile residual stresses are present, which effectively increases the stress ratio, R. Therefore, the mean strain is not zero, but a tensile mean strain is present. To account for this, Smith et al. [1970] proposed the following relationship (often called the Smith-Watson-Topper or SWT model):

$$\frac{\Delta\varepsilon}{2} = \frac{\left(\sigma_f'\right)^2}{\sigma_{\max} E}\left(N_{init}\right)^{2b} + \frac{\sigma_f'\varepsilon_f'}{\sigma_{\max}}\left(N_{init}\right)^{b+c} \tag{2.5}$$

where $\sigma_{\max}$ is the maximum local stress accounting for plasticity. All other parameters are as defined in equation (2.1). The fatigue parameters ($\sigma_f', b, \varepsilon_f', c$) are the same as for a completely reversed test and thus need not to be determined again.

Stable Fatigue Crack Propagation

The stable fatigue crack propagation stage is modeled here with a linear elastic fracture mechanics (LEFM) approach. Paris & Erdogan [1963] showed that the log of the crack growth rate in the stable propagation stage, da/dN, is directly proportional to the log of the stress intensity factor range, $\Delta K = K_{\max} - K_{\min}$. This relationship is expressed as:

$$\frac{da}{dN} = C \cdot \Delta K^m \tag{2.6}$$

where C and m are material constants determined from crack growth tests as explained in Chapters 3 and 4.

The stress intensity factor, K_i, is a measure to describe the stress field at the tip of a crack. K_i is a function of the crack size and shape, the location of the crack relative to a free surface, the crack size relative to the plate size in which the crack is located, and the applied stress magnitude and distribution. A general expression for K_i is as follows [Albrecht & Yamada 1977]:

$$K_i = \beta_E \cdot \beta_S \cdot \beta_W \cdot \beta_G \cdot \sigma_i \cdot \sqrt{\pi a} \tag{2.7}$$

where σ_i is the magnitude of the stress field at some distance away from the crack tip (e.g. the structural nominal stress), a is the crack size, and:

β_E	:	crack shape correction factor (e.g. elliptical versus straight crack front)
β_S	:	free surface correction factor
β_W	:	finite width (or thickness) correction factor
β_G	:	stress gradient correction factor (accounting for non-uniform stress distribution along the anticipated crack path)

Numerous relationships for the computation of the correction factors, β_i, are given in the literature. The advantage of calculating K_i with equation (2.7) is the availability of the solution for β_i and σ_i for a wide range of conditions, thus rendering this method very practical. However, in complex structural components the solution for β_i and σ_i is not readily available. In such cases finite element procedures are preferred, where the considered component or part thereof, including flaws or cracks, is modeled to the desired degree of detail. One of the following three methods is commonly used to compute K_i from finite element analysis results:

- displacement method [Banks-Sills 1991]
- stress or force method [Raju & Newman 1979]
- energy method [Rice 1968]

However, these analytical methods are not practical for a probabilistic assessment, where a multitude of crack and flaw sizes, shapes and locations need to be considered using finite element models. Therefore, these three numerical methods are not further considered and the reader is referred to the references given above for more information.

As stated above, the stress intensity factor range is normally defined as the algebraic difference between the stress intensity factors corresponding to the maximum and minimum applied stresses, i.e., $\Delta K = K_{\max} - K_{\min}$. ASTM standard E647 *Standard Test Method for Measurement of Fatigue Crack Growth Rates* [ASTM 2000] allows the use of $\Delta K = K_{\max}$ for stress ratios of $R < 0$, which essentially means that only the tension portion of the stress cycle needs to be considered. This results in $\Delta\sigma = \sigma_{\max} - \sigma_{\min}$ for $R > 0$ and $\Delta\sigma = \sigma_{\max}$ for $R \le 0$.

The stable crack propagation life, N_{prop}, can be determined by integrating equation (2.6) from an initial crack size, a_0, to a final crack size, a_f:

$$N_{prop} = \int_{a_0}^{a_f} \frac{da}{C \cdot \Delta K^m} \tag{2.8}$$

The relationship between ΔK and da/dN is schematically represented on the log-log scale of Figure 2.10. It has been observed in numerous tests that, analogous to the constant amplitude fatigue limit, no crack growth occurs for stress range intensity factors below a threshold value, ΔK_{th} [Dowling 1999]. In order to correctly predict the crack growth, this threshold has to be incorporated into equation (2.6). The transition shown in Figure 2.10 is best modelled by [Ohta et al. 1986]:

$$\frac{da}{dN} = C \cdot \left(\Delta K^m - \Delta K_{th}^m\right) \Rightarrow N_{prop} = \int_{a_0}^{a_f} \frac{da}{C \cdot \left(\Delta K^m - \Delta K_{th}^m\right)} \tag{2.9}$$

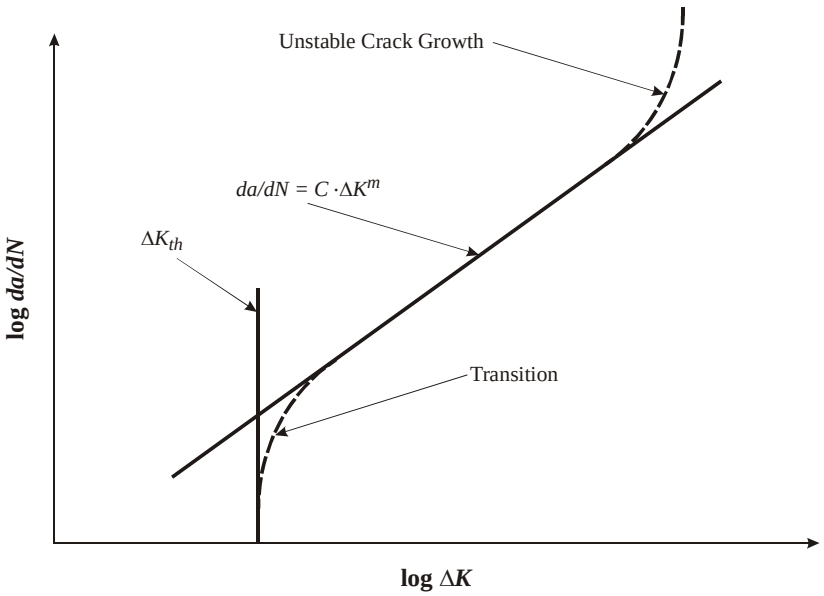

***Figure 2.10** – Schematic $da/dN - \Delta K$ curve.*

The threshold stress intensity factor range, ΔK_{th}, is not just a material constant, but depends on several factors with the most significant being the stress ratio, R [Gurney 1979b].

Combining Crack Initiation and Stable Crack Propagation

In order to combine the crack initiation and stable crack propagation approaches outlined above, the transition between these crack stages needs to be adequately defined. If the initial flaw size a_{init}, is larger than the crack size corresponding to the transition between the crack initiation stage and the crack propagation stage, a_{trans}, only the stable crack propagation life needs to be taken into account with $a_0 = a_{init}$ in equation (2.9). However, if $a_{init} < a_{trans}$, the crack initiation life, N_{init}, determined using equation (2.5), and the stable crack propagation life, N_{prop}, calculated using equation (2.9) with $a_0 = a_{trans}$, have to be added to get the total fatigue life, N.

The definition of the transitional crack size, a_{trans}, is not trivial. Socie et al. [1979] and Dowling [1979] have independently proposed approaches to define this crack size. Socie et al. [1979] proposed that a fatigue crack has initiated when the fatigue damage due to crack propagation mechanisms exceeds that due to crack initiation or strain cycle fatigue mechanisms. This concept is illustrated in Figure 2.11, where the crack initiation and propagation growth rates, da/dN_{init} and da/dN_{prop}, respectively, are plotted as a function of the distance from the notch root along the expected crack path. The transitional crack size, a_{trans}, is defined as the distance from the notch root, where the two crack growth rates are equal.

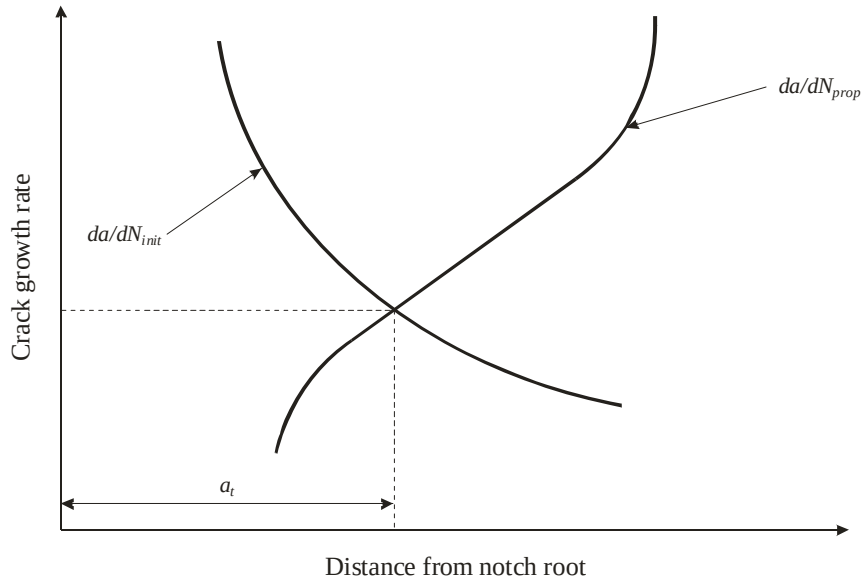

Figure 2.11 *– Crack initiation and propagation growth rates as a function of the distance from the notch root [Socie et al. 1979].*

Although the Socie et al. [1979] approach is intuitive and should result in a reliable definition of a_{trans}, its implementation in probabilistic models is not very practical because it involves the computation of the crack initiation and propagation growth rates. Therefore, this approach was not adopted for the work that follows. However, the underlying theory of the Socie et al. [1979] approach is of relevance because it illustrates that the crack propagation phenomena for small cracks (i.e., during and shortly after initiation) and large cracks (i.e., during propagation) are very different.

According to Dowling [1979], a_{trans} can be obtained by equating the stress intensity factors for short and long cracks, $K_s = 1.12 k_t \sigma \sqrt{\pi \Delta a}$ and $K_l = \beta \sigma \sqrt{\pi (a_{init} + \Delta a)}$, respectively, resulting in:

$$a_{trans} = \frac{a_{init}}{(1.12 \cdot k_t / \beta)^2 - 1} + a_{init} \tag{2.10}$$

wherein a_{init} is the initial flaw size as defined above, Δa is the crack extension measured from the edge of the initial flaw, σ is the applied stress, and

k_t : elastic stress concentration factor for a short crack, $k_t = 3.0$ for a circular notch;

β : product of the stress intensity correction factors in equation (2.7).

Dowling's assumption of a circular notch is applicable only in special situations, as for example at bolt holes or at perfectly circular and flat inclusions. To account for other flaw shapes (e.g. ellipsoid), a more general expression for a_{trans} should be used.

It has been documented that small cracks can propagate faster than large cracks and do so even below the threshold stress intensity factor range, ΔK_{th}, defined in equation (2.9) [Davidson 2004]. Several mechanisms are believed to be at the origin of the fundamental difference in crack propagation behaviour of small and large cracks. One of the most important observations in small cracks is that mode II loading (sliding or in-plane shear mode) is present in addition to mode I loading (tensile or opening mode). This is mainly due to anisotropic deformation within the plastic zone in front of small cracks. An accurate incorporation of small and large crack growth behaviour into a single crack propagation model is very complex. A simple approximation to compensate for the small crack effect is the extrapolation of the Paris equation (2.6) below ΔK_{th} [Owen et al. 1989], therefore neglecting ΔK_{th} in equation (2.9). It has to be noted that using this approximation can either result in conservative or non-conservative predictions, depending on the small crack behaviour [Stephens et al. 2001].

Some Comments Concerning Fracture Mechanics

As stated in Section 2.2.3, a fracture mechanics approach is often preferred to the use of $\Delta\sigma - N$ curves when more detailed analyses of the fatigue behaviour of a component are necessary. However, the fracture mechanics approach has several shortcomings:

- Many of the parameters in equations (2.5) and (2.9), which will be used in the present work to describe the crack initiation and stable crack propagation stages, are subjected to significant variability. These uncertainties need to be adequately accounted for with a reliability-based approach.
- Both equations are based on a combination of solid mechanics principles and observations from fatigue tests and are thus not exact scientific approaches.
- More expertise is required to apply fracture mechanics than a $\Delta\sigma - N$ approach.

2.2.5 Fatigue Failure Criteria

There is no unique definition of fatigue failure. Depending on the design philosophy, the accepted level of fatigue damage can vary widely. Therefore, it is important to define a design philosophy for the particular case under consideration. Stephens et al. [2001] distinguish the following four design criteria:

- Infinite-life design: For this design approach all stresses – or strains – are kept below the fatigue limit so that the structure has essentially an infinite fatigue life.
- Safe-life design: The structure is designed to withstand all load cycles during its expected service life. For a structure that is kept in place after the desired service life has expired, fatigue damage is possible.
- Fail-safe design: The formation of cracks is not excluded and the structure is designed so that cracks will not lead to failure before they are detected and repaired. Such designs include load path redundancies and crack stoppers.
- Damage-tolerant design: Cracks are assumed to exist and fracture mechanics principles and tests are used to determine the propagation and failure criterion of such cracks. The adequate definition of inspection intervals guarantees that the structure can be repaired or replaced before failure occurs.

A damage-tolerant design approach should be adopted for the assessment or retrofit of existing structures [Sedlacek et al. 1992, Kunz & Hirt 1993]. Inspection techniques, the crack growth behaviour, and the residual strength of the component in the presence of the detected crack are the three main considerations in damage-tolerant design. It can be expected that for the components considered in the present work, a damage can always be detected before failure takes place, as long as adequate inspection intervals and techniques are set in place.

The residual strength is commonly governed by yielding of the gross section, ductile or brittle fracture of the cracked section, or a combination of both. Failure can also occur by buckling for components subjected to compressive stresses or by a loss of stiffness or leakage problems resulting in unacceptable serviceability performance. In practice, it is often easier to define the final – or failure – crack size, a_f, at a certain stage in crack propagation. For example, a_f is conveniently defined as a through-thickness crack for containment vessels where leakage becomes a serviceability problem. As crack propagation rates for through-thickness cracks are substantially higher than for surface or embedded cracks, resulting in comparably small residual lives once a part-through crack becomes a through-thickness crack, this failure criterion is also reasonable for other structural components.

For more information on the residual strength of cracked components the reader is referred to the literature [e.g. Rolfe et al. 1989, Brozzetti et al. 1991, Stranghöner et al. 1998, Barsom & Rolfe 1999]

2.3 Fatigue Repair Methods

2.3.1 Introduction

Once a crack has been detected in a structure, various courses of action can be taken:

1. Monitor the crack over time based on a fracture control plan defining inspection intervals and techniques;
2. Repair the crack by adequate means;
3. Replace the cracked component.

In civil engineering structures it is often advantageous to take the first course of action and monitor the crack, which usually takes years to grow to a critical size. This, however, may not be possible in heavy mining equipment, where cracks can grow to a critical size within days. Replacement of the cracked component is usually not economical since the machine would have to be temporarily taken out of service. Therefore, repair of the detected cracks, which ought to be easily and quickly done, have to be carried out. These repairs have to be reliable as to ensure safe operation of the equipment until a planned shut-down of the machine can be implemented, where the component can be substantially repaired or replaced. In Section 2.3.2 some repair methods are presented. Possibilities of welded repairs are listed in Section 2.3.3, with more detailed information given concerning welded cover plating and gouging with subsequent rewelding. Sections 2.3.2 and 2.3.3 present only the most commonly used repair methods for civil engineering structures and heavy mining equipment. Information on additional repair methods can be found elsewhere, e.g. Manson [1971], Rodriguez-Sanchez et al. [2004], or Perez-Guerrero & Liu [2005].

2.3.2 Mechanical Repairs

Mechanical repairs are considered herein as all the repair methods that do not use any welding or weld improvement methods. Among the most commonly employed are:

- Detail improvement [Connor & Fisher 2006]
- Drilling of stop hole [Pedersen 2004]
- Drilling of stop hole and insertion of a pretensioned bolt [Roeder et al. 2005]
- Drilling of stop hole with subsequent hole expansion [Ball & Lowry 1998]
- Bolted cover splices [Hassan & Bowman 1996]
- Composite patches [Colombi et al. 2003]

A further possibility leading to a potential improvement of the crack growth behaviour is overloading [Wei & Shih 1974]. However, this is rarely done because the application of such an overload is difficult and, furthermore, could lead to detrimental effects on other parts of the structure.

Detail improvement should always be the priority concerning the fatigue performance of new structures. However, for existing structures detail improvement may not be possible. An exception are displacement induced fatigue details, such as the web gaps in stiffened girders, whose fatigue behaviour can readily be improved by reducing or stopping the distortion [Connor & Fisher 2006].

The majority of repairs in bridges are of the mechanical type [Fisher 1984, IIW 2002]. The reason for this is mainly the belief – and sometimes the evidence – that welded repairs are often ineffective due to the introduction of stress concentration, high tensile residual stresses, and flaws such as slag inclusions or entrapped gas. Since fatigue repairs on bridges have to be carried out in the field, quality assurance criteria are often difficult to meet. However, with skilled welders and modern welding procedures weld repairs become economically viable for bridge structures [Gregory et al. 1989].

2.3.3 Welded Repairs

Welded repairs can be divided into three main categories:

- Weld improvement methods;
- Crack bridging with welded plates;
- Rewelding.

Weld Improvement Methods

As indicated earlier, the reduced fatigue performance of welded details is generally attributed to stress concentrations, weld flaws, and high tensile residual stresses introduced by welding. To improve the fatigue performance of welded structures it is therefore necessary to address one or more of these deficiencies. This can be done either

by improving the design, by controlling the quality of fabrication, or by treating the weld after fabrication. These improvement methods are discussed below.

Design Considerations

The most efficient and least expensive fatigue improvement of welded structures can be achieved at the design stage. Welded details are best placed in low stress regions. This, however, is not always practical. For example, stiffeners in girders need to be positioned according to shear design considerations and high bending moment regions in the vicinity of a stiffener cannot always be avoided. Nevertheless, even in such cases good design can reduce the probability of fatigue failure. Among the most important design considerations are:

- Using continuous welds in preference to discontinuous welds;
- Using gradual changes and not sudden changes in stiffness;
- Using full penetration groove welds rather than fillet welds;
- Avoiding intersecting welds;
- Using thin and/or short attachments;
- Applying protection on corrosion susceptible details;
- Controlling the weld shape [Haagensen et al. 1987];
- Using advanced welding technologies [Bright &.Smith 2004] or special electrodes [Ikeda et al. 1978].

With the introduction of high performance steels for structural applications it was hoped that the fatigue resistance of a given detail could be increased in the design stage. However, high strength steels often complicate the fatigue design since they are subjected to higher stresses [IABSE 2005], more than offsetting the potential increase in fatigue resistance.

Quality of Fabrication

Welds always contain flaws that can create localized stress concentrations [Gourd 1995]. The acceptability of a weld flaw depends on a number of factors, such as its size, shape, and location, the loading condition (static, dynamic, fatigue, etc.), the service temperature the detail is subjected to, the material constraint (plane strain, plane stress, etc.), the material properties of the detail, and the consequence of the failure of a weld or component. The most common welding flaws having a significant effect on the fatigue behaviour are [Radaj 1990]:

- Cracks
- Pores and shrinkage cavities
- Solid inclusions
- Lack of fusion and inadequate penetration
- Undercuts, misalignment and other shape imperfections

Controlling the quality of fabrication reduces the severity of or even eliminates detrimental flaws. Guidelines for the acceptability of flaws for different applications can be found in several specifications and codes such as BSI [2005], ASME [2004], or AASHTO [2002].

Post Weld Treatment

Post weld treatment methods aim at improving one or several of the three weaknesses inherent to welding, i.e., stress concentrations due to the weld geometry, presence of initial flaws, and high tensile residual stresses. The following methods are commonly employed in structural engineering:

- Local machining, such as grinding, is aimed at reducing stress concentrations due to weld geometry. It may also remove surface flaws, but it can introduce new mechanical flaws such as surface scratches.
- Tungsten inert gas (TIG) dressing or plasma arc dressing primarily aim at reducing stress concentrations due to improved weld geometry. It may also remove surface flaws.
- Prior overloading aims at introducing compressive residual stresses at the critical locations.
- Stress relieving either by thermal treatment, vibratory stress relief, spot heating, or Gunnert's method[1] aims at relieving tensile residual stresses.
- Peening is used to introduce high compressive residual stresses where tensile residual stresses existed.

An exhaustive account of post weld treatment techniques can be found in Kirkhope et al. [1999a, 1999b]. Several researchers have demonstrated that ultrasonic peening, which is a relatively new post weld treatment application, results in more significant fatigue life improvements than overloading, TIG-dressing, or thermal stress-relieving [Haagensen et al. 1998, Huo et al. 2005, Kudryavtsev et al. 2005]. Furthermore, Kudryavtsev et al. [2005] have shown that repairing a fatigue crack by rewelding with subsequent application of ultrasonic peening is more effective than repairing an identical crack by drilling a stop hole (with and without installation of a pretensioned bolt).

Crack Bridging with Welded Plates

Crack bridging with welded plates is commonly referred to as "fishplating". The term "fishplate" was originally used in the railway industry for the splice plates that connect

[1] In spot heating material, a specific distance away from the weld toe is heated. By choosing the right spot, the subsequent cooling will result in compressive residual stresses at the weld toe (equilibrating the tensile residual stresses at the heated spot). In Gunnert's method the weld toe itself is heated and then rapidly quenched. Differential cooling introduces compressive residual stresses at the weld toe.

the ends of two rails.[1] Welded fishplates have been widely used as an expedient and rapid repair method for fatigue cracks heavy mining equipment. They are attached to the cracked plate with a circumferential fillet weld, the thickness of the fishplate usually being the same as the cracked plate. Welded fishplates create a significant stress concentration at the abrupt change of geometry, which in addition to the usual conditions of potential cracking at the toe of a fillet weld further diminish the fatigue resistance of the detail. Fishplating is not commonly used for the repair of fatigue cracks in bridges mainly for this reason. However, with the application of post weld treatment methods such as grinding or peening, there is potential to at least partially offset this shortcoming, resulting in an economical and expedient repair.

Rewelding

Prior to rewelding, an existing crack needs to be removed by gouging [Gregory et al. 1989]. The *Structural Welding Code – Steel* [AWS 2006] defines gouging as "a thermal cutting process variation that removes metal by melting or burning the entire removed portion, to form a bevel or groove." After gouging the repair is completed by filling the bevel with weld metal. Gouging and rewelding has been used as a repair method for fatigue cracks in different structures, such as mining equipment [Vandenberg 2005], bridges [IIW 2002], ships [Kelly & Dexter 1997] and railway rails [Jeffus 1999]. However, there seems to be little scientific grounds to quantify its efficiency and economics.

Since fishplating creates a fatigue detail similar to end welded cover plates, which have been extensively investigated [Albrecht & Lenwari 2007], emphasis in the present work will be placed on gouging and rewelding. One of the main objectives is to establish an analytical procedure to quantify the effectiveness of this crack repair method. The procedure should be formulated in a general way as to ensure its applicability to fishplating or any other fatigue detail, whether new or repaired.

2.4 Reliability Concepts and Probabilistic Analyses

2.4.1 Introduction

Structural engineering strives to achieve an optimal design of a structure and its components, i.e., the structure should perform satisfactorily throughout the desired service life, considering economic aspects. However, there is always a probability that a structure or part thereof will need to be repaired or even replaced prematurely. The probability of premature failure can be lowered by "overdesigning" but to the detriment

[1] The origin of the term "fish" is not quite clear but could come from the French word "fiche" which means fixation.

of higher costs. This, of course, is not desirable, either for the client or for the engineer. Therefore, adequate safety at reasonable cost must be the goal. This can be achieved by implementing reliability concepts. The bases of these concepts are briefly described in the following section. The current use of probabilistic analyses in fatigue life predictions of welded structures is presented in Section 2.4.3.

2.4.2 Reliability Concepts in Structural Engineering Applications

The general perception of a structural failure is often associated with collapse. But even unsatisfactory performance, such as excessive deflections or cracking of concrete, can be interpreted as failure [Ang & Cornell 1974]. Modern design standards define failure associated with collapse as an ultimate limit state and that of unsatisfactory performance as a serviceability limit state [Kulak &Grondin 2002]. These limit states are generally described by limit state functions, $G(\mathbf{Z})$, which take the following form:

$$\begin{aligned} G(\mathbf{Z}) > 0 \quad &\Rightarrow \text{the limit state is satisfied, i.e., there is no failure} \\ G(\mathbf{Z}) < 0 \quad &\Rightarrow \text{the limit state is violated, i.e., there is failure} \end{aligned} \tag{2.11}$$

where $\mathbf{Z}$ is the vector of the design variables, z_i, needed to describe the various sources of uncertainty associated with the limit state. The particular case of $G(\mathbf{Z}) = 0$ is called the failure surface [Madsen et al. 1986].

Basic Reliability Problem

The basic reliability problem in structural engineering can be described by two statistical random variables, which are assumed to be independent: one representing the resistance, R, and the other representing the load effect – also called solicitation – S [Melchers 1999]. For $R > S$, the structure is safe. The failure surface is defined by $R = S$ or expressed as a limit state function $G(\mathbf{Z}) = R - S = 0$. It follows that the probability of failure, p_f, is defined as:

$$p_f = P(G(\mathbf{Z}) < 0) = P(R - S < 0) \tag{2.12}$$

where $P(\bullet)$ denotes the probability of occurrence of event "$\bullet$".

If the statistical design variables, z_i, are assumed to be normally distributed, then R and S are also normally distributed [Weisstein 2003] and the probability of failure, p_f, takes the form of [Melchers 1999]:

$$p_f = \Phi\left(\frac{-(\mu_R - \mu_S)}{\sqrt{{\sigma_R}^2 + {\sigma_S}^2}}\right) = \Phi\left(\frac{-\mu_{\mathbf{Z}}}{\sigma_{\mathbf{Z}}}\right) = \Phi(-\beta) \tag{2.13}$$

where μ_R and μ_S are the mean values of the resistance and the load effect (solicitation), respectively, and σ_R and σ_S are the corresponding standard deviations. Figure 2.12a shows the basic reliability problem in terms of the probability density functions (pdf) of

R, $f_R(z)$, and S, $f_S(z)$. Where the two curves overlap, the resistance is smaller than the load effect and the structure fails, i.e., the shaded area under the curves is a measure of the probability of failure, p_f. The same information can be presented with respect to the limit state function $G(\mathbf{Z}) = R - S$, as illustrated on Figure 2.12b. Here the probability of failure, p_f, is described by the part of the curve to the left of the origin ($\mathbf{Z} = 0$). The distance from the mean value of $G(\mathbf{Z})$, $\mu_{\mathbf{Z}}$, to the origin is defined as $\beta \cdot \sigma_{\mathbf{Z}}$, where $\sigma_{\mathbf{Z}}$ is the standard deviation of $G(\mathbf{Z})$ and β is called the safety index [Cornell 1969].

It is evident from Figure 2.12b that by moving the origin to the right, the probability of failure, p_f, increases. Since $\mu_{\mathbf{Z}}$ and $\sigma_{\mathbf{Z}}$ remain unchanged for a given problem, the safety index, β, decreases. Conversely, to decrease the probability of failure, p_f, the safety index, β, has to increase. This concept is the basis of limit states design.

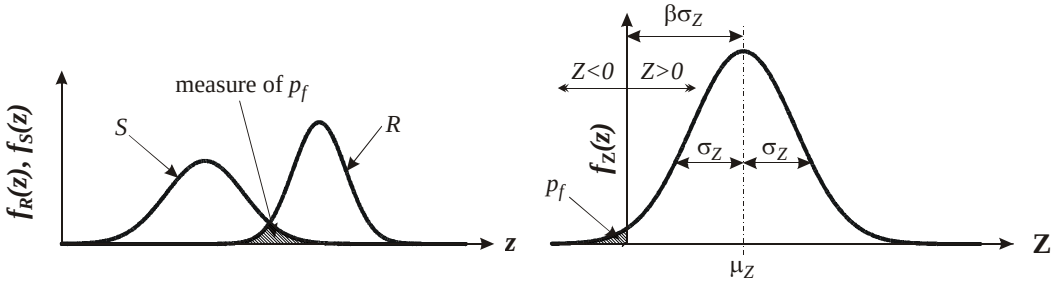

a) in terms of the pdf's of R and S *b) in terms of the pdf of $G(\mathbf{Z}) = R - S$*

***Figure 2.12** – The basic reliability problem.*

Limit State Function in Structural Engineering

The limit state function in modern structural engineering standards is written in the form of [Galambos & Ravindra 1977, Bartlett et al. 2003]:

$$(\phi \cdot R_n)_k \geq \left(\sum_{i=1}^{n} \gamma_i \cdot S_{ni} \right)_j \tag{2.14}$$

where ϕ is the resistance factor and R_n the nominal resistance of the structural element for the limit state k. S_{ni} is the nominal load effect due to the load i, which is multiplied by its respective load factor, γ_i, for the load combination j. Combinations of ϕ and γ_i can be determined from equation (2.14). Since there is an infinite number of such combinations, code writers first have to establish reasonable values of γ_i, because these should preferably be material independent. The resistance factor, ϕ, can then be determined from the desired value of the safety index. The definition of a reasonable value for the safety index, β, poses some problems. Most code writers have adopted the approach of calibrating β based on past performance using the allowable stress design method. Subsequent experience in practical applications of a design standard can then result in adjustments of β.

Generalized Reliability Problem

Unfortunately, not all variables, x_i, can be assumed to be normally distributed and the rather straight forward use of equation (2.13) is not valid for any distribution of x_i. Therefore, the generalized expression of the probability of failure, p_f, for the limit state function, $G(\mathbf{Z})$, has to be applied [Ang & Tang 1984]:

$$p_f = P(G(\mathbf{Z}) < 0) = \int_{G(\mathbf{Z})<0} \dots \int f_{z_1,\dots,z_n}(z_1 \dots z_n) \mathrm{d}z_1 \dots \mathrm{d}x_n = \int_{G(\mathbf{Z})<0} f_{\mathbf{Z}}(\mathbf{z}) \mathrm{d}\mathbf{z} \qquad (2.15)$$

where $f_{z_1,\dots,z_n}(z_1 \dots z_n) = f_{\mathbf{Z}}(\mathbf{z})$ is the joint probability density function (pdf) of the design variables $Z_1, \dots, Z_n = \mathbf{Z}$.

Direct integration of equation (2.15) is very rarely practical and one of the two following approaches, which will be discussed in more detail in Chapter 7, is usually adopted:

- use of numerical methods such as Monte Carlo simulation (MCS)
- use of analytical methods such as the first order reliability method (FORM)

More detailed information about reliability concepts can be found in a number of references, such as Ang & Tang [1984], Madsen et al. [1986], Sundararajan [1995], Melchers [1999], or Haldar & Mahadevan [2000].

2.4.3 Probabilistic Analyses of the Fatigue Behaviour of Welded Structures

Numerous research projects involving probabilistic analysis of the fatigue behaviour of welded structures have been reported in the literature. Probabilistic analysis of fatigue behaviour is quite complicated, since the uncertainty is large. Laboratory test results, which are carried out under controlled loading conditions and often using high fabrication quality standards, show a great scatter in fatigue strength. This uncertainty in resistance is further amplified by the uncertainty of the loading. In many structural engineering applications such as mining equipment or bridges the loads are highly variable. Both the scatter in resistance and the randomness of the loads have to be adequately modeled in a probabilistic analysis.

Probability- Based Approaches in Fatigue

The probabilistic analysis of the resistance of cyclically loaded specimens is often limited to the classical approach of a statistical analysis of the test results [ASCE 1982]. This approach is used to derive the $\Delta\sigma - N$ curves discussed in Section 2.2.3. Because of the many short-comings of the $\Delta\sigma - N$ approach (cf. Section 2.2.3), Zhao et al. [1994a] proposed the use of a linear elastic fracture mechanics (LEFM) approach to evaluate the fatigue reliability of steel bridges. A limit state function based on a critical crack size, a_f, was defined. Uncertainties related to the initial defect size and the crack growth parameters were included, but all other parameters, including a_f, were assumed to be deterministic. The crack initiation life was neglected. Lukic & Cremona [2001] proposed

a more detailed LEFM model for welded joints. The limit state function was based on failure by either brittle fracture, yielding or a combination of both and was solved using a first order reliability method (FORM). Uncertainties in initial defect size and shape, weld geometry, material properties, solicitations and service temperature were considered and a simple approach for a sensitivity study of all variables was proposed.[1] Again, the crack initiation life was neglected. More recently, Walbridge [2005] proposed a detailed LEFM model, incorporating a large number of fatigue relevant parameters and solving the limit state function using either a Monte Carlo Simulation (MCS) or FORM. A more sophisticated method for a sensitivity study of the statistical variables using the magnitude of the direction cosines of FORM was presented. The application of the proposed approach to the design and analysis of a sample bridge, including a preliminary economic evaluation of post weld treatment benefit, was also demonstrated. Although the effect of hammer peening was closely investigated, crack initiation life was neglected for all calculations.

Loading

The loading on a structure is best modeled using field measurements [Bailey 1996]. The results of such measurements have to be carefully examined as to be certain that only statistically relevant data are included. The randomness of the loading is usually accounted for by some cycle counting method, such as the rainflow or reservoir analyses [Fisher et al. 1997]. Cycle counting methods are used to transform a load history into a load spectrum summarizing the number of cycles for each load range experienced by a structure. The load spectrum can be transformed into an equivalent load range using a fatigue damage accumulation method such as the Palmgren-Miner model [Miner 1945].

Role of Inspection

Several studies have outlined the importance of inspection in obtaining more accurate reliability-based predictions of the fatigue behaviour. Zhao et al. [1994b] demonstrated the beneficial effect of incorporating inspection results to update a reliability-based LEFM model for bridges. The authors indicate that for a particular inspection method, several factors, such as modeling effects, human factors, and inspection factors, affect the inspection results. Zhang & Mahadevan [2001] accounted for the uncertainties of these factors (probability of detection, size measurement accuracy, false call probability) into a mathematical model to update the reliability of a structure. From an example they illustrated that the updating yields substantial gain in reliability for the time immediately after inspection, but does not affect the probability of failure for long term loading. Sire et al. [1992] showed that for a repaired detail in a container ship an initial inspection is most beneficial, with subsequent inspections even further improving the reliability of the structure. Moan & Song [2000] and Faber et al. [2006] demonstrated that a substantial

[1] The approach compares the safety index calculated using all random variables with the safety index calculated using all variables as random, except one, which is assumed to be deterministic.

increase in fatigue reliability can be achieved for an entire population of a detail in offshore structures by specific inspection of a limited number of critical details.

Pardi et al. [2005] suggested risk-based inspection and maintenance of bridges need to address groups of similar structures, as is often the case in other industries, such as the nuclear and offshore sectors. They also emphasized that detailed inspection planning helps optimize the cost of maintenance and that a more profound exchange of information between different industrial sectors, agencies and research institutes across political borders can maximize the benefits of inspection. The authors also recognized that the level of risk and reliability methods applied to the management of existing bridges lags behind other industries, such as the nuclear or offshore sectors.

A more general review of risk-based inspection and maintenance dealing mainly with plant risk in the nuclear industry can be found in Vo & Balkey [1995].

Multiple Crack Sites

Multiple crack sites, investigated by several researchers [Walbridge 2005], are not considered in the present work. It is assumed that only one crack of known origin contributes to the failure of the structure.

Codes and Recommendations for Probabilistic Fatigue Assessment

An important part of the research in reliability analysis of structural systems has been driven by the offshore and nuclear industries. Consequently, design standards and recommendations dealing with probabilistic fatigue assessment and inspection of structures or structural components have primarily originated from these industries [DNV 1992, CSA 1994, HSE 1999, JCSS 2001a, ASME 2004].

Appropriate Probabilistic Fatigue Analysis

A probabilistic analysis of the fatigue behaviour of welded details should include the following:

- The appropriate level of safety has to be defined. In some cases, as for a secondary highway bridge where no cracks are apparent, a simple reliability approach might be sufficient. In other cases, as in the nuclear industry, for example, where fatigue failures can be of devastating consequences, a sophisticated reliability approach incorporating economical aspects might be desirable.
- All fatigue relevant parameters have to be accounted for. Based on the desired level of safety, accurate statistical analyses of the significant parameters have to be carried out.
- All phases of fracture mechanics have to be incorporated. So far only models considering the crack propagation stage have been used. However, crack

initiation has to be accounted for in reliability analysis, especially when post weld treatment methods are investigated. Reasonable models and approaches for each of the phases have to be adopted.

- A reasonable value of the safety index, β, has to be defined.
- The level of sophistication of the inspection methods has to be accounted for over the service life of the structure or structural component.

2.5 Summary

The necessary background information to carry out a reliability-based assessment of fatigue failures was presented in this chapter. First, general concepts concerning the fatigue behaviour of steel structures were presented. The two most commonly applied design approaches, the $\Delta\sigma - N$ curves and fracture mechanics were then discussed, demonstrating that fracture mechanics is the preferred method to assess existing structures. It was shown that the most promising manner to incorporate all stages of crack growth in a fracture mechanics approach is to use a strain-based correlation approach to describe the crack initiation stage, equation (2.5), and a linear elastic fracture mechanics approach to describe the stable crack propagation stage, equation (2.9). The unstable crack propagation stage corresponds to the failure criterion, generally either being a brittle failure according to fracture mechanics criteria or being a ductile failure according to a yielding criterion. However, often it is more practical to define the failure criteria according to a certain stage in crack propagation.

Different fatigue repair methods were briefly discussed. Although most repairs in bridges are of the mechanical type, welded repairs, most commonly fishplating or rewelding, are often preferred in mining equipment. This is mostly due to the ease of application of these techniques and the readily available workforce on most sites which are qualified to perform such repairs. However, little about the efficiency of welded repairs is known and for this reason the more sustainable repair method of gouging and welding will be investigated in the present work. It has been well established that weld improvements prolong the fatigue life of welded structures considerably. One of the most promising weld improvement techniques is ultrasonic peening, which will be discussed in detail in Chapter 3.

The bases of modern reliability concepts were briefly described at the end of the chapter. The basic and generalized reliability problems were introduced. More detailed information about reliability based fatigue investigations was given, highlighting the need to define the appropriate level of reliability, to account for all fatigue relevant parameters, to statistically analyse the most significant parameters, to include all phases of fracture mechanics, to define a reasonable value for the safety index, β, and to account for inspection methods and intervals.

Based on the background provided in this chapter, the most critical parameters for welded details are potentially the fatigue material properties, the initial crack size and shape, the residual stress field, and post weld treatment methods, such as ultrasonic peening. The literature for these four parameters will be reviewed in detail in Chapter 3.

3. LITERATURE REVIEW OF SELECTED TOPICS

3.1 Introduction

Based on the information presented in Chapter 2, a literature review of the following issues is conducted in this chapter: fatigue material properties (Section 3.2), initial weld imperfections, especially initial flaw size and shape (Section 3.3), residual stresses due to welding (Section 3.4), and ultrasonic peening (Section 3.5). These four issues are believed to be affecting the fatigue behaviour of the welded structural details investigated in the present work. The review of post weld treatment methods presented in Chapter 2 showed that the most significant increase in fatigue life is expected with ultrasonic peening (see Section 2.3.3). Therefore, only this relatively new method is looked into here.

3.2 Fatigue Material Properties

3.2.1 Introduction

Abundant research on fatigue material properties has been conducted and results published in sources such as Barsom [1971], Boller & Seeger [1987], ASM [1996], and SAE [2002]. Concerning the crack initiation phase, only recent studies conducted at the University of Alberta will be reviewed here (Section 3.2.2). Individual test data are available from these studies, thus allowing for a statistical analysis of the fatigue initiation properties, $\sigma_f^{'}$, $\varepsilon_f^{'}$, b, and c. Furthermore, they are characteristic of the steel grade investigated in the present work. Since all the reviewed reliability-based fatigue assessments dealt with welded details, where crack initiation life was assumed to be negligible, no probabilistic data are available for this crack stage.

Crack propagation tests carried out on Grade 350WT steel will be reviewed in Section 3.2.3. Also presented in Section 3.2.3 are several probabilistic distributions of the crack propagation parameters, C and m, as used in reliability-based fatigue assessments reported in the literature.

A summary and some conclusions about the fatigue material properties are presented in Section 3.2.4.

3.2.2 Crack Initiation

Research on CAN/CSA G40.21-04 Grade 350WT steel [CSA 2004] was conducted at the University of Alberta to determine the fatigue properties for the crack initiation stage [Wang 2010]. Chen et al. [2005] conducted tests on high performance HPS Grade 485W

and ASTM Grade A7 steel, which are two other steel grades encountered in civil engineering structures, A7 being an "old" and HPS an innovative grade.

Chen et al. [2005] carried out crack initiation tests on smooth specimens according to ASTM standard E 606 *Standard Practice for Strain-Controlled Fatigue Testing* [ASTM 2004b]. Two heats of high performance steels, HPS Grade 485W, one with a rather low toughness, believed to be an early heat of high performance steel and designated as HPS(LT), and one with a higher toughness, HPS(HT), and one heat of ASTM Grade A7 steel were tested. The HPS(LT) series was tested both in its rolling and transverse directions, the HPS(HT) was tested only in its rolling direction and the A7 series only in its transverse direction. A total of 44 specimens were tested under completely reversed loading ($R = -1$). From these 44 tests, 33 were conducted under strain control while the remaining were conducted under stress control. In order to investigate the effect of mean stress, an additional ten specimens with $R = 0$ and three specimens with $R = 0.5$ were tested under stress control conditions. The test program is summarized in Table 3.1.

Table 3.1 *– Matrix of crack initiation tests carried out by Chen et al. [2005].*

Steel Grade	Orientation	Control	*R*	No. of Specimens
HPS(LT)	Longitudinal	Strain	-1	16
		Stress	-1	6
			0	6
			0.5	3
	Transverse	Strain	-1	5
HPS(HT)	Longitudinal	Strain	-1	6
		Stress	-1	5
			0	4
A7	Transverse	Strain	-1	6

The strain controlled tests were carried out with strain amplitudes, $\Delta\varepsilon/2$, varying from 0.10% to 0.67%. The stress controlled tests were carried out with stress amplitudes, $\Delta\sigma/2$, from 143 MPa to 304 MPa. The material constants defining the cyclic material properties expressed by equation (2.5) and as determined by Chen et al. [2005] through regression analyses are presented in Table 3.2.

Chen et al. [2005] concluded that the two steels have similar fatigue properties and the variation in fatigue initiation properties lies within expected – and accepted – levels of accuracy in any fatigue analysis.

Using the same procedure as Chen et al. [2005], Wang [2010] carried out crack initiation tests on Grade 350WT steel, which is commonly used in Canada for fabricated steel structures. A total of 15 smooth specimens were tested under completely reversed loading ($R = -1$) and an additional 23 specimens were tested with a non zero mean stress ($R > -1$). A detailed description and statistical analyses of the tests carried out by Wang [2010] are presented in Chapter 4.

Table 3.2 *– Cyclic material properties obtained by Chen et al. [2005].*

Steel Grade	Orientation	σ_f' [MPa]	b	ε_f'	c
HPS(LT)	Longitudinal	851	-0.069	0.775	-0.701
	Transverse	741	-0.052	1.917	-0.830
HPS(HT)	Longitudinal	776	-0.073	6.207	-0.940
A7	Transverse	760	-0.121	0.196	-0.486

Radaj & Sonsino [1998] have reported fatigue initiation properties of fine grained (σ_y of 375 MPa and 460 MPa) and C-Mn (σ_y of 375 MPa) steels and their corresponding weld metal (σ_y of 500 MPa for fine grined, σ_y of 520 MPa for C-Mn) and HAZ. Similar fatigue initiation response was observed for the base and the weld metals as well as the HAZ. This supports the conclusion drawn by Chen et al. [2005] that the fatigue initiation properties are similar for different grades of steel having yield strengths not differing more than 300 to 400 MPa.

3.2.3 Crack Propagation

Taheri et al. [2003] carried out crack propagation tests on middle tension M(T) specimens made from Grade 350WT steel according to ASTM standard E 647 *Standard Test Method for Measurement of Fatigue Crack Growth Rates* [ASTM 2000]. Three specimens were tested at a stress range of $R = 0.1$. One specimen each was tested at $R = 0.2$, $R = 0.3$, and $R = 0.4$. Yin et al. [2006] carried out crack propagation tests on single-edge tension SE(T) specimens made from 350WT steel. Six and two specimens of 350WT steel were tested at $R = 0.1$ and $R = 0.5$, respectively. Although ASTM [2000] does not specifically include the SE(T) specimen geometry, Blatt et al. [1994] have demonstrated that da/dN versus ΔK data obtained from specimens of the SE(T) configuration correlate well with data obtained from the standard compact tension C(T) specimens defined in ASTM [2000]. The crack propagation parameters to be used in equation (2.9) as determined by Taheri et al. [2003] and Yin et al. [2006] through regression analyses are presented in Table 3.3. It is noted that Yin et al. [2006] only used

test results with da/dN values larger than approximately 5×10^{-5} mm/cycle. No reason for truncating the data at this limit is given.

Statistical analyses of the Taheri et al. [2003] and the Yin et al [2006] test results are presented in Chapter 4.

Chen et al. [2005] compared the crack propagation properties obtained by Yin et al. [2006] to the properties obtained from their own studies on High Performance Steel (HPS). As for the crack initiation properties, they concluded that the difference in the crack growth properties between these two steel grades might be insignificant.

Table 3.3 *– Crack propagation parameters obtained by Taheri et al. [2005] and by Yin et al. [2006] for 350WT steel.*

Reference	R	C	m
Taheri et al. [2003]	0.1	3.97×10^{-13}	2.94
	0.2	2.02×10^{-13}	3.06
	0.3	7.06×10^{-14}	3.22
	0.4	6.67×10^{-14}	3.27
Yin et al. [2006]	0.1	2.53×10^{-13}	3.03
	0.5	1.19×10^{-14}	3.59

Several probabilistic distributions of the crack propagation parameters, C and m, have been presented in the literature. Investigations have shown a strong correlation between C and m [Gurney 1979a]. Therefore, most probabilistic approaches assume a deterministic value for m and account for the uncertainty in crack propagation rate by considering only C as a random variable. Table 3.4 presents a summary of the probabilistic parameters proposed in two design guides and seven research programs. In all the research programs presented in Table 3.4, m is assumed to be constant and C is assumed to follow a lognormal distribution, LN(α,β), where α and β are the sample mean and standard deviation, respectively. The mathematical expression for the probability density function (pdf) for the lognormal distribution is defined in Appendix B.

Engesvik & Moan [1983] analysed test results from the heat affected zone (HAZ) of stress relieved structural steel with an average yield strength of 250 MPa. The uncertainty in the crack propagation parameters was accounted for by using a normal distribution N(3.70,0.11) for m. Engesvik & Moan [1983] assumed a correlation between C and m through the relationship $\log(C) = -6.177 - 1.603m$.

In a probabilistic assessment of a steel bridge, Zhao et al. [1995a] used a lognormal distribution for C, LN(1.26×10^{-13}, 7.94×10^{-14}), and a normal distribution for m, N(3.0,0.3). No correlation between C and m was assumed. The lognormal distribution for C was also adopted by Cheung & Li [2003] (see Table 3.4). Lukic & Cremona [2001] also considered both parameters as random variables with C following LN(2.50×10^{-13}, 9.23×10^{-14}) and m following N(3.0,0.3). A strong correlation of $\rho(m,\ln(C)) = -0.99$ was assumed.

Table 3.4 *– Probabilistic crack propagation parameters proposed in the literature.*

Reference	Distribution for C	m	Remarks
Bokalrud & Karlsen [1982], DNV [1992]	LN(3.47×10^{-13},2.06×10^{-13})	3.1	Steel used for non corrosive environment; based on 2207 measurements of various steel types with $0.10 \le R \le 0.85$
Shetty & Baker [1990]	LN(2.02×10^{-13},5.05×10^{-14})	3.0	Steel used in air; average yield strength of 380MPa
Lotsberg et al. [2000]	LN(6.31×10^{-13},2.59×10^{-13})	2.88	Steel used in air; $R \ge 0.5$
Moan & Song [2000]	LN(1.10×10^{-13},5.98×10^{-14})	3.1	Tubular steel in off-shore structures
Banz & Nussbaumer [2001]	LN(1.89×10^{-13},4.73×10^{-14})	3.0	Common bridge steel with nominal yield strength of approximately 350 MPa
Cheung & Li [2003]	LN(1.26×10^{-13},7.94×10^{-14})	3.0	Common bridge steel
BSI [2005]	LN(3.98×10^{-13},1.40×10^{-13})	2.88	Steels in air; $R < 0.5$
	LN(5.86×10^{-13},3.52×10^{-13})	2.88	Steels in air; $R \ge 0.5$
Walbridge [2005]	LN(3.61×10^{-13},2.15×10^{-13})	3.0	Common tubular bridge steel with nominal yield strength of approximately 350 MPa

Note: C in (mm/cycle)$\cdot\left(\text{MPa}\sqrt{\text{mm}}\right)^{-m}$ and m is dimensionless

The probability density function of C for all the distributions of Table 3.4 as well as the one proposed by Lukic & Cremona [2001] are plotted in Figure 3.1. For ease of illustration C is expressed in its natural logarithmic form, $\ln(C)$.

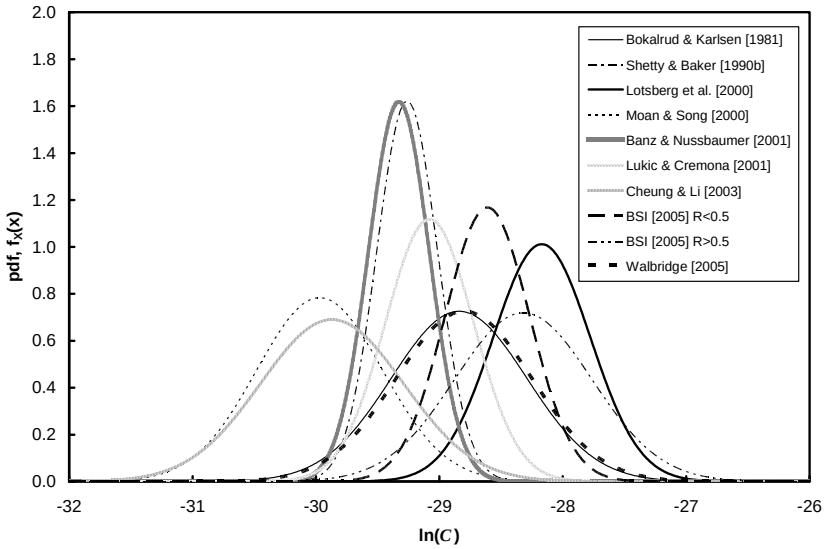

Figure 3.1 *– Probability density functions (pdf) for the crack growth parameter* C.

Although crack growth rates depend on the stress ratio, R, most of the distributions shown in Figure 3.1 neglect this effect. A few investigations [Walbridge 2005] take it into account by using crack closure effects, thus normalizing R.

The crack propagation tests carried out by Taheri et al. [2003] and by Yin et al. [2006] on 350WT steel were done on the base metal. However, it is not clear whether the distributions used in the probabilistic assessments described above, where cracks always propagated through the heat affected zone (HAZ), are for the base metal, the HAZ, or the weld metal. Investigations by Dowse & Richards [1971] and Maddox [1973, 1974] showed that the crack growth rates obtained for weld metal and HAZ in structural steel did not differ significantly from results for the parent metal, as long as fracture was transgranular. For HAZ with an increased hardness, it was found that intergranular fracture can take place, increasing the crack growth rate substantially.

According to equation (2.9), the threshold stress intensity factor range, ΔK_{th}, plays an significant role in crack propagation at low ΔK values. It is generally accepted that ΔK_{th} strongly depends on R. Barsom & Rolfe [1999] proposed the following relationship where ΔK_{th} is expressed in $\text{MPa}\sqrt{\text{mm}}$:

$$\Delta K_{th} = 210(1 - 0.85R) \qquad \text{for } R > 0.1$$
$$\Delta K_{th} = 190 \qquad \text{for } R \le 0.1 \tag{3.1}$$

BSI [2005] proposes more conservative values for ΔK_{th} (in $\text{MPa}\sqrt{\text{mm}}$):

$$\Delta K_{th} = 63 \qquad \text{for } R \ge 0.5$$
$$\Delta K_{th} = 170 - 214R \qquad \text{for } 0 \le R < 0.5 \tag{3.2}$$

Ohta et al. [1986] conducted a statistical analysis of fatigue crack propagation test results from different steel grades. Base metal, as well as weld metal and HAZ were investigated for different welding processes (shielded metal arc, gas metal arc, and submerged arc welding). A significant drop in ΔK_{th} for the weld metal and HAZ compared to the base metal was observed for all steel grades. The data showed that the stress ratio, R, does not significantly affect ΔK_{th} for the weld metal and HAZ. The value of ΔK_{th} for the HAZ and weld metal were found to be virtually the same for the three welding procedures investigated. Conversely, R has a significant effect on ΔK_{th} for the base metal. An analysis of the test data for various weld metals and welding processes leads to an average value of $\Delta K_{th} = 75\ \text{MPa}\sqrt{\text{mm}}$ with a standard deviation of $5\ \text{MPa}\sqrt{\text{mm}}$ for any values of *R*.

Many probabilistic fracture mechanics models used in the literature neglect the effect of ΔK_{th}. If ΔK_{th} is considered, it is often done with a deterministic value. Lotsberg et al. [2000] used $\Delta K_{th} = 63\ \text{MPa}\sqrt{\text{mm}}$, which is the value proposed by BSI [2005] for $R \ge 0.5$. Banz & Nussbaumer [2001] used a very similar value of ΔK_{th}, namely, $60\ \text{MPa}\sqrt{\text{mm}}$.

Shetty & Baker [1990] modeled ΔK_{th} at $R = 0$, denominated $\Delta K_{th,0}$, for structural steel (nominal yield strength 355 MPa) with a lognormal distribution, LN(240,36). The effect of R is considered through a deterministic relationship, which, according to Walbridge [2005], takes the following form:

$$\Delta K_{th} = (1 - 0.72R)\Delta K_{th,0} \qquad \text{for } \forall\ R \tag{3.3}$$

Walbridge [2005] also modeled ΔK_{th} with a lognormal distribution, LN(100,15). Since crack closure due to residual stresses was incorporated in the crack propagation model, R is implicitly accounted for, resulting in an effective threshold stress intensity factor range, $\Delta K_{th,eff}$.

3.2.4 Summary and Conclusions

Research to determine the fatigue properties for the crack initiation phase of Grade 350WT, HPS 485W and ASTM A7 steel was conducted at the University of Alberta. No

significant difference between these steel grades was observed. This confirms findings on crack initiation tests done by Radaj & Sonsino [1998] on matching base and weld material, where the fatigue response was found to be very similar in the three different zones, namely the base metal, the weld metal, and the HAZ. The results for Grade 350WT steel as tested by Wang [2010] will be statistically analysed in Chapter 4 and compared to other data.

Crack propagation tests carried out on Grade 350WT steel as well as several probabilistic distributions for the crack growth parameters proposed in the literature were reviewed and will be analyzed in Chapter 4. Following the school of thought that uncertainty in the crack propagation rate should be considered entirely by C, regression analyses of the 350WT specimens tested Taheri et al. [2003] and by Yin et al. [2006] will also be carried out in Chapter 4 with m fixed at the generally accepted value of 3.0.

Most investigations on fatigue material properties have been carried out on base metal and only little is known about the fatigue material properties of the weld metal and HAZ. Therefore, an experimental investigation on initiation and propagation properties of weld metal matching Grade 350WT steel is carried out as part of the present work. The experimental program and the results will be presented in Chapter 4.

3.3 Initial Flaw Size and Shape

3.3.1 Introduction

An inherent characteristic of welded details is the presence of imperfections (cf. Chapter 2). Generally, it is accepted that under fatigue loading flaws and cracks[1], defined by their initial depth or length, a_{init}, and their aspect ratio, $(a/c)_{init}$, are the most harmful weld discontinuities. Existing cracks can be detected by non-destructive methods, such as magnetic particle, liquid penetrants, radiography or ultrasound. However, since initial cracks are, due to their small size and/or subsurface location, not easily detectable, an assessment of their size and shape with these detection methods is difficult and might even result in unreliable predictions [Aoki et al. 1986]. Undoubtedly the best way to measure initial crack geometry is by destructive methods, such as fatigue testing up to failure with subsequent microscopic examination of the crack surface. This will be done for the specimens tested within the present work (cf. Chapter 5). Of course, this approach is not practical for existing structures and often the size of initial weld discontinuities has to be estimated. This can be done e.g. by adopting the largest flaw size and shape

[1] The term flaw is used here in a general way and describes any discontinuity in the weld, such as lack of fusion, slag inclusions, undercuts, porosity, incomplete penetration, etc., without considering whether the discontinuity is acceptable or not from an inspection point of view. A flaw can take different shapes (elliptical, spherical, etc.), but is considered here as not having a sharp tip. A crack is defined as a discontinuity with a sharp tip.

acceptable by application standards or by assuming that the crack size corresponds to the smallest crack that can be reliably detected by a specific inspection method. However, both of these approaches have the disadvantage that the initial flaw geometry is assumed to be a deterministic upper bound value, most likely resulting in excessively conservative fatigue life predictions. A statistical analysis of data obtained from research investigations can reduce this shortcoming. Although acceptable deterministic defect sizes as defined in standards and codes of practice will not be directly used in the present work, it is important to compare the adopted initial crack geometry with acceptable levels. Therefore, first a selection of literature dealing with acceptable initial flaws as imposed by design standards and guidelines is presented in Section 3.3.2. This is followed by an examination of some literature on research investigations (Section 3.3.3), where initial crack geometries were measured or used in LEFM models. Mathematical definitions of probability distributions used in reliability assessments are given in Appendix A. All crack sizes are given in mm.

Welds investigated in the present work include complete joint penetration (CJP) welds and fillet welds. For both weld types cracks are most likely to start from the toe or the root of the weld [Gurney 1979b, Radaj 1990, Maddox 1991]. Therefore, the following will focus on these locations. Whether the cracks for the specimens tested in the present work actually initiate from these locations will be verified in Chapter 5.

3.3.2 Codes and Recommendations

USA

The American National Standard AWS D1.1 *Structural Welding Code – Steel* [AWS 2008] covers welding provisions for any type of welded structure made from carbon and low-alloy structural steels. The weld inspection requirements are presented in Section 6 of the code. All welds need to be visually inspected according to an acceptance checklist. For welds subjected to cyclic loading no visible surface porosity is allowed. The code specifies the maximum acceptable dimensions, a and c, of embedded discontinuities, their minimum spacing, which depends on the applied state of stress (tension or compression), the weld size, and the inspection method. Cracks are not permitted in any case.

The American Specification D1.5 *Bridge Welding Code* [AASHTO/AWS 2008] has provisions for welded bridges that are similar to those presented in AWS D1.1 [AWS 2008]. Section 6 deals with weld inspection. In addition to visual inspection, AASHTO/AWS D1.5 requires that complete joint penetration (CJP) groove welds in butt joints subject to calculated tension or reversal of stress be inspected by radiography. For example, the greatest dimension for any porosity or fusion-type discontinuity for the large scale welds tested in Chapter 5, which are 35 mm groove welds, is 11 mm. The clearance between such discontinuities has to be at least 100 mm. If a smaller discontinuity is present, say 5 mm, the minimum clearance reduces to roughly 40 mm.

Undercut in cyclically loaded members shall not exceed 0.25 mm when the weld is transverse to the applied stresses.

Fillet welds joining primary components of main members need to be inspected by magnetic particle testing. The acceptance criteria for flaws are basically the same as in the case of CJP groove welds.

Canada

The Canadian standard *W59-03 – Welded Steel Construction (Metal Arc Welding)* [CSA 2003] covers welding requirements for most applications of welded carbon and low-alloy steel construction. Specifications concerning the quality of welds are presented in Section 12.5.4 of the standard. The procedures and acceptance criteria for welds cyclically loaded in tension are identical to AWS D1.1 [AWS 2008]. The Canadian Highway Bridge Design Code [CSA 2006] requires that in addition to visual inspection of all welds a complete radiographic inspection of groove welds in flange splices under tension or stress reversal has to be carried out. This corresponds to the requirements of AASHTO/AWS [2008].

Europe

ISO 5817 *Arc Welded Joints in Steel – Guidance on Quality Levels for Imperfections* was adopted as European Standard EN 25817 in 1992 [EN 1992]. Similarly to the North American standards, EN 25817 does not allow any surface cracks and gives maximum dimensions for discontinuities. Limitations for any flaws are given for three quality levels: moderate (D), intermediate (C), and stringent (B). The required quality level must be selected based on design considerations such as type of loading, service conditions (temperature and environment), and consequence of failure. Based on these criteria it would be prudent to demand quality B (stringent) for the types of application considered in the present work (welded repairs subjected to dynamic loading at low operating temperatures). For quality B the maximum dimension of single pores is limited to 3 mm and solid inclusions are limited to 2 mm. Undercut for quality B welds shall not exceed 0.5 mm.

The German Welding Institute (DVS) published a more comprehensive version of EN 25817 [DVS 1993]. In addition to reproducing the acceptance criteria of EN 25817, examples of different acceptable weld imperfections are given on so-called reference cards showing radiographic images of complete welds. Furthermore, different types of weld gauges to measure weld imperfections are presented.

Great Britain

The British Standard Document BS 7910 *Guide to Methods for Assessing the Acceptability of Flaws in Metallic Structures* outlines the derivation of acceptance levels

for flaws based on the concept of fitness for purpose [BSI 2005]. The Guide addresses situations where flaw sizes exceed the quality control levels specified in applicable codes. Fracture mechanics is used to determine an acceptable flaw size for a desired quality of structural detail. In a general procedure, equation (2.9) is used to calculate the acceptable crack size from knowledge of the critical crack size and all relevant fatigue parameters including the estimated number of fatigue cycles. A simplified procedure using $\Delta\sigma - N$ curves, from which a required quality level and thus a maximum acceptable flaw can be deduced, is also proposed in BSI [2005]. Since the fitness for purpose approach operates on detected and measured cracks, BSI [2005] cannot be used to estimate an initial crack size in a component that has not been inspected.

Norway

The Norwegian recommendation *Structural Reliability Analysis of Marine Structures (Classification Notes No. 30.6)* [DNV 1992] proposes an exponentially distributed initial crack depth with a mean value of 0.11 mm, based on work by Bokalrud & Karlsen [1982]. However, it is indicated that the distribution of a_{init} is not well founded and more research on this topic is required. A brief description of the work of Bokalrud & Karlsen [1982] follows.

3.3.3 Crack Sizes Reported in Research Projects

Initial discontinuity sizes in welds have been investigated in several studies and the findings implemented in probabilistic fatigue assessments. Although these discontinuities must, according to the acceptability criteria of both North American and European standards, not be cracks, they were treated as such in the probabilistic assessments. The reason for this is the assumption that the discontinuities are severe enough to give rise to a significant stress concentration, resulting in practically no initiation life. The initial discontinuity size thus corresponds to the initial crack size used to describe the stable crack propagation stage.

The following summarizes studies conducted in order to determine the initial weld imperfection size. Furthermore, probabilistic distributions for the initial crack sizes, a_{init}, and crack aspect ratios, $(a/c)_{init}$, reported in the literature are presented.

Bokalrud & Karlsen [1982]

Bokalrud & Karlsen [1982] report both initial surface (undercuts at weld toe) and embedded discontinuities in butt welded joints obtained from measurements on production welds in ships. A total of 827 randomly selected measurements of the weld toe region revealed 325 regions with an undercut. Microscopic analysis of these undercuts resulted in an exponential frequency distribution with a mean value of the depth of 0.11 mm.

Embedded defects were measured with ultrasonic testing on about 3,200 m of randomly selected welds over a total length of 40,000 m. Since ultrasonic testing does not permit to establish the exact height of a flaw or crack, Bokalrud & Karlsen [1982] presented an estimation of the defect height resulting in a mean value of 3.5 mm. The corresponding length was assumed to be infinite.

The exponential distribution of the surface undercut proposed by Bokalrud & Karlsen [1982] was subsequently adopted in other research programs [Lotsberg et al. 2000, Moan & Song 2000, Straub & Faber 2004] and guidelines [DNV 1992, HSE 1999].

Brückner & Munz [1982]

Brückner & Munz [1982] performed statistical goodness of fit analyses of defect size distributions measured by Raussi & Tiainen [1980] using X-Rays in nuclear power plant pipes. Since the inverse quadratic distribution proposed by Raussi & Tiainen [1980] has some drawbacks, Brückner & Munz [1982] recommended to use either a Weibull distribution with parameters $\theta = 0.436$ and $\tau = 0.507$, W(0.436,0.507), or a lognormal distribution with a mean value of 1.07 mm and a standard deviation of 3.77 mm, LN(1.07,3.77). Both these distributions were obtained by the χ^2 method of curve fitting.

In a sample calculation Brückner & Munz [1982] used a normal distribution for a/c, with $\mu = 0.55$ and $\sigma = 0.18$. No source for these values is reported.

Smith & Smith [1982]

Smith & Smith [1982] measured defect sizes in fillet welds of non load carrying gusset attachments using optical microscopic inspection of cut-out samples. The average defect depth at the weld toe was found to be 0.045 mm, with only very few defects deeper than 0.1 mm. They further concluded that the aspect ratio, a/c, can conservatively be assumed as being a constant value of 0.5 throughout the entire through-thickness crack propagation stage. No statistical analyses of the measurements were reported.

Engesvik & Moan [1983]

Engesvik & Moan [1983] investigated the fatigue capacity of non-load-carrying fillet welded attachments based on a probabilistic analysis. A comparison of measurements of undercut, crack and slag inclusions sizes performed by other researchers lead to two models for the variability in a_{init}: a log-normal distribution and a shifted exponential distribution, both having a mean value of 0.125 mm and a standard deviation of 0.046 mm.

Based on observations of the crack surface of fatigue specimens tested by Engesvik & Moan [1983], it was concluded that the aspect ratio, a/c, can be expressed by equation (3.4) for cracks up to 3 mm deep. At this stage it is assumed that the crack front becomes

straight, i.e., that the crack can be treated as an edge crack ($a/c = 0$) rather than a surface crack.

$$\begin{aligned} \frac{a}{c} &= \frac{2a}{6.34a - 0.27} && \text{for } a \le 3 \text{ mm} \\ \frac{a}{c} &= 0 && \text{for } a > 3 \text{ mm} \end{aligned} \tag{3.4}$$

The lognormal distribution of a_{init} as proposed by Engesvik & Moan [1983] was adopted in other studies [Yamada & Nagatsu 1989, Banz & Nussbaumer 2001, Lukic & Cremona 2001].

Yamada & Nagatsu [1989]

In addition to adopting Engesvik's initial crack size distribution, Yamada & Nagatsu [1989] analyzed data from other researchers to obtain a histogram of the initial crack shape, $(a/c)_{init}$ and proposed a log-normal distribution with a mean value of 0.395 and a standard deviation of 0.164. The crack aspect ratio was assumed to be constant with $a/c = (a/c)_{init}$ up to a crack depth of 1 mm, gradually changing to $a/c = 1/3$ as the crack depth reaches 9 mm. At larger crack depths the ratio is again kept constant at $a/c = 1/3$.

The lognormal distribution of $(a/c)_{init}$ proposed by Yamada & Nagatsu [1989] was also adopted in other studies [Banz & Nussbaumer 2001, Lukic & Cremona 2001].

Shetty & Baker [1990]

Kountouris & Baker [1990] inspected about 30 km of weld using ultrasonic testing and about 76 km of weld using magnetic particle. Using the measurement results reported by Kountouris and Baker, Shetty & Baker [1990] modelled the initial crack depth as a lognormal variable with LN(0.73, 0.78). The initial crack depth ratio $(a/c)_{init}$ was also modelled as a lognormal variable with LN(0.62, 0.25).

Lopez Martinez & Korsgren [1993]

Special test coupons were used by Lopez Martinez & Korsgren [1993] to measure initial imperfection sizes. The distribution of the initial depth of undercut was found to be affected by the welding procedure and fabricator. One of the distributions observed was a lognormal distribution with LN(0.1, 0.19). This is similar to the exponential distribution suggested by Bokalrud & Karlsen [1982]. Initial imperfection depth ratios between 0.1 and 1.0 were also measured, but the distribution for these imperfections was not reported.

Darchuk [2003]

Based on an analyses of defect sizes reported in the literature Darchuk [2003] concluded that the initial crack depth in welded joints is best modelled by a lognormal distribution with LN(0.96, 0.35). The crack aspect ratio was assumed to be a function of the crack size a .

Righiniotis & Chryssanthopoulos [2003]

Righiniotis & Chryssanthopoulos [2003] estimated the initial crack depth and the initial crack aspect ratio by comparing fracture mechanics analysis results to experimentally-based $\Delta\sigma - N$ curves, as well as to individual experimental results from butt welded plates. Different lognormal distributions for a_{init} and $(a/c)_{init}$ were investigated using this approach. The bounds used in the investigations are LN(0.6, 0.24) and LN(0.1, 0.02) for a_{init}, and LN(0.5, 0.1) and LN(0.01, 0.002) for $(a/c)_{init}$. The low mean value of $(a/c)_{init} = 0.01$ basically corresponds to a through-thickness crack. Righiniotis & Chryssanthopoulos [2003] demonstrated that a variation of the mean value of a_{init} has a significant effect on the fatigue strength, whereas changes in the variance only slightly affect the results. Increasing $(a/c)_{init}$ increases the fatigue strength considerably, but the effect is not as profound as for a_{init}. The large range of a_{init} and $(a/c)_{init}$ selected by Righiniotis & Chryssanthopoulos [2003] was justified by the fact that the initial crack distribution depends on the welding process, the operator, and the type of detail considered. As such the initial crack size and crack aspect ratio are subject to many uncertainties.

Walbridge [2005]

Based on a thorough literature review and fracture surface examinations on tests conducted by Schumacher [2003], Walbridge [2005] adopted a lognormal distribution for the initial defect size, with LN(0.2, 0.045). The initial crack aspect ratio was originally assumed to be lognormally distributed with LN(0.5, 0.16). Subsequent calibration of the crack growth model with test results from Schumacher [2003] confirmed the validity of this distribution.

Summary (including some additional literature)

Table 3.5 and Figure 3.2 summarize the most commonly used distributions for the initial weld defect size, a_{init}, as found in the literature. The mathematical formulations of the probability density functions (pdf) are presented in detail in Appendix B.

Table 3.5 *– Summary of distributions from the literature for* a_{init} .

Distribution	**1st paramter**	**2nd parameter**	**Reference** [1)]
Exponential (λ)	0.11 mm	---	Bokalrud & Karlsen [1982]
			Vårdal et al. [1999], Lotsberg et al. [2000], Moan & Song [2000], Straub & Faber [2004], DNV [1992], HSE [1999]
Lognormal (α, β)	1.1 mm	3.8 mm	Brückner & Munz [1982]
	0.13 mm	0.046 mm	Engesvik & Moan [1983]
			Yamada & Nagatsu [1989], Banz & Nussbaumer [2001], Lukic & Cremona [2001]
	0.73 mm	0.78 mm	Shetty & Baker [1990]
	0.10 mm	0.19 mm	Lopez Martinez & Korsgren [1993]
	0.50 mm	0.25 mm	Zhao et al. [1994a]
	0.76 mm	0.38 mm	Cheung & Li [2003]
	0.96 mm	0.35 mm	Darchuk [2003]
	0.60 mm	0.24 mm	Righiniotis & Chryssanthopoulos [2003] upper bound
	0.10 mm	0.020 mm	Righiniotis & Chryssanthopoulos [2003] lower bound
	0.20 mm	0.045 mm	Walbridge [2005]
Weibull (θ, τ)	0.436	0.507	Brückner & Munz [1982]
Deterministic	0.045 mm	---	Smith & Smith [1982]
Deterministic	0.1 mm	---	Agerskow & Nielsen [1999]

1) The main reference is shown first. Studies where the same distribution is used are also shown.

Figure 3.3 and Table 3.6 summarize the most commonly used distributions for the initial crack aspect ratio, $(a/c)_{init}$, as reported in the literature.

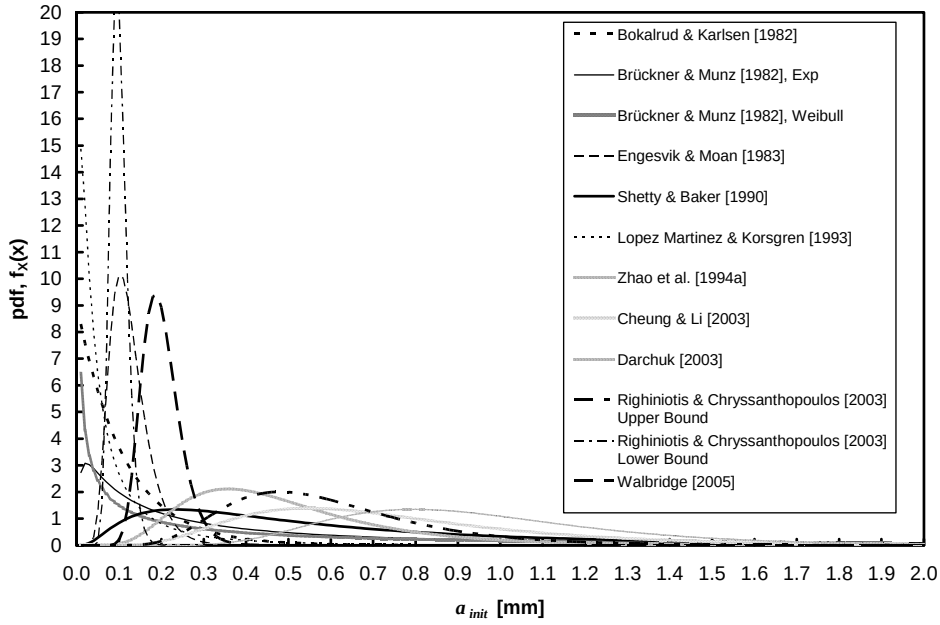

Figure 3.2 *– Probability density functions (pdf) of the initial crack depth,* a_{init} .

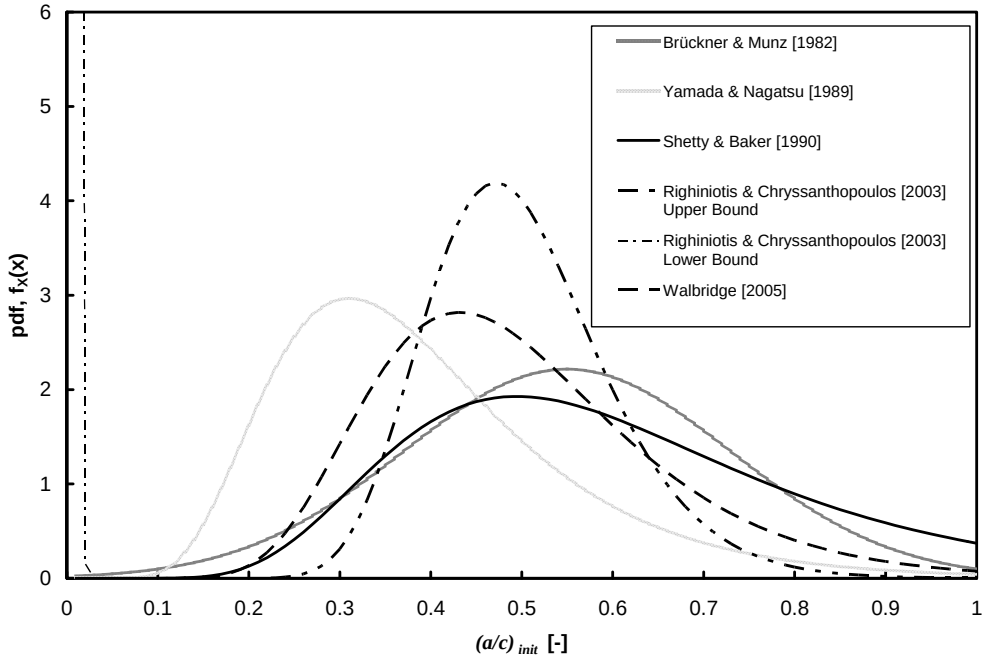

Figure 3.3 *– Probability density functions (pdf) of the initial crack aspect ratio,* $(a/c)_{init}$.

Table 3.6 *– Summary of distributions from the literature for* $(a/c)_{init}$ *.*

Distribution	**1st parameter**	**2nd parameter**	**Reference** [1)]
Normal (μ, σ)	0.55	0.18	Brückner & Munz [1982]
Lognormal (α, β)	0.40	0.16	Yamada & Nagatsu [1989]
			Banz & Nussbaumer [2001], Lukic & Cremona [2001]
	0.62	0.25	Shetty & Baker [1990]
	0.50	0.10	Righiniotis & Chryssanthopoulos [2003] upper bound
	0.01	0.0020	Righiniotis & Chryssanthopoulos [2003] lower bound
	0.50	0.16	Walbridge [2005]
Deterministic	0.5	N.A.	Smith & Smith [1982]
			Moan & Song [2000]
	0.3	N.A.	Agerskow & Nielsen [1999]
	0.1 – 1.0	N.A.	Lopez Martinez & Korsgren [1993]
	0.2	N.A.	Lotsberg et al. [2000]

1) The main reference is shown first. Studies, where the same distribution is used, are also shown

Additional Comments

It is evident that both the initial crack size, a_{init}, and the crack aspect ratio, $(a/c)_{init}$, show a considerable scatter. This variability has several causes: 1) The methods used to determine the discontinuity sizes are often not very reliable in measuring actual sizes and thus are subject to large uncertainties [Simonen 1995]. 2) Discontinuity sizes are a function of welding processes and parameters. The settings of welding parameters for identical processes and welds often vary from welder to welder, each welder adjusting the parameters so that he or she is most comfortable depositing the weld. 3) The quality of a weld is affected by the skill of the welder.

Due to the considerable scatter in a_{init} and $(a/c)_{init}$ no reliable prediction of the fatigue behaviour can be made without specific data from the investigated structural component. In the present work initial flaw sizes are determined from examinations of the fracture surfaces of the tested specimens reported in Chapter 5.

3.3.4 Summary and Conclusions

Design standards generally require that welds be inspected for surface imperfections. In all the design standards reviewed in this chapter, cracks are not permitted. In addition, welds subjected to cyclic tension should be inspected for internal flaws. The maximum allowable flaw size differs between North American and European standards. The most stringent limitations for embedded discontinuities in large welds are found in EN [1994], where the size of single pores is limited to a maximum of 3 mm and inclusions are limited to a maximum of 2 mm. According to AASHTO/AWS [2008] undercuts in cyclically loaded connections shall not be more than 0.25 mm. All the welds that were inspected and reported in the literature met even the most stringent standard. This can be attributed to the fact that in an actual weld, code requirements have to be met and often in case of doubt weld imperfections are rather rejected than accepted. Nevertheless, reported discontinuity sizes in the literature suggest that significant scatter in initial crack size, a_{init}, does exist and must be considered. The size of initial discontinuities reported in the literature ranges from about 0.1 mm to 1.0 mm. The initial aspect ratio, $(a/c)_{init}$, of cracks also shows a large variability and often changes during crack propagation. In probabilistic approaches, both a_{init} and $(a/c)_{init}$ are most commonly modeled with lognormal distributions.

3.4 Residual Stresses

3.4.1 Introduction

Residual stresses generally arise because of differential plastic deformation of adjacent zones in a material. Welding residual stresses are a consequence of heating and subsequent differential cooling of the base and weld material during the welding process. Restraints arising from the detail geometry (e.g. attachments) or provided to limit distortions (e.g. clamps) often accentuate the magnitude of residual stresses. By definition, residual stresses are not a result of externally applied loads and consequently have to be self-equilibrated. Assuming an elastic-perfectly-plastic material behaviour, the magnitude of residual stresses cannot exceed the yield strength of the parent or weld material. However, the actual distribution of residual stresses is very complex and depends on such factors as the type and size of the welded joint and the welding process. Unfortunately, only limited data modelling the residual stress field for repair and fillet welds are available [Stacey et al. 2000]. Literature concerning welding residual stresses for repair (Section 3.4.2) and fillet welds (Section 3.4.3), as well as investigations concerning the relaxation of residual stresses during fatigue loading (Section 3.4.4) is presented in the following. Only stress fields in the through-thickness direction – so-called transverse stresses (perpendicular to the weld length) – prior to the application of any post weld treatment method are considered. For the details considered in the present work, these stresses act in the same direction as the applied stresses and thus affect the

fatigue response. Residual stresses after post weld treatment by peening are discussed in Section 3.5. It has to be noted that many proposed residual stress distributions are idealized and thus often not self-equilibrated.

3.4.2 Repair Welds

Stacey et al. [2000]

Stacey et al. [2000] analysed residual stress measurements carried out by other researchers on partial (part-depth) and full penetration (full-depth) repair welds of structural and pressure vessel steels. Based on their analyses, Stacey et al. [2000] concluded that for full-depth repair welds the residual stress field should be assumed to be of tensile yield magnitude throughout the entire thickness. Although Stacey et al. [2000] acknowledged that the tensile residual stresses decrease with depth from the surface, this conservative approach is recommended because the residual stress gradient through the thickness strongly depends on the existing restraint, which is difficult to predict.

For part-depth repair welds Stacey et al. [2000] suggested that the tensile residual stresses vary from the yield strength of the weld metal at the bottom of the repair to zero at a depth which depends on the welding energy input and the yield strength of the material. This idealized stress field is illustrated in Figure 3.4.

BSI [2005]

The British Standard BS 7910 *Guide to Methods for Assessing the Acceptability of Flaws in Metallic Structures* BSI [2005] proposes for all repair welds to generally use a constant through-thickness residual tensile stress field corresponding to the room temperature yield strength, σ_y, of the material in which the crack is located. For part-depth repair welds the idealized stress field proposed by Stacey et al. [2000] is adopted.

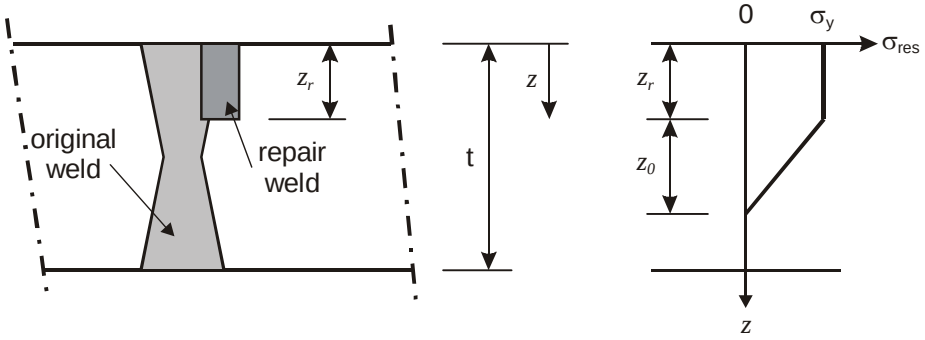

Figure 3.4 *– Idealized transverse residual stress field of a part-depth repair weld according to BSI [2005].*

The terms used in Figure 3.4 are:

z_r : repair depth

$z_0 = \sqrt{\frac{122E_1}{\sigma_y}}$ for ferritic steels and $z_0 = \sqrt{\frac{161E_1}{\sigma_y}}$ for austenitic steels

E_1 : electrical energy per unit length of the largest weld pass at the toe (J/mm)

The distances z, z_r and z_0, and the plate thickness t are in mm and yield strength σ_y is in MPa.

Brown et al. [2006]

Brown et al. [2006] investigated part-depth and full-depth repair welds in 50 to 100 mm thick plates made of a normal strength (yield strength of approximately 310 MPa) and a high strength (yield strength of approximately 700 MPa) steel. Finite element analyses were carried out to predict the residual stress fields and then verified by measurements using the deep hole drilling and X-Ray diffraction techniques. Generally, good agreement between the finite element predictions and the measurements could be observed. The tensile residual stresses were always maximum at or very close to the plate surface at the weld toe, reaching almost the yield strength of the plate material. The stresses decreased with increasing depth. The resulting stress fields are similar to the ones reported by Stacey et al. [2000].

3.4.3 Fillet Welds and Groove Welds at T-Joints

Porter Goff et al. [1988]

Porter Goff et al. [1988] used block sectioning to measure residual stresses in welded tubular Y-nodes (Y-series) and pipe-on-plate joints (P-series). The resulting stress field through the material thickness at the toe of the weld all showed similar features: the maximum tensile stresses are within 2 to 3 mm of the surface and often reach the yield strength of the base material; the surface stresses are slightly lower than the maximum stresses; a rapid decrease in tensile stresses occurs after the maximum stress; compressive stresses exist in the middle portion of the thickness, with a maximum roughly at mid-thickness; tensile stresses of about 50% of the material yield strength develop at the surface opposite to the weld.

Cheng & Finnie [1993]

Cheng & Finnie [1993] used the crack compliance method to obtain the through-thickness residual stress field near the toe of a weld between a 166 mm thick plate and an attached bracket. Although the low carbon steel of the plate was cladded with a special surface protection agent used in nuclear pressure vessels, the residual stresses determined by Cheng & Finnie [1993] showed a pattern similar to the one found by Porter Goff et al. [1988]: the maximum tensile residual stress was obtained very close to the surface and

decreased rapidly to become compressive in the middle portion of the plate before changing into a comparatively small tension on the face of the plate opposite to the weld.

Stacey et al. [2000]

Stacey et al. [2000] analysed data from several investigations on T-butt, pipe-to-plate, tubular T- and Y-joint connections. They concluded that for thick plates ($t > 25$ mm) the residual stresses are tensile and at yield level near the weld toe and compressive in the central region. On the face of the plate opposite to the weld, the transverse stresses are usually tensile. For thin plates ($t < 15$ mm) the reduction in tensile residual stresses towards the centre of the plate is much more moderate and conservatively a uniform tensile stress throughout the thickness should be assumed.

BSI [2005]

For a level 1 assessment (preliminary assessment) of the acceptability of a flaw, BSI [2005] proposes to use a constant residual tensile stress field through the plate thickness equal to the room temperature yield strength, σ_y, of the material, in which the flaw is located. For a level 2 assessment (normal assessment) either an idealized distribution, as shown in Figure 3.5, or the following fourth order polynomial is recommended:

$$\sigma_{res} = \sigma_y \left(0.97 + 2.327\left(\frac{z}{t}\right) - 24.125\left(\frac{z}{t}\right)^2 + 42.485\left(\frac{z}{t}\right)^3 - 21.087\left(\frac{z}{t}\right)^4 \right) \qquad (3.5)$$

where σ_y is the average room temperature yield strength of plate material (MPa), and z and t are defined in Figure 3.5. Equation (3.5) is based on the proposed upper bound fit of data from T-butt, pipe-to-plate, tubular T- and Y-joint connections analysed by Stacey et al. [2000].

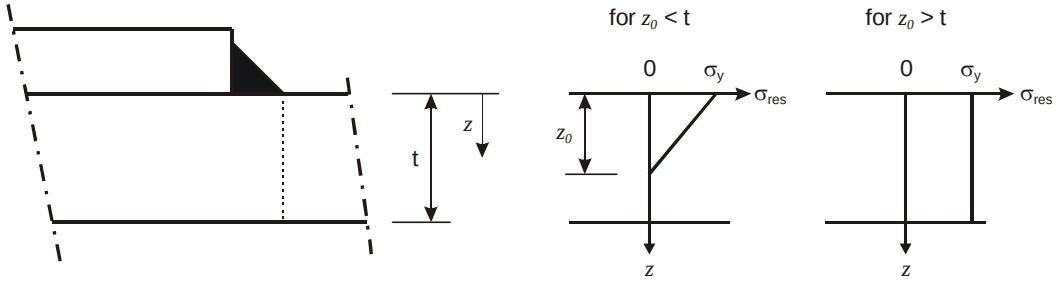

Figure 3.5 *– Idealized distribution of transverse residual stresses at toe of fillet weld according to BSI [2005] for level 2 assessment.*

The terms used in Figure 3.5 are as defined above (Figure 3.4).

Residual Stresses as Random Variables

Since the residual stress field in the vicinity of a weld is difficult to measure and depends on several factors, such as the welding procedure, the joint geometry or the material properties of the base and weld metal, residual stresses need to be treated as a random variable in a probabilistic approach. The following presents some of the statistical distributions of residual stresses assumed in the literature. Tensile residual stresses are taken as positive.

Shetty & Baker [1990]

Based on the findings of Porter Goff et al. [1988], Shetty & Baker [1990] proposed to model the residual stress field at the weld toe with a lognormal distribution, LN(300 MPa, 75 MPa). In addition, the residual stresses at the surface are linearly reduced with crack growth. Shetty & Baker [1990] also suggested that residual stresses are of minor importance during the crack propagation stage but may become significant for the fracture limit state.

The lognormal distribution of the residual stresses at the surface proposed by Shetty & Baker [1990] is also assumed in HSE [1999].

Lukic [1999]

Since the residual stresses near the surface are close to or at the yield strength level of the base material, Lukic [1999] conservatively assumed a uniform through-thickness stress following a lognormal distribution, LN(420 MPa, 42 MPa) for S355 steel (nominal yield strength of 355 MPa). This distribution is also applicable to butt welded joints and repair welds.

JCSS [2001b]

JCSS [2001b] recommends that the residual stresses due to welding follow a lognormal distribution, LN(300 MPa, 60 MPa). Although it is recognized that residual stresses vary through the thickness of the plate, one of the proposed models assumes a uniform stress field, which is believed to yield conservative results for deep cracks and less conservative results for shallow cracks. This assumption is also applicable to butt welded joints and repair welds.

Walbridge [2005]

Walbridge [2005] modeled welding residual stresses in the through-thickness direction by shifting equation (3.5) to approximate the average residual stress field. This results in the following relationship:

$$\sigma_{res} = \sigma_y \left(0.62 + 2.327\left(\frac{z}{t}\right) - 24.125\left(\frac{z}{t}\right)^2 + 42.485\left(\frac{z}{t}\right)^3 - 21.087\left(\frac{z}{t}\right)^4 \right) \qquad (3.6)$$

Equations (3.5) and (3.6) as well as the data reported on T-butt, pipe-to-plate, tubular T- and Y-joint connections in Stacey et al. [2000] are plotted in Figure 3.6.

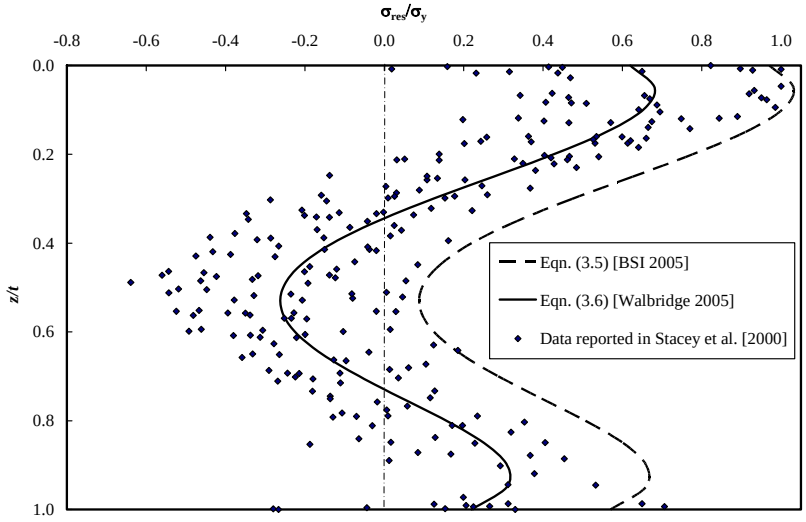

Figure 3.6 *– Measured and proposed distributions of transverse residual stresses at the toe of a weld in the through-thickness direction (positive = tension, negative = compression).*

In order to consider uncertainty in the residual stress field, Walbridge [2005] multiplied equation (3.6) by a variability coefficient Var_{weld} , resulting in the following expression:

$$\sigma_{res} = \sigma_y \left(0.62 + 2.327\left(\frac{z}{t}\right) - 24.125\left(\frac{z}{t}\right)^2 + 42.485\left(\frac{z}{t}\right)^3 - 21.087\left(\frac{z}{t}\right)^4 \right) \cdot Var_{weld} \qquad (3.7)$$

Walbridge [2005] assumed that the variability coefficient Var_{weld} follows a normal distribution, N(1.0, 0.25), which corresponds to the variability proposed by Shetty & Baker [1990].

3.4.4 Relaxation of Residual Stresses during Fatigue Loading

Lawrence [1981]

In the absence of any post weld treatment, Lawrence [1981] assumed that the residual stresses are equal to the material yield strength at the beginning of the service life of the structure. Relaxation of the residual stresses takes place during cyclic loading depending

on the applied number of load cycles and the strain amplitude. As a consequence of this relaxation, Lawrence [1981] suggested that residual stresses need not be accounted for in the crack propagation stage. However, they play an important role in the crack initiation stage.

Nitschke & Wohlfahrt [2001]

Nitschke & Wohlfahrt [2001] suggested that two types of relaxation of tensile residual stresses take place under cyclic loading. During the first load cycle some residual stress relaxation occurs as a result of the peak stress reaching the monotonic yield strength of the material (static relaxation). Further relaxation takes place after the first load cycle, especially in higher strength steels. This subsequent relaxation is attributed to the reduction of yield strength under cyclic loading (cyclic relaxation) as discussed in Chapter 2. Therefore, cyclic relaxation occurs over time until the cyclic stress-strain response has stabilized. The overall relaxation mainly depends on the magnitude of the applied load and the yield strength of the steel, being most prominent for high applied loads and low yield strengths. For common structural steel, the relaxation is predominately static. This is due to the magnitude of the residual stresses that generally reach the yield strength of the steel. For high strength steels, residual stresses do not necessarily reach the yield strength and cyclic relaxation will be more significant.

Jang et al. [2004]

Jang et al. [2004] demonstrated with thermal elasto-plastic finite element analyses that residual stresses change during fatigue loading. This is mainly caused by a redistribution of the residual stresses due to crack growth and a relaxation of the residual stresses due to cyclic plasticity and softening. Assuming an initial residual stress field similar to that proposed by Porter Goff et al. [1988] and Cheng & Finnie [1993], Jang et al. [2004] showed that the maximum tensile residual stresses can relax by about 30% due to cyclic loading, depending on the applied stress range.

3.4.5 Summary and Conclusions

It is generally accepted that the tensile residual stresses due to welding can reach the yield strength of the weld or base material close to the weld. For thick plates ($t > 25$ mm) the transverse tensile residual stresses drop quite rapidly in the through-thickness direction of the base material to become compressive in the central portion of the plate, before changing into moderate tensile residual stresses at the plate surface opposite the weld. This profile is more pronounced for fillet welds than for repair welds. In thin plates ($t < 15$ mm) the reduction in tensile residual stresses towards the centre of the plate is much more moderate and conservatively a uniform tensile stress throughout the thickness should be assumed. For repair welds, it is prudent to assume that the transverse residual stresses stay constant through the entire plate, irrespective of the plate thickness.

Several researchers agree that the residual stresses are not an important factor in crack propagation, but are significant for the initiation stage [Lawrence 1981, Bignonnet et al. 1987, Shetty & Baker 1990]. This is mainly due to relaxation of tensile residual stresses during fatigue loading, especially during crack propagation.

In order to consider uncertainty in the residual stress field, it is appropriate to treat this parameter as a random variable in a reliability-based approach.

3.5 Ultrasonic Peening

3.5.1 Introduction

Ultrasonic peening is a special application of conventional hammer or needle peening. It has recently become a competitive post weld improvement method, said to be faster and less noisy than conventional peening. In order to better understand the effect of ultrasonic peening on the fatigue behaviour of welded details, Section 3.5.2 first presents some general information about peening and Section 3.5.3 outlines a method to determine the peening intensity. A brief history of ultrasonic peening is then summarized in Section 3.5.4. This is followed by an explanation of the mechanism of ultrasonic peening in Section 3.5.5. Finally, the effects of ultrasonic peening on the fatigue behaviour of welds are discussed in Section 3.5.6 and some practical applications of ultrasonic peening in structural engineering are, without pretence of completeness, reviewed in Section 3.5.7.

3.5.2 Peening

Peening is the mechanical cold working of metal surfaces through impact. Most commonly used impact techniques in structural fabrication are hammer or needle blows, as well as shot impingement. All these techniques rely on the same principle: the impact energy deforms the material at its surface. The atoms on the surface become crowded and attempt to go back to their initial position after the peening process. This, however, is resisted by the atoms below the surface, which pull the surface atoms back. Therefore, tensile residual stresses arise below the surface, which are equilibrated by compressive residual stresses at the surface. Since cracks usually start at the toe of a weld, i.e., on the surface of the structure, the formation of such cracks is delayed or even prevented due to the introduction of beneficial compressive residual stresses. Also, peening often results in a better weld profile by reducing small stress raisers and by eliminating small surface flaws through the applied cold working process. This further improves the resistance to crack initiation.

Hammer peening is carried out using a pneumatic or electric hammer with a single hardened steel bit that has a rounded hemispherical tip of 6 – 16 mm in diameter. The

impact frequency is typically between 25 and 100 Hz with an impact energy of 5 to 15 Joules [Haagensen & Maddox 2002]. The impact depth depends on the type of steel, the treatment speed and the number of passes. Kirkhope et al. [1999a] recommend a treatment speed along the weld toe of 1500 mm/min. Using four passes at this speed produces indentations of about 0.6 mm and 0.5 mm for mild and high strength steel, respectively. Haagensen & Maddox [2002] suggest that the minimum indentation depth of 0.3 mm can be achieved in one pass by using lighter, vibration-damped hammer guns at a travel speed of 60 to 90 mm/min. Proper hammer peening should result in a smooth dent with a uniform depth of at least 0.3 mm, preferably 0.5 mm along the weld toe. The hammer should be held at an angle of 60° to 80° with respect to the plate surface and not less than 75° with respect to the line of the weld (cf. Figure 3.7).

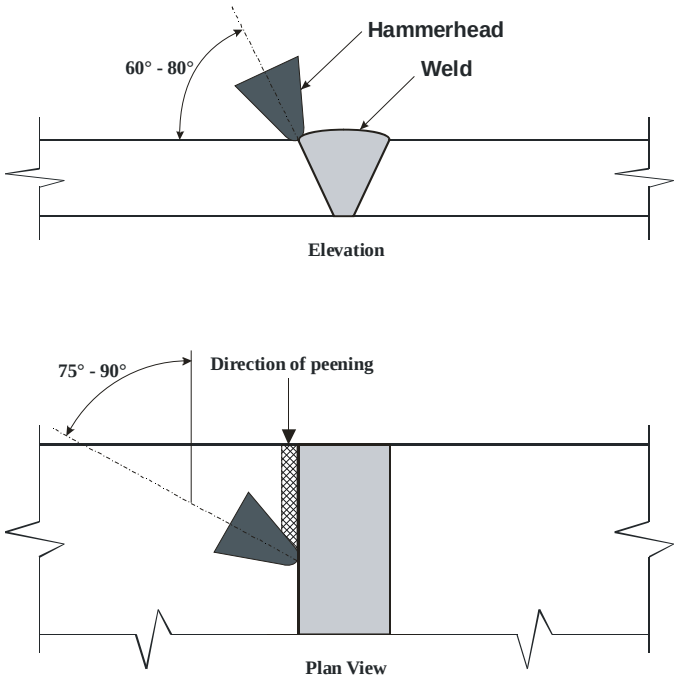

***Figure 3.7** – Proper tool position for hammer peening.*

Needle peening is similar to hammer peening, but uses a bundle of hardened steel wires of approximately 2 mm diameter instead of the single hammer. It has been recommended that the peening speed be around 100 mm/min ensuring that full coverage is achieved to give satisfactory results [Nussbaumer & Imhof 2001].

Shot peening uses small spherical particles called shots to impact the metal surface. Shots range in size from 0.2 to 1.0 mm in diameter and hit the surface at velocities between 40 and 60 m/s.

Hammer and needle peening can result in substantial improvements in fatigue strength compared to untreated details [Haagensen & Fredborg 2003]. Hammer peening is usually more effective than needle peening [Bremen 1989]. However, needle peening is easier to apply and therefore often preferred to hammer peening. Major disadvantages of both methods are their relative slow treatment speeds and high noise emissions. Although faster treatment is achieved by shot peening [Nachman 1999], unless automated, it is more difficult to control the quality and intensity of the treatment. Ultrasonic peening circumvents many of the shortcomings of conventional peening.

Before ultrasonic peening and its applications in structural engineering are discussed in more detail, it is appropriate to briefly present the most common method to determine peening intensity, namely the Almen method.

3.5.3 Peening Intensity – the Almen Method

Although peening intensity is truly characterized by the magnitude and depth of residual stresses introduced by the peening process, the quantification of the residual stresses is difficult and impractical. The intensity of peening is most conveniently assessed using so-called Almen strips made of spring steel (UNS G10700 / AISI 1070 carbon steel) seated in special holding fixtures [Almen & Black 1963]. When the Almen strip is peened from one side the strip bows towards the peened surface after the strip is removed from the holding fixture (convex curvature at the exposed surface). The amount of bow is directly related to the peening intensity and is measured with an Almen gauge. Individual strips are exposed to increasing time periods and the amount of bow is measured for each strip. Plotting the peening time versus the amount of bow generates a so-called saturation curve. The curve shows that for small exposure times, the amount of bow increases rapidly with time but the curve tends to flatten out for higher exposure times. Full intensity, also called saturation, is achieved when, after doubling the exposure time, less than a 10% increase in the amount of bow is observed. A schematic saturation curve showing the intensity time, T , is illustrated in Figure 3.8.

The Almen strip gauge method is widely used to control the intensity of peening [e.g. ASTM 2004a, MIL 1989, SAE 2006]. It is predominantly applied to automated shot-peening. ASTM [2004a] even states that "Manual or hand peening … shall not be permitted, …, since these processes are not as controllable and the results are less predictable than those obtained by automated shot peening." Nevertheless, with diligent workmanship it is expected that acceptable quantifications of the peening intensity for manually peened surfaces can be obtained.

Although the Almen strip gauge method has some inherent disadvantages, its straight-forward procedure along with the integration of numerous parameters has rendered this method the preferred method for controlling the impact intensity [Fuchs 1984]. However, it has to be noted that the Almen intensity does not give a direct measure of the

introduced residual stresses and other methods have to be used to measure the residual stresses in peened metals [Guagliano 2001].

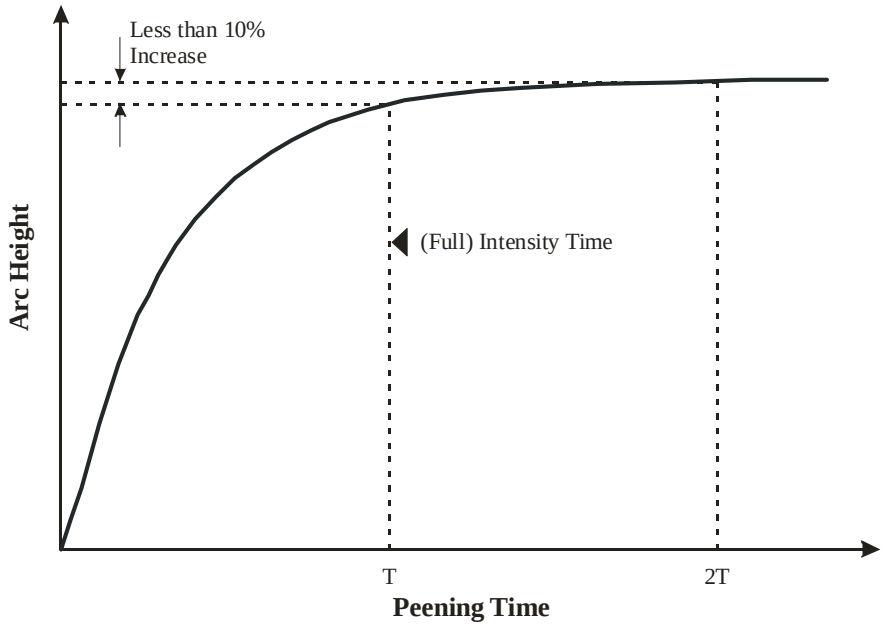

***Figure 3.8** – Almen saturation curve.*

The Almen strip gauge method will be used in Chapter 5 to assess the peening intensity of needle and ultrasonically peened surfaces.

3.5.4 History of Ultrasonic Peening

The following is a summary of a more detailed historical review of ultrasonic peening presented in Kudryavtsev et al. [2004], which also includes a comprehensive list of references.

Research on ultrasonic treatment of metals started in the 1950s in the U.S.A., Austria and the former Soviet Union. This research was rather theoretical and mainly concentrated on demonstrating the beneficial effect of ultrasound on ductility and strength properties of metals. At the same time first attempts were made to improve the geometry of welded joints through deformation treatment employing ultrasound. However, these attempts showed little success. The main problem lay in the design of the equipment for ultrasonic treatment. In the 1960s and 70s advances in equipment design were achieved in the U.S.A. and the former Soviet Union. Intensive investigations were especially carried out at the Institute for Metal Physics (IMP) in Kiev, leading to the still employed intermediate element-striker technology (see next section). With the technology at hand, the IMP started to focus on improving the fatigue behaviour of welds, but due to political boundaries these findings were mainly kept to the Eastern European scientific and

industrial world. Only after the fall of Communism, the benefits of weld improvement treatment by ultrasonic peening became better known in the West, leading to close cooperation between the IMP and the Western industry. Presently, the research mainly concentrates on developing optimal and user friendly applications of ultrasonic peening for the industry, employing expert systems.

3.5.5 Mechanism of Ultrasonic Peening

In ultrasonic peening the strikers (hammer or needles) are activated by a transducer. In the early models of ultrasonic peener the strikers were directly attached to the transducer, resulting in uneconomical use of the ultrasonic energy and difficult handling of the tool. The development of the intermediate element-striker technology allowed for a much more optimal use of the ultrasonic energy. This technology is still state of the art and is explained in the following [Statnikov 1999, Kudryavtsev et al. 2004].

The two basic tools for ultrasonic peening consist of a generator and a transducer as shown in Figure 3.9. The generator supplies the electrical energy, which is converted into ultrasonic vibrations by either a magnetostrictive or piezoelectric transducer.

Magnetostrictive transducers use the property of certain materials to expand and contract when placed under changing magnetic fields. First, the ultrasonic energy from the generator has to be transformed into an alternating magnetic field through the use of a wire coil. Resonant strips of the magnetostrictive material are then used to induce the desired vibrations.

Piezoelectric transducers use a similar principle by changing the dimensions of a material susceptible to electrical charge. Since the electric energy is directly transformed into ultrasonic vibrations, piezoelectric transducers are more efficient than magnetostrictive transducers, which require dual energy conversion from electric to magnetic to ultrasonic. The efficiency of modern piezoelectric transducers is over 95% compared to roughly 35% for typical magnetostrictive transducers. Furthermore, magnetostrictive transducers are normally heavier due to their need for a water cooling system. Therefore, piezoelectric transducers are more commonly used today.

Modern transducers employ the intermediate element-striker technology. Figure 3.10 shows a schematic section through an ultrasonic tool. The forced oscillation of the ultrasonic transducer (1) is transferred to a concentrator of oscillating velocity, called waveguide (2). The output end of the waveguide impacts upon the strikers (3), which are not connected to the transducer (1) and thus free to move. At the output end of the waveguide the ultrasonic oscillation (A) is transformed to impacts (B), which indent the work piece (4). A complex interaction between the waveguide, the strikers, and the work piece results in a superposition of non-periodic stress pulses and ultrasonic periodic stress waves in the work piece.

Figure 3.9 *– Ultrasonic generator and transducer.*

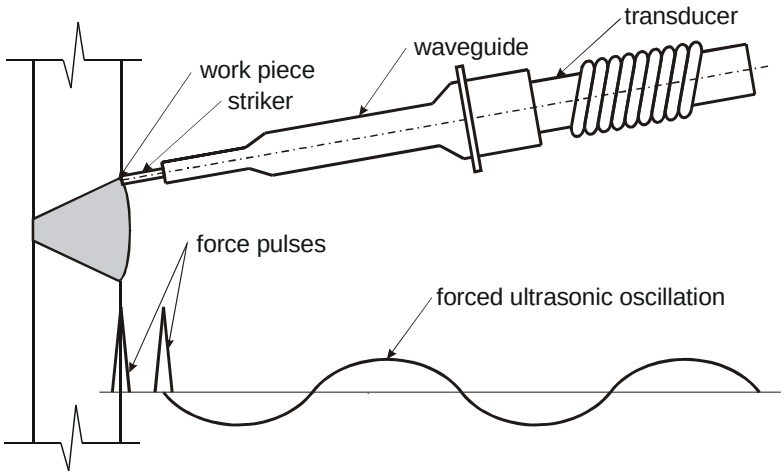

Figure 3.10 *– Mechanism of ultrasonic peening.*

The oscillation frequency of the transducer is normally between 20 and 30 kHz, resulting in hundreds to thousands of impacts per second on the work piece. Compared to conventional peening the striker frequency can therefore be up to 1,000 times higher. The output of the transducer oscillates typically at an amplitude of 20 – 40 μm.

3.5.6 Effects of Ultrasonic Peening on the Fatigue Behaviour of Welds

As for conventional peening, the beneficial effects of ultrasonic peening on the fatigue life of welds are achieved mainly through the introduction of compressive residual stresses into the surface layers of the work piece, improvement of the weld toe profile and the diminution of surface flaw sizes, which results in a reduction in stress concentration. It has also been indicated that ultrasonic peening enhances the mechanical properties of

the surface layer by nanocrystallization, resulting in better corrosion and wear resistance, and the relieving of tensile residual stresses due to the ultrasonic oscillations in the work piece [Kudryavtsev et al. 2004]. Tangible evidence of these factors has yet to be demonstrated. Nevertheless, both effects are thought to be of lesser importance than the residual stresses and the improvement of the weld profile.

The four fatigue improvement factors are illustrated in Figure 3.11 and Figure 3.12. Figure 3.11 distinguishes three zones affected by ultrasonic peening: Zone A, where compressive residual stresses are introduced, Zone B, where tensile residual stresses are relieved, and Zone C, where nanocrystallization takes place. Figure 3.12 shows the improved weld toe profile due to ultrasonic peening. Investigations have shown that it is sufficient to only treat the weld toe zone to achieve optimum fatigue enhancement [Kudryavtsev et al. 1995]. The desirable groove profile depends on the steel grade and should always allow for a smooth transition from the base to the weld metal at the weld toe [Kudryavtsev et al. 1995].

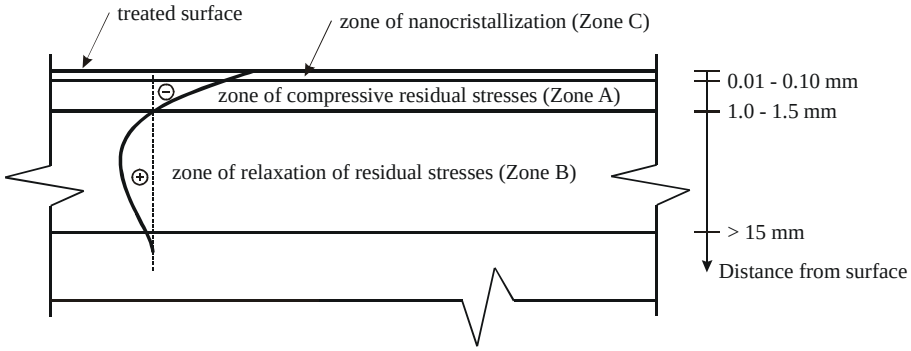

***Figure 3.11** – Schematic cross-section of work piece treated by ultrasonic peening.*

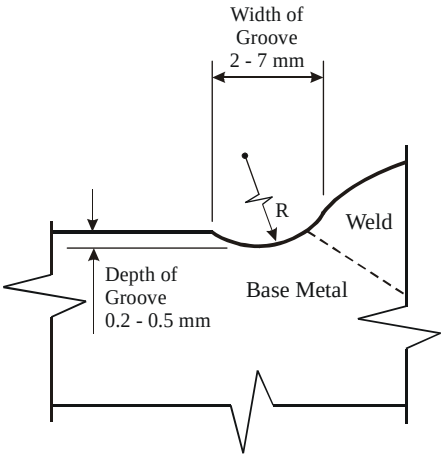

***Figure 3.12** – Improved weld toe profile due to ultrasonic peening [Kudryavtsev et al. 2004].*

Residual Stresses Due to Ultrasonic Peening

Statnikov [1997] measured the residual stresses in grade U3 steel (nominal yield strength of 410 MPa and minimum tensile strength of 690 MPa) after ultrasonic peening. The residual stresses were measured by layered metal etch removal. Compressive residual stresses of 600 MPa were measured at the surface and they were found to decrease below the surface, resulting in a treatment depth of 1.2 mm (depth at which the residual stresses reach zero). Unfortunately, the actual yield and tensile strengths of the steel were not reported. Since these residual stress measurements were carried out on plain steel plates, the applicability of these measurements to welded structures is not clear. Cheng et al. [2003] measured residual stresses in ultrasonically peened base plates and welded specimens using X-Ray diffraction and neutron diffraction methods. It was shown that for both the base and the weld metals compressive residual stresses reached their maximum value at or very close to the surface, exceeding the yield strength of the base metal. The compressive stress zone was approximately 1.5 mm deep. Kuhlmann et al. [2006] used the hole-drilling method to measure the residual stresses to a depth of 1.1 mm in high strength steel plate (nominal yield strength of 690 MPa). The compressive residual stresses were found to exceed the yield strength of the steel and were nearly constant through the 1.1 mm surface layer over which the measurements were made.

The residual stresses measured by Statnikov [1997], Cheng et al. [2003] and Kuhlmann et al. [2006] are all in good agreement. In all investigations compressive residual stresses surpassing the static yield strength of the material determined from a monotonic test were observed. [Prokopenko & Kuz'mich 1994] attribute this to an accumulation of plastic strains, which are obtained under impact loading even at stress levels lower than the static yield strength and cannot completely relax due to the short time interval between ultrasonic impacts. However, it is possible that these high compressive residual stresses are simply a consequence of the high impact energy of ultrasonic peening, resulting in strains that are large enough to induce strain hardening.

It is important to note that the compressive residual stress zone resulting from ultrasonic peening (approximately 1.5 mm deep) is significantly larger than the equivalent zone obtained from conventional peening (approximately 0.2 to 0.5 mm [Blodgett & Nagy 2004, Fathallah et al. 2004]). This observation further suggests that ultrasonic peening might be more effective at improving the fatigue resistance of welded details than conventional peening.

Relaxation of Compressive Residual Stresses

As was discussed for tensile residual stresses, compressive residual stresses are also affected by cyclic loading. Bignonnet et al. [1987] investigated the changes of shot-peening residual stresses due to cyclic loading. The X-ray diffraction method was used to measure the stresses. Only the test with the highest stress range ($\Delta\sigma = 320$ MPa) showed

a substantial drop of about 40% after the initial cycles, quickly reaching a stabilized value. The other three tests with $\Delta\sigma = 300$ MPa, 250 MPa, and 200 MPa showed no significant change in residual stress over their entire fatigue life. X-ray diffraction was also used by Bremen [1989] to measure residual stresses in five test specimens; an untreated base plate and one each on heat-treated, shot, hammer, and needle peened welded specimens. The surface residual stresses were measured before any load application, after 1,000 load cycles at a nominal maximum stress of 200 MPa ($R = 0.1$), and after an additional 1,000 load cycles at a nominal maximum stress of 256 MPa ($R = 0.1$). In all cases a reduction in compressive residual stresses was observed after the first 1,000 load cycles. The reduction of residual stresses was as high as 40% for the needle and 30% for the shot peened specimens. The stress-relieved and hammer peened specimens showed smaller reductions of roughly 10%. No reduction was observed in the subsequent 1,000 load cycles in any of the specimens, which is consistent with the observations made by Bignonnet et al. [1987] for the high stress range, $\Delta\sigma = 320$ MPa. Based on measurements by several researchers, Zhuang & Halford [2001] proposed an analytical approach to model the loss in compressive residual stresses during cyclic loading. This model uses the Bauschinger effect to show that most, if not all, of the reduction in compressive residual stresses is obtained after the first few load cycles, which is consistent with the observations made by Bignonnet et al. [1987] and Bremen [1989].

Several studies [e.g. Bignonnet et al. 1987, Dubois 1994] have shown that a substantial reduction in compressive residual stresses can occur after a compressive overload. Consideration of this reduction in compressive residual stresses results in a considerable complication of the crack initiation and propagation model. This is therefore beyond the scope of the present work.

3.5.7 A Review of Practical Applications of Ultrasonic Peening in Structural Engineering

Numerous research projects investigating the effects of ultrasonic peening on the fatigue behaviour of welded components have been conducted in the last 15 years. The following presents a review of some of the more relevant applications in structural engineering.

Wright [1996]

Direct tension tests on non-load carrying cruciform-type fatigue specimens were carried out at the Turner-Fairbank Highway Research Center in McLean, Virginia. The specimens were made of structural steel with a nominal yield strength of 345 MPa. All tests were conducted at a stress range of approximately 130 MPa and a stress ratio of 0.5. The average number of cycles to failure for the five untreated specimens was 550,000 and for the six specimens treated by ultrasonic peening it was 4,450,000. This corresponds to an increase in fatigue life of approximately 700% for the specimens that

were treated by ultrasonic peening. Since all the tests were conducted at the same stress range and stress ratio, no conclusions concerning the slope and the cut-off of the $\Delta\sigma - N$ curve were obtained. No information concerning the location of the fatigue failures relative to the peened area was given.

Haagensen et al. [1998]

Direct tension fatigue tests on non-load carrying cruciform-type welded high strength steel (nominal yield strength of 700 MPa) were carried out by Haagensen et al. [1998]. Five specimens were left untreated and five were treated by ultrasonic peening. They were tested at several constant stress ranges, resulting in fatigue lives between 10,000 and a little more than 10,000,000 cycles. The stress ratio for all tests was 0.1. Most failures observed in the ultrasonically peened specimens occurred at the toe of the treated weld. However, some failures were also obaserved to start at the root and some even away from the weld, in the base metal. Regression analyses of the test data resulted in two $\Delta\sigma - N$ curves with slope $m = 3.02$ and fatigue life constant $A = 1.39\text{x}10^{12}$ for the untreated and $m = 6.54,\ A = 1.66\text{x}10^{21}$ for the ultrasonically peened specimens. The two curves are illustrated in Figure 3.13. The tests showed substantial improvement in fatigue life due to the ultrasonic peening, especially at lower stress ranges.

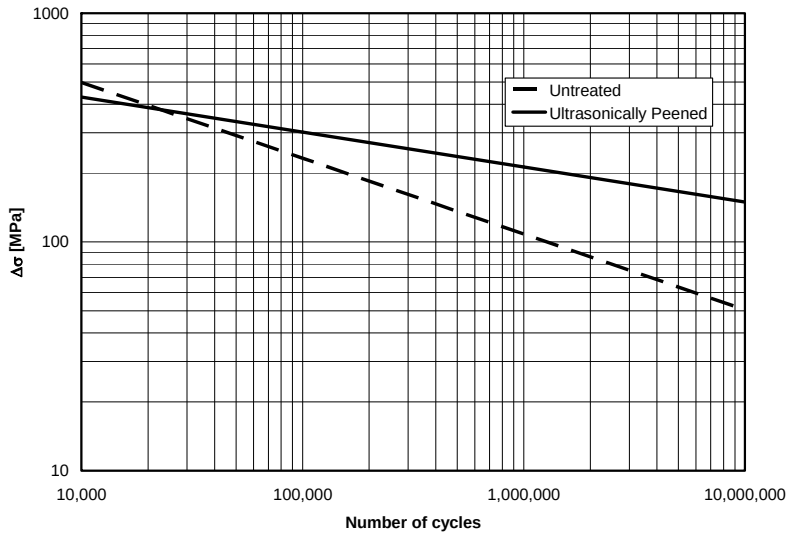

Figure 3.13 *– $\Delta\sigma - N$ curves for untreated and ultrasonically peened test specimens [Haagensen et al. 1998].*

Lobanov & Garf [1998]

Over 50 tests on tubular joints of varying configurations (thickness and number of chords, angle between chords) were carried out by Lobanov and Garf [1998]. The connections were subjected to a combination of axial load and bending moment. The

steel grade of the tubes was not reported. The tests were carried out at several constant stress ranges (the stress ratio was not reported), resulting in fatigue lives between 10,000 and 10,000,000 cycles (run-outs). In all cases the beneficial effect of ultrasonic peening on the fatigue resistance was observed. Lobanov & Garf [1998] also concluded that the slope of the $\Delta\sigma - N$ curves for the treated specimens is shallower ($m \approx 8$ compared to $m \approx 4$ for the untreated specimens), resulting in an increase in fatigue resistance at lower stress ranges. No information concerning the location of the failures was reported.

Huo et al. [2000, 2005]

Direct tension fatigue tests were carried out on welded butt joints and non-load carrying cruciform joints in the as-welded and ultrasonically peened condition [Huo et al. 2000]. The profile of the groove welds in the butt joints was left as-is, i.e., it was not ground. The specimens consisted of steel plates with a specified yield strength of 267 MPa. The tests were carried out at several constant stress ranges, resulting in fatigue lives between 250,000 and 3,000,000 cycles. The stress ratios was set at 0.1 for the butt joints and at 0.25 for the cruciform specimens. The fatigue life for the treated specimens was found to be at least 20 times longer than for the untreated specimens for both types of test specimens. The $\Delta\sigma - N$ constants, m and A, obtained through regression analyses of the test data are presented in Table 3.7. The corresponding curves are illustrated in Figure 3.14. They again show the substantial improvement in fatigue life due to ultrasonic peening, especially at low stress ranges. All of the untreated specimens failed due to cracks starting at the weld toe. However, Huo et al. [2000] reported that in some ultrasonically peened specimens the failure location shifted away from the weld into the base metal.

***Table 3.7** – $\Delta\sigma - N$ constants, m and A, from Huo et al. [2000].*

Type of Joint	Condition	*m*	*A*
Butt Joint	As-Welded	5.7	0.270×10^{19}
	Ultrasonically Peened	17.6	0.719×10^{48}
Cruciform Joint	As-Welded	5.6	0.496×10^{18}
	Ultrasonically Peened	13.0	0.298×10^{37}

Huo et al. [2005] later investigated the effect of variable amplitude loading on the fatigue strength of untreated and ultrasonically peened non-load carrying cruciform specimens. The specimens were prepared from steel plates with a nominal yield strength of 390 MPa. Three blocks of constant stress ranges (direct tension) were applied in a predefined sequence. The sequence was repeated until failure of the specimen occurred, resulting in fatigue lives between 200,000 and 3,000,000 cycles. The stress ratios in all blocks were kept approximately constant at 0.1. A comparison with the constant amplitude test results

[Huo et al. 2000], based on Miner's equivalent stress range, showed that a slightly lower fatigue strength at two million cycles is expected under variable amplitude loading (reduction of 5% for the untreated and 7% for the ultrasonically peened specimens). The researchers attributed this to a possible loss in compressive residual stresses at the toe of the treated weld due to the higher peak loads applied during the variable amplitude loadings. Nevertheless, the fatigue life improvement of the ultrasonically peened specimens was still substantial compared to the untreated specimens (increase of the fatigue strength at two million cycles from $\Delta\sigma \approx 150$ MPa for the untreated to $\Delta\sigma \approx 210$ MPa for the ultrasonically peened specimens). Almost all failures of the ultrasonically peened specimens occurred at the weld toe.

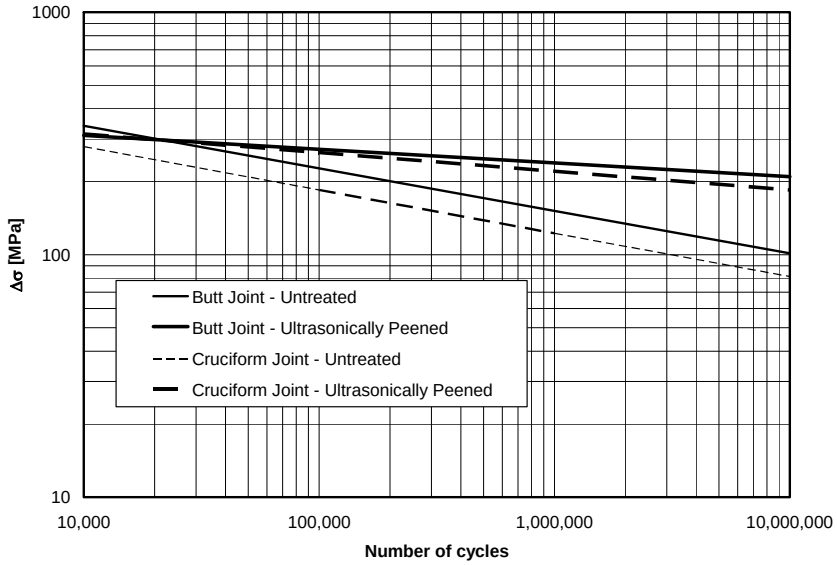

Figure 3.14 *– $\Delta\sigma - N$ curves for untreated and ultrasonically peened test series from Huo et al. [2000].*

Takamori & Fisher [2000] and Roy et al. [2003]

Fatigue tests on plate girders with welded stiffeners and cover plates were conducted by Takamori & Fisher [2000]. The plate girders were tested in four point bending to create a zone of constant moment. The nominal yield strength of the steel for the plate girder was 485 MPa and the stiffeners and cover plates were of 345 MPa steel. Different test series with untreated and ultrasonically peened welds were run at several constant stress ranges. The stress ratio was about 0.1 for all tests. Fatigue lives between 1,000,000 and over 10,000,000 cycles (run-outs) were obtained. Only one of the 13 treated details failed before the tests had to be stopped due to failures at other locations. The failure location for this specimen was not reported. Since most of the results for the ultrasonically peened details were run-outs, no regression analyses on these could be conducted. Nevertheless, the tests showed that ultrasonic peening improved the fatigue strength of both the

stiffener and cover plate details substantially, from AASHTO [2007] Category C to at least Category B for the stiffeners and from Category E' to at least Category C for the cover plates.

Fatigue tests were also carried out by Roy et al. [2003]. Rolled wide flange beams with a yield strength varying from 366 to 435 MPa were tested under several constant stress ranges in four point bending. The beams contained welded stiffeners and cover plates, both having a minimum yield strength of 407 MPa. All critical welds were ultrasonically peened. The minimum applied stress was kept constant for each of four sets of tests, implying that the stress ratio varied from about 0.06 to about 0.6. The tests showed a substantial enhancement in fatigue strength due to ultrasonic peening compared to earlier work carried out in the same laboratory on similar untreated details. The enhancement was greatest at low stress ranges. Effectiveness of the peening process was reduced with increased stress ratio, i.e., the higher the mean stress, the smaller the benefit. All specimens failed by cracking of the tension flange at the end of the cover plates. A total of 18 out of the 19 failures started at the toe of the weld; one was in the root of the weld. No regression analysis was carried out. The test results were just compared to the AASHTO curves [AASHTO 2007], suggesting an increase in fatigue strength from Category C to at least Category B for the stiffener details and from Category E′ to at least Category D for the cover plate details.

Lihavainen et al. [2003]

Direct tension fatigue tests were carried out on non-load carrying attachments in the as-welded and ultrasonically peened condition. The specimens consisted of steel plates with a nominal yield strength of 355 MPa. The tests were carried out at several constant stress ranges, resulting in fatigue lives between 200,000 and 6,000,000 cycles. The stress ratio for one set of tests was 0.1. The other set of tests was also carried out at several constant stress ranges, but the maximum stress was always kept equal to the measured yield strength of the base material, resulting in varying and rather high stress ratios. Ultrasonic peening was found to lead to substantial improvement in fatigue strength. The researchers observed a slope of the $\Delta\sigma - N$ curve close to 10 for the treated specimens. The effect of stress ratio did not seem to be more pronounced than in untreated specimens. The fatigue cracks in the treated specimens initiated at the weld toe.

Galtier & Statnikov [2004]

Fatigue tests were carried out on non-load carrying T-attachments in the as-welded and peened conditions. The tests were carried out in four point bending. The specimens consisted of steel plates with a nominal yield strength of 355 MPa and 700 MPa, respectively. The tests were carried out at several constant stress ranges and the observed fatigue life was between 100,000 and 2,000,000 cycles. The stress ratio was set at 0.1 for all tests. A substantial improvement in fatigue strength of the specimens treated by

ultrasonic peening was observed. Due to the introduction of higher compressive residual stresses, the improvement is significantly more marked for the higher strength steel.

Lixing et al. [2004]

Direct tension fatigue tests were carried out on complete penetration groove welded butt joints and on non-load carrying fillet welded attachments in the as-welded and ultrasonically peened conditions. The profile of the groove welds was left as-is, i.e., it was not ground. The specimens were made from steel plates with a nominal yield strength of 235 MPa. The tests were carried out at several constant amplitude stress ranges, resulting in fatigue lives between 300,000 and more than 20,000,000 cycles (run-out). The stress ratio was 0.1 for all tests. Regression analyses of the test results showed that ultrasonic peening improved the fatigue resistance and resulted in a much shallower slope of the $\Delta\sigma - N$ curve. All the cracks of the untreated specimens started at the weld toe, whereas 7 of the 13 butt joint specimens and 4 of the 7 fillet weld specimens that were treated by ultrasonic peening fractured in the base metal or did not fail at all. For both test series, the weld toe failures of the ultrasonically peened specimens occurred only at high stress ranges ($\Delta\sigma > 210$ MPa).

Günther et al. [2005]

Direct tension fatigue tests were carried out on non-load carrying attachments [Günther et al. 2005]. The test specimens were prepared with steel plates with a nominal yield strength of 460 MPa. A first set of tests on untreated specimens was carried out under several constant stress ranges, all with a stress ratio of 0.1. Similar specimens were tested under the same conditions to about 75 to 90% of the fatigue life determined in the first series of tests and were inspected for cracks. After it was established that the specimens did not contain any detectable cracks, i.e., cracks smaller than about one millimetre, the specimens were treated with ultrasonic peening. Although some fatigue damage could have been present before the treatment, all five tests showed a significant improvement in fatigue strength compared to the untreated reference test results. At a stress range of $\Delta\sigma \approx 210$ MPa the increase in fatigue life was approximately 200%, at $\Delta\sigma \approx 130$ MPa no failures were recorded after a fatigue life extension of more than 400%. This confirmed the increased benefit of ultrasonic peening for lower stress ranges, i.e., higher fatigue lives, found by other researchers. No information concerning the location of the failures is given.

Kudryavtsev et al. [2005, 2006]

Direct tension fatigue tests were carried out on non-load carrying attachments [Kudryavtsev et al. 2005]. The specimens were made of steel plates with a nominal yield strength of 260 MPa. The tests were carried out at several constant stress ranges. The stress ratio for all the tests was 0. Three sets of tests were conducted. The first set consisted of untreated specimens. The second set was ultrasonically peened before any

load was applied. The third set underwent cyclic loading to 50% of its expected fatigue life and was then ultrasonically peened. The two sets that were treated showed a substantial improvement in fatigue strength compared to the untreated set, with the improvement being more significant at the lower stress ranges. Interestingly, the specimens that were peened after being subjected to cyclic loading showed higher fatigue strength than the specimens that were treated before any load application. According to the researchers this "… could be explained by a more beneficial redistribution of residual stresses and/or 'healing' of fatigue damaged material by UP [ultrasonic peening] …". No information concerning the location of the failures was presented.

In a subsequent investigation Kudryavtsev et al. [2006] tested a T-joint of rectangular hollow cross-section members in direct tension. No information about the steel grade of the tubes is given. Nine untreated and three ultrasonically peened specimens were tested. The tests were carried out at several stress ranges. All 12 specimens were tested under completely reversed loading ($R = -1$). The three treated specimens showed significantly longer fatigue lives than all the untreated specimens. Failure of the untreated specimens always occurred at the weld toe near the end of the weld. The failure location in the treated specimens shifted to within the weld away from the end of the weld.

Nitschke et al. [2007]

Nitschke et al. [2007] compared several post weld treatment methods (TIG-dressing, spot heating, burr grinding, shot and ultrasonic peening). The researchers concluded that the improvement of the weld profile is as important, if not more important, than the introduction of residual stresses. A poor weld profile with a strong notch effect will exhibit a low fatigue life, even after peening. They also observed that in soft metals, such as aluminium, ultrasonic peening is often not as effective as conventional peening at improving the fatigue resistance. This is attributed to the greater mechanical damage introduced in the specimen due to the higher peening intensity of ultrasonic peening. Nevertheless, for common structural steels Nitschke et al. [2007] emphasized the beneficial effect of ultrasonic peening.

Ummenhofer & Weich [2007]

Fatigue tests and measurements of residual stresses were carried out on several fillet welded details by Ummenhofer & Weich [2007]. In particular high strength structural steel with a nominal yield strength of 690 MPa was investigated. A substantial increase in fatigue life of ultrasonically peened welds was observed. As for several other test programs, the improvement in fatigue life was most noticeable at lower stress ranges and for higher strength steel. For high strength structural steel a shift of the crack initiation site into the base metal could be observed. The treatment depth was determined to reach at least 0.3 mm.

Peening Intensity

Most of the references discussed above did not give any information about treatment intensity. Often the peening was carried out by the tool manufacturer and exact tool speeds and number of passes were not reported. Huo et al. [2000] treated their specimens with at least two passes at a minimum tool speed of approximately 500 mm/min. Roy et al. [2003] used three to five passes at an average tool speed of 300 mm/min. From the limited information presented in other references it ensues that the intensities reported in Huo et al. [2000] and Roy et al. [2003] are representative.

Discussion

A large number of investigations have been conducted over the past 15 years to assess the effect of ultrasonic peening on the fatigue life of welded details. All these investigations, which were carried out in different parts of the world, demonstrated that the fatigue behaviour is substantially improved by ultrasonic peening, even when applied after a large number of stress cycles. Furthermore, these investigations showed three important characteristics distinguishing treated welds from untreated welds:

- The slope of the $\Delta\sigma - N$ curve for ultrasonically peened welds ranges from approximately $m = 6$ to $m = 20$ compared to roughly $m = 3$ for untreated welds.
- The fatigue strength of untreated welded structures is not significantly affected by the steel grade. However, the improvement of the fatigue strength due to ultrasonic peening seems to be more significant for high strength steels compared to normal strength steels. This is due to the higher compressive residual stresses developed in high strength steel.
- Untreated welds generally fail through cracking at the weld toe. Although the majority of the reported cracks in ultrasonically peened specimens still started at the weld toe, a shift of the crack initiation site into the weld or away from the weld into the base metal was observed for some specimens. This shift was more pronounced for groove welded butt joints than for fillet welded attachments.

It is generally accepted that the stress ratio plays only a small role, if any, in the fatigue life prediction of untreated welded structures. However, as the tests by Roy et al. [2003] have shown, this might not be true for peened welds. Since just a few tests with varying stress ratios have been reported, the observations concerning this parameter are not conclusive and more research is necessary.

3.5.8 Summary and Conclusions

Ultrasonic peening is based on the well known cold working weld improvement methods of hammer or needle peening. In addition to the beneficial effects of introducing compressive residual surface stresses and improving the weld profile as well as reducing

surface flaw size, ultrasonic peening results in nanocrystallization of the surface layer, giving the material better corrosion and wear resistance, and in relieving tensile residual stresses due to the ultrasonic oscillations in the work piece. Furthermore, ultrasonic peening is claimed to have the advantage of being a faster, less noisy, and easier controllable post weld improvement method than conventional peening.

Compressive residual stresses due to ultrasonic peening can surpass the yield strength of the base material, but tend to relax after the first few load cycles. The relaxation can reach 50% of the initially introduced residual stresses.

Several investigations have been conducted in the last 15 years to assess the effect of ultrasonic peening on the fatigue life of welded structures. All investigations have shown a substantial improvement in fatigue strength due to ultrasonic peening. Analysis of the test results leads to shallower $\Delta\sigma - N$ curves for ultrasonically peened welds compared to untreated welds. The beneficial effect of ultrasonic peening seems to be more marked for higher strength steels. No conclusive results concerning the effect of mean stress have been found yet.

All of the reviewed literature on applications of ultrasonic peening dealt with fillet welds and non-ground welds in butt joints. These welds have significant stress raisers at the toe of the weld, which makes post weld treatment methods such as peening quite effective at extending the fatigue life. Since all the welds of the large scale specimens tested in the present work are ground flush, the natural stress concentration at the weld toe is removed and the efficiency of ultrasonic peening may decrease.

3.6 Summary

The background information in Chapter 2 showed that the fatigue life of welded structures is primarily governed by the material response, the weld quality, restraints during welding, and post weld treatment. Based on these findings, the literature of the four main issues affecting the fatigue behaviour of the welded structural details investigated in the present work were reviewed in this chapter: fatigue material properties (Section 3.2), initial weld imperfections, especially initial crack size and shape (Section 3.3), residual stresses (Section 3.4), and ultrasonic peening (Section 3.5).

Sufficient information on the fatigue material properties of 350WT is available from different test series. The results from these tests will be analyzed in Chapter 4. However, no valuable data for weld material matching 350WT steel are available. Therefore, crack initiation and propagation tests on weld metal are conducted within the present work and the results are presented and analyzed in Chapter 4.

Several research projects investigated the size of initial flaws. All reported flaw sizes are smaller than acceptable levels from North American and European welding codes.

Nevertheless, due to different welding procedures and human factors, a great variability in initial crack size and shape is observed. Several probabilistic fracture mechanics models have made use of the results from these investigations, implementing crack sizes in the range of approximately 0.1 mm and 1.0 mm. Investigations of fracture surfaces in the large and small scale tests described in Chapter 5 will be used here to compare with the data reported in the literature.

Residual stress fields due to welding are complex and often only approximately known. It is generally agreed that the tensile residual stresses due to welding reach or are close to the yield strength of the weld or base material close to the weld. The transverse tensile residual stresses drop quite rapidly in the through-thickness direction of the base material to become compressive in the central portion of the plate, before changing into moderate tensile residual stresses at the plate surface opposite the weld. This profile is more pronounced for fillet than for repair welds. Since the magnitude of residual stresses are a function of the existing restraint, which can hardly be predicted, it is prudent for repair welds to assume that the transverse residual stresses stay constant through the entire plate thickness.

Several investigations have been conducted in the last 15 years to assess the effect of ultrasonic peening on the fatigue resistance of welded structures. All investigations have shown a substantial improvement in fatigue strength due to ultrasonic peening. Analysis of the test results show a shallower $\Delta\sigma - N$ curve for welds treated by ultrasonic peening compared to untreated welds. All the reviewed tests were conducted on specimens with significant stress raisers. Whether ultrasonic peening is as efficient for ground flush full penetration welds, where the natural stress concentration is much smaller, is investigated in the present work through an experimental program presented in Chapter 5 and analyzed in Chapters 6 and 7.

With the tools presented in this chapter and Chapter 2 as well as the definition of appropriate fatigue material properties in Chapter 4, it will be possible to deterministically predict the fatigue life of specimens tested in Chapter 5. This is done in Chapter 6. In Chapter 7 the actual test results obtained in Chapter 5 will be compared to the predicted fatigue lives established in Chapter 6 and the model will be calibrated using a probabilistic parametric study. A general reliability-based approach of the calibrated model will then be developed in Chapter 8 and applied to other test results on welded and non-welded details from the literature and to a practical application from the heavy mining industry.

4. FATIGUE MATERIAL PROPERTIES

4.1 Introduction

This chapter defines the material properties used to solve equations (2.5) and (2.9) in order to predict the fatigue life of the details investigated in Chapter 5. The properties of the base metal, CSA G40.21 Grade 350WT [CSA 2004], which are taken from work carried out earlier at the University of Alberta and elsewhere, are analysed in Section 4.2. These properties are compared to properties found in the literature for other steel grades as discussed in Chapter 3. Section 4.3 summarizes the experimental and analytical investigations carried out in the present work on the fatigue properties of weld metal matching Grade 350WT steel.

4.2 Base Metal: Grade 350WT Steel

4.2.1 Introduction

The fatigue properties of Grade 350WT steel have been investigated at the University of Alberta and Dalhousie University. The crack propagation properties are determined from tests carried out by Taheri et al. [2003] and Yin et al. [2006]. The obtained initiation and propagation properties are compared to properties reported in the literature for other comparable steel grades. Before these test results are analysed, Section 4.2.2 first outlines the CAN/CSA G40.21 material standard requirements for Grade 350WT steel. The Ramberg-Osgood parameters for the cyclic stress-strain curve, equation (2.3), are then presented in Section 4.2.3. The crack initiation parameters used in equation (2.5) and the crack propagation parameters used in equation (2.9) are analysed in Sections 4.2.4 and 4.2.5, respectively.

4.2.2 Material Standard Requirements

The material properties requirements for grade 350WT steel are governed by the Canadian standard CAN/CSA G40.21-04 *Structural Quality Steel* [CSA 2004]. Grade 350WT steel is a weldable steel with controlled toughness and a nominal yield strength of 350 MPa. According to CSA G40.21 [2004], the tensile strength for plates of grade 350WT must be between 480 and 650 MPa. The minimum absorbed CVN impact energy needs to be 27 J at 0°C for Category 1 and at -45°C for Category 4 steel. Category 4 steel is commonly used for plates in bridges and heavy mining equipment in Northern Alberta. The required chemical composition is given in Table 4.1.

4.2.3 Cyclic Properties

Wang [2010] derived the Ramberg-Osgood parameters of the cyclic stress-strain curve, equation (2.3), from strain controlled fatigue crack initiation tests. Equation (2.3) should be used in fatigue analyses in-lieu of the monotonic stress-strain curve.

$$\varepsilon = \frac{\sigma}{E} + \left(\frac{\sigma}{K'} \right)^{1/n'} \tag{2.3}$$

Applying the procedure outlined in Chapter 2, Wang [2010] obtained the following material constants:

$E = 213{,}000$ MPa
$K' = 727$ MPa
$n' = 0.150$

Table 4.1 – *Required chemical composition of 350WT steel (in % by weight) according to CSA G40.21 [2004].*

C, max	Mn	P, max	S, max	Si	Grain refining elements [1)]	Grain Size
0.22	0.80-1.50	0.03	0.04	0.15-0.40	0.10	2)

1) Typically Columbium (Niobium) and/or Vanadium are used
2) WT steel shall be supplied using a fine grain practice

Figure 4.1 shows the resulting cyclic stress-strain curve, as well as the monotonic stress-strain curve obtained from a coupon taken from the same plate as the crack initiation specimens. A comparison of the two curves reveals that the tested Grade 350WT steel experiences significant cyclic softening.

4.2.4 Crack Initiation Properties

The SWT relationship, equation (2.5), is used to model crack initiation. It is recalled that the relationship takes the following form:

$$\frac{\Delta\varepsilon}{2} = \frac{\left(\sigma_f^{'}\right)^2}{\sigma_{\max} E} \left(N_{init}\right)^{2b} + \frac{\sigma_f^{'} \varepsilon_f^{'}}{\sigma_{\max}} \left(N_{init}\right)^{b+c} \tag{2.5}$$

where $\sigma_f^{'}$, b, $\varepsilon_f^{'}$, and c are the required crack initiation parameters. The modulus of elasticity, E, is the same as the one used in equation (2.3).

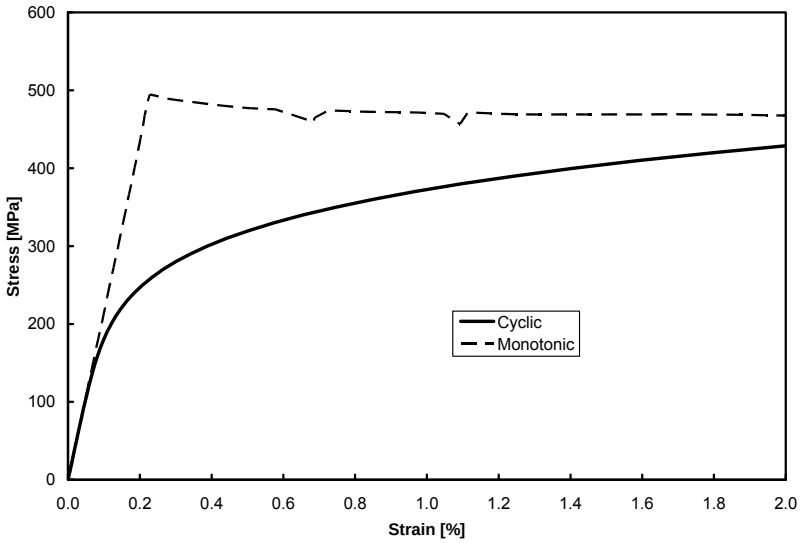

Figure 4.1 *– Cyclic and monotonic stress-strain curves as obtained by Wang [2010] on Grade 350WT steel (only the tension portion is shown).*

Wang [2010] carried out crack initiation tests on 350WT steel under fully reversed cyclic loading ($R = -1$). A total of 15 smooth specimens were obtained from a 6 mm thick steel plate. However, only nine test results are usable for the determination of the crack initiation properties.[1] All tests were run under constant strain amplitude with a mean stress of zero. The maximum strain varied from 980 με to 6,230 με. The test data reported by Wang [2010] are presented in the $\Delta\varepsilon/2$ versus N_{init} plot of Figure 4.2. In addition to the total strain amplitude, the elastic and plastic strain amplitudes are presented as well.

The fatigue constants required in equation (2.5) were determined by Wang [2010] using linear regression analyses for the elastic and the plastic fatigue initiation properties: $\sigma_f^{'} = 542$ MPa, $b = -0.0719$, $\varepsilon_f^{'} = 0.0922$, and $c = -0.429$. The resulting regression lines are also shown in Figure 4.2. The properties as determined by Wang [2010] will be compared at the end of this chapter to properties reported in the literature for similar steel grades.

As for the crack propagation properties, it is assumed in the present work that a strong (negative) correlation between the exponents, b and c, and $\sigma_f^{'}$ and $\varepsilon_f^{'}$, respectively, exists. Considering the exponents as deterministic parameters and using values obtained from the regression analysis, i.e., $b = -0.072$ and $c = -0.43$, average values and standard

[1] One specimen got damaged during the set-up, one failed due to an obvious imperfection, and four did not fail at all. Since the strain amplitude for the four run-outs was rather low and it is not known how close to the fatigue limit they are, they were omitted from the anlysis.

deviations for $\sigma_f^{'}$ and $\varepsilon_f^{'}$ can be determined, which are shown in Table 4.2. Both parameters are modeled here with a lognormal distribution.

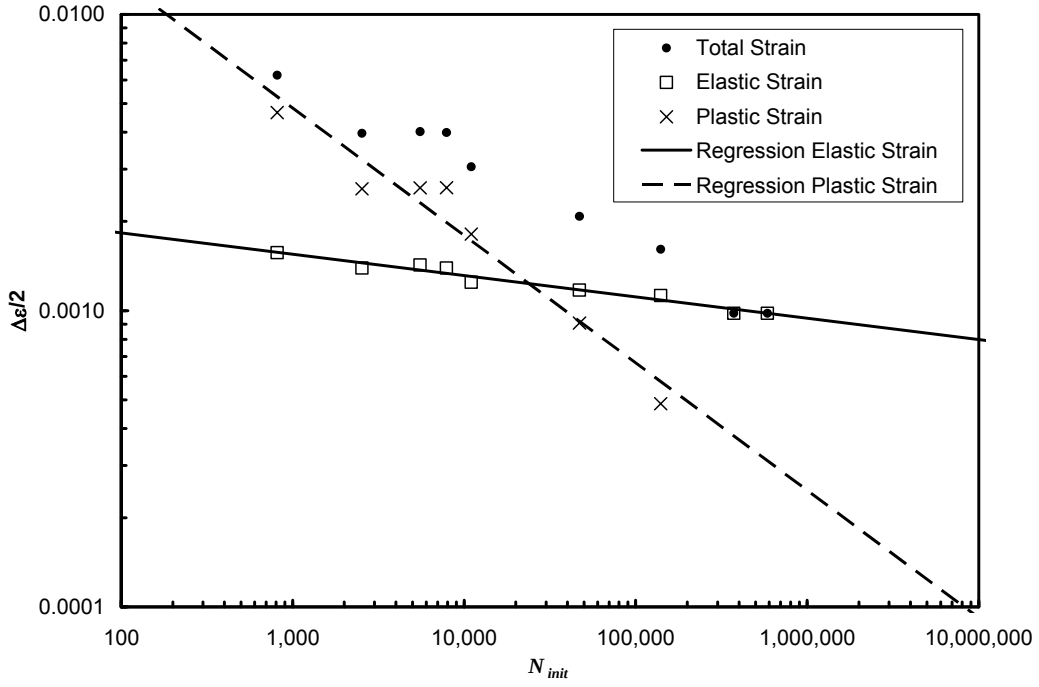

Figure 4.2 *– Crack initiation test results from 350WT steel tested under completely reversed loading by Wang [2010].*

Table 4.2 – *Average values of $\sigma_f^{'}$ and $\varepsilon_f^{'}$ and corresponding standard deviations as obtained through statistical analyses of the test data reported in Wang [2010].*

	Average	**Standard Deviation**
$\sigma_f^{'}$ [MPa]	543	18
$\varepsilon_f^{'}$ [-]	0.0940	0.017

Further tests on smooth specimens subjected to stress ratios $R > -1$, i.e., with mean stress levels greater than zero, confirmed that the SWT model (equation 2.5) adequately predicts the fatigue initiation life of specimens subjected to non-zero mean stress.

4.2.5 Crack Propagation Properties

The Paris-Erdogan relationship accounting for the threshold stress intensity factor range, ΔK_{th}, equation (2.9), is used to model crack propagation:

$$\frac{da}{dN} = C \cdot \left(\Delta K^{m} - \Delta K_{th}^{m}\right) \Leftrightarrow N_{prop} = \int_{a_0}^{a_f} \frac{da}{C \cdot \left(\Delta K^{m} - \Delta K_{th}^{m}\right)} \tag{2.9}$$

with C, m, and ΔK_{th} being the required crack propagation properties.

Taheri et al. [2003] carried out crack propagation tests on middle tension M(T) specimens made from Grade 350WT steel according to ASTM standard E 647 *Standard Test Method for Measurement of Fatigue Crack Growth Rates* [ASTM 2000]. Three specimens were tested at a stress range of $R = 0.1$. One specimen each was tested at $R = 0.2$, $R = 0.3$, and $R = 0.4$. Yin et al. [2006] carried out crack propagation tests on 350WT steel. Eight samples were machined from a 35 mm thick steel plate. Four were taken close to one surface, two close to the other surface, and two from the middle plane of the plate. Two from each location were tested at a stress ratio $R = 0.1$. The remaining two surface specimens were tested at a stress ratio $R = 0.5$. Both, the Taheri et al. [2003] and the Yin et al. [2006] results showed that a significantly faster crack growth rate is observed in tests run at large stress ratios ($R = 0.3$ and higher) compared to tests run at $R = 0.1$. However, the Taheri et al. [2003] results confirmed the findings reported in Chapter 2 and 3 that the crack growth rates are not noticeably affected anymore by the mean stress for stress ratios greater than approximately 0.3. The Yin et al. [2006] results indicated that the location of the test specimens through the plate thickness is not influential.

Taheri et al. [2003] and Yin et al. [2006] determined regression values for both C and m for each of the stress ratios (see Table 3.3). However, the literature review in Chapter 3 showed that a strong negative correlation between C and m exists, which is expected since the two parameters are determined through a regression analysis. It is therefore more adequate to assume a fixed value for m and account for the uncertainty in crack propagation rate by considering only C as a random variable. The generally accepted value of $m = 3.0$ is assumed in the present work. Only the tests with $R = 0.1$ and $R \geq 0.4$ are analysed here. Since the mean stress for large stress ratios does not significantly affect the crack growth rates, the Taheri et al. [2003] results for $R = 0.4$ and the Yin et al. [2006] for $R = 0.5$ are treated as one set of results. Using only the test results with $da/dN > 1.2 \times 10^{-5}$ mm/cycle (limit above which ΔK_{th} should not significantly affect the crack growth rate anymore) linear regression analyses on the $\log(\Delta K)$ versus $\log(da/dN)$ data for the two stress ratios ($R = 0.1$ and $R \geq 0.4$) were carried out.[1] The resulting mean C-values and their standard deviations, s_C, are shown in Table 4.3 (for da/dN in mm/cycle and ΔK in MPa$\sqrt{\text{mm}}$).

[1] Although the results of the Taheri et al. [2003] and the Yin et al. [2006] tests might show a statistically significant difference, they were grouped into one sample for each stress ratio. This was done to give a more representative mean value and standard deviation of *C*. It is understood that by simply combining all the data, the test program with more data points has a stronger weight.

Table 4.3 – *Average C-values and corresponding standard deviations,* s_C .

R	C	s_C
0.1	2.71×10^{-13}	5.83×10^{-14}
≥0.4	3.81×10^{-13}	5.36×10^{-14}

The individual test data as reported by Taheri et al. [2003] and by Yin et al. [2006] for both sets of stress ratios are shown in the log-log plot of Figure 4.3. Also shown in Figure 4.3 are the regression lines for the two stress ratios using the C -values from Table 4.3.

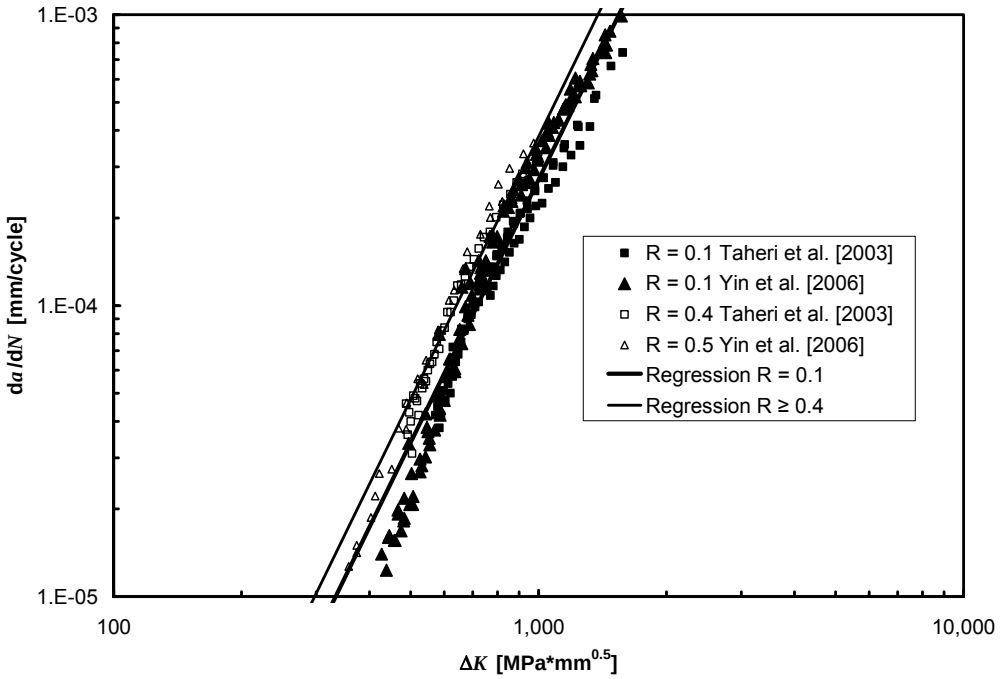

Figure 4.3 *– Crack propagation test results from 350WT specimens.*

All tests carried out by Taheri et al. [2003] and by Yin et al. [2006] were run at stress intensity factor ranges, ΔK , too high to determine ΔK_{th} . According to the literature review carried out in Chapter 3, the mean value of ΔK_{th} is approximately 100 MPa$\sqrt{\text{mm}}$. According to Walbridge [2005] the coefficient of variation can be assumed to be 0.15 (see Chapter 3), resulting in the lognormal distribution, LN(100,15), for ΔK_{th} of the base metal.

4.2.6 Summary

Based on the analysis of tests carried out at the University of Alberta and on information from the literature, the following material properties for the base metal Grade 350WT steel are proposed in the present work:

- Cyclic properties:
  E = 213,000 MPa
  K' = 727 MPa
  n' = 0.150
- Crack initiation properties[1]:
  $\sigma_f^{'}$ = LN(543,18)
  b = -0.072
  $\varepsilon_f^{'}$ = LN(0.0940,0.017)
  c = -0.43
- Crack propagation properties[2]:
  m = 3.0
  C = LN(2.71×10^{-13},5.83×10^{-14}) for small stress ratios or models accounting for crack closure
  LN(3.81×10^{-13},5.36×10^{-14}) for high stress ratios
  ΔK_{th} = LN(100,15)

4.3 Weld Metal: Matching Grade 350WT

4.3.1 Introduction

One of the main objectives of the present work is to determine the fatigue properties of weld metal matching Grade 350WT steel. To assure consistency, the same welding process (FCAW) using one type of electrode (Megafil®713R, E491T1 according to ANSI/AWS standard A5.20 *Specification for Carbon Steel Electrodes for Flux Cored Arc Welding* [AWS 2005]) was applied for all welding. The Megafil®713R is a seamless wire manufactured by the German company Drahtzug Stein. Although the toughness requirements for this wire are less stringent than for Category 4 steel (see further down), it was chosen because of its reduced hydrogen content due to the absence of a seam. The same welder deposited all the welds. More information about the welding procedure can be found in Appendix B.

---

[1] $\sigma_f^{'}$ in MPa, all other parameters dimensionless

[2] C in (mm/cycle)$\cdot\left(\text{MPa}\sqrt{\text{mm}}\right)^{-m}$, ΔK_{th} in $\text{MPa}\sqrt{\text{mm}}$

To confirm that the weld metal matches Grade 350WT steel several ancillary tests were carried out. First, the chemical composition of the weld metal was determined (Section 4.3.2). The special plates were then welded (Section 4.3.3) and all-weld metal coupons were obtained to determine the stress-strain characteristics (Section 4.3.4) and CVN toughness (Section 0) of the weld metal. The determination of the fatigue properties was done on crack initiation (Section 4.3.6) and crack propagation coupons (Section 4.3.7) machined from the welded plates.

4.3.2 Chemical Composition

A pad for the chemical analysis of the undiluted weld metal was prepared in accordance with AWS A5.20 [2005]. A sample was taken from the core of the pad and a chemical analysis was conducted. The chemical composition by weight is presented in Table 4.4. The weld metal composition indicates that the content of each element analyzed is well within the maximum values specified in AWS A5.20 [2005] (shown in brackets), except for chromium, which is about 20% higher than the maximum specified. Furthermore, a comparison with Table 4.1 shows that the chemical composition of the weld metal is similar to the specifications for grade 350WT steel, with the exception of the silicon content, which is slightly higher in the weld metal. This is expected since silicon acts as a deoxidizer during welding.

Table 4.4 – *Chemical composition (% per weight) of weld metal used in the present work.*

Main Elements	%	Grain Refining Elements	%	Other Elements	%
C	0.060 [0.12]	Nb	0.0502	Cr	0.0247 [0.2]
Mn	1.41 [1.75]	V	0.0163 [0.08]	Cu	0.132 [0.35]
P	0.0084 [0.03]			Ni	0.232 [0.5]
S	0.0074 [0.03]			Ti	0.0603
Si	0.567 [0.9]			N	0.003

The values in closed brackets are maximum values specified in AWS A5.20 [2005]

4.3.3 Welded Plates

Grade 350WT, Category 4 steel plates were cut, bevelled and welded in the I. F. Morrison Laboratory at the University of Alberta. Preliminary tension and CVN coupons from the base metal yielded tensile properties (average yield value of 456 MPa and tensile strength of 557 MPa from 3 tests) and an energy absorption (average of 96 J at -45°C from three tests, with the minimum being 65 J) confirming the steel grade of the plates [Wang 2010]. The plates were welded according to AWS A5.20 [2005] using the flux cored arc welding (FCAW) process. The procedure was identical to the one used for the welds in the small scale specimens and the initial procedure for the repair welds of the large scale tests described in Chapter 5. The dimensions of the welded plates are shown in Figure 4.4.

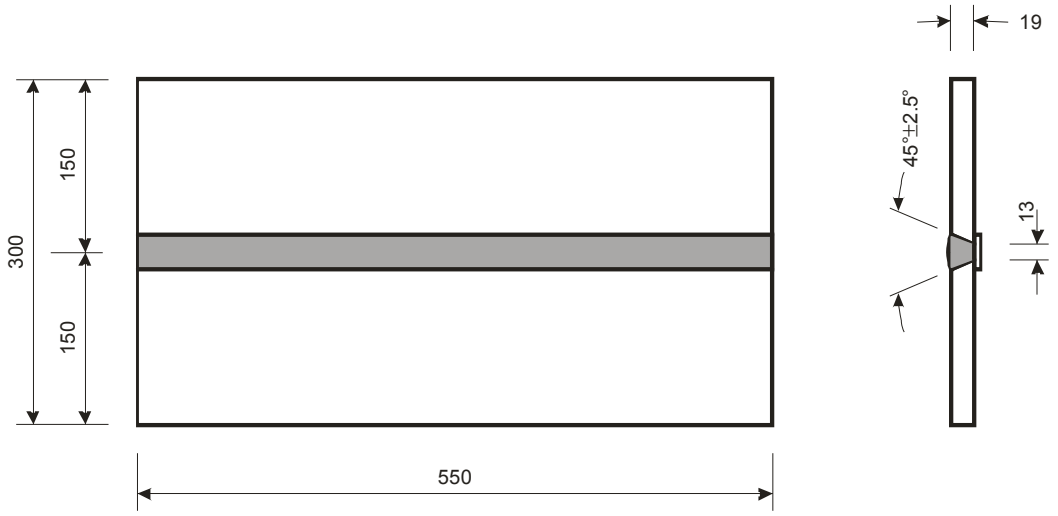

***Figure 4.4** –Welded plates (dimensions in mm).*

Tension coupons, CVN specimens as well as crack initiation and propagation specimens were machined from these plates.

4.3.4 Tension Coupon Tests

To confirm that the weld metal matched grade 350WT steel, sheet-type tension coupons were machined from the welded plates. Four coupons perpendicular to the weld were prepared (see Figure 4.5). Prior to machining the reduced section, the backing bar and the weld profile were removed by grinding and the ground surfaces milled in order to obtain a constant specimen thickness. According to ANSI/AWS standard B4.0M *Standard Methods for Mechanical Testing of Welds* [AWS 2000] tension coupons need not be stress relieved. However, for comparison reasons, two of the perpendicular coupons (TT-SR1 and TT-SR2) were stress relieved at 600°C for two hours. The other two

perpendicular coupons (TT-1 and TT-2) were tested as machined. All coupons used a 50 mm gauge length. The tests were run in a universal testing machine (MTS® 810) in the I. F. Morrison Structures Laboratory of the University of Alberta and followed the testing procedure outlined in AWS B4.0 [2000], which is the same procedure as specified in ASTM standard A370-05 *Standard Test Methods and Definitions for Mechanical Testing of Steel Products* [ASTM 2005]. An extensometer, mounted on one of the faces of the reduced section, was used to measure the strains beyond the strain at the ultimate strength, ε_u. It was removed shortly before failure of the specimens occurred. The strain at rupture was measured manually from light punch marks placed on the test specimen at the start of testing, and from measurement of the cross-sectional area at the fracture location. The engineering stresses were determined by dividing the recorded load by the measured initial cross-sectional area of each specimen. The test strain rate was incrementally increased from approximately 10 με/sec in the elastic range to 1,500 με/sec as the test approached rupture.

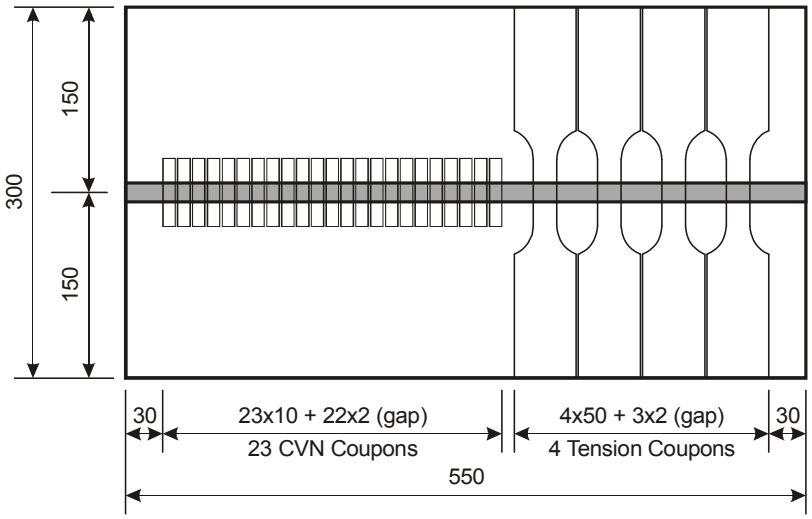

***Figure 4.5** – Tension and CVN coupons machined from the welded plates.*

The stress-strain curves obtained from the tension coupon tests are shown in Figure 4.6 and the results are summarized in Table 4.5. The test results indicate that the tensile properties of the welded coupons are within the strength limitations for grade 350WT steel (minimum yield strength of 350 MPa, ultimate strength between 480 MPa and 650 MPa, see Section 4.2.2). As expected, the stress-relieved coupons show a more ductile behaviour (roughly 20% more relative elongation at rupture), but a smaller yield strength (roughly 6% reduction) than the non-stress-relieved coupons.

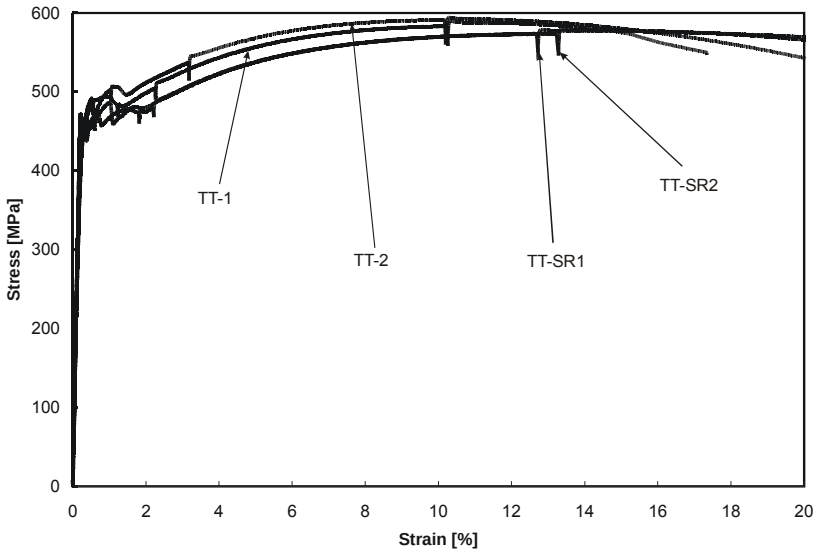

Figure 4.6 *– Stress-strain curves from the weld coupons.*

Table 4.5 – *Summary of the tension coupon test results of the welded specimens.*

Specimen Designation	Orien-tation	E [MPa]	σ_{ys} [MPa]	ε_{SH} [%]	σ_{us} [MPa]	ε_u [%]	ε_r [%]	RA [%]
TT-1	Perpen-dicular to weld (trans-verse)	217,000	470	1.5	560	10	26	43
TT-2		217,000	470	1.5	560	11	32	67
TT-SR1		215,000	440	1.2	550	14	36	68
TT-SR2		216,000	440	0.9	550	14	35	62

E: Modulus of elasticity
σ_{ys}: Static yield strength
ε_{SH}: Strain at onset of strain hardening (determined with 10 mm gauge extensometers)
σ_{us}: Static ultimate strength
ε_u: Strain at ultimate strength (determined with 10 mm gauge extensometers)
ε_r: Strain at rupture (hand measured on 50 mm gauge marks)
RA: Reduction in area at rupture

4.3.5 CVN Tests

Although Charpy V-Notch (CVN) impact tests do not provide an exact measure of material toughness [Barsom & Rolfe 1999], they are commonly used in industry for quality control, mainly because of their simple testing procedure and low cost. Standard CVN tests were therefore carried out on coupons machined from the welded plates to confirm that the weld metal corresponds to CSA G40.21 Category 4 steel (at least an

average of 27 J from three tests at a temperature of -45°C) and to establish the CVN-energy versus temperature curve for future reference. The tests were conducted in a commercial testing laboratory according to ASTM A370 [ASTM 2005]. The orientation of the specimens was chosen in accordance with AWS A5.20 [AWS 2005], i.e., with the notch parallel to the weld axis (see Figure 4.5 and Figure 4.7). Strips slightly larger than the CNV dimensions were saw cut and then stress relieved at 600°C for 2 hours. The coupons were machined to the desired dimensions at the University of Alberta and the notch finally broached at the commercial testing laboratory.

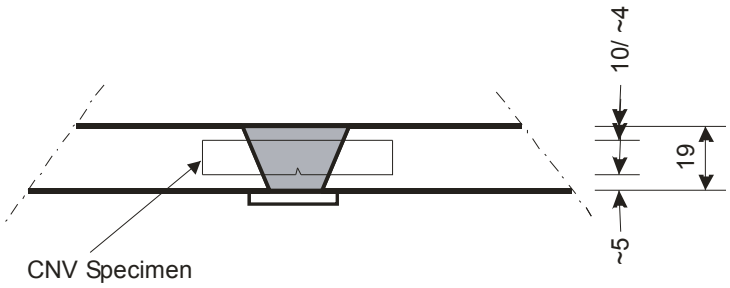

***Figure 4.7** – CVN coupons machined from the welded plates (dimensions in mm).*

A total of 21 specimens were tested[1], three each at -45°C, -30°C, -15°C, 0°C, 10°C, 20°C, and 30°C. The results of each test are presented in Table 4.6 and plotted in Figure 4.8.

The required energy absorption for AWS E491T1 weld metal is 27 J at -20°C. This requirement is obviously met since all specimens tested at -30°C show a higher energy absorption than 27 J. In comparison to CAN/CSA G40.21 [CSA 2004], the CVN results of the weld material indicate that the toughness would respect the requirements for Category 4 base material, since the average of the three specimens tested at –45°C is 39 J (which is greater than the 27 J requirement at –20°C) and the minimum value is 23 J (which is greater than two-thirds of 27 J).

[1] Two specimens were prepared as spares, but did not need to be tested (none of the tested coupons contained a weld imperfection).

Table 4.6 – *Summary of the CVN test results for the weld metal.*

Temperature [°C]	**Specimen Designation**	**CVN Energy [J]**
-45	CVN-45.1	24
	CVN-45.2	23
	CVN-45.3	71
-30	CVN-30.1	98
	CVN-30.2	91
	CVN-30.3	52
-15	CVN-15.1	123
	CVN-15.2	66
	CVN-15.3	35
0	CVN0.1	110
	CVN0.2	117
	CVN0.3	115
10	CVN10.1	141
	CVN10.2	132
	CVN10.3	163
20	CVN20.1	126
	CVN20.2	165
	CVN20.3	157
30	CVN30.1	152
	CVN30.2	156
	CVN30.3	152

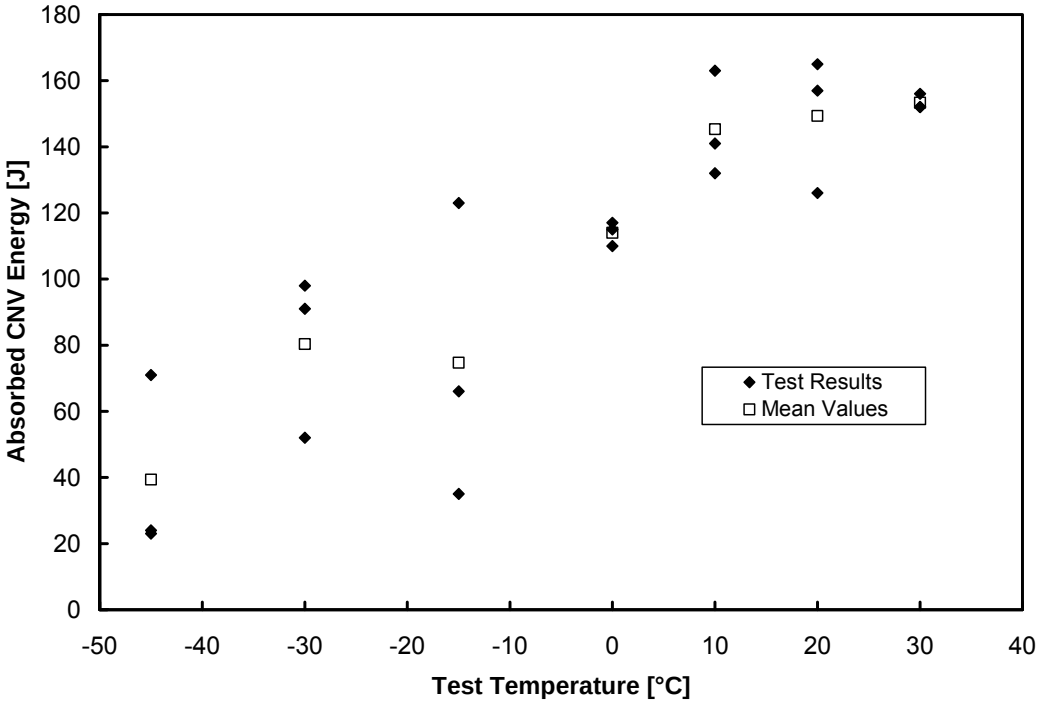

Figure 4.8 *– CVN-Energy versus Temperature curve for the weld metal.*

4.3.6 Crack Initiation Tests

Test Specimens

Smooth specimens were machined from the welded plates. For comparison and consistency, identical flat sheet fatigue specimens with rectangular cross-section as tested by Chen et al. [2005] and Wang [2010] were prepared. All specimens were designed, machined and tested according to ASTM standard E606 *Standard Practice for Strain-Controlled Fatigue Testing* [ASTM 2004b]. The specimens were machined to a overall thickness of 6 mm and a width of 25.4 mm and 8.3 mm in the grip area and the test section, respectively. The specimen geometry is shown in Figure 4.9. The longitudinal axis of all specimens was perpendicular to the weld. The specimens were machined to a surface finish of roughly 10 μm and were then stress relieved at 600°C for 2 hours. All the specimens were then polished with 600 grit sandpaper (CAMI Designation) and a fine emery cloth to further reduce the surface roughness in the tested section.

Test Matrix

The findings of other researchers that the SWT model gives good predictions for the crack initiation phase of specimens subjected to non zero mean stress [Dowling 1999] were confirmed by both the Chen et al. [2005] and the Wang [2010] investigations. Therefore, only completely reversed tests were carried out in this test program to

determine the fatigue crack initiation properties of the weld metal. These properties will be used in the SWT relationship, equation (2.5). The strain amplitudes, $\Delta\varepsilon/2$, were set to cover a range of initiation lives from a few thousands up to roughly ten million. Run outs, i.e., tests that did not fail, were stopped at ten million cycles. No retesting at a strain amplitude resulting in a run out was carried out, since the data can not be used offhand in a statistical analysis. As shown in All tests were conducted under strain control at frequencies varying between 1 and 10 Hz depending on the strain amplitude. The sinusoidal cyclic signal was generated by the software FastTrack2TM WaveMaker to the defined frequency and strain amplitudes. Stress and strain readings were sampled at a rate of 100 Hz. Real time stress versus time, strain versus time, and stress-strain curves were continuously displayed to facilitate the monitoring of the tests. These curves were also recorded at predefined cycle intervals, ranging from every cycle at the beginning of each test (up to 100 cycles) to every 2,000 cycles for tests running several million cycles. The cycles were counted by the FastTrack2TM Console software interface and continuously displayed as well as recorded along with the real time curves. The maximum and minimum strains were kept within ±2% of the desired values for the entire duration of the tests.

Table 4.7, a total of 19 tests were carried out.

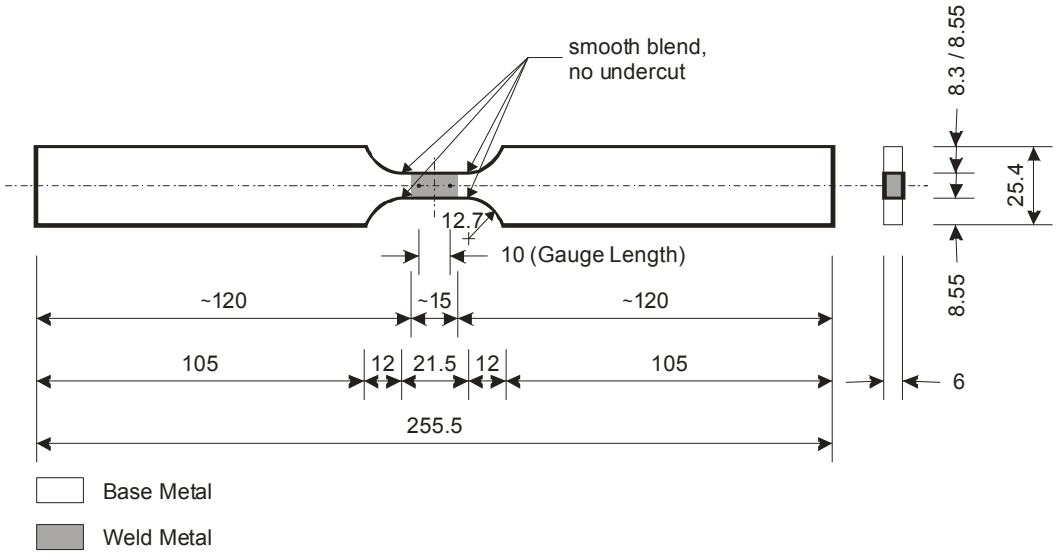

***Figure 4.9** – Smooth specimen for fatigue crack initiation tests (dimensions in mm).*

Test Set-Up and Instrumentation

All tests were carried out at room temperature on a servohydraulic universal testing machine with a fatigue rating of 100 kN (Instron® 8801). Figure 4.10 shows a typical test set-up. Stresses were determined from load measurements and the measured initial area of the test specimens. Sample measurements of the reduced section confirmed that the

coupons were machined to within an accuracy of 1 μm. The axial strain in the reduced section was determined with a 10 mm gauge length extensometer having a full scale strain range of 2.0%.

All tests were conducted under strain control at frequencies varying between 1 and 10 Hz depending on the strain amplitude. The sinusoidal cyclic signal was generated by the software FastTrack2™ WaveMaker to the defined frequency and strain amplitudes. Stress and strain readings were sampled at a rate of 100 Hz. Real time stress versus time, strain versus time, and stress-strain curves were continuously displayed to facilitate the monitoring of the tests. These curves were also recorded at predefined cycle intervals, ranging from every cycle at the beginning of each test (up to 100 cycles) to every 2,000 cycles for tests running several million cycles. The cycles were counted by the FastTrack2™ Console software interface and continuously displayed as well as recorded along with the real time curves. The maximum and minimum strains were kept within ±2% of the desired values for the entire duration of the tests.

Table 4.7 – *Test matrix for crack initiation specimens.*

Specimen Designation	***Δε/2*** **[%]**	**Number of Tests**
FI-500	0.500	3
FI-300	0.300	3
FI-250	0.250	2
FI-200	0.200	3
FI-150	0.150	3
FI-130	0.130	2
FI-125	0.125	1
FI-120	0.120	1
FI-100	0.100	1

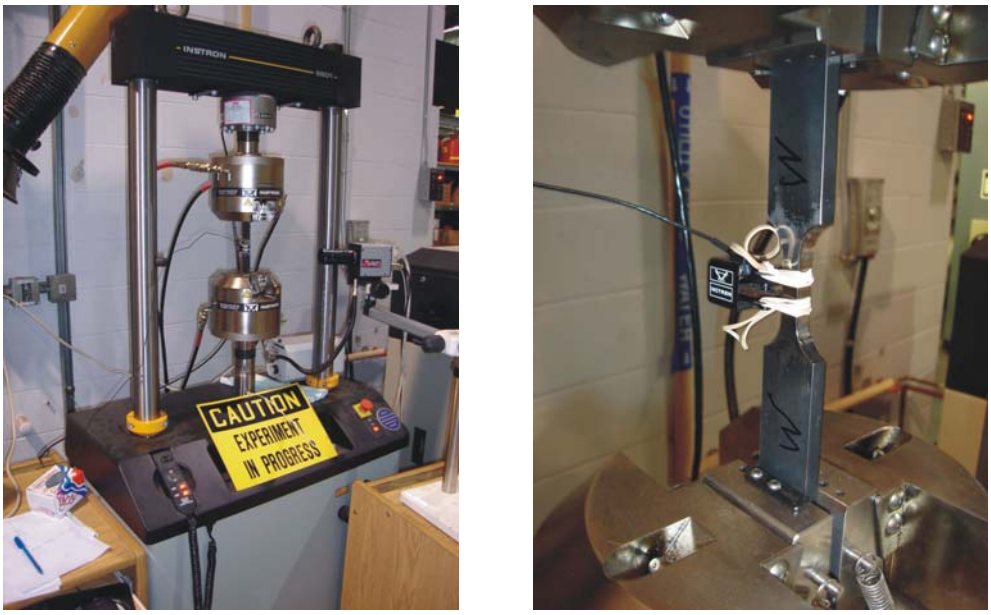

Figure 4.10 *– Typical fatigue crack initiation test set-up: overview (left) and detail of specimen with extensometer (right).*

The fatigue initiation life, N_{init}, was defined as the number of cycles when the maximum tensile load dropped to about 50% of its initial value.[1] This is consistent with the work of Chen et al. [2005] and Wang [2010]. For safety reasons, the tests were automatically terminated at a preset stroke limit, which was always higher than the stroke corresponding to the 50% load drop criterion. The specimens that were not severed at this stage were subjected to a monotonic tensile load until complete failure took place, exposing the fracture surface.

In order to account for the bending stresses resulting from the out-of-straightness of the test specimens, four separate static tests were conducted before starting the fatigue tests with the extensometer placed on the different faces of the test specimen.

To protect the specimens and instrumentation from unexpected events, lower and upper bound limits on loads and strains were set in addition to the stroke limit that triggered the termination of the tests.

Special precautions were taken to prevent bending of the specimens during gripping. First, the specimens were fully gripped at the top and the proper alignment confirmed. The lower grip pressure was then turned on and the load checked. If more than 0.01 kN were applied to the specimen, the specimen was released, realigned, and regripped.

---

[1] The 50% load drop corresponds to the failure criterion defined in ASTM [2004b], which states the number of cycles corresponds to the number of cycles where the ratio of the modulus following a peak tensile stress, E_{NT}, and the initial modulus, E_{CT}, drops below 0.5

Effective Strain Amplitude

The static tests indicated that the coupons were deformed about the two principal axes. During the cyclic testing the extensometer was always placed on the North face as illustrated in Figure 4.10. As a consequence of the biaxial bending, the strain was non-uniform over the cross-section. The strain amplitude was always controlled to the desired level on the North face. Therefore, the nominal strain amplitude needed to be adjusted for each test depending on the curvature of the test specimen. Two correction factors were used:

- To determine the cyclic stress-strain (Ramberg-Osgood) parameters E, K', and n': The cyclic stress-strain curve is based on an average response of the specimens. Therefore the nominal strain amplitude for these calculations was adjusted by the ratio of the average of the four measured strains (one on each face of the test specimen) divided by the strain on the North face, namely,

$$F_{av} = \frac{\text{Average}(\varepsilon_N, \varepsilon_S, \varepsilon_E, \varepsilon_W)}{\varepsilon_N} \tag{4.1}$$

  The values of F_{av} for the test specimens of this test program are presented in the third column of Table 4.8. The correction factor varied from 0.967 to 1.071, with an average value of 1.013.

- To determine the crack initiation parameters σ_f', b, ε_f', and c: Most cracks initiated at the corner or the face where the strain readings during the static tests were highest. Therefore the nominal strain amplitude for these calculations was adjusted by the ratio of the maximum measured strain to the strain on the North face, namely,

$$F_{\max} = \frac{\text{Max}(\varepsilon_N, \varepsilon_S, \varepsilon_E, \varepsilon_W)}{\varepsilon_N} \tag{4.2}$$

  The values of $F_{\max}$ for the test specimens of this test program are presented in the third column of Table 4.9. The correction factor varied from 1.000 to 1.112, with an average value of 1.062.

The subscripts in equations (4.1) and (4.2) stand for the North, South, East, and West face, respectively. Due to the loss of some data for specimen FI-500.1 no correction factors could be determined and the nominal strain amplitude was used in the analyses of the test data.

Cyclic Stress-strain Curve

The cyclic stress-strain curve is obtained by joining the peak values of the stabilized hysteresis loops of each specimen. All tests showed strain softening, with the material response stabilizing after about 1,000 cycles, as illustrated in Figure 4.11 for specimen FI-30.1.

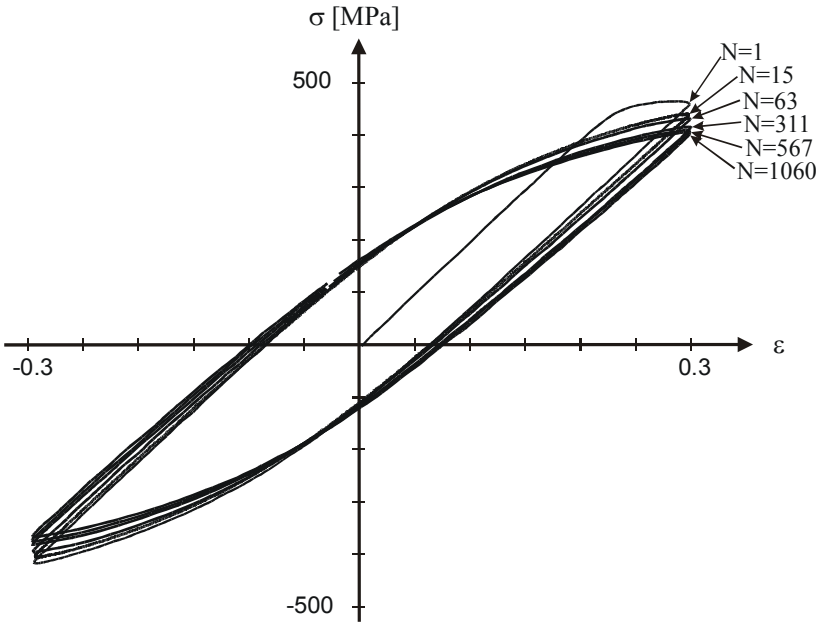

Figure 4.11 *– Example of hysteresis loops (specimen FI-30.1).*

The positive peaks (strain amplitude and stabilized maximum stress) taken from the hysteresis loops of all specimens at approximately 1,000 cycles are presented in Table 4.8. The nominal strain amplitude, $\Delta\varepsilon/2$, is adjusted by the correction factor F_{av} to get the effective strain amplitude, $(\Delta\varepsilon/2)_{av}$.

Figure 4.12 presents the positive peaks on a stress-strain diagram. A regression curve, also shown in Figure 4.12, was fitted through the data points, resulting in the following Ramberg-Osgood parameters:

$E_{av} = 207{,}000$ MPa
$K' = 532$ MPa
$n' = 0.037$

Figure 4.12 also shows the monotonic stress-strain curve for tension coupon TT-1. A comparison of the two curves shows that the tested weld metal experiences cyclic softening. However, the modulus of elasticity is not influenced by the cyclic stresses.

In the probabilistic approach used later in this work, the modulus of elasticity is taken as a random variable. A statistical analysis of all tests that stayed in the elastic range ($\Delta\varepsilon/2 \le 0.150\%$) resulted in a standard deviation for the modulus of elasticity of $E_{stdev} = 5{,}000$ MPa.

Table 4.8 – *Positive peaks of all crack initiation specimens at approximately 1,000 cycles.*

Specimen Designation	$\Delta\varepsilon/2$ **[%]**	F_{av} **[-]**	$(\Delta\varepsilon/2)_{av}$ **[%]**	σ_{max} **[MPa]**
FI-500.1	0.500	1.000	0.500	420
FI-500.2	0.500	1.001	0.501	440
FI-500.3	0.500	0.994	0.497	430
FI-300.1	0.300	1.030	0.309	420
FI-300.2	0.300	0.985	0.296	410
FI-300.3	0.300	1.002	0.301	410
FI-250.1	0.250	1.033	0.258	400
FI-250.2	0.250	1.009	0.252	410
FI-200.1	0.200	1.071	0.214	360
FI-200.2	0.200	0.967	0.193	380
FI-200.3	0.200	1.021	0.204	400
FI-150.1	0.150	0.988	0.148	320
FI-150.2	0.150	1.004	0.151	310
FI-150.3	0.150	1.032	0.155	320
FI-130.1	0.130	1.037	0.135	270
FI-130.2	0.130	1.008	0.131	270
FI-125.1	0.125	1.009	0.126	260
FI-120.1	0.120	1.034	0.124	250
FI-100.1	0.100	1.030	0.103	220

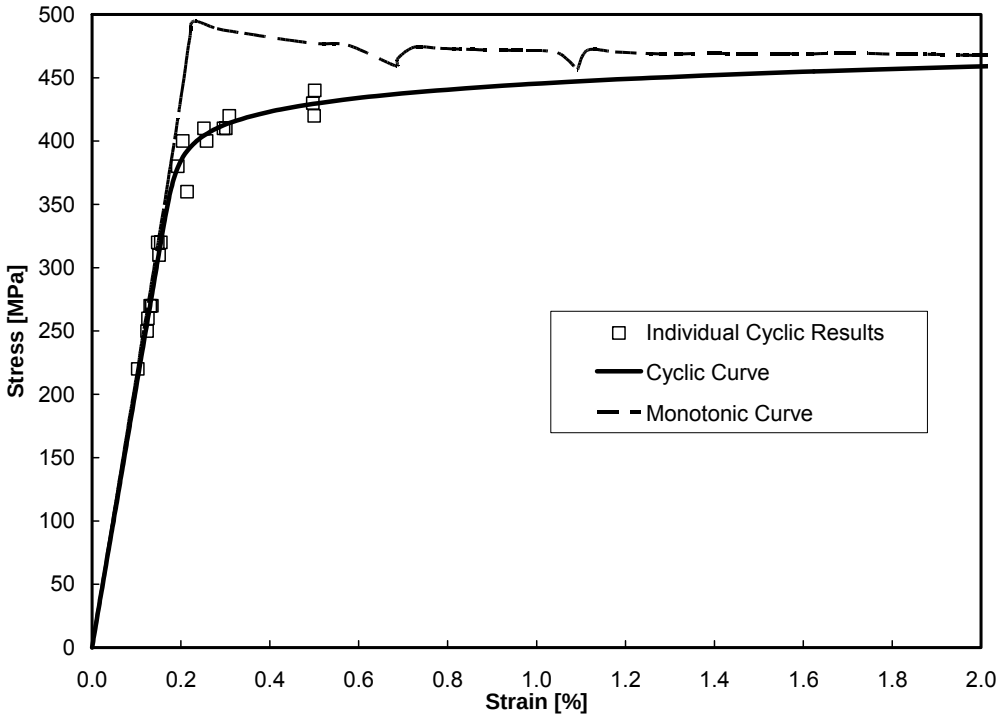

Figure 4.12 *– Cyclic and monotonic stress-strain curves for the weld material.*

Test Results

The results of the 19 crack initiation tests are presented in Table 4.9, showing for each specimen designation the nominal strain amplitude, $(\Delta\varepsilon/2)_{nom}$, the correction factor, $F_{\max}$, the effective strain amplitude, $\Delta\varepsilon/2$, the fatigue crack initiation life, N_{init}, and the elastic and plastic components of the strain amplitude, $\Delta\varepsilon_{el}/2$ and $\Delta\varepsilon_{pl}/2$, respectively. The results are presented graphically in the logarithmic plot of Figure 4.13, where the results of other crack initiation test programs are also plotted for comparison. The weld specimens show slightly lower fatigue lives at high strain amplitudes, but seem to perform at least as well as base metals at low strain amplitudes.

Initiation Locations and Fracture Surfaces

It is of great interest to determine whether the cracks initiated in the weld metal or the heat affected zone (HAZ). In order to determine this, one end of the fractured specimens was etched, revealing the interface between the weld metal and the HAZ. In 13 of the 17 failed specimens the cracks initiated in the HAZ. One crack initiated at the fusion line (FI-250.2). The remaining three failed in the weld (FI-300.3, FI-250.1, and FI-130.1). This suggests that in the absence of a stress concentration the heat affected zone is more predisposed to fatigue failure than the weld metal.

The cracks generally propagated on a plane practically parallel to the fusion line between the weld and the base material, as shown in Figure 4.14. This is not necessarily expected since the principal stresses are parallel to the specimen axis and the fusion line is inclined at approximately 20° (see Figure 4.4).

Table 4.9 – *Results of crack initiation tests.*

Specimen Designation	$(\Delta\varepsilon/2)_{nom}$ **[%]**	F_{max} **[-]**	$\Delta\varepsilon/2$ **[%]**	N_{init} **[cycles]**	$\Delta\varepsilon_{el}/2$ **[%]**	$\Delta\varepsilon_{pl}/2$ **[%]**
FI-500.1	0.500	1.000	0.500	1,800	0.203	0.297
FI-500.2	0.500	1.036	0.518	1,200	0.213	0.305
FI-500.3	0.500	1.049	0.525	1,100	0.208	0.317
FI-300.1	0.300	1.065	0.320	8,700	0.203	0.117
FI-300.2	0.300	1.029	0.309	7,000	0.198	0.111
FI-300.3	0.300	1.088	0.326	7,400	0.198	0.128
FI-250.1	0.250	1.075	0.269	9,200	0.193	0.076
FI-250.2	0.250	1.065	0.266	7,500	0.198	0.068
FI-200.1	0.200	1.112	0.222	26,000	0.174	0.048
FI-200.2	0.200	1.034	0.207	15,000	0.184	0.023
FI-200.3	0.200	1.069	0.214	15,000	0.193	0.021
FI-150.1	0.150	1.051	0.158	87,000	0.158	---
FI-150.2	0.150	1.070	0.161	106,000	0.161	---
FI-150.3	0.150	1.068	0.160	91,000	0.160	---
FI-130.1	0.130	1.079	0.140	2,240,000	0.140	---
FI-130.2	0.130	1.075	0.140	730,000	0.140	---
FI-125.1	0.125	1.049	0.131	1,135,000	0.131	---
FI-120.1	0.120	1.082	0.130	20,000,000+	0.130	---
FI-100.1	0.100	1.078	0.108	10,000,000+	0.108	---

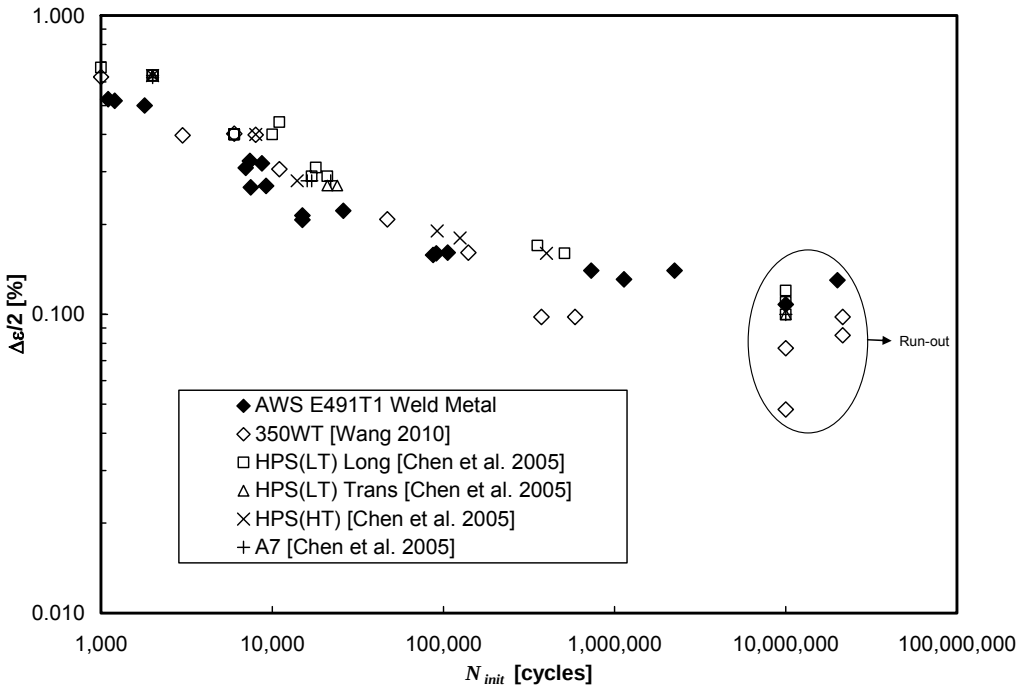

Figure 4.13 *– Crack initiation test results from weld specimens and different base metals tested under completely reversed loading.*

All fracture surfaces were examined under an optical microscope with a maximum magnification of 70x. Initial flaws from which the fatigue crack had started were detected only in two specimens. FI-130.1 contained an embedded inclusion in the weld and FI-250.2 an embedded inclusion at the fusion line. Both inclusions showed as dark spots. The other two specimens that failed in the weld as well as all specimens that failed in the HAZ did not show any trace of flaws on the fracture surface.

The inclusions detected in specimens FI-130.1 and FI-250.2 were further examined under a scanning electron microscope (SEM), see Figure 4.15 (FI-130.1) and Figure 4.16 (FI-250.2). Both inclusions show a greater porosity than the sound metal. This along with their natural darker colouring suggests that the defects are most likely slag inclusions. A chemical analysis using energy dispersive X-ray spectroscopy (EDX) confirmed this conclusion, as the main elements found were oxygen (over 40%) and titanium (over 20%), with only a relatively small amount of iron present (less than 10%).

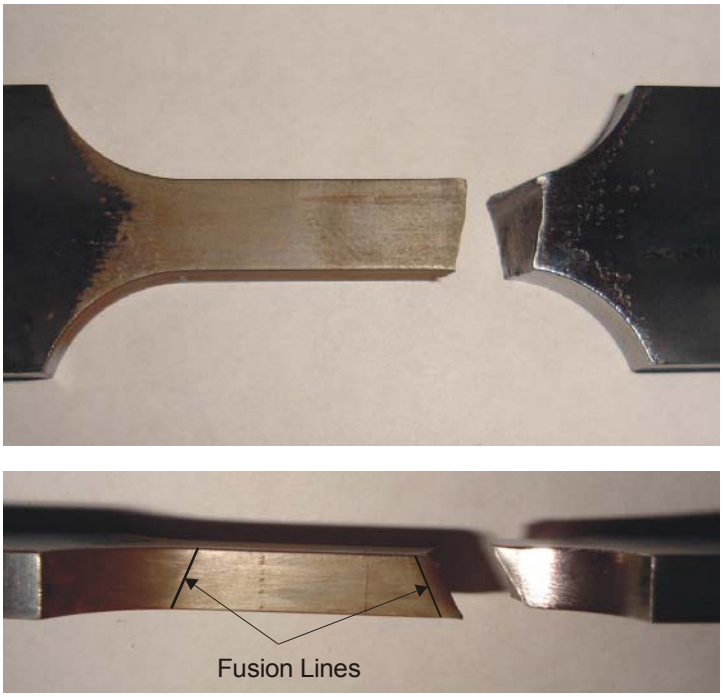

Figure 4.14 *– Typical failure of the crack initiation specimens (FI-200.1).*

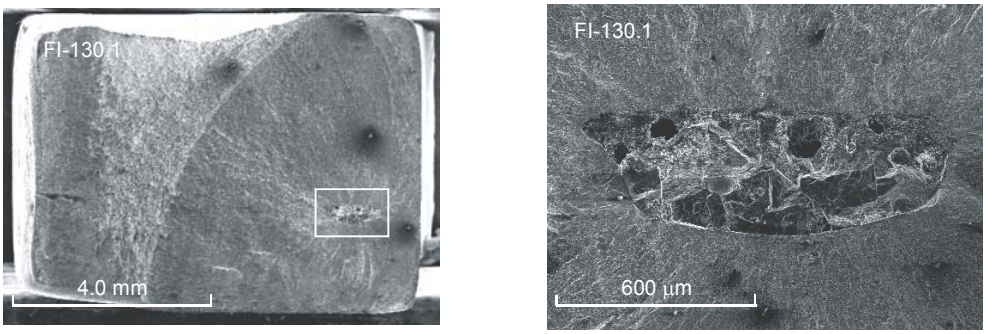

Figure 4.15 *– Inclusion in FI-130.1 (weld) under the SEM.*

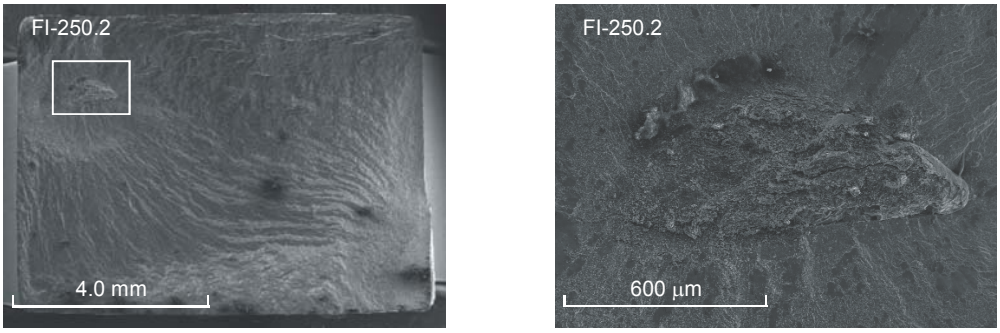

Figure 4.16 *– Inclusion in FI-250.2 (fusion line) under the SEM.*

Crack Initiation Parameters

Linear regression analyses of the elastic and plastic strain components were carried out. Since specimen FI-100.1 did not fail, it is not considered in the regression analysis. However, specimen FI-120.1 was included as it seemed to be very close to the fatigue limit (FI-125.1, which was subjected to only a slightly higher strain amplitude than FI-120.1, failed after 1.135 million cycles without any detectable flaw). The plastic components for the FI-200 specimens were not considered because of their very small values that could no longer be reliably determined owing to the precision of the extensometer. Although the crack in specimens FI-130.1 and FI-250.2 obviously initiated due to an inclusion, both results are taken into account in the regression analysis. This is justified considering the number of cycles at failure, which was substantially higher for FI-130.1 compared to FI-130.2 and not much lower for FI-250.2 compared to FI-250.1, suggesting that the inclusions did not significantly affect the test results.

The regression analyses resulted in the following crack initiation parameters:

$\sigma_f^{'} = 674$ MPa
$b = -0.0592$
$\varepsilon_f^{'} = 0.291$
$c = -0.635$

The coefficient of determination, r^2, for the elastic and plastic components were 0.933 and 0.881, respectively. Figure 4.17 shows the elastic and plastic components of the crack initiation test results carried out in the present work on a log $(\Delta\varepsilon/2)_{\max}$ versus log (N_{init}) plot. The regression lines of each component are also shown in Figure 4.17.

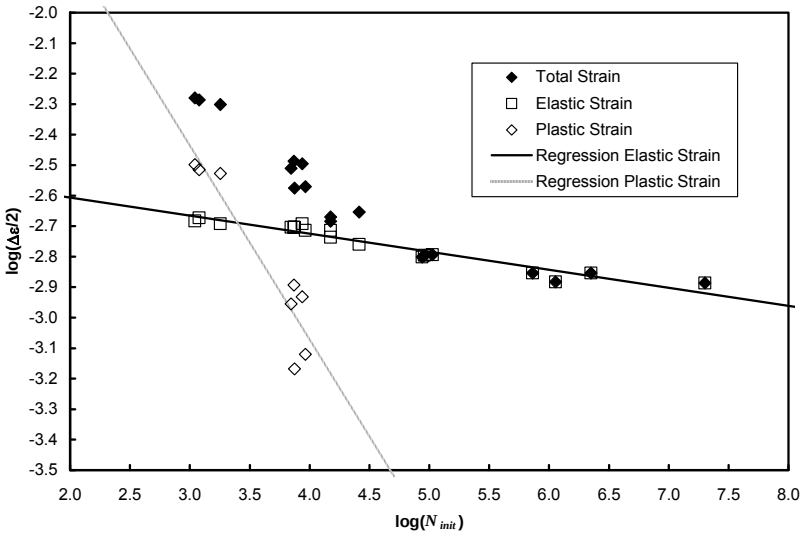

Figure 4.17 *– Elastic and plastic components of crack initiation test results on weld metal matching 350WT steel.*

Probabilistic Analysis of Crack Initiation Parameters

As stated above, it is reasonable to assume that a strong correlation between σ_f' and b, as well as between ε_f' and c exists. Considering the exponents, b and c, as the deterministic parameters and using rounded values given by the regression analysis, i.e., $b = -0.059$ and $c = -0.63$, average values and standard deviations for σ_f' and ε_f' can be determined. These statistical parameters are presented in Table 4.10. Both parameters are again modeled with lognormal distributions.

Table 4.10 – *Average values of σ_f' and ε_f' and corresponding standard deviations as obtained through statistical analyses of the weld metal test data.*

	Average	**Standard Deviation**
σ_f' [MPa]	625	29
ε_f'	0.338	0.071

4.3.7 Crack Propagation Tests

Single edge notch test specimens were obtained from the welded plates to determine the fatigue crack propagation properties. Identical flat-sheet specimens as tested by Chen et al. [2005] and Yin et al. [2006] were prepared. All specimens were designed and tested following ASTM standard E647 *Standard Test Method for Measurement of Fatigue Crack Growth Rates* [ASTM 2000].

Test Specimens

Compact tension, C(T), specimens are commonly used to measure crack propagation parameters [Broek 1989]. These specimens require special grips, which were not readily available for this project. As an alternative, ASTM E647 [2000] allows the use of the middle tension, M(T), specimen, which is a flat sheet type specimen with a machined centre notch. The specimen can be gripped in hydraulic grips. Chen et al. [2005] encountered problems in satisfying the ASTM E647 [2000] requirement that the two crack fronts emanating from the notch shall not differ by more than 2.5% of the specimen width. In order to avoid this problem, single-edge tension, SE(T), specimens were tested by Chen et al. [2005] and Yin et al. [2006]. Apart from eliminating the problem of crack symmetry, these specimens offer the practical advantage of requiring the monitoring of only one crack tip.

Although ASTM E647 [2000] does not specifically include the SE(T) specimen geometry, Blatt et al. [1994] have demonstrated that da/dN versus ΔK data obtained from these specimens correlate well with data obtained from the standard compact tension C(T) specimens defined in ASTM [2000]. Chen et al. [2005] compared the crack

growth behaviour of a standard M(T) test with a SE(T) test and concluded that the crack growth behaviour obtained from these two methods are in good agreement, further confirming the suitability of the SE(T) specimen geometry for crack propagation measurements.

SE(T) specimens were prepared from the welded plates. As for the fatigue crack initiation specimens, the SE(T) specimens were machined from both sides to a thickness of 6 mm. The specimen dimensions are shown in Figure 4.18. The longitudinal axis of all specimens was perpendicular to the weld. The notch geometry, illustrated in Figure 4.18, was obtained by wire-EDM machining. The resulting root radius was approximately 0.07 mm. The specimens were approximately 50 mm wide and 300 mm long. Before machining, all specimens were stress relieved at 600°C for 2 hours. The machined surfaces were left as is, without any special demands on roughness.

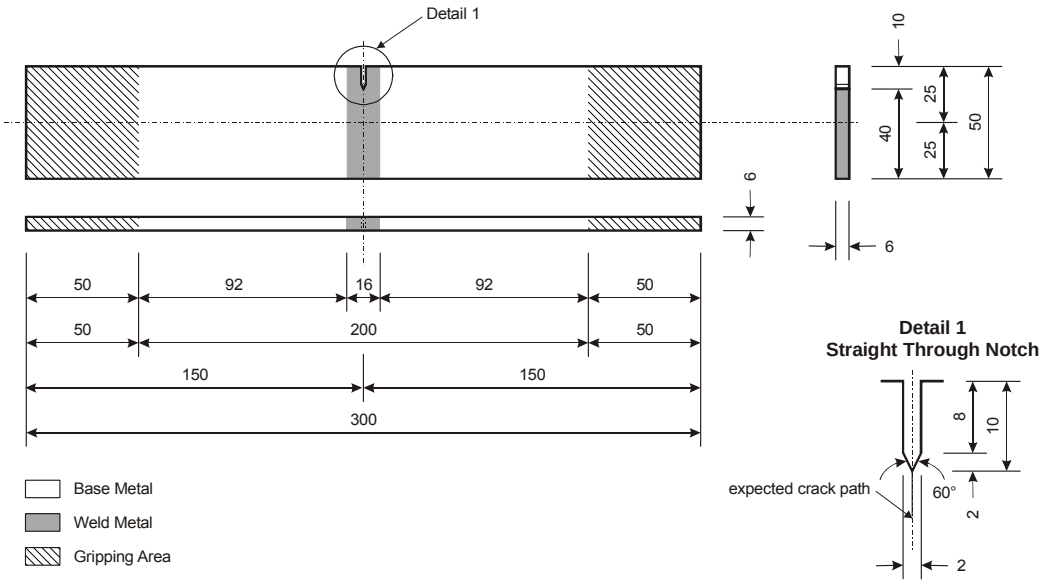

***Figure 4.18** – SE(T) specimen for crack growth rate tests (dimensions in mm).*

Test Matrix

All fatigue presented later in Chapter 5 were carried out at stress ratios $R \leq 0.1$. Therefore, the crack propagation tests were all conducted at low stress ratios to provide a better relation with these tests. In order to compare the test results to the base metal properties obtained by Taheri et al. [2003] and Yin et al. [2006], a stress ratio of $R = 0.1$ was chosen. Three specimens were notched in the centre of the weld (as shown in Figure 4.18) and three were notched in the heat affected zone. All specimens were tested at a constant gross section stress range of $\Delta\sigma_{app} = 45$ MPa. The test matrix is summarized in Table 4.11.

Table 4.11 – *Text matrix for crack initiation specimens.*

Specimen Designation	Tested Region	R [–]	P_{min} [kN]	P_{max} [kN]	$\Delta\sigma_{app}$ [MPa]	Number of Tests
FP-45-01.W	Weld	0.1	1.5	15	45	3
FP-45-01.H	HAZ					3

Test Set-Up and Instrumentation

All tests were carried out at room temperature on a servohydraulic universal testing machine with a fatigue rating of 100 kN (Instron® 8801). Figure 4.19 shows a typical test set-up. The grip length at both ends of the specimens was approximately 50 mm, leaving a free testing length of 200 mm, resulting in a specimen free length to width ratio of $H/W = 4.0$.

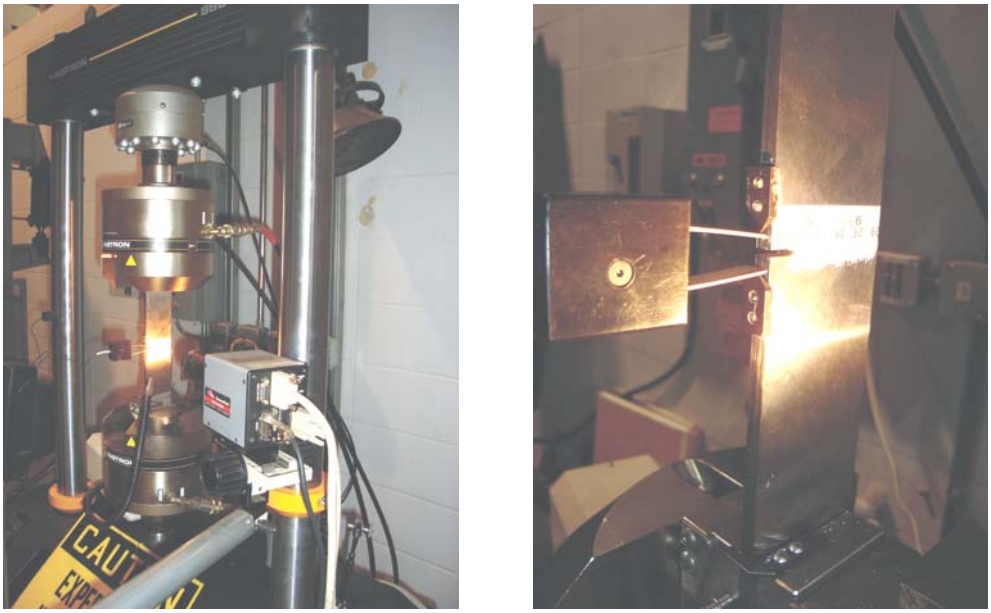

Figure 4.19 *– Typical fatigue crack propagation test set-up.*

The tests were conducted under load control at a constant frequency of 10 Hz. The sinusoidal cyclic signal was generated by the software FastTrack2™ WaveMaker to the defined frequency and peak loads. Load readings were sampled at a rate of 100 Hz and the real time versus load curve continuously displayed to facilitate the monitoring of the tests. This curve was also recorded at predefined time intervals. The number of cycles was counted by the FastTrack2™ Console software interface and continuously displayed as well as recorded along with the real time versus load curve.

The minimum and maximum loads were kept within ±2% of the desired values for the duration of all tests. The test was stopped when the crack length calculated through the FastTrack2™ software (see further down under *Crack Length Measurements*) reached 48 mm. This assured that the specimens did not completely fail under cyclic loading, to prevent damage to the instrumentation. Once this limit was reached in a test, the crack mouth opening gauge (see further down) was removed and the specimen was monotonically loaded in strain control until complete failure took place to expose the fracture surface.

Special care was taken to align the specimens correctly to prevent bending during gripping.

Precracking

ASTM E647 [2000] requires that specimen precracking be carried out prior to monitoring the da/dN versus ΔK response[1]. This guarantees that a sharpened fatigue crack of adequate size and straightness is present at the start of recording. In order to limit the time of precracking without obtaining an excessive plastic zone ahead of the crack, the specimens were initially subjected to a maximum load of 20 kN until a crack initiated and grew to about 15 mm, including the notch. The maximum load was then reduced to 17 kN and the fatigue crack was extended another 2 mm. At this point the peak load was reduced to 15 kN. The minimum load was always kept at 1.5 kN. Recording of the data started after the crack was further extended by approximately 4 mm. This precracking procedure prevented any retardation effects.

Crack Length Measurement

ASTM [2000] proposes to measure the crack length "… by means of a visual, or equivalent, technique capable of resolving crack extensions of 0.10 mm …" Chen et al. [2005] and Yin et al. [2006] successfully used an electronic imaging system. The system consisted of a high speed digital camera (Duncan Tech DT 1100) with high resolution (1392x1040 pixels). Images were taken at predefined load cycles. A LabVIEW® program triggered a multiple release around the maximum load, ensuring that the measurements occurred as the crack was fully opened.

ASTM E647 [2000] also allows the use of the compliance method to determine the crack length during a crack propagation test. The compliance method assumes that the crack mouth opening displacement (CMOD) can be related to the crack length. The CMOD is measured with a crack mouth opening gauge (CMOG) that spans the crack at the edge of the plate (i.e., at the crack mouth). Unfortunately the noise in the CMOG (10 mm gauge with 4 mm maximum travel) was too large to determine crack lengths within the required

[1] For the specimens used here the crack extension measured from the tip of the notch has to be at least 2 mm (equal to notch width) before monitoring can be started.

accuracy of 0.1 mm. Hence, the compliance method was not used to establish the crack propagation parameters. However, it allowed for setting crack length limits at which tests could be automatically interrupted. This was especially convenient during precracking, to reposition the camera, and to ensure cyclic loading stopped before complete failure of the specimens took place. Thus only periodic inspection of the tests was necessary.

The electronic imaging system was used in the present investigation to determine the crack lengths. Photographs were taken at intervals of 100 cycles. The file name of each photograph corresponded to the Instron cycle count (e.g. 100000.png for the photograph taken at 100,000 cycles). In order to reduce the amount of data, only the images corresponding to crack growth increments of 1 mm were stored after the completion and analysis of a test. A magnification of 50x resulted in the desired resolution to accurately determine the crack length. With this resolution only an area of about 9 mm by 7 mm could be captured, thus requiring camera repositioning during testing. To facilitate the detection of the crack tip, a fibre optic lamp illuminated the specimens. Furthermore the specimens were coated with whitewash in the region of the expected crack path. The whitewash provided better contrast for the detection of the crack tip. A scale with a resolution of 1 mm was attached to the specimens. This resolution along with a graphics editor permitted the determination of the crack extension to the required accuracy of 0.1 mm. A sample photograph is shown in Figure 4.20. It is noted that the scale never started at exactly 0 mm and thus an offset had to be considered. The offset is determined by subtracting the reading at the tip of the notch from the actual notch length, which was always 10.0 mm. In the case of Figure 4.20 the offset is 10.0-9.4 = 0.6 mm. To obtain the actual crack length this offset has to be added to the scale reading, i.e., the actual crack length is 14.9+0.6 = 15.5 mm.

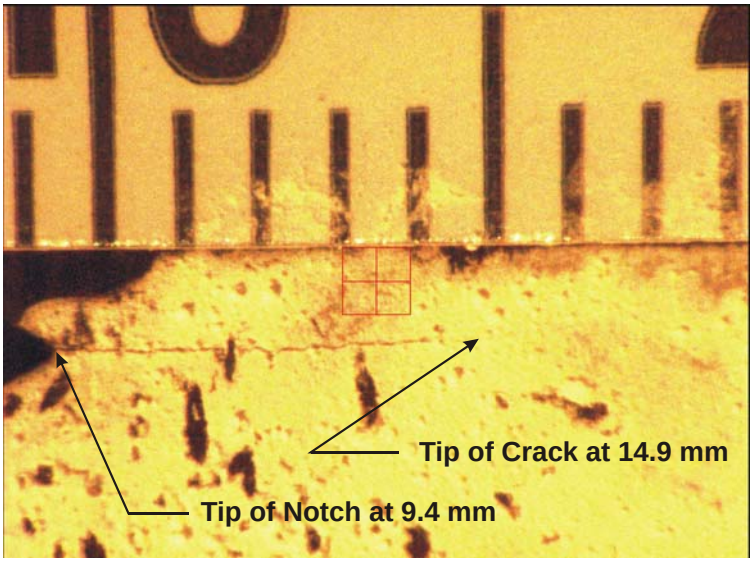

Figure 4.20 *– Sample of a high resolution photograph taken with the electronic imaging system.*

Since the camera system only captures the crack length on one face of a specimen it cannot confirm that the ASTM E647 [2000] requirement of a deviation of maximum 1.5 mm (1/4 of the thickness) between the two crack faces is met. Therefore, at the end of each test the beach marks on the fracture surfaces were examined with a magnifying glass to determine whether the crack front met the ASTM E647 requirements. The largest observed difference in crack length between the front and the back of the plate specimens was about 1.0 mm, therefore respecting the limits given in ASTM E647 [2000]. The crack front was slightly curved in all specimens, but was never more than 0.5 mm ahead of the crack front at the surface of the plate.

Test Results

Blatt et al. [1994] propose the following expression to determine the stress intensity factor range, ΔK, for a SE(T) specimen:

$$\Delta K = \beta \cdot \Delta\sigma\sqrt{\pi a} \tag{4.3}$$

where the global correction factor β is a function of the crack length, a, measured from the edge of the plate, the specimen width, W, and the ungripped length, H. Blatt et al. [1994] determined β through an analytical approach and verified the results with a finite element analysis. They proposed a seventh order polynomial to approximate the finite element solution for $0 \le a/W \le 0.95$. A simpler and better fit for the practically relevant range of $0.15 \le a/W \le 0.85$ is used here, resulting in the following expression for $H/W = 4$:

$$\beta = 6.46\left(\frac{a}{W}\right)^4 - 11.41\left(\frac{a}{W}\right)^3 + 8.77\left(\frac{a}{W}\right)^2 - 1.41\left(\frac{a}{W}\right) + 1.25 \tag{4.4}$$

The resulting curve along with the finite element analysis results and the seventh order polynomial presented in Blatt et al. [1994] are shown in Figure 4.21. Equation (4.4) gives an r^2 value of 1.0.

Figure 4.22 shows for all six tests the crack length, a, as a function of the number of cycles, N, for crack lengths between 21 and 37 mm. The cycle counting was zeroed at a crack length, a, of 21 mm. In general it seems that the cracks propagate somewhat faster in the weld than in the HAZ. An exception is the second portion ($a > 24$ mm) of the HAZ specimen FI-45-01.H3, which has an accelerated crack growth rate at this stage. In fact, the crack in FI-45-01.H3 deviated from a horizontal plane and propagated towards the weld metal, rationalizing the faster crack growth rate. In all other tests the crack propagated on a horizontal plane.

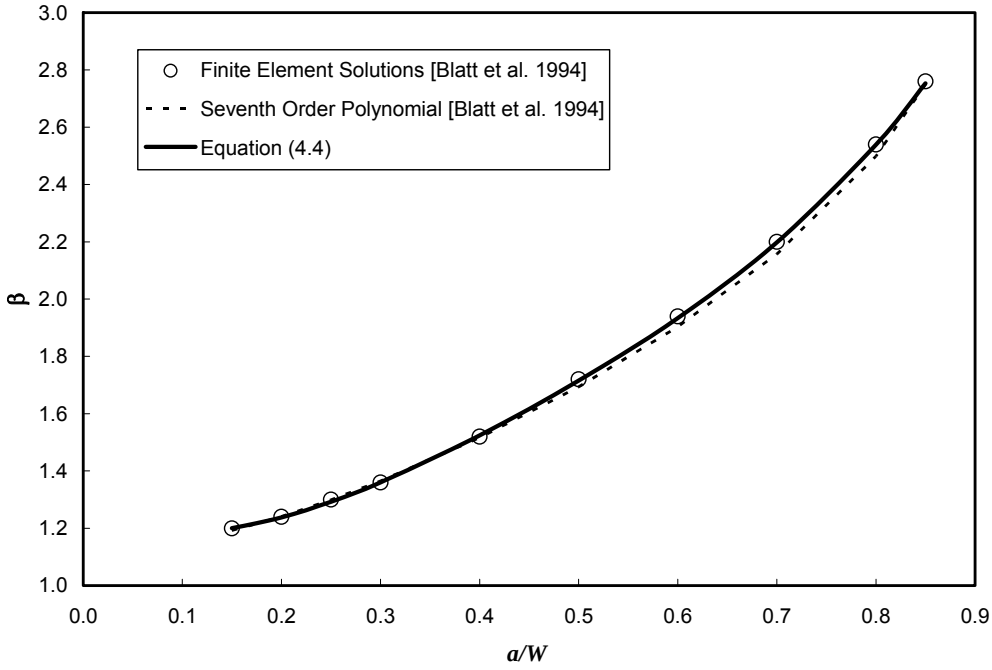

Figure 4.21 *– Correction factor, β , as a function of a/W for a SE(T) specimen with $H/W = 4.0$.*

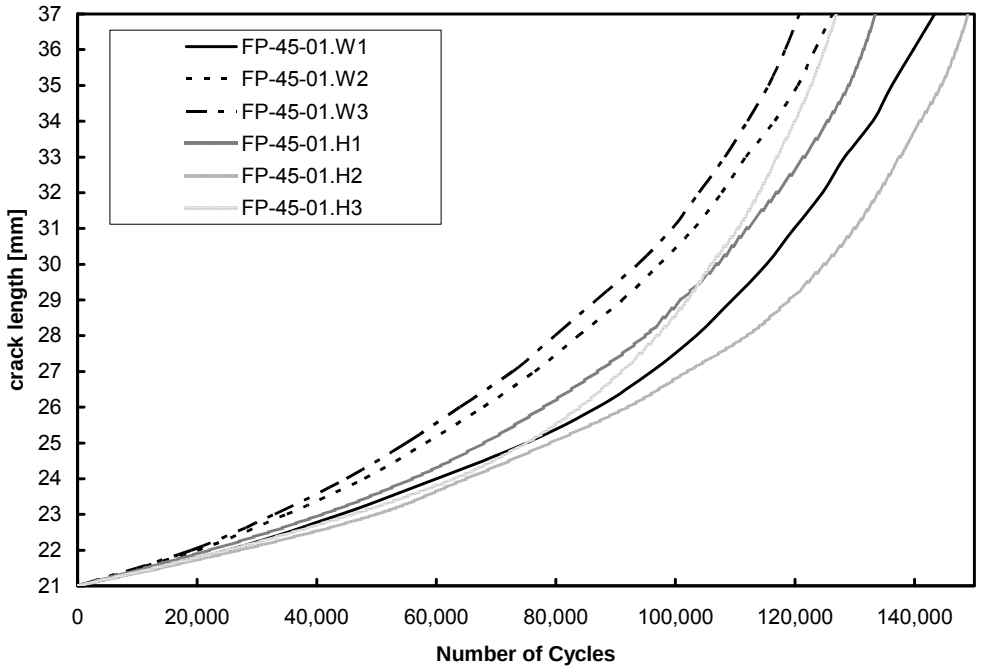

Figure 4.22 *– Crack length, a, versus number of cycles, N, for all six tests.*

Paris-Erdogan Parameters, C and m, for the Cracks in the Weld Metal

Crack growth rate data, $\mathrm{d}a/\mathrm{d}N$, were derived from the a versus N records determined with the imaging system and plotted with the corresponding ΔK-values calculated using equations (4.3) and (4.4). The resulting $\mathrm{d}a/\mathrm{d}N$ versus ΔK data for the three crack propagation tests with the notch in the weld are presented in the logarithmic plot of Figure 4.23. In order to guarantee that the results are not affected by the threshold stress intensity factor range or are part of the unstable crack propagation stage, only crack lengths between 21 and 37 mm, corresponding to ΔK-values of roughly 500 and 1,000 $\mathrm{MPa}\sqrt{\mathrm{mm}}$, respectively, were analysed.

Statistical analyses showed that there is no significant difference between the three crack growth rate tests on the weld metal, Therefore, all results were grouped into one sample. Assuming a fixed deterministic slope of $m = 3.0$, a least square linear regression analysis of the data was carried out. The resulting regression line is plotted in Figure 4.23. Assuming a lognormal distribution for C, the mean value and its standard deviation result in $C = \mathrm{LN}(3.87\times10^{-13}, 4.74\times10^{-14})$.

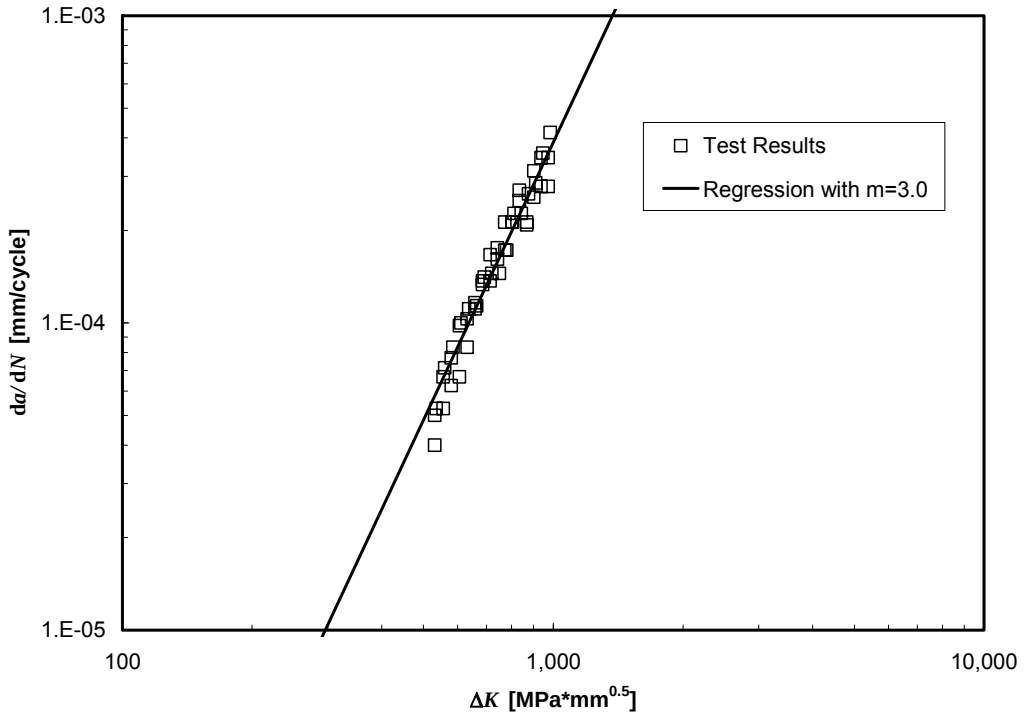

Figure 4.23 *– Crack propagation test results of the weld metal.*

Paris-Erdogan Parameters, C and m, for the Cracks in the HAZ

The $\mathrm{d}a/\mathrm{d}N$ versus ΔK data for the three crack propagation tests with the notch in the HAZ are presented in the logarithmic plot of Figure 4.24.

Statistical analyses showed that there is no significant difference between the three crack growth rate tests from the HAZ. Therefore, all results were grouped into one sample. As for the weld metal, a fixed deterministic slope of $m = 3.0$ was assumed and a linear regression analysis of the data was carried out. The resulting regression line is also plotted in Figure 4.24. Assuming a lognormal distribution for C, the mean and standard deviation result in $C = \mathrm{LN}(3.54\times10^{-13}, 6.98\times10^{-14})$.

Although there is not a large discrepancy between the crack growth constants, C, found for the weld material and the HAZ, a statistical analysis suggest that the difference is significant and the results should therefore not be combined.[1]

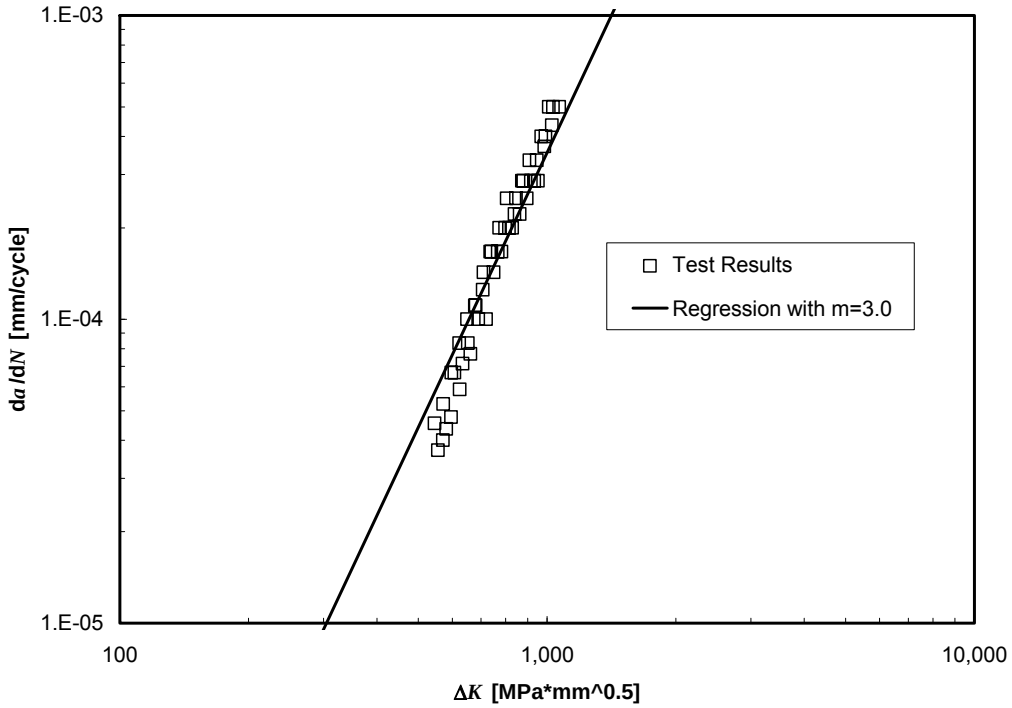

Figure 4.24 *– Crack propagation test results of the HAZ.*

Threshold Stress Intensity Factor Range, ΔK_{th}

No special tests were conducted to determine the threshold stress intensity factor range. According to Ohta et al. [1986], ΔK_{th} for the weld metal and HAZ is considerably smaller than for the base material. This is attributed to the presence of tensile residual stresses. However, ΔK_{th} is also a function of several other factors, such as the yield

[1] Comparing the mean values of the two series (weld and HAZ), the Student *t*-test results in a level of significance of less than 1%, therefore suggesting that a significant difference between the two series exists.

strength, Young's modulus, the microstructure, and the mode of crack tip opening [Barsom and Rolfe 1999], which were apparently not investigated by Ohta et al. [1986]. Dowling [1999] states that some steels show a reduced threshold after heat treatment, i.e., with an increase in yield strength.

A reasonable mean value is the deterministic value of $\Delta K_{th} = 60$ MPa$\sqrt{\text{mm}}$ defined in Banz & Nussbaumer [2001], which corresponds well to data reported in Ohta et al. [1986]. Based on the work by Ohta et al. [1986] a COV of approximately 0.1 can be assumed, resulting in a lognormal distribution LN(60,6) for ΔK_{th} of the weld metal and HAZ.

4.3.8 Summary

Based on the analysis of tests carried out in this study and the results of tests from other sources, the following material properties for the weld metal matching Grade 350WT steel are proposed:

- Cyclic properties:
  E = 207,000 MPa
  K' = 532 MPa
  n' = 0.037
- Crack initiation properties[1]:
  σ_f' = LN(625,29)
  b = -0.059
  ε_f' = LN(0.338,0.071)
  c = -0.63
- Crack propagation properties[2]:
  m = 3.0
  C = LN(3.87×10^{-13},4.74×10^{-14}) for the weld
  C = LN(3.54×10^{-13},6.98×10^{-14}) for the HAZ
  ΔK_{th} = LN(60, 6)

4.4 Comparison with Properties Reported in the Literature

4.4.1 Crack Initiation

The crack initiation material properties as determined in Section 4.2.4 from the tests conducted by Wang [2010] on Grade 350WT steel and as obtained in Section 4.3.6 for the weld/HAZ are compared to the properties reported in ASM [1996] for similar steel

[1] σ_f' in MPa, all other parameters are dimensionless

[2] C in (mm/cycle)$\cdot\left(\text{MPa}\sqrt{\text{mm}}\right)^{-m}$, ΔK_{th} in MPa$\sqrt{\text{mm}}$

grades. The properties are summarized in Table 4.12. The resulting $\Delta\varepsilon/2$ versus N_{init} curves are presented in Figure 4.25. $E = 205{,}000$ MPa was used for all grades.

Table 4.12 – *Crack initiation material properties.*

Steel Grade	**Actual Yield Strength [MPa]**	σ_f' **[MPa]**	b **[-]**	ε_f' **[-]**	c **[-]**	**Reference**
350WT Plate	365	542	-0.0719	0.0922	-0.429	Wang [2010]
350WT Weld/HAZ	470	674	-0.0592	0.291	-0.635	Present study
A36 Plate	351	600	-0.0900	0.103	-0.384	ASM [1996]
A36 HAZ	534	838	-0.0700	0.130	-0.430	ASM [1996]
A516 Grade 70 Plate	325	1100	-0.122	0.665	-0.561	ASM [1996]
St 52 Plate	378	733	-0.0780	0.305	-0.569	ASM [1996]

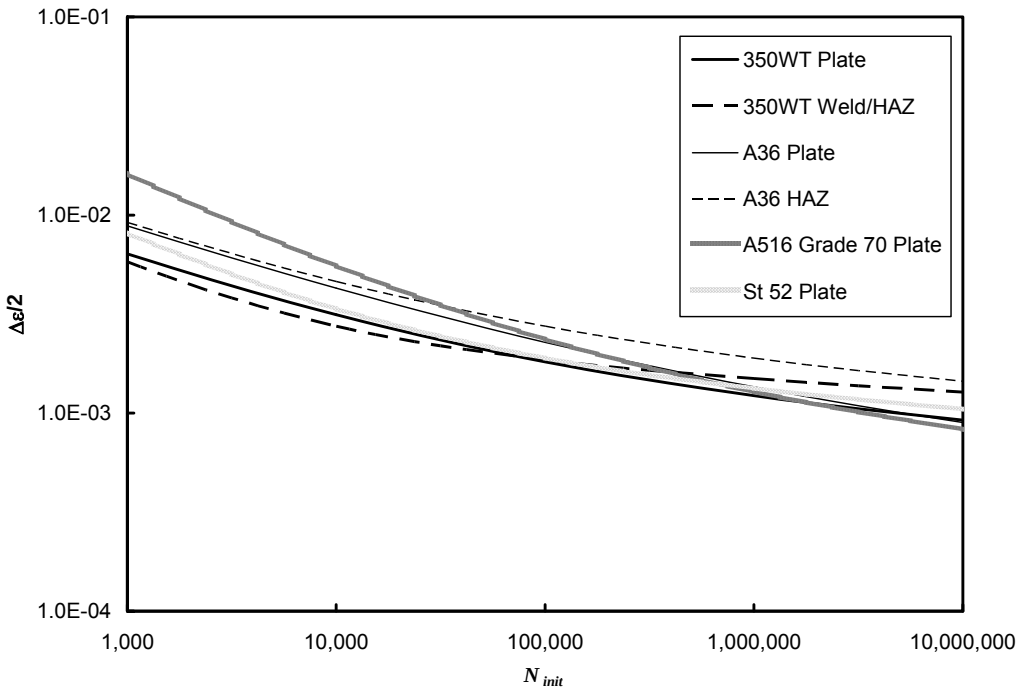

Figure 4.25 *– $\Delta\varepsilon/2$ versus N_{init} curves for different steel grades.*

Figure 4.25 indicates that the fatigue crack initiation properties of 350WT steel and its corresponding weld/HAZ fall within the response of similar structural steel grades. The HAZ of both the A36 and the 350WT steels has a noticeably longer crack initiation life at low strain amplitudes than the base plates. For example, the crack initiation life of the 350WT HAZ at a strain amplitude of 1.3×10^{-3} is more than ten times longer than for the base metal (670,000 cycles for the base metal and 7,600,000 cycles for the HAZ). This suggests that different initiation properties for the base metal and HAZ should be adopted in a fatigue analysis.

4.4.2 Crack Propagation

Figure 4.26 shows the lognormal distributions of C for $R = 0.1$ as determined in Section 4.2.5 from the Taheri et al. [2003] and the Yin et al. [2006] tests on Grade 350WT steel as well as the distribution of C obtained in Section 4.3.7 for the weld metal and the HAZ. All the lognormal distributions presented in Figure 2.15 (for $m = 3.0$) are also plotted in Figure 4.26.

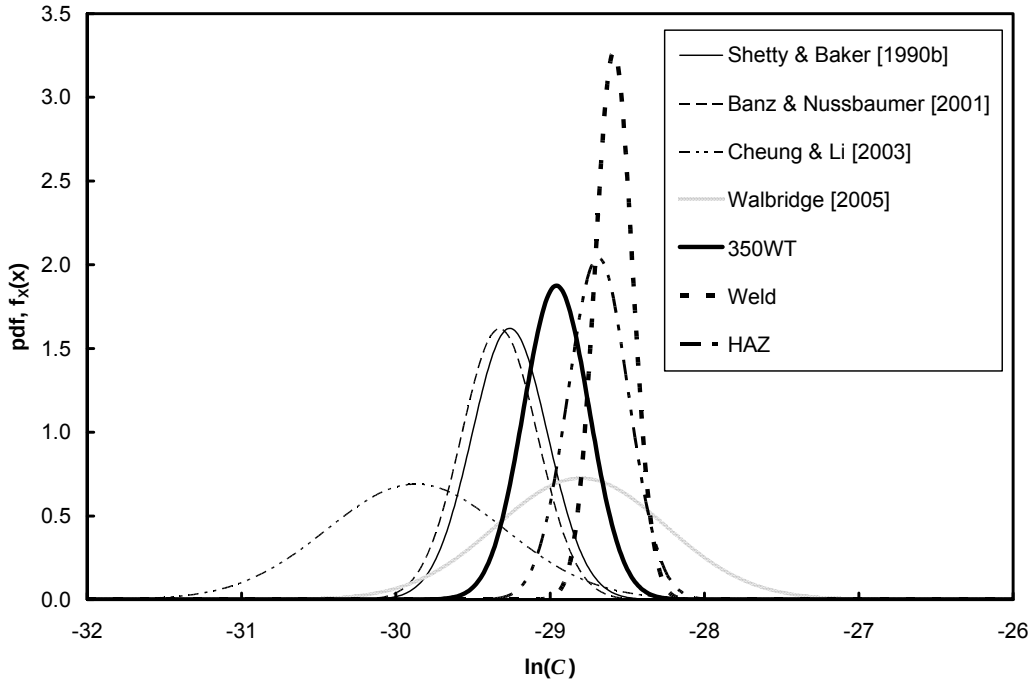

***Figure 4.26** – Probability density functions (pdf) for the crack growth parameter C from analyses having a fixed $m = 3.0$.*

Both the mean values and standard deviations of the tests analysed in this chapter (350WT, weld, and HAZ) fall within the range of the other distributions. The C-value obtained for the HAZ, which will be shown to be the most likely crack propagation

location for the test specimens presented in the next chapter, will be calibrated in Chapter 7.

4.5 Summary and Conclusions

The material properties used to predict the crack initiation life (equation (2.5)) and the crack propagation life (equation (2.9)) were presented. The properties of CSA G40.21 Grade 350WT steel [CSA 2004], obtained from two independent sources, were analysed in Section 4.2. Section 4.3 presented the experimental and analytical investigations carried out in the present work on the fatigue properties of AWS E491T1 weld metal, which is a matching electrode for Grade 350WT steel. The relevant material properties required to predict the fatigue life of the investigated details are summarized in the following.

Cyclic Stress-strain Curves

The Ramberg-Osgood parameters (equation (2.3)) of the base and weld metals are presented in Table 4.13 and the resulting stress-strain curves are plotted in Figure 4.27. These curves should be used in place of the monotonic stress-strain curves to determine the local strain amplitudes in the investigated details.

Although cyclic softening was observed in both the base material and the weld metal, the weld metal shows a much less pronounced effect. The softening for the base material is rather large and since only four data points in the plastic region were available for the regression analysis the Ramberg-Osgood properties obtained from this analysis should be treated critically.

Table 4.13 – *Ramberg-Osgood parameters for the base and weld metal.*

Metal	***E*** **[MPa]**	***K'*** **[MPa]**	***n'*** **[–]**
Base	213,000	727	0.150
Weld	207,000	532	0.037

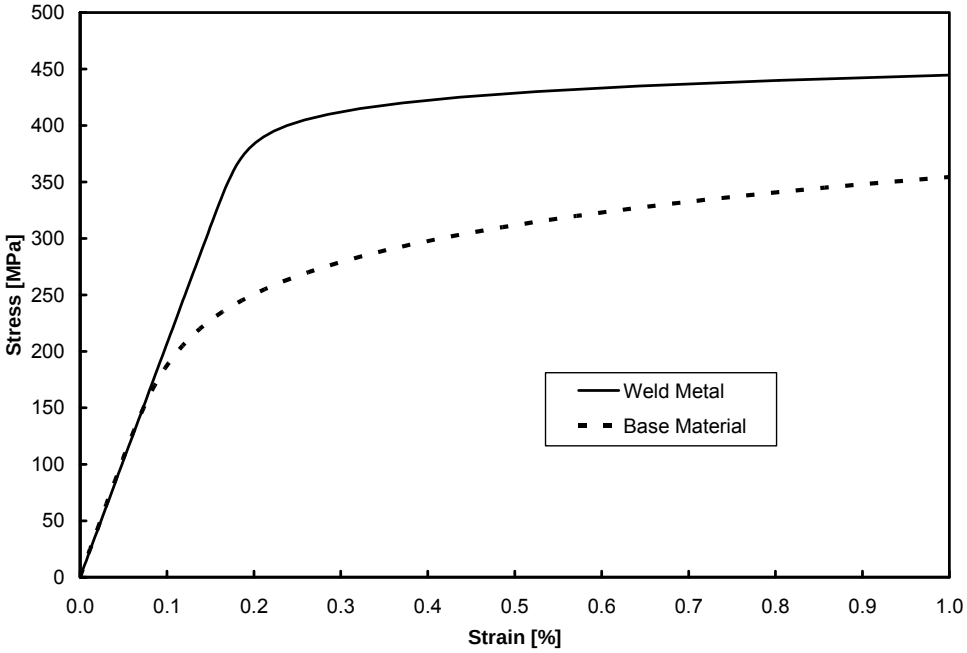

Figure 4.27 *– Cyclic stress-strain curves for the base and weld metal.*

Fatigue Initiation Parameters

The fatigue initiation parameters used in the SWT relationship, equation (2.5), for the base and weld metals are presented in Table 4.14. Both fatigue exponents, b and c, are assumed to be deterministic. The fatigue strength coefficient, $\sigma_f^{'}$, and the fatigue ductility coefficient, $\varepsilon_f^{'}$, are modelled with lognormal distributions. The probability distributions of these two parameters are shown in Figure 4.28 for $\sigma_f^{'}$ and in Figure 4.29 for $\varepsilon_f^{'}$.

Table 4.14 – *Fatigue initiation parameters for the base and weld metals.*

Metal	σ_f' **[MPa]**	b **[–]**	ε_f' **[–]**	c **[–]**
Base	LN(532,18)	Det(-0.07)	LN(0.0715,0.013)	Det(-0.4)
Weld	LN(625,29)	Det(-0.059)	LN(0.338,0.071)	Det(-0.63)

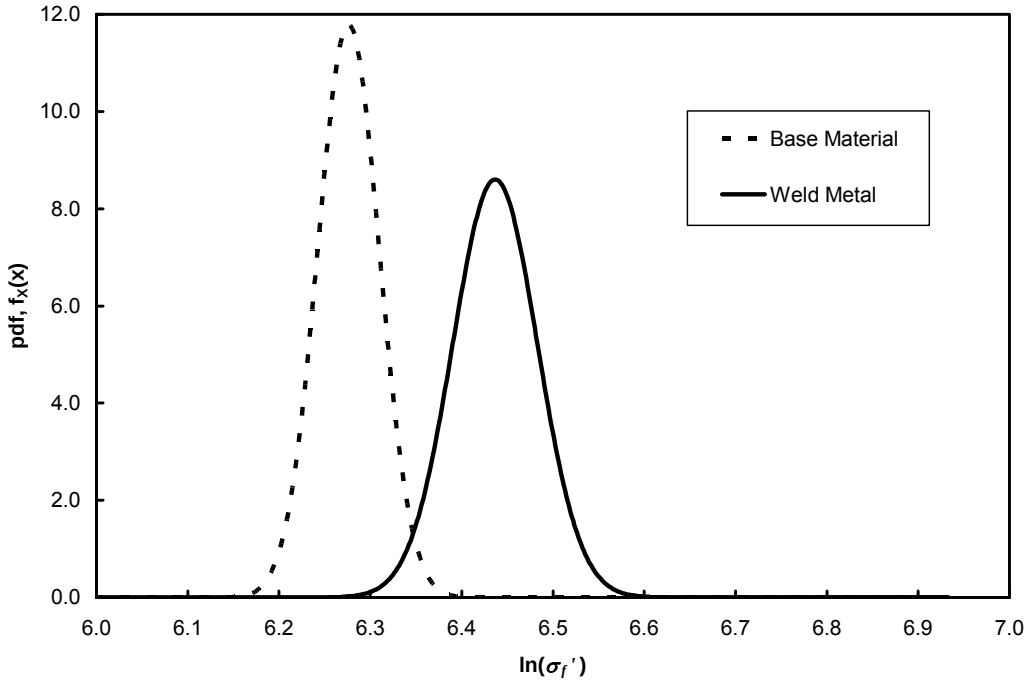

Figure 4.28 *– Lognormal distributions of* σ_f' *for the base and weld metals.*

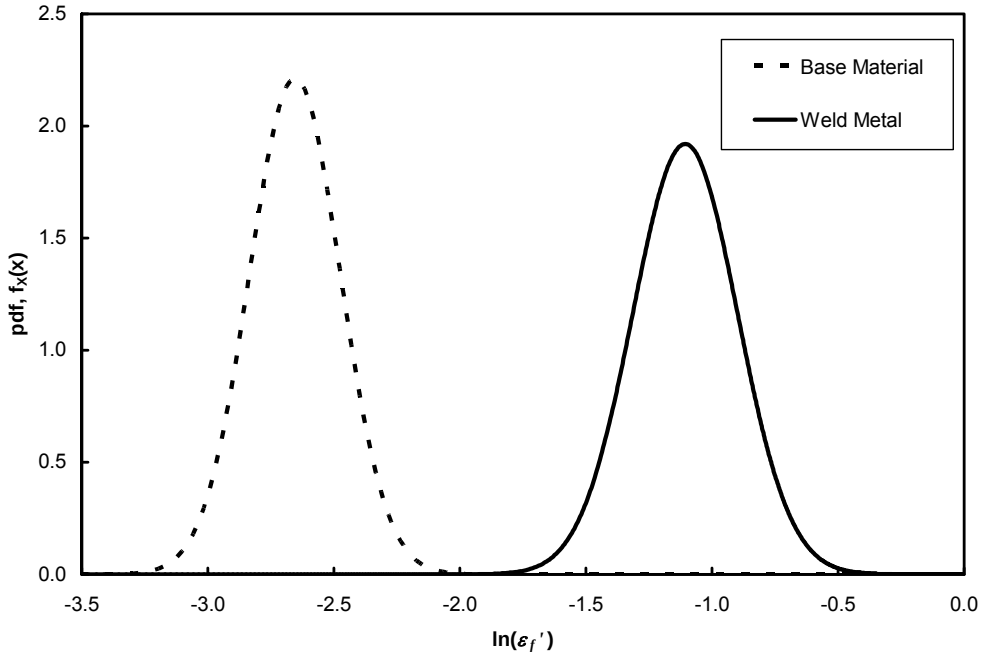

Figure 4.29 *– Lognormal distributions of* ε_f' *for the base and weld metals.*

A comparison between the parameters for the weld metal and the base metal shown in Figure 4.28 and in Figure 4.29 is not possible due to the different exponents b and c used for the base material and weld metal. Nevertheless, it is evident that the variability of both parameters is similar for the two materials. An examination of Figure 4.13 indicates that the crack initiation lives for high strain amplitudes is shorter for the weld metal than for the base metal, whereas it becomes longer for low strain amplitudes.

It is important to note that in the absence of stress raisers, cracks are more likely to initiate in the HAZ than in the weld metal. This is evident from the crack initiation tests, where 14 failures occurred in the HAZ compared to only three failures in the weld metal.

Fatigue Propagation Parameters

The fatigue propagation parameters used in the Paris-Erdogan relationship (equation (2.9)) for the base metal, the weld metal, and the HAZ are presented in Table 4.15. The exponent, m, is assumed to be deterministic, whereas the coefficient, C, and the threshold stress intensity factor range, ΔK_{th}, follow lognormal distributions. A comparison of the base metal, weld material, and HAZ distributions for $\ln(C)$ is shown in Figure 4.30. The units of force and length are N and mm, respectively, and the fatigue life is in cycles.

According to the tests carried out on grade 350WT steel and its matching weld metal and HAZ, a crack in the weld propagates faster than a crack in the HAZ, which in return propagates faster than a crack in the base metal. A comparison with Figure 4.26 shows that the crack growth constant, C, for all three materials lies within reasonable boundaries with respect to other proposed values. However, the standard deviations, especially for the weld metal, are comparably small. This is most likely because all data are from the same source. Therefore, the standard deviation for the proposed C values should be increased for the statistical analyses. This is discussed in Chapter 7, where the results of fatigue tests are predicted with a probabilistic approach.

Table 4.15 – *Fatigue propagation parameters for the base and weld metals.*

Metal	***m***	***C***	ΔK_{th}
Base	Det(3)	LN(2.71×10^{-13},5.83×10^{-14})	LN(100,15)
Weld	Det(3)	LN(3.87×10^{-13},4.74×10^{-14})	LN(60,6)
HAZ	Det(3)	LN(3.54×10^{-13},6.98×10^{-14})	LN(60,6)

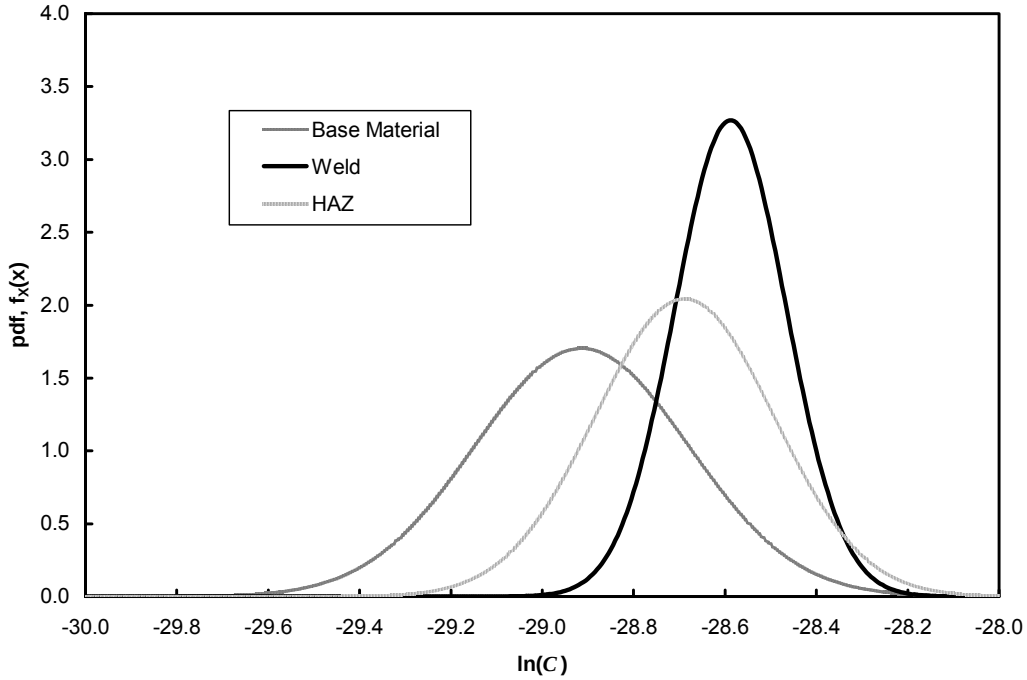

Figure 4.30 *– Lognormal distributions of C for the base metal, the weld metal, and the HAZ.*

5. EXPERIMENTAL PROGRAM

5.1 Introduction

This chapter presents the experimental program conducted to assess the performance of welded repairs with and without post weld treatment. The results are also used to validate the deterministic and probabilistic approaches proposed later in the present work. Preliminary tests on small scale butt welded coupons were carried out to investigate the potential benefit of different post weld treatment methods. The set-up and results of the small scale tests are described in Section 5.2. To better represent the conditions in large scale structures such as mining equipment and bridges, large scale tests on gouged and welded plates were also performed. The set-up of the large scale tests is described in Section 5.3. The preparation of these test specimens consisted of gouging virgin plates and welding the gouged area to simulate a fatigue crack repair. An initial gouging and welding procedure, described in Section 5.4, resulted in poor welds that did not meet Canadian and American welding standard requirements, leading to potentially low fatigue resistance. Changes in the procedures, described in Section 5.5, yielded much improved welds. Although only specimens prepared with the improved procedure passed inspection requirements, the performance of the initial procedure was still of interest and of practical importance. The test results of the initial and improved gouging and welding procedures are also presented in Sections 5.4 and 5.5, respectively.

5.2 Small Scale Tests

5.2.1 Introduction

The literature review in Chapter 3 suggests that ultrasonic peening is superior to other post weld treatment methods. This is attributed to the ease of application of ultrasonic peening and its aptitude to considerably increase the fatigue life. A series of preliminary tests on small scale butt welded coupons was carried out to investigate this suggestion. The ultrasonic peening was compared to two common post weld treatment methods for small scale specimens, namely, stress relieving and conventional peening. As a reference, non-treated specimens were also tested. It is appreciated that these small scale tests do not represent actual structural components. The residual stresses from welding are altered considerably due to the preparation process of these specimens and their small size. Nevertheless, the small scale tests should provide useful information concerning the potential relative benefits of the three investigated post weld treatment methods.

A first set of specimens with ground flush weld faces predominately failed in the gripped area, therefore not yielding any useful results. Therefore, a second set of specimens, with the weld left unground, was prepared. Since the general preparation and procedure of the two sets of test specimens is basically identical, this section first outlines in detail the test

procedure (Sections 5.2.2 to 0) and the test results (Section 5.2.6) for the initial set. The changes made in the second set of test specimens and the corresponding test results are presented in Section 5.2.7. The section concludes with a discussion of the small scale testing program.

5.2.2 Welded Plates

Welded plates identical to those used for the material tests described in Chapter 4 were prepared. The geometry of the plates and the details of the steel grade (Grade 350WT, Category 4) and the welding procedure (FCAW, Voltage ~30 V, current ~300 A, travel speed ~3.4 mm/s) are presented in Section 4.3.3 and Appendix B, respectively.

5.2.3 Test Specimens and Test Matrix

Two sets of specimens were designed. First, non-standard test specimens were machined from the welded plates. The coupons were flat-sheet type with a reduced test cross-section. The backing bars were removed and both weld faces ground flush. The plate thickness of 19 mm was left as is in the test portion of the coupon, but it was reduced to 15 mm in the grip section to accommodate the grip geometry of the hydraulic testing machine. The specimen dimensions are shown in Figure 5.1. The longitudinal axis of all specimens was perpendicular to the weld axis.

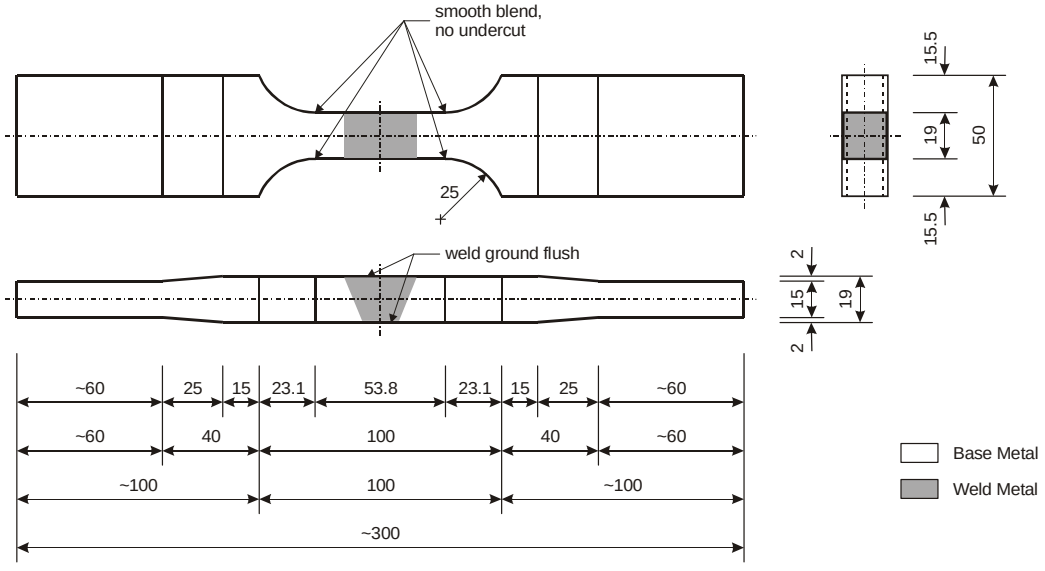

***Figure 5.1** – Small scale specimens (dimensions in mm).*

A total of sten specimens were machined. Four specimens were left as is (i.e., ground, but non-treated) and two each were stress relieved, conventionally peened, and ultrasonically peened. All specimens were tested in direct tension under load control conditions. The

dimensions of each specimen were measured at five to seven locations after final machining, but before the application of any post weld treatment.

5.2.4 Preparation of the Coupons

General

After welding the plates, the backing bars were removed and the front and back weld surfaces ground flush with a 7 in. flat wheel grinder. The plates were then cut with a band saw into strips slightly wider than 50 mm. In order to CNC-machine the reduced cross-sections and the trimmed grip areas, the strips first had to be accurately machined to their final width and length of 50 mm and 300 mm, respectively. The reduced section was then machined on a CNC machine, cutting from the side towards the centre. Due to residual stresses from welding, grinding, cutting, and machining, the specimens were warped and bent. This made an accurate machining of the trimmed grip areas impossible and the specimens were straightened by cold bending in a hydraulic testing machine. It is expected that the cold bending changed the residual stress field. This, however, is not of major concern since the residual stress field before cold bending was already complex and unknown. Furthermore, since the same procedure was used for all the specimens the preparation procedure was consistent for all the test specimens. Once the specimens were flat, the trimmed grip areas were machined. All four surfaces of the reduced sections were ground and the edges sanded with 100 grit sandpaper (CAMI Designation), resulting in similar surface conditions on all faces. Special care was given to having all the grinding marks parallel to the longitudinal axis of the specimens. Finally, the grip areas of all specimens were peened to reduce the risks of fatigue failure in the grip section.

Stress Relieving and Peening

Two specimens were stress relieved at 600°C for two hours and then left to cool slowly in the furnace. The oxide layer that formed during the stress relieving process was left in place.

Two specimens were conventionally peened with a pneumatic needle scaler, as shown in Figure 5.2a. The scaler consisted of 19 needles each having a diameter of 2.85 mm. The applied air pressure was about 620 kPa.

Two specimens were ultrasonically peened, as shown in Figure 5.2b. The ultrasonic frequency emitted from the UP 500 generator was approximately 22 kHz. The head consisted of 5 pins each having a diameter of 5 mm. All four surfaces of the entire reduced sections (weld, HAZ, and base metal) were treated by the conventional and ultrasonic peening.

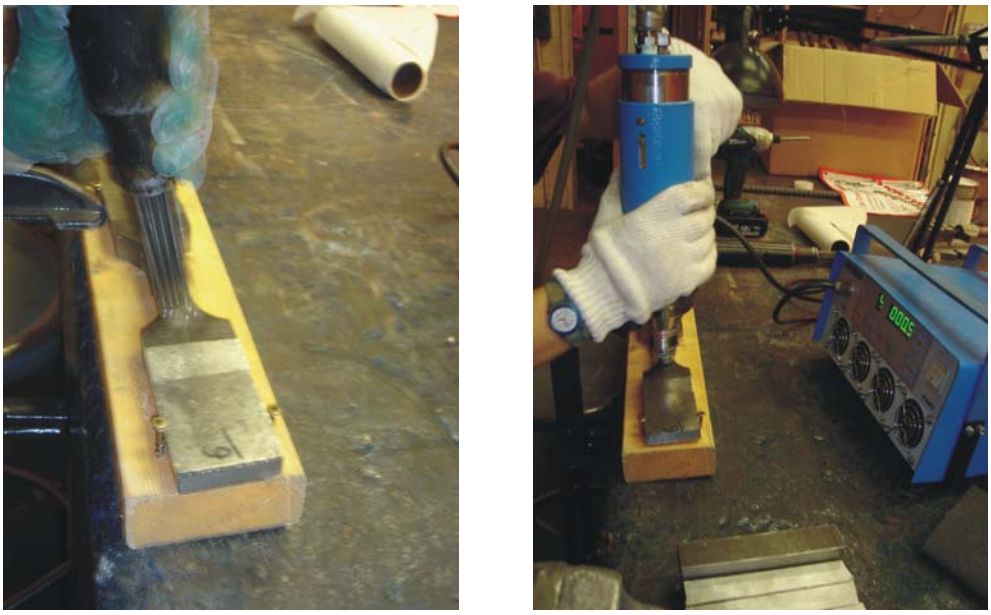

a) Conventional peening *b) Ultrasonic peening*

***Figure 5.2** –Peening of small scale specimens.*

The peening intensity is characterized by the magnitude of deflection of a standard strip (Almen strip) subjected to peening on one face of the strip. Almen A-strips (76×19×1.29 mm, UNS G10700 carbon steel (cold rolled spring steel)) were used to establish the peening intensity. Satisfactory intensity was accomplished when saturation according to ASTM standard B851-04 *Automated Controlled Shot Peening of Metallic Articles Prior to Nickel, Autocatalytic Nickel, or Chromium Plating, or as Final Finish* [ASTM 2004a] was achieved, i.e., when the arc height (deflection) of the Almen strips did not increase by more than 10% after doubling the peening time (see Figure 3.8). The Almen strips, holder and gauge used to quantify the peening intensity met the requirements of SAE Specification J442 *Test Strip, Holder, and Gage for Shot Peening* [SAE 2006]. A strip in the holder and the gauge with a peened strip are shown in Figure 5.3.

Figure 5.4 shows the saturation curves for the conventional and the ultrasonic peening. The conventional peening generated the expected shape of the curve, namely, a rising curve followed by a plateau. Saturation was achieved after 90 seconds. The ultrasonic peening shows an erratic curve and even after 12 minutes of peening, saturation is not achieved. It is also evident that for the same peening time, conventional peening resulted in larger deflection of the Almen strips. The unpredictability and the smaller amount of deflection obtained from ultrasonic peening was further demonstrated by exposing six strips each to 2 minutes of conventional and ultrasonic peening. The average amount of arc height, h, and its standard deviation, s_h, for the conventional peening was $h = 0.248$ mm and $s_h = 0.0160$ mm, resulting in a coefficient of variation of 0.06. The

ultrasonic peening yielded a smaller average arc height, $h = 0.072$ mm and a relatively higher standard deviation, $s_h = 0.0183$ mm, resulting in a coefficient of variation of 0.26.

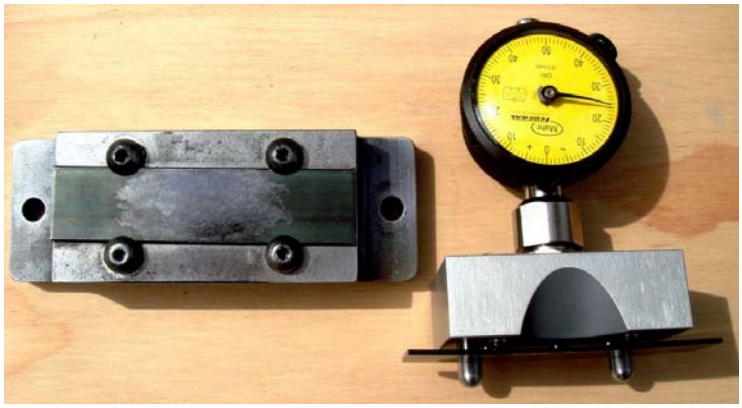

Figure 5.3 *– Almen strips, holder and gauge.*

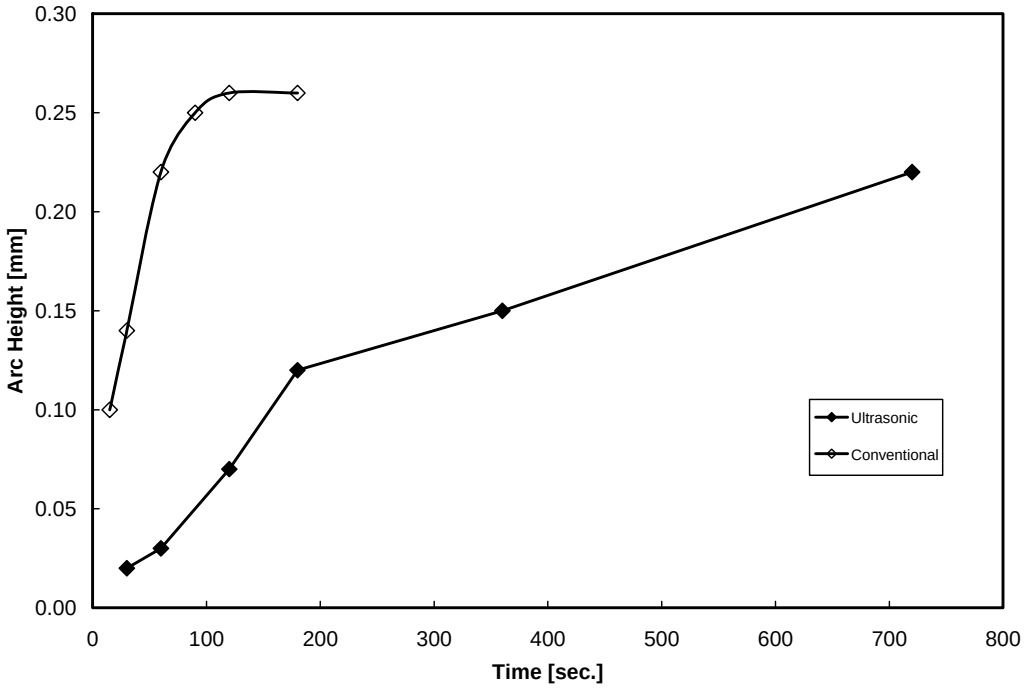

Figure 5.4 *– Saturation curves for the conventional and ultrasonic peening of Almen A-strips.*

The lower amount of arc height and the larger variation in the results for the ultrasonic peening is most likely due to an excessive peening intensity on the A-strip. It is reported that the compressive residual stresses from ultrasonic peening penetrate approximately

1.5 mm into the material [Kudryavtsev et al. 2004]. Since the A-strips are only 1.29 mm thick, ultrasonic peening is likely to deform plastically the Almen strip over its full thickness, thus preventing the formation of a residual stress gradient through the thickness of the strip. A look at the impacted surfaces substantiates this hypothesis. Figure 5.5 shows the peened surfaces of a conventionally and an ultrasonically peened strip. The indents are evidently more visible on the ultrasonically peened surface, indicating a higher peening intensity and thus higher introduced compressive residual stresses [Kuhlmann et al. 2006].

Figure 5.5 *– Impacted surfaces of conventionally (top) and ultrasonically (bottom) peened Almen A-strip.*

Based on these findings, the Almen method with type A-strips seems to work well for the conventionally peened surfaces, but is not applicable to ultrasonic peening. Therefore, the determination of the intensity for the ultrasonic peening was attempted with the thicker C-strips ($t = 2.4$ mm). Even with these thicker strips, no clear saturation could be achieved, as shown in Figure 5.6. It seems that not much gain in intensity is reached after a peening time of approximately 180 sec. It has to be noted that the largest measured arc height was 0.05 mm, which is much less than required for the use of C-strips [ASTM 2004a]. Therefore, the intensity of ultrasonic peening cannot be determined with conventional Almen strips.

The area of each of the four treated specimen surfaces is about 2,000 mm^2. The peened surface on a strip was approximately 1,000 mm^2. Therefore, the peening time for the conventionally peened specimens was set at twice the saturation time determined from Figure 5.4, i.e., $2 \times 90 = 180$ seconds. The ultrasonic peening intensity was adapted from the literature [Huo et al. 2000, Roy et al. 2003], resulting in the same peening time as for the conventional peening (180 seconds).

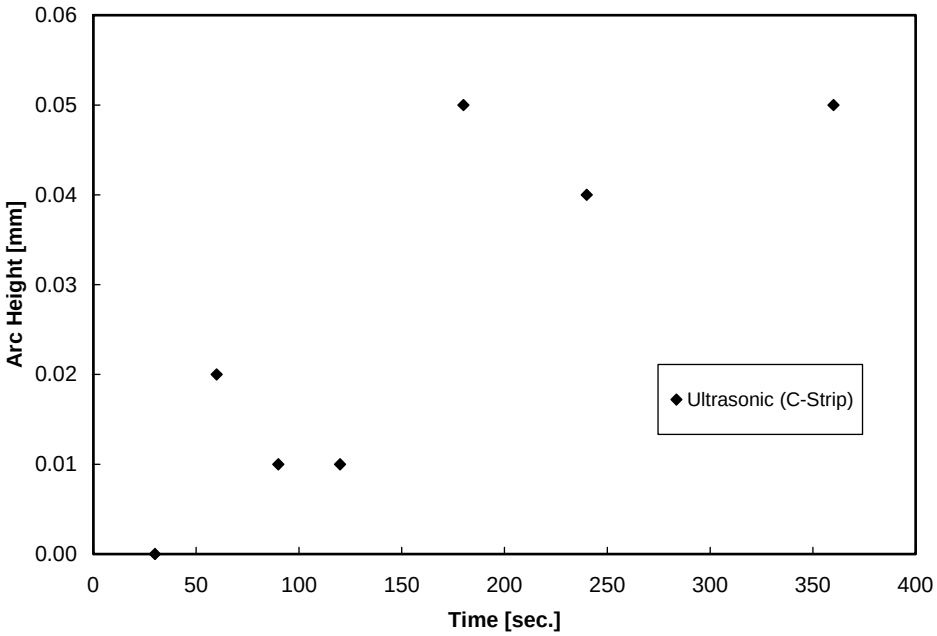

Figure 5.6 *– Saturation curve for ultrasonic peening of Almen C-strips.*

5.2.5 Test Set-Up and Instrumentation

All tests were conducted at room temperature in servohydraulic universal testing machines. The first test, a non-treated pilot test, was conducted in a machine with a fatigue rating of 100 kN (Instron® 8801). A stress range of $\Delta\sigma = 220$ MPa and a stress ratio of $R = 0.1$ were used. This loading was basically at the capacity of the testing machine. Since no failure of the specimen occurred after 10 million cycles, a larger stress range needed to be applied. Subsequent tests were therefore carried out in a machine with a fatigue rating of 500 kN (MTS® 810). Figure 5.7 shows a typical test set-up in the MTS testing machine.

Although the specimens were straightened prior to machining the trimmed grip areas, some out-of-flatness was still present in all coupons. This initial imperfection introduces bending stresses during testing. Strain gauges were therefore mounted on the concave and convex faces of the specimens.[1] The load range was established by multiplying the stress range with the measured cross-sectional area of the reduced section (see Section 5.2.3), not taking into account any potential bending.

[1] The specimen shown in Figure 5.7 is from the second set of tests, where extensometers instead of strain gauges were used to determine bending during static tests. The extensometers were removed for the cyclic testing, when these pictures were taken.

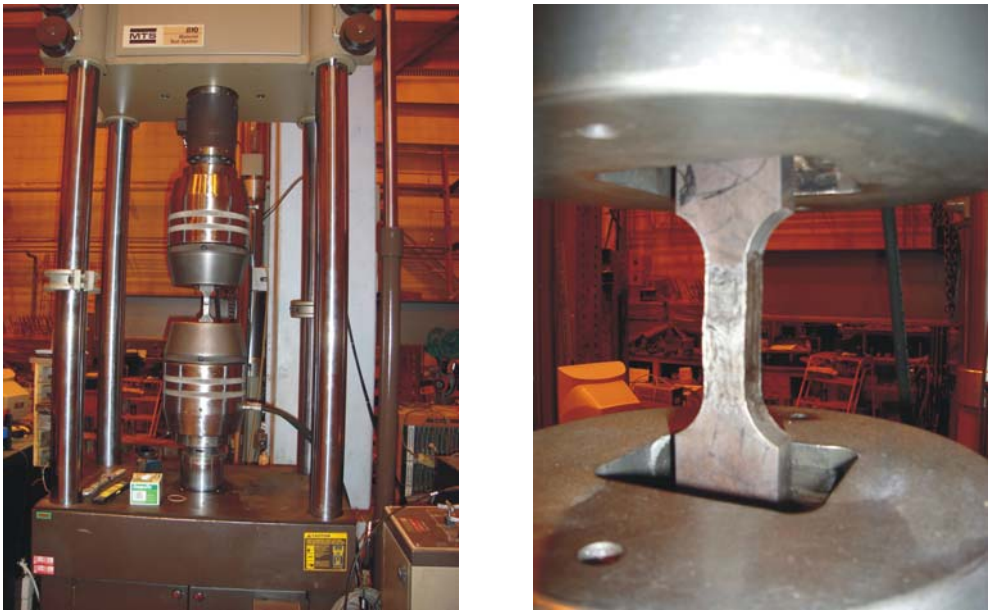

overall view *specimen detail*

***Figure 5.7** – Typical small scale test set-up (left: overall view; right: specimen detail).*

All tests were carried out in load control at a constant frequency of 10 Hz. The sinusoidal cyclic signal was generated by the software FastTrack2™ WaveMaker on the Instron testing machine and by LabView on the MTS testing machine to the defined frequency and minimum and maximum loads. The loads were continuously measured with built-in load cells. The overall stroke of the testing machine and the strain readings were also monitored. Both the load and stroke readings were sampled at a rate of 100 Hz. In addition to showing any bending in the specimens, the strain gauges confirmed that the desired peak strain and therefore peak stress was actually reached. Real time versus load and real time versus stroke curves were continuously displayed to facilitate the monitoring of the tests. These curves, along with the strain measurements, were also recorded at predefined time intervals. The elapsed cycles were counted by the FastTrack2™ Console and LabView software interfaces, respectively, and continuously displayed as well as recorded along with the real time curves.

To protect the specimens and testing machine from unexpected events, lower and upper bound limits on load and displacement were set. The tests stopped automatically when one of these limits was reached.

Special care was given to the alignment and gripping of the specimens to prevent additional axial loading, bending, or twisting during gripping. First, the specimens were gripped at the top. The lower grip pressure was then turned on slowly to allow for sufficient adjustment time of the desired displacement set point so that once the full pressure was reached in the lower hydraulic grip, the axial force on the test specimens was close to 0.0 kN.

5.2.6 Results of Tests on Ground Flush Specimens

Failure of the specimens was defined as the complete severing of the reduced cross-section. After the pilot test, which did not fail at a stress range of $\Delta\sigma = 220$ MPa, three more tests on non-treated specimens were carried out at a stress range of $\Delta\sigma = 350$ MPa and a stress ratio of $R = 0.1$. This stress range is unusually high for any engineering applications and almost results in overall yielding of the cross-section. The results for the four tests are presented in Table 5.1.

Table 5.1 – *Results of initial small scale tests.*

Specimen Designation	Post Weld Treatment	$\Delta\sigma$ [MPa]	N [cycles]	Failure
S220NT0	Non-Treated	220	10,000,000+	No failure after 10^7 cycles
S350NT0	Non-Treated	350	253,000	Failure in weld (inclusion)
S350NT1	Non-Treated	350	1,478,000	Failure in grips
S350NT2	Non-Treated	350	4,000,000	Failure in grips

Specimens S220NT0 and S350NT0 were machined from the ends of the welded plate and intended as pilot tests

Only specimen S350NT0 failed in the weld. The crack initiated at a slag inclusion, which was at the surface and visible to the naked eye prior to testing. The other two non-treated specimens tested at $\Delta\sigma = 350$ MPa prematurely failed in the trimmed grip section. Even the addition of aluminium shim plates glued to the grip surfaces of specimen S350NT2 did not retard the cracking in the grips long enough, although a marked improvement in the fatigue behaviour of the grip area was observed.

Since no useful results for the specimens tested at the relatively high stress range of $\Delta\sigma = 350$ MPa were obtained, redesigned specimens with a lower expected fatigue life in the weld area were machined. The changes in the preparation of theses specimens as well as the test results are presented in the next sub-section.

5.2.7 Specimens in the As-Welded Condition

Flush grinding a weld profile significantly improves the fatigue resistance of a groove weld [AASHTO 2007] since it eliminates the stress concentration at the weld toes. In order to achieve reasonable results for the small scale tests, new specimens in the as-welded condition, i.e., not ground, were therefore prepared. The backing bar was still removed and the weld root ground flush. The dimensions of the specimens were the same

as for the initial set, except that there was no need to trim the grip sections.[1] This also eliminated the need for cold bending, since the specimens did not have to be straight for machining. Consequently, higher bending stresses were present in these specimens compared to the ground flush specimens

A total of eight specimens (two each on non-treated, stress-relieved, conventionally peened, and ultrasonically peened) were machined. The tests were carried out at a nominal stress range of $\Delta\sigma_{nom} = 280$ MPa and a stress ratio of $R = 0.1$. The nominal stress range, $\Delta\sigma_{nom}$, was calculated from the smallest measured cross-sectional area in the base metal on either side of the weld toes. The test matrix is shown in Table 5.2.

Table 5.2 – *Matrix of second set of small scale tests.*

Specimen Designation	Post Weld Treatment	$\Delta\sigma_{nom}$ [MPa]	R [–]	T [mm]	B [mm]	P_{min} [kN]	P_{max} [kN]
S280NT11	Non-Treated	280	0.1	18.9	19.2	11.3	113
S280NT12				18.8	19.2	11.2	112
S280SR11	Stress Relieved	280	0.1	18.7	19.2	11.2	112
S280SR12				18.7	19.2	11.2	112
S280CP11	Conventionally Peened	280	0.1	18.8	19.2	11.2	112
S280CP12				18.7	19.2	11.2	112
S280UP11	Ultrasonically Peened	280	0.1	18.8	19.2	11.2	112
S280UP12				18.7	19.2	11.2	112

$\Delta\sigma_{nom}$: Nominal stress range
R: Stress ratio
T: Measured thickness at either side of the weld toes corresponding to the minimum area
B: Measured width at either side of the weld toes corresponding to the minimum area
P_{min}: Minimum applied load
R: Stress ratio

The tests were carried out in the MTS® 810 universal testing machine. Between the previous test series and this second set of small scale tests, new controllers were installed on the testing machine. These allowed for an increase in testing frequency to 20 Hz. The sinusoidal cyclic signal was generated by the MTS® 793 Control Software FlexTest™ 60 (Basic TestWare®) to the defined frequency and minimum and maximum loads. The load

[1] All specimens from the second set were tested in the MTS testing machine, which was capable of gripping the full plate thickness.

was continuously measured with a built-in load cell. The overall stroke of the testing machine was also monitored. Both the load and stroke readings were sampled at a rate of 100 Hz. Real time versus load curves were continuously displayed to facilitate the monitoring of the tests. These curves along with the stroke measurements were also recorded at predefined time intervals. The number of cycles was counted by the controller and continuously displayed as well as recorded along with the real time curves.

Due to the weld profile, strain gauges could not be installed and the bending effect was determined with two 50 mm gauge extensometers. All the specimens were installed with the flush ground face (root) facing north. Consistent bending in all the specimens could be measured, decreasing the strain range on the south side. This confirmed visual observations made on the straightness of the specimens, which all showed that the weld face was on the concave side of the specimens. The out-of-straightness of the specimens was found to be between 0.1 and 0.5 mm. Table 5.3 gives the corrected stress ranges on the south (weld) and north (flush ground) faces of each specimen. The corrected stress ranges, $\Delta\sigma_{cor,i}$, were determined as follows:

$$\Delta\sigma_{cor,i} = \frac{\Delta\varepsilon_i}{\Delta\varepsilon_{av}}\Delta\sigma_{nom} \tag{5.1}$$

where the index i stands for south or north faces and $\Delta\varepsilon_{av}$ is the average strain range determined from the two measured strain ranges, $\Delta\varepsilon_i$. The extensometers were removed after the static tests.

Table 5.3 – *Corrected stress ranges, $\Delta\sigma_{corr,i}$, due to measured bending effect.*

Specimen Designation	$\Delta\sigma_{nom}$ **[MPa]**	$\Delta\sigma_{cor,south}$ **[MPa]**	$\Delta\sigma_{cor,north}$ **[MPa]**
S220NT11	280	266	294
S220NT12		253	307
S220SR11	280	256	304
S220SR12		253	307
S220CP11	280	244	316
S220CP12		245	315
S220UP11	280	254	306
S220UP12		241	319

The results for the eight tested specimens are summarized in Table 5.4. The failure criterion was again the complete severing of the reduced cross-section. The location of the crack initiation and its cause, which was determined from optical microscope inspection (up to a magnitude of 70), are also given in Table 5.4.

Table 5.4 – *Results of small scale tests with as-is weld profile.*

Specimen Designation	***N*** **[cycles]**	**Crack Initiation Site**
S220NT11	213,000	North face due to small inclusions
S220NT12	327,000	North face due to small inclusions
S220SR11	229,000	North face due to small inclusions
S220SR12	226,000	South face at weld toe due to small inclusions
S220CP11	1,243,000	North West corner (no visible flaw)
S220CP12	493,000	North West corner (no visible flaw)
S220UP11	10,000,000+	No failure
S220UP12	25,000,000+	No failure

South = face with weld face
North = ground flush face (backing bar removed)

The results are shown in the $\Delta\sigma - N$ plot of Figure 5.8 (using the nominal stress range of $\Delta\sigma = 280$ MPa) and compared to the AASHTO [2007] Category A and B fatigue curves.

All test results fall above the Category B curve. However, due to the variability, the non-treated and stress relieved specimens might have to be categorized as fatigue Category C details.[1] The conventionally peened specimens are at least Category B and the ultrasonically peened specimens Category A, i.e., the latter show a fatigue resistance that is equal to the virgin material. Figure 5.9 shows all six failed specimens.

In one specimen (S280CR12) the crack initiated at the toe of the weld. The other three cracks of the non-treated and stress-relieved specimens initiated on the North face at the root of the weld. The two conventionally peened specimens failed away from the weld in the HAZ although the HAZ was also peened. The cracks initiated at a corner of the North (ground) face. All six cracks propagated through the HAZ. A post-mortem examination of the test specimens using an optical microscope revealed small inclusions at the crack

[1] The AASHTO curves are design curves, i.e., they are below the average test curve (see Chapter 2).

initiation site in all non-treated and stress-relieved specimens. No flaws were detected in the conventionally peened specimens.

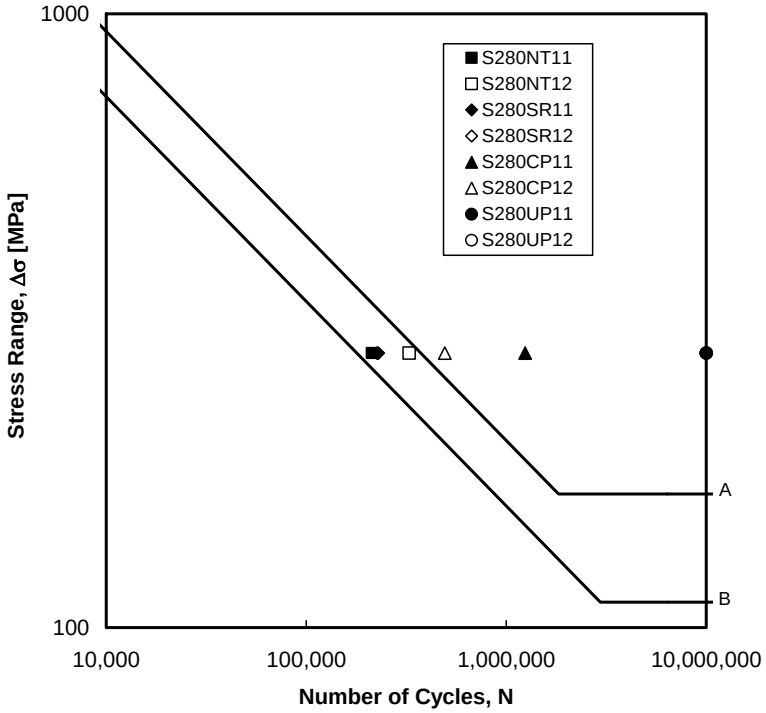

***Figure 5.8** – Results of small scale tests with as-welded profile.*

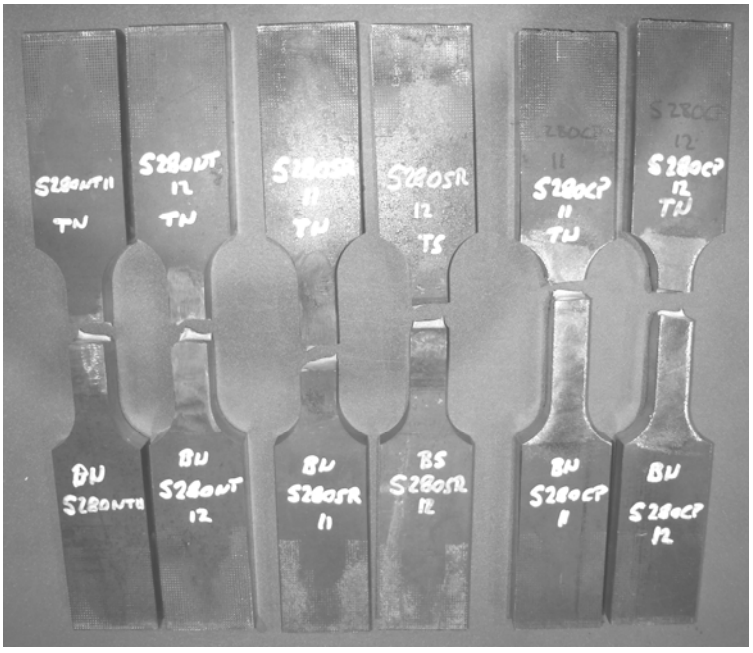

***Figure 5.9** – Failed small scale specimens with as-is weld profile.*

The fracture surfaces of the four non-peened specimens, which were affected by the presence of inclusions, were examined under a scanning electron microscope (SEM). The inclusions ranged in size from a few micrometers to roughly 0.3 mm in diameter. Figure 5.10 shows a typical inclusion. Energy dispersive X-ray spectroscopy (EDX) was used to compare the chemical composition of the sound weld with the inclusions. According to these results the inclusions are most likely slag (high oxygen, titanium and manganese contents, with a rather low fraction of iron present).

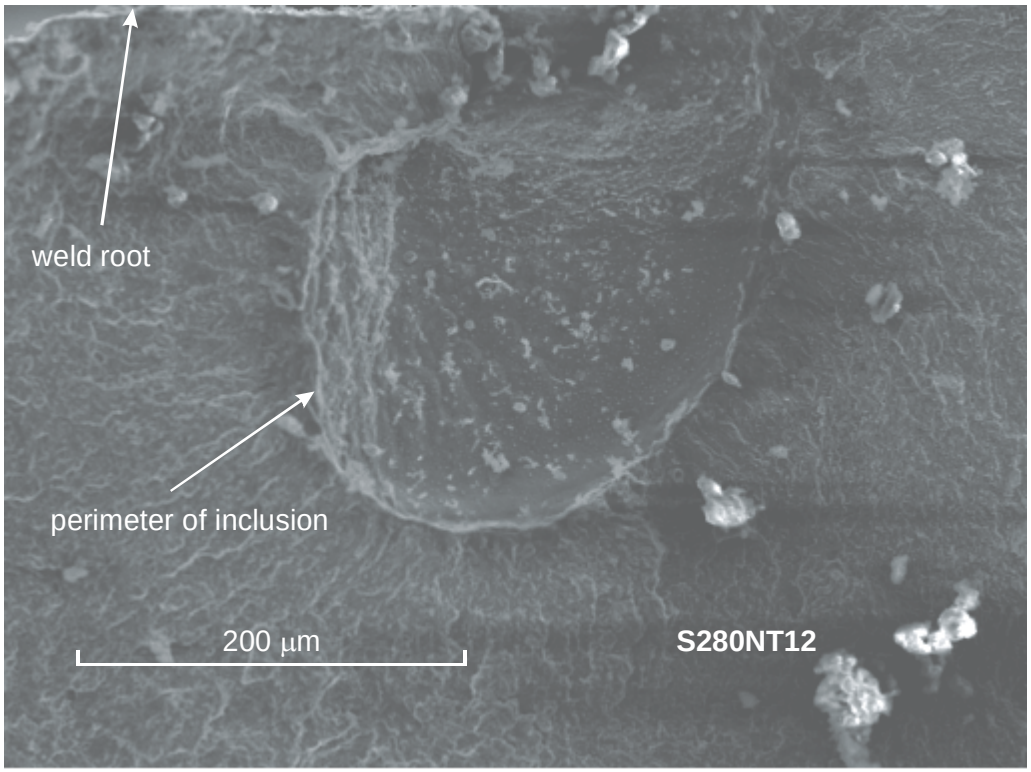

Figure 5.10 *– Typical inclusion seen under the SEM.*

5.2.8 Discussion of Small Scale Tests

The small scale tests showed that even for non-treated welded specimens significant fatigue resistance can be obtained, as long as the weld is sound. This is evident from the failure in the grips of the initial specimens, where the weld face was ground flush and the specimens straightened prior to fatigue testing. In order to ensure failure in the desired region of the weld, the specimen geometry and the weld profile had to be adapted while the initial curvature was left as-is. Furthermore, the nominal stress range had to be increased to 280 MPa, which is very high for most engineering applications. The non-treated and stress-relieved specimens showed roughly the same fatigue resistance, failing at between 200,000 and 320,000 cycles. It is therefore reasonable to assume that at the

high stress range used for these tests, the residual stresses were not of significance for these specimens.

The conventionally peened specimens showed longer fatigue lives than the non-treated and stress-relieved specimens. This could be due to two effects from peening: 1) the introduction of beneficial compressive residual stresses, and 2) the elimination of flaws (either at the surface or close to the surface). The conventionally peened specimens failed in the base metal with no visible flaws at the initiation site. Conversely, the non-treated and stress-relieved specimens failed at the root or toe of the weld due to small slag inclusions ranging from a few micrometers to roughly 0.3 mm in diameter.

The ultrasonically peened specimens did not fail after over 10 million load cycles. The increased fatigue resistance of the ultrasonically peened specimens suggests that a higher level of compressive residual stresses is introduced with ultrasonic peening compared to conventional peening.

5.3 Large Scale Test Set-Up

5.3.1 Introduction

The small scale tests described in the previous section demonstrated that ultrasonic peening was the most efficient of the investigated post weld improvement methods, prolonging the fatigue life at the tested stress range by more than 50 times compared to the non-treated weld. However, small scale specimens often do not satisfactorily represent actual component behaviour, primarily because the residual stresses are usually much more moderate and the probability of containing a harmful imperfection is smaller (i.e., size effect). It was therefore essential to validate this observation in large scale tests. The repair method of gouging and welding was selected. Following proper preparation procedures, the weld profiles were all ground flush, resulting in a further significant difference compared to the second set of the small scale specimens.

This section presents a description of the set-up of the large scale tests. Details and results of two sets of tests, one fabricated with the welding procedure used for the material and the small scale tests and one fabricated with an improved welding procedure, are presented later in Sections 5.4 and 5.5, respectively. Section 5.3.2 gives a description of the test specimens. The preparation of the specimens, i.e., ancillary testing, the gouging and welding processes, non destructive inspection of the welds, and the installation of the specimens in the test setup, is presented in Section 5.3.3. An outline of the test procedure is given in Section 5.3.4.

5.3.2 Description of Test Specimens and Set-Up

Steel plates 350 mm wide by 35 mm thick of grade 350WT were used for the preparation of the test specimens. The plates contained a gouged and full penetration groove weld repair, as shown in Figure 5.11.

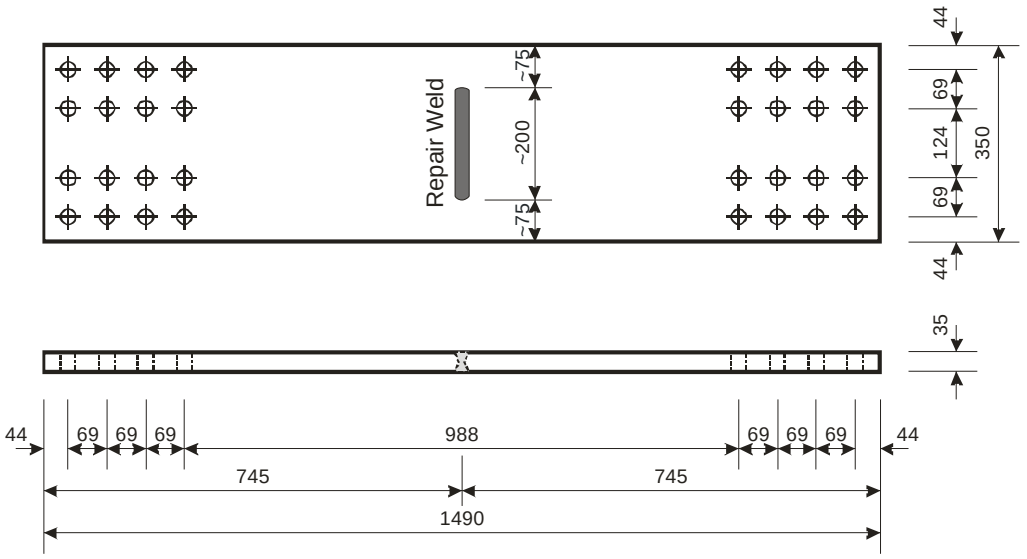

Figure 5.11 *– Gouged and welded test plate.*

In order to load the plates in tension, a set-up was designed, which consisted of a fabricated steel reaction beam (made of grade 350W steel) with a coped flange at mid length and loaded under four point bending. The splice plate bridging the coped portion of the beam acted as the specimen. A schematic elevation of the set-up and a section of the beam with the tested splice plate are illustrated in Figure 5.12. The points of support, spaced at 780 mm, were placed under the cope. The point loads were located at 1750 mm from the supports to create a zone of constant moment and tension at the top of the beam. The inverted configuration of the reaction beam facilitated placement and inspection of the test specimens during testing. The beam was designed to resist an infinite number of load cycles and could thus be re-used, with the splice plate being replaced after each test.

The beam was loaded using two hydraulic actuators with a maximum dynamic capacity of approximately 500 kN each. Each of the supports consisted of a cylindrical roller bearing sandwiched between two hardened steel plates with concave surfaces. This allowed for a symmetrical response of the test, allowing free rotation and enough translation in the longitudinal direction to avoid any introduction of unwanted stresses in the beam and splice plate. Overall lateral movement of the beam was restrained by roller bracings at the ends of the beam that allowed for free vertical movement of the beam. The actuators provided sufficient stiffness to prevent any longitudinal movement of the

load points and thus acted as an overall longitudinal translation restraint. Rotation of the load points was free using a concave reaction plate on a convex bearing. The supports rested on a large stiffened plate girder with a convenient height for installation and inspection of the reaction beam and the splice plates. Stiffeners were clamped to the beam web under the loading points and over the supports.

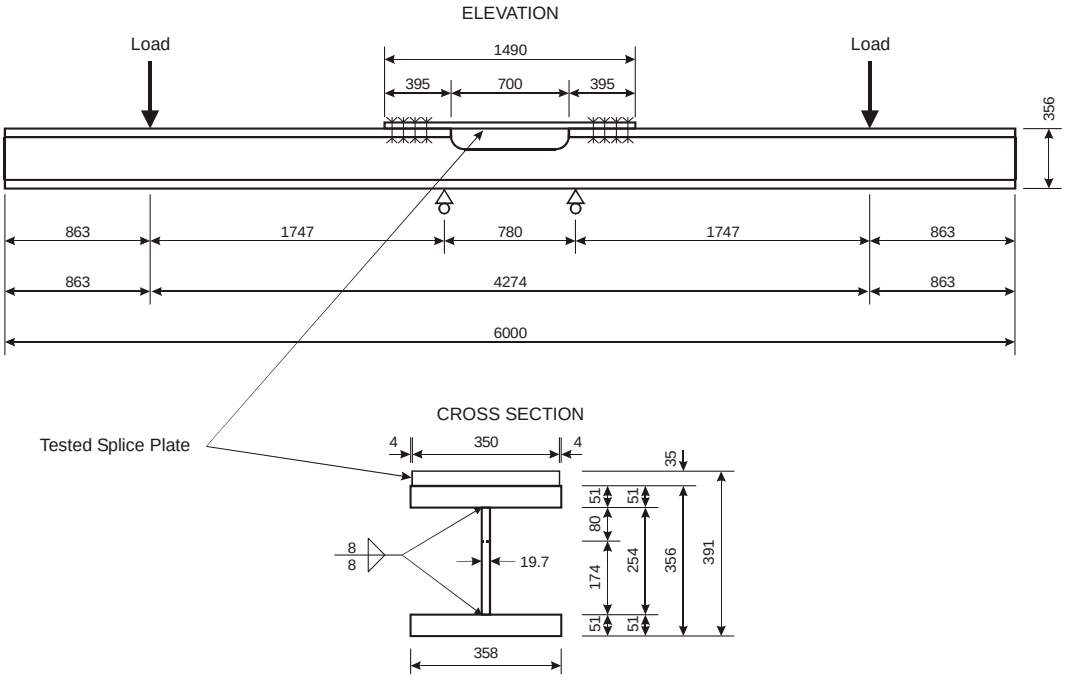

***Figure 5.12** – Schematic set-up of the large scale tests (dimensions in mm).*

The set-up resulted in constant tension in the test specimen and in zero shear in the coped section. The top and bottom fibre stresses in the plate were approximately 47 MPa and 33 MPa, respectively, for every 100 kN load in each actuator, resulting in a total tension force in the plate of roughly 500 kN per 100 kN actuator force. Thus, a maximum dynamic tension force of about 2,500 kN could be introduced into the splice plates with the set-up.

The beam was initially designed for a different repair method that required less tension in the splice plate. In order to prevent slip at the higher loads needed here, additional bolted plates ("slip plates") were installed that extended from the load points to the splice plate connection, creating a second slip plane at the connection.

An overall end view of the test set-up is shown in Figure 5.13. The support region with the splice and slip plates is illustrated in Figure 5.14.

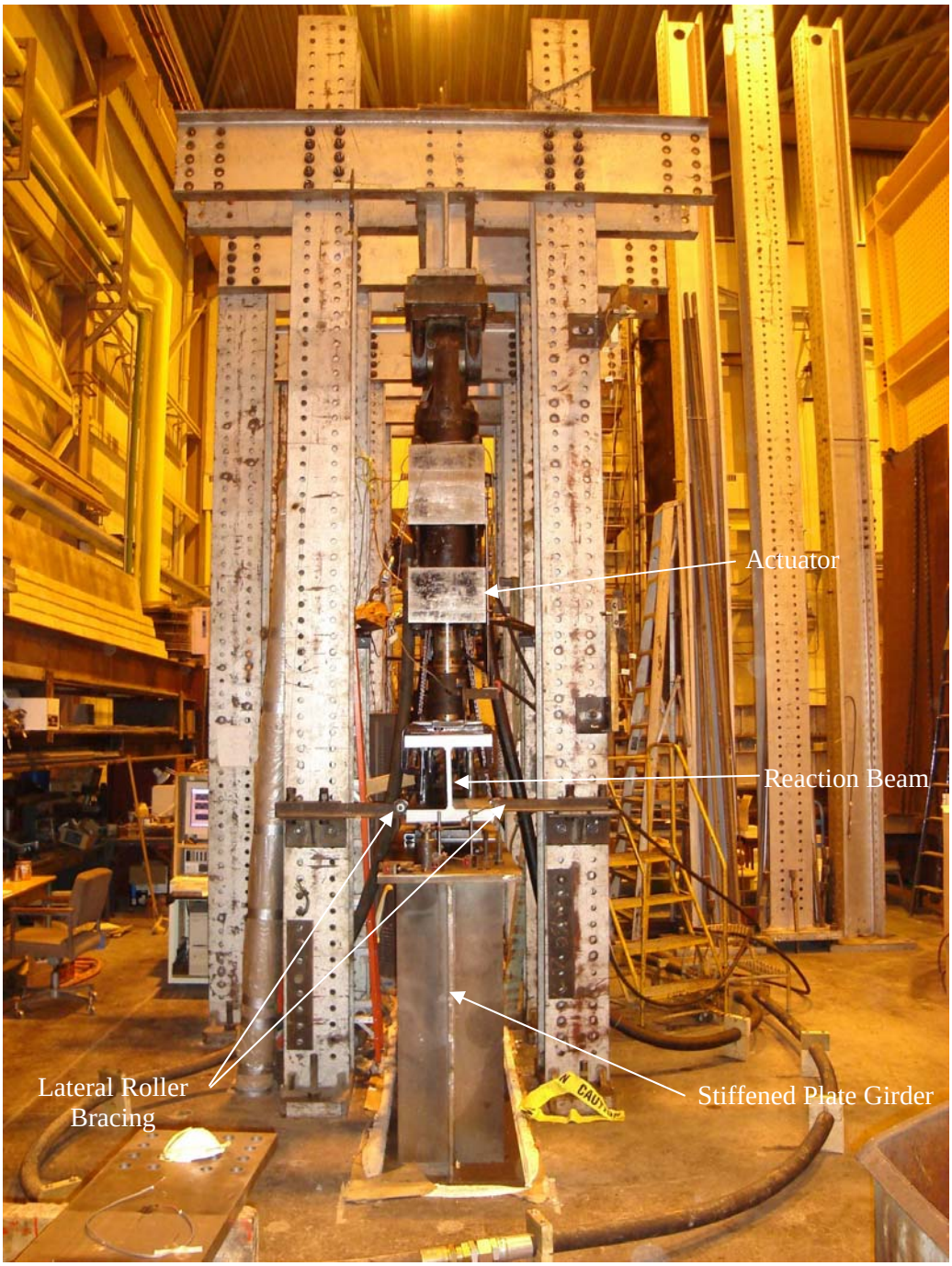

Figure 5.13 *– End view of large scale test set-up.*

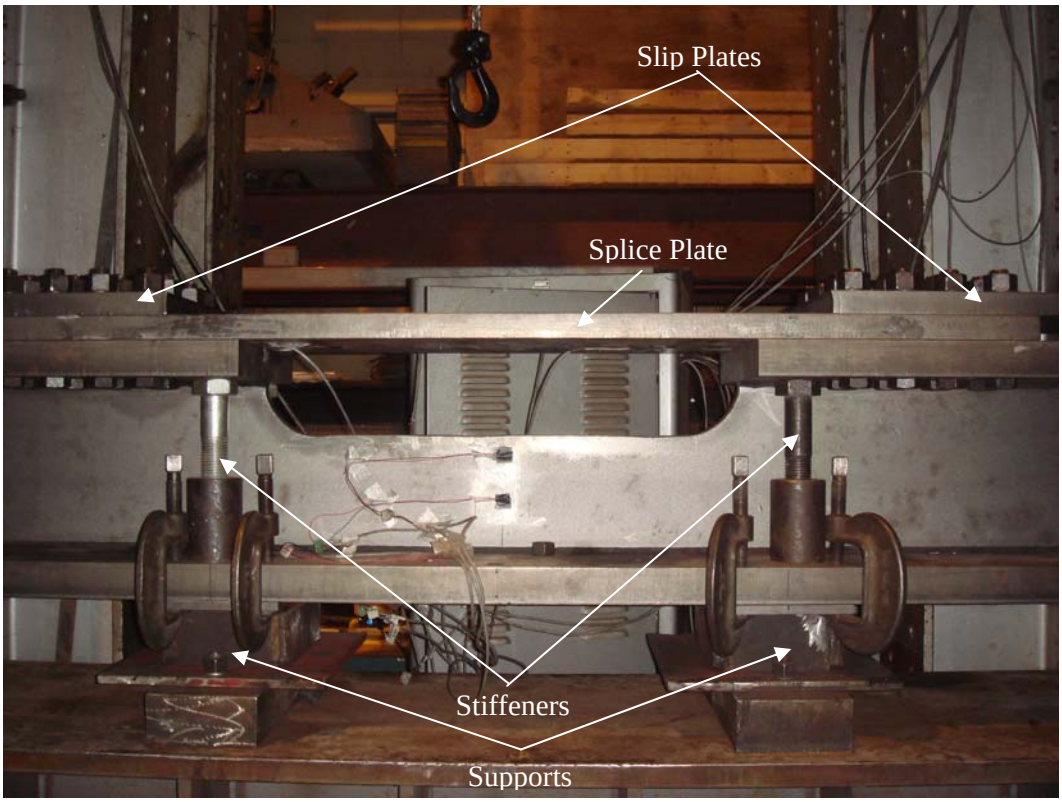

Figure 5.14 *– Detail of the splice plate and support region.*

5.3.3 Preparation of Test Specimens

Ancillary Tests

To confirm that the plates were of grade 350WT steel, standard sheet-type tension coupons and CVN prisms were obtained from the plates. Three tension coupons were prepared, all being machined parallel to the longitudinal axis of the plate. The tests were run in a universal testing machine (MTS® 810) according to ASTM standard A370-05 *Standard Test Methods and Definitions for Mechanical Testing of Steel Products* [ASTM 2005]. All coupons used a 50 mm gauge length with a reduced section width of 40 mm (Plate-Type Specimens). An extensometer mounted on one of the machined faces of the reduced section measured the strains up to the strain at ultimate strength, ε_u. To prevent damage to the extensometer it was removed once the load started to drop and the strain at rupture was measured manually. The stresses were determined by dividing the load by the measured cross-sectional area of each specimen. The testing strain rate was incrementally increased from approximately 10 με/sec in the elastic range to 1,500 με/sec near rupture. Unfortunately, a rubber band fixing the extensometer to specimen TP-2 snapped in the yield plateau and the strain at the onset of strain hardening, ε_{SH}, as well as the strain at ultimate strength could not be measured for TP-2.

The three coupons produced practically identical stress-strain responses. Figure 5.15 shows the stress-strain curves of coupons TP-1 and TP-3. The results for all three tests are summarized in Table 5.5. According to the test results the tensile properties of the plates correspond to grade 350WT steel (yield strength at least 350 MPa, tensile strength between 480 and 650 MPa, see Section 4.2.2). Notable is also the large ductility of the plate material.

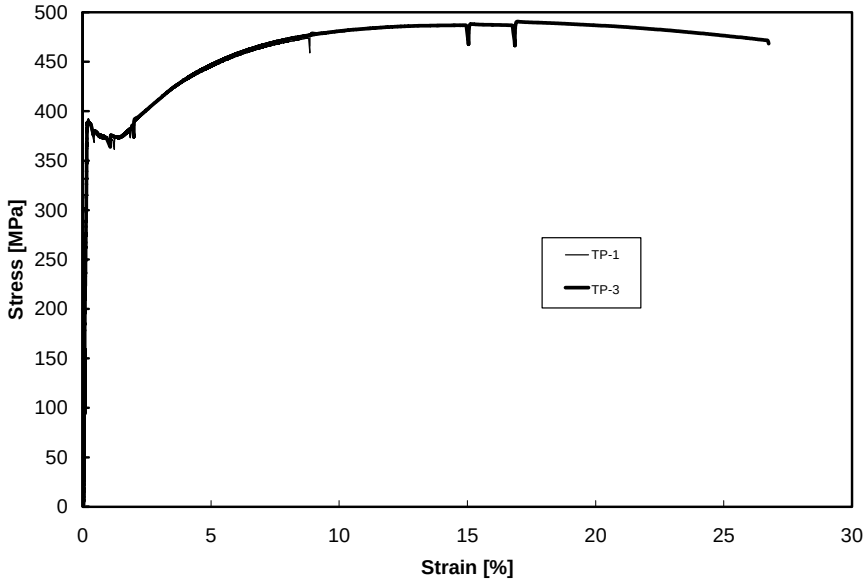

Figure 5.15 *– Stress-strain curve of TP-1 and TP-3.*

Table 5.5 – *Summary of the tension coupon test results taken from the splice plates.*

Specimen Designation	**Orientation**	E **[MPa]**	σ_{ys} **[MPa]**	ε_{SH} **[%]**	σ_{us} **[MPa]**	ε_u **[%]**	ε_r **[%]**	***RA*** **[%]**
TP-1	Parallel to longitu-dinal plate axis	210,000	360	1.3	460	10	65	72
TP-2		212,000	360	---	460	---	64	72
TP-3		214,000	360	1.5	470	16	65	72

E: Modulus of elasticity
σ_{ys}: Static yield strength
ε_{SH}: Strain at onset of strain hardening
σ_{us}: Static ultimate strength
ε_u: Strain at ultimate strength
ε_r: Strain at rupture
RA: Reduction in area at rupture

Three CVN specimens were tested at -30°C and -45°C each. These two temperatures correspond to the testing temperatures for Category 3 and Category 4 toughness in accordance to CAN/CSA G40.21-04 [CSA 2004]. The average absorbed CVN impact energy from three specimens for these temperatures needs to be at least 27 J to qualify for grade 350WT steel. Table 5.6 presents the absorbed energy for each test. The very high CVN values even at the lower test temperature of -45°C confirm that the plates meet the requirement of Category 4 steel.

Table 5.6 – *CVN test results of the splice plate material.*

Specimen Designation	Test Temperature [°C]	CVN Energy [J]
CVNP-30.1	-30	304
CVNP-30.2		334
CVNP-30.3		336
CVNP-45.1	-45	342
CVNP-45.2		374
CVNP-45.3		382

The tensile properties and the CVN energy absorption of the weld metal have been presented in Sections 4.3.4 and 4.3.5.

Fabrication of the Beam and Plates

The beam and plates were prepared by a local steel fabricator. Tolerances according to CAN/CSA S16-01 [CSA 2001] were prescribed and met. All surfaces were sandblasted to obtain a high coefficient of friction. The splice plates were Grade 350WT steel, the beam 350W steel, and the slip plates 300W steel.

Gouging and Welding of Splice Plates

Although no fatigue crack was present in the test specimens, gouging was performed and the gouged area was welded to simulate the repair procedure for fatigue cracks. Details of the gouging and welding procedures are listed in Appendix B. The following work sequence was used:

1. Marking the area to be gouged with felt pen on both sides of the splice plate;
2. Grinding a small groove (~1 mm) on the top side;
3. Carbon arc gouging to a depth of ~12.5 mm on the top side;
4. Grinding to a depth of ~20 mm on the top side to clean the gouged area;

5. Deposition of two weld passes on the top side;
6. Grinding a small groove (~1 mm) on the bottom side;
7. Carbon arc gouging to a depth of ~12.5 mm on the bottom side (back gouging);
8. Grinding to a depth of ~20 mm on the bottom side, assuring that the root of the top weld is removed;
9. Deposition of five weld passes on the bottom side;
10. Adding three weld passes on the top side;
11. Flush grinding of the welds on both sides.

The opening of the grooves before welding was approximately 40 mm at the plate surface. The grooves had a convex shape, with an average groove angle of about 60° and a root radius of approximately 25 mm.

Non Destructive Inspection of Welds

According to current specifications, all welds subjected to fatigue loading need to be inspected for embedded flaws. Historically, radiography has been the preferred non destructive inspection method. However, with recent technical advances, radiography is often replaced by ultrasound. This is mainly due to the less complicated and safer handling of ultrasound. For this project, all repair welds were inspected with ultrasound by a commercial company specialized in non destructive testing of welds. Shear wave and straight beam inspections were performed with a portable ultrasonic flaw detector (Krautkramer USN 58L). In addition, magnetic particle inspection of the weld surfaces was carried out. Acceptability criteria of CAN/CSA W59-03 [CSA 2003] were used. The findings of these inspections are presented in Sections 5.4 and 5.5.

Installation of Splice Plates

To allow for convenient replacement of the splice plates, bolts were used to fasten the plate to the top flange of the reaction beam. Two aspects in the design of the bolted connection were critical: 1) Slip between the test plate and flanges had to be avoided; slips would have led to a permanent bending of the beam during a test, resulting in high stresses in the web, possibly leading to premature fatigue cracking of the beam; 2) The connection had to be far enough away from the centreline of the plate to guarantee a uniform stress distribution across the width of the plate in the repair zone. These two considerations led to the use of sixteen 1-in. diameter A490 bolts per side. The bolts were pretensioned using the turn-of-nut method [CSA 2001, CSA 2006].

5.3.4 Test Procedure

Test Control and Data Acquisition

Static and cyclic loads and strokes were controlled by electrical servovalves on the actuators. Load and stroke feedback was provided by built-in load cells and LVDTs. Two

controllers (Kelsey Instruments K7500 Servocontroller), one per actuator, generated the desired output. One controller acted as a master and the other as a slave. This guaranteed that the cyclic loading of the two actuators was synchronized. The cyclic loads followed a sine wave function, with a frequency of 3.0 Hz for all tests.

The strains in the beam and splice plate were measured with electrical resistance strain gauges and the corresponding stresses were calculated using the measured modulus of elasticity from the tension coupon tests for the plate (~210,000 MPa) and a reasonable average modulus of elasticity of 205,000 MPa for the beam[1] [Galambos & Ravindra 1978].

A total of nine strain gauges were mounted on the beam. The first test had six strain gauges on the splice plate. The location of these fifteen strain gauges is illustrated in Figure 5.16. With the good agreement between analytical results and the strain readings (see next section), the number of strain gauges on the plate was reduced from the fourth test on.

During fatigue testing the loads and strokes were continuously monitored by the Kelsey controller and the peaks displayed. The strains as well as the feedback from the load cells and LVDTs were also continuously acquired through the software LabVIEW. The sampling frequency for both the Kelsey controller and the LabVIEW program was 100 Hz.

To protect the specimens and testing machine from unexpected events, lower and upper bound limits on loads and displacements were set. The test was stopped automatically when any one of these limits was exceeded.

Static Tests and Comparison with Analytical Solutions

Static tests were conducted under load control for each specimen before fatigue loading was started. The stresses at different load levels up to the maximum load of the cyclic test were determined and compared to numerical solutions. Theoretically, the stresses at the locations of the strain gauges, σ_z, can be determined through the general bending stress relationship (beam theory):

$$\sigma_z = \frac{M}{S(z)} \tag{5.2}$$

where M is the bending moment between the two supports and $S(z)$ is the elastic section modulus at a strain gauge location z, measured from the centroidal axis. However, due to microslips in the connections plane sections do not remain plane and the beam theory is not applicable. Therefore, the entire beam with the splice plate was

[1] No tension coupons were taken from the girder.

analyzed with the finite element program ANSYS. Due to symmetry only a quarter of the beam and plate needed to be modelled. The model is illustrated in Figure 5.17.

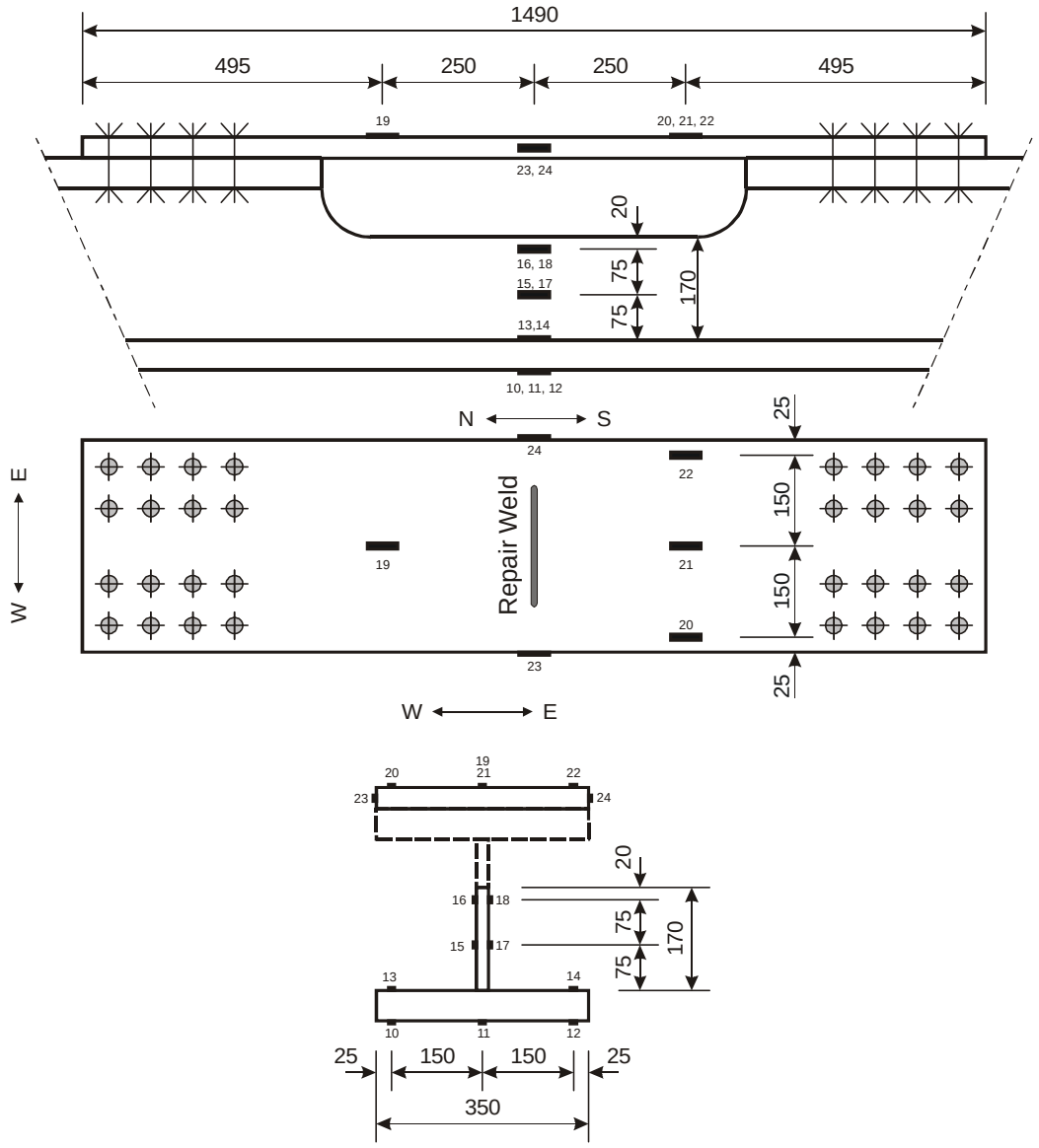

Figure 5.16 *– Location of strain gauges for initial test.*

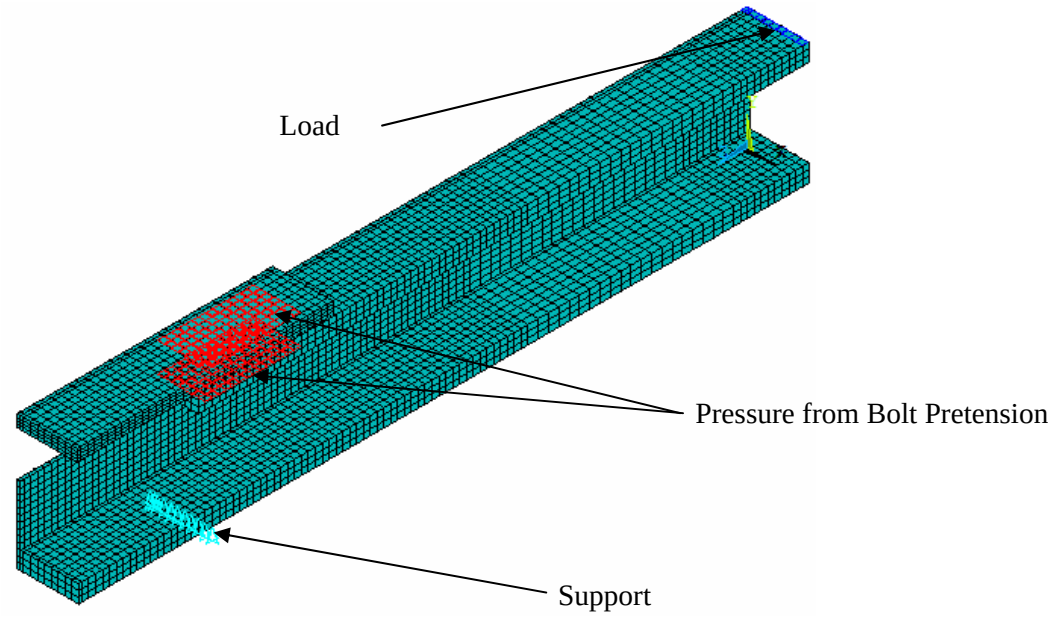

Figure 5.17 *– Finite element model of beam with plate.*

Eight node solid elements (Solid45) were used everywhere. The interface between the top flanges and the splice plate was modelled with contact elements having a coefficient of friction of 0.5. This coefficient of friction is to be expected for sandblasted surfaces [Kulak et al. 2001]. For simplicity, the bolt holes were omitted in the model. A check with a finite element model of the plate showed that the bolt holes do not affect the strain distribution in the vicinity of the repair weld even if the load transfer is assumed to be by full bearing of the bolts. The bolt pretension was introduced by surface pressures on both the plate and flanges corresponding to the estimated tension developed in the bolts.

The stress distribution at midspan determined from the finite element analysis for a load of 400 kN per actuator (maximum applied load in any of the tests) is plotted in Figure 5.18. The stress measurements from the first test (L175NT1) as well as the theoretical stresses according to beam theory (equation (5.2)) are also shown. It has to be noted that the stresses calculated from the strain measurements of the second loading sequence are presented here. During the first loading microslips occurred, resulting in a slight non-linear behaviour. All subsequent static tests behaved linearly.

It is evident from Figure 5.18 that the stress distribution according to beam theory is not representative of the actual behaviour. However, the finite element model shows excellent agreement with the stresses calculated from the measured strains. The same observations were also made for all other specimens. Based on these results, the stress range for each test was determined by averaging the readings from strain gauges 19 and 21 (top of plate along the centreline). The minimum and maximum loads that were expected to yield the targeted stress range were calcualted before each test and the actual stress range was then determined from the strain readings. Due to slight differences in

geometry and behaviour between the specimens variations in stress range and ratio are expected between tests with same maximum and minimum loads.

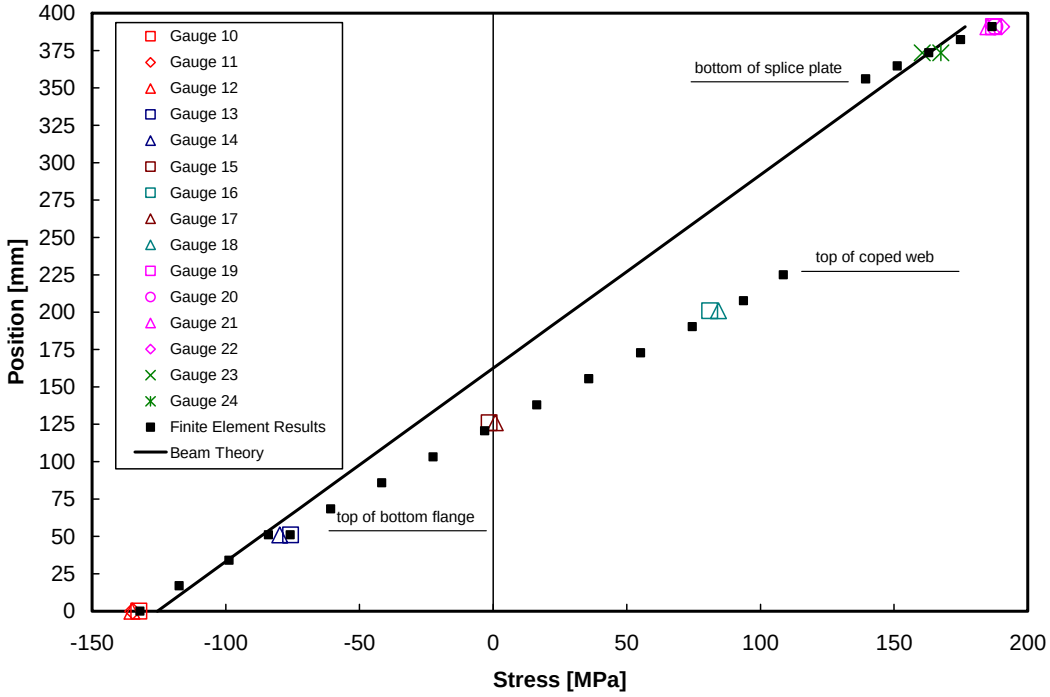

Figure 5.18 *– Stress distribution at mid-span for a load of 400 kN per actuator (for location of the strain gauges, see Figure 5.16).*

Cyclic Tests

A concern of the inverted four point bending set-up was the possibility of "tipping" the beam if the two loading actuators are not perfectly synchronized. A pilot test conducted in load control showed that the peak loads were not reached simultaneously in both actuators. Changing to stroke control did not eliminate this problem. An oscilloscope was hooked up to the Kelsey controllers to check whether an offset in peak load time on the two actuators existed. The trace on the oscilloscope confirmed that the two actuators were not synchronized. Decreasing the phase offset for the slave actuator showed better agreement between the two actuators. At a cyclic frequency of 3 Hz an offset of -45° was needed to synchronize the two actuators.

The disadvantage of cyclic testing in stroke control is that the load drops as the fatigue crack grows larger. As a consequence, the stroke amplitude had to be continuously adjusted once a crack became significant enough to affect the stiffness of the entire system. This posed no particular problem for the first two tests (L175NT1, L145NTT), but resulted in frequent shut-downs during the third test (L145NT1). Therefore, during

this test the control was switched back to load. Adjusting the slave actuator phase offset to +15° showed a perfect match of the two actuator oscillations and all remaining large scale tests were run in load control, keeping the slave phase offset at +15°.

Inspection for Cracks

The welds were ground flush and the surface was shiny after grinding, which helped with visual crack detection, requiring only the assistance of a strong light. The shiny surface was partially obliterated by peening and a magnifying glass was used for inspection of the treated specimens. Magnetic particles or dye penetrants were not required to detect fatigue cracks since cracks as small as 20 mm were easily detected by visual inspection.

Inspection intervals were set according to the expected fatigue life, increasing the inspection frequency when approaching the predicted end of a test. Inspection was performed at least once a day until first crack detection, and then more frequently depending on the crack propagation. Two web cameras were also used to continuously monitor the test. One was set on one end of the beam and allowed observation of test progression. The other camera was focused on the weld at the top of the plate. Larger cracks (roughly 50 mm and longer) could be seen and their propagation monitored with this camera.

Failure Criterion

For practical reasons the failure criterion for a surface crack was defined as the crack size at which it became a through-thickness crack, i.e., when the crack was visible on both surfaces of the plate. For an embedded crack[1], failure was defined when the crack was first detected on one face. The test was still continued until the crack was through the thickness and long enough to expose the fracture surface.

Post Test Examination

After completion of a test, the splice plate was removed. A manageable area around the crack was cut out, without touching the crack tips. The crack was then opened by successively cutting with a band saw from sound material towards the crack tips until the two halves on each side of the crack were separated. All cracks were first inspected visually with the naked eye. Since inclusions were found in all specimens prepared with the initial welding procedure, none of these fracture surfaces were further investigated. The fracture surfaces of the specimens prepared with the improved procedure were examined with an optical microscope.

---

[1] Whether a crack was a surface or embedded crack could only be determined after having inspected the fracture surface (i.e., it could not be established during the test). The cycle counts when a crack was detected on each face, as well as the corresponding lengths, were noted in the test log.

5.4 Initial Gouging and Welding Procedure

5.4.1 Introduction

Six plates were gouged and welded with the initial procedure used for field repairs (see Appendix B) using the flux cored arc welding (FCAW) process with a seamless wire (Drahtzug Stein Megafil® 713R, E491T1 according to AWS 5.20 [2005]) as the filler metal. The ultrasonic inspection revealed severe inclusions, mostly at the interface between the ground metal and the first weld bead. These flaws were rated in all plates as unacceptable and the welds would have to be rejected according to current standards [AWS 2008, CSA 2003]. No surface defects were detected in any of the welds.

Five of the six inspected plates were tested in spite of the severe inclusions. Since the detected inclusions could also be present in field applications it was found useful and informative to investigate the fatigue resistance of such weld repairs with large defects. An additional plate was prepared using exactly the same weld procedure, but a different wire (Hobart Brothers Tri-Mark® TM-711M, E491T1 according to AWS 5.20 [2005]). Since the welder was familiar with this wire and did not have any problems with it, it was hoped that a sound weld could be achieved. However, the repair weld also showed one very severe inclusion, extending along the entire weld.

The following presents the test matrix (Section 5.4.2), the test results (Section 5.4.3), the findings from the examination of the fracture surfaces (Section 5.4.4), and a general discussion (Section 5.4.5) of the six tested specimens prepared with the initial procedure. A comparison with test results from an improved procedure (see Section 5.5) is discussed at the end of the chapter in Section 5.6.

5.4.2 Test Matrix

The first test was conducted on a plate that was not further treated after grinding the weld flush. A stress range of $\Delta\sigma = 175$ MPa was applied, targeting a number of cycles to failure of around 200,000. If ultrasonic peening had an effect on the fatigue life of these specimens then this selected stress range for the non-treated case should still lead to a finite life for peened specimens. Because the first test specimen failed much before 200,000 cycles and since ultrasonic peening is not expected to substantially increase the fatigue resistance of welds with such large and deeply embedded defects, the next three tests were carried out at $\Delta\sigma = 145$ MPa. However, due to improved welds (most likely because the welder got used to the procedure and was able to reduce the severity of the defects) one of the plates did not fail after more than 5 million cycles and the stress range was again increased to 175 MPa for the last two tests. Both Megafil welded plates tested at $\Delta\sigma = 145$ MPa, as well as two Megafil welded plates tested at $\Delta\sigma = 175$ MPa and the Tri-Mark welded plate tested at $\Delta\sigma = 145$ MPa were left non-treated (recall that the welds in all specimens were ground flush). One Megafil welded plate tested at $\Delta\sigma = 175$ MPa was ultrasonically peened. The ultrasonic peening intensity was adapted

from the literature [Huo et al. 2000, Roy et al. 2003], resulting in a peening time of approximately 20 minutes per weld face (~15,000 mm^2 per face as only the weld, but not the HAZ was peened). The minimum load per actuator was kept constant at 20 kN, resulting in varying stress ratios, R, which were all smaller than 0.1. Table 5.7 presents the test matrix of the large scale tests from the first series (initial welding procedure).

5.4.3 Test Results

The results of all the large scale tests prepared with the initial gouging and welding procedures are presented in Observations of some crack propagation rates confirmed that once a crack reached both faces the crack growth rate becomes very high, being close to unstable. This underlines the suitability of the chosen failure criterion.

Table 5.8. In addition to the identification of the specimens (designation, applied stress range, $\Delta\sigma$, and ratio, R), two cycle counts are reported. N_1 corresponds to the number of cycles at which a crack was detected at the top face whereas N_2 corresponds to the number of cycles at which the crack was detected at the bottom face. Often, the first and second numbers of cycles are identical because a crack was detected only after it had reached both faces of the plate. For each of these cycle counts the length of the crack at the top, $a_{t,i}$, and at the bottom, $a_{b,i}$, faces is also given.

Table 5.7 – *Matrix of large scale tests from first series.*

Specimen Designation	**Wire**	**Treatment**	P_{min} **[kN]**	P_{max} **[kN]**	$\Delta\sigma$ **[MPa]**	R **[-]**
L175NT1	Megafil	Non-Treated	20	400	175	0.06
L145NTT	Tri-Mark	Non-Treated	20	335	143	0.05
L145NT1	Megafil	Non-Treated	20	335	146	0.06
L145NT2	Megafil	Non-Treated	20	335	145	0.08
L175UP1	Megafil	Ultrasonically Peened	20	400	174	0.06
L175NT2	Megafil	Non-Treated	20	400	176	0.05

P_{min}: Minimum applied load per actuator
P_{max}: Maximum applied load per actuator
$\Delta\sigma$: Stress range at top of plate (determined from strain readings, see previous section)
R: Stress ratio (due to microslips the stress ratio is not exactly the ratio of P_{min} over P_{max})

Observations of some crack propagation rates confirmed that once a crack reached both faces the crack growth rate becomes very high, being close to unstable. This underlines the suitability of the chosen failure criterion.

Table 5.8 – *Results of large scale tests prepared with the initial gouging and welding procedures.*

Specimen Designation	$\Delta\sigma$ [MPa]	R [-]	N_1 [cycles]	$a_{t,1}$ [mm]	$a_{b,1}$ [mm]	N_2 [cycles]	$a_{t,2}$ [mm]	$a_{b,2}$ [mm]
L175NT1	175	0.06	118,000	~50	---	183,000	~130	~40
L145NTT	143	0.05	28,000	~50	~50	28,000	~50	~50
L145NT1	146	0.06	876,000	~120	~110	876,000	~120	~110
L145NT2	145	0.08	Test stopped after 5,360,000 cycles with no visible cracks					
L175UP1	174	0.08	1,130,000	~100	~100	1,130,000	~100	~100
L175NT2	176	0.05	210,000	~30	---	268,000	~150	~40

Figure 5.19 shows the test results, expressed in terms of the number of cycles at which a crack was detected on the top surface of the plate, N_1, plotted in a $\Delta\sigma - N$ diagram. The AASHTO fatigue curves are also shown in Figure 5.19 for comparison.

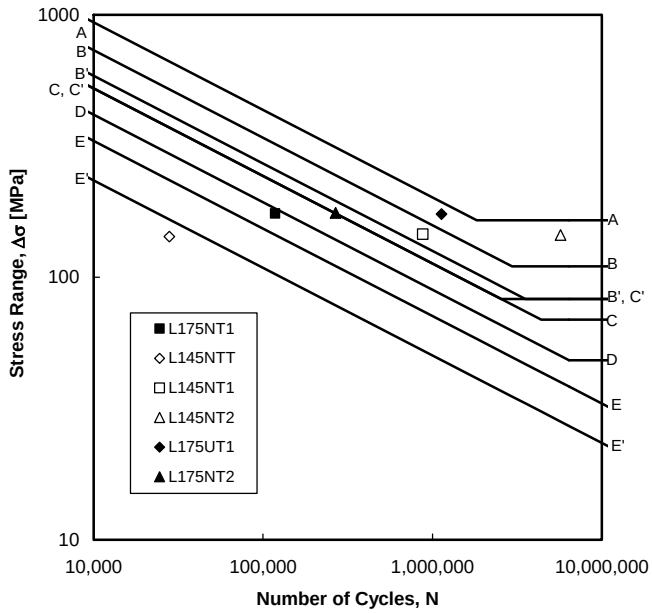

Figure 5.19 *– Results of large scale tests prepared with the initial gouging and welding procedures.*

5.4.4 Examination of Fracture Surfaces

As expected from the ultrasonic inspection, the fracture surface revealed severe slag inclusions in all the tested welds from the first series of large scale tests. The most severe inclusions were observed in L175NT1 and L145NTT. These two specimens were welded first with a travel speed of about 2.1 mm/s. The welder felt very uncomfortable with this travel speed[1] and increased it to roughly 3.4 mm/s for the other four specimens. Figure 5.20 shows the fracture surfaces of specimen L145NTT, which exhibits the most continuous slag inclusion, yet still being representative for all the tested plates. The crack initiation sites are clearly discernable at the slag inclusion, propagating in a stable manner towards the two faces of the plate. Just after having reached the bottom face the crack growth rate increases significantly (evidenced by the rougher appearance of the fracture surface, i.e., by more shear deformations).

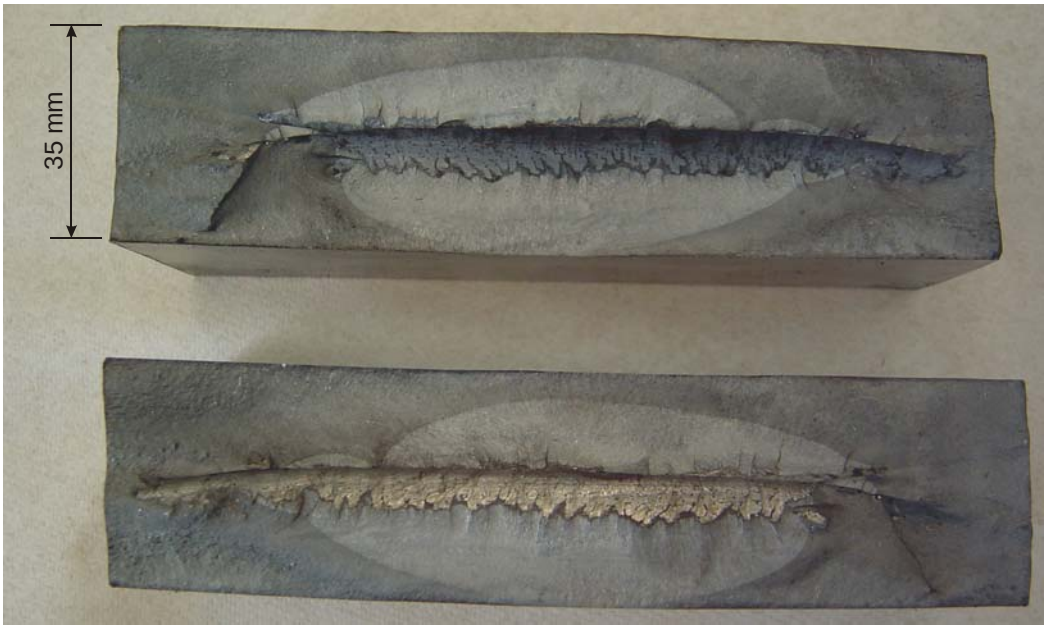

***Figure 5.20** – Fracture surfaces of specimen L145NTT.*

Visual inspection of the fracture surfaces indicated that:

- If more than one layer of slag inclusions was present, the governing crack always started at the slag inclusion closest to the top of the plate, where stresses were the highest.

[1] The welder felt that due to the rather slow travel speed the deposition rate was too high and the arc pressure could not stir the weld pool enough to make the slag rise to the surface of the molten weld pool, causing it to get trapped. Furthermore, the heat was so high that after some time it melted the gas nozzle (which had to be replaced several times).

- The crack propagation patterns on opposing sides of an inclusion were never quite the same (as is evident in Figure 5.20), indicating that two independent cracks formed.
- Once the crack reached a face of the plate, the crack propagation rate increased significantly as evidenced by the rougher crack surface appearance, supporting the statements and observation made earlier that little residual life is present at this stage.

5.4.5 Discussion

Six welded repairs for which ultrasonic inspection showed severe inclusions resulting in rejectable welds were tested in fatigue. A large scatter in test results is observed. The first two welded plates showed the lowest fatigue resistance of all six test specimens. These two plates (L175NT1, L145NTT) were welded at a lower travel speed and showed the most severe slag inclusions. These led, especially for specimen L145NTT, to a significantly lower fatigue resistance, suggesting that the travel speed might have a marked effect on the quality of the weld. Whether the very poor performance of specimen L145NTT, which used a different wire than all other tests, is uniquely due to the travel speed or whether other parameters in the welding procedure played a role cannot be determined from just this one result.

Only one test was carried out on an ultrasonically peened weld. Its improved fatigue performance compared to non-treated specimens suggests that ultrasonic peening increases the fatigue life even when embedded imperfections are governing. However, due to the insufficient number of comparable test results, this conclusion has to be treated with caution.

Comparison of the test results with the AASHTO curves suggests that even with these rejectable inclusions, relatively high fatigue lives can be obtained. In fact, the last four tests (L145NT1, L145NT2, L175UP1, L175NT2) can be approximately classified as a Category C detail, which is the detail defined for non ground, but sound, full penetration groove welds with the stresses applied perpendicular to the weld axis (ground flush, full penetration groove welds are classified as Category B).

5.5 Improved Gouging and Welding Procedure

5.5.1 Introduction

The first seven large scale specimens all contained severe slag inclusions and the welds should have been rejected according to current North American specifications [AWS 2008, CSA 2003]. After some experimentation an increased travel speed was adopted (from 3.4 mm/s to 6.0 mm/s with slight weaving), which reduced the deposition rate and

resulted in a shallower molten metal pool, allowing the slag to rise to the surface and thus avoiding its entrapment (see Appendix B). All the other welding parameters were kept the same as specified for the preparation of the first set of test specimens. Eight plates were prepared with the improved procedure. Ultrasonic and magnetic particle inspections did not reveal any unacceptable flaws except in one specimen, in which a crack-like discontinuity was detected about 10 mm below the surface. The discontinuity was estimated to be about 3 mm long. The discontinuity was not removed, thus allowing for an investigation of the effect of this weld defect on the fatigue resistance of the welded repair.

During the preparation of the initial set of specimens some problems with the gouging were encountered. Therefore, the grooves of the new specimens were completely ground. This change in procedure for removing the fictitious crack had nothing to do with eliminating the slag inclusions; it was merely more practical.

The following presents the test matrix (Section 5.5.2), the test results (Section 5.5.3), the findings from the examination of the fracture surfaces (Section 5.5.4), and a general discussion (Section 5.5.5) of the eight tested specimens prepared with the improved procedure. A comparison with the test results from the initial procedure (see Section 5.4) is presented at the end of the chapter in Section 5.6.

5.5.2 Test Matrix

All eight plates were welded using the Megafil wire. Two ground flush but non-treated specimens were tested first at a stress range of 195 MPa. However, both plates failed away from the repair weld, near the connection to the beam flange. The remaining six plates were consequently redesigned with a reduced 250 mm wide “dog bone” section. The reduced section was cut by water jet, which should not appreciably alter the residual stress pattern in the weld and HAZ. Furthermore, water jet cutting creates a smooth surface with no heat affected zone. The geometry of the “dog bone” plates is shown in Figure 5.21 and a photo of a plate is shown in Figure 5.22.

The first two of the “dog bone” plates were tested in the as-welded condition at a stress range in the reduced section of 240 MPa (L240NT21 and 22). However, one of the test specimens did not fail after more than five million cycles, indicating that the treated specimens might last beyond ten million cycles. The stress range was therefore increased to 255 MPa for the remaining four specimens. Two specimens (L255NT21 and 22) were ground flush and two other specimens (L255UP21 and 22) were ultrasonically peened after grinding. The peened specimens were treated for approximately 60 minutes on each face. The peened area is also shown in Figure 5.21 (~50 000 mm^2), encompassing the HAZ. Specimen L255UP22 contained the rejectable internal flaw (see Section 5.5.1). For all eight tests the minimum hydraulic actuator force was kept at 20 kN and the maximum load was adjusted to obtain the desired stress range. This resulted in varying stress ratios,

R, for varying stress ranges. The stress ratio was smaller than 0.1 for all the tests. Table 5.9 presents the test matrix for the large scale tests prepared with the improved welding procedure.

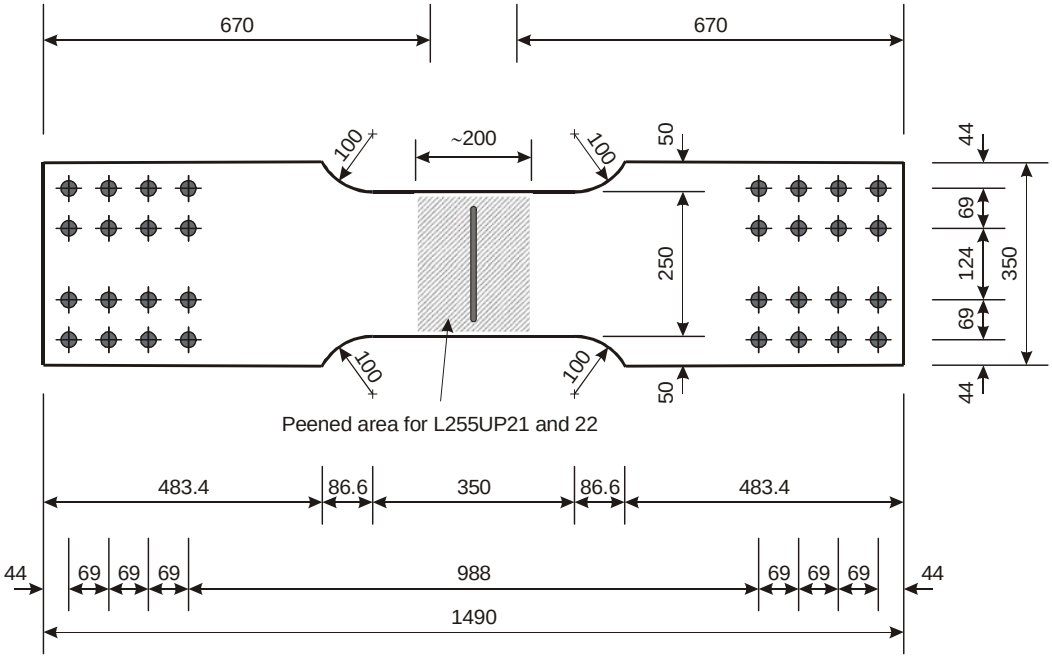

Figure 5.21 *– Geometry of "dog bone" plates (dimensions in mm).*

Figure 5.22 *– Typical "dog bone" plate.*

Table 5.9 – *Matrix of large scale tests prepared with the improved procedure.*

Specimen Designation	Wire	Treatment	P_{min} [kN]	P_{max} [kN]	$\Delta\sigma$ [MPa]	R [-]
L195NT11	Megafil	Non-Treated	20	450	195	0.04
L195NT12					196	0.04
L240NT21	Megafil	Non-Treated, "Dog Bone" Section	20	400	241	0.05
L240NT22					234	0.05
L255NT21	Megafil	Non-Treated, "Dog Bone" Section	20	420	257	0.03
L255NT22					259	0.05
L255UP21	Megafil	Ultrasonically Peened, "Dog Bone" Section	20	420	255	0.05
L255UP22 [1)]					253	0.05

P_{min}: Minimum applied load per actuator
P_{max}: Maximum applied load per actuator
$\Delta\sigma$: Stress range at top of plate (determined from strain readings, see previous section)
R: Stress ratio (due to microslips the stress ratio is not exactly the ratio of P_{min} over P_{max})
[1)] Specimen L255UP22 contained a rejectable internal flaw

5.5.3 Test Results

L195NT11 and L195NT12

The first two specimens prepared with the improved welding procedure were tested at a stress range of approximately 195 MPa. Specimen L195NT11 developed a crack on top of the test plate, where it was in contact with the end of one of the slip plates. The crack was detected after 1.58 million cycles. The crack clearly initiated due to fretting between the slip plate and the test specimen. In order to attempt to postpone or even prevent such a failure in specimen L195NT12, the sharp edges of the slip plates were removed and the surface of the test specimens around the contact area of the two plates was ultrasonically peened. However, a crack at the same location as in specimen L195NT11 was detected after 1.50 million cycles. In addition, a crack also initiated at the net section, in the first row of bolts. No cracks were detected in the vicinity of the repair weld in both test specimens.

If the two results from L195NT11 (1.58 million) and L195NT12 (1.50 million) are plotted on a $\Delta\sigma - N$ diagram (using the stresses determined from the strain readings, i.e., the gross section stresses), they fall almost exactly on the average curve for a

Category B detail.[1] Category B is the detail used for slip critical connections in AASHTO [2007].

L240NT21 through L255UP22

Since no failures in the vicinity of the repair weld were obtained in specimens L195NT11 and L195NT12, the plate cross-section was reduced from 350 mm to 250 mm at the weld location ("dog bone" shape) for the remaining six test specimens. In order to improve the fatigue resistance of the transition zone, the transition radius was ultrasonically peened. The first two "dog bone" shaped plates were tested at a stress range of approximately 240 MPa. L240NT21 failed after roughly 800,000 cycles due to a surface flaw in the HAZ. L240NT22 did not fail after over five million cycles. Unfortunately, a diagonal crack starting under the North actuator developed in the beam web. The crack was repaired by rewelding, but due to a lack of proper access to the cracked area, the fatigue crack re-initiated at the web to top flange fillet weld. Additional cracks were detected in the support region of the reaction beam, starting in the web to bottom flange fillet weld. Since the cracks were in the compression zone of the beam, they self-arrested in the flange and could be stopped by hole drilling in the web. The load history of the beam is summarized in Appendix C.

Because of the poor performance of the weld repair of the diagonal web crack, it was decided to fabricate a new beam with stiffeners under the actuators and full penetration groove welds between the web and the flanges. Furthermore, the web thickness was increased from 20 to 25 mm to improve out-of-plane stability. All welds of the new beam were ultrasonically peened.

The maximum load for the four remaining tests was increased from 400 to 420 kN, resulting in a stress range of approximately 255 MPa at the top surface of the reduced section of the test specimens.

Both, L255NT21 and L255NT22 failed from a fatigue crack initiating at the bottom of the plate in the HAZ (approximately 15 mm away from the weld toe). This was somewhat unexpected since the stress range at the bottom of the plate was significantly lower (approximately 225 MPa) than at the top (approximately 255 MPa). The number of cycles until the crack became a through-thickness crack was 1,000,000 for L255NT21 and 1,140,000 for L255NT22.[2]

---

[1] According to Klippstein [1987] the average curve of a detail is obtained by adding two standard deviations of the intercept to the design curve. The standard deviation of the intercept is assumed to be 0.25 (log scale) for all details.

[2] In both specimens the cracks were approximately 40 mm long on the bottom when first detected after 980,000 and 1,100,000 cycles, respectively. At this stage, the cracks were not visible on the top (i.e., the cracks were not through the thickness). The first detected crack length at the top was approximately 30 mm in both specimens.

The first ultrasonically peened specimen, L255UP21, failed after 970,000 cycles away from the weld and HAZ in the transition radius of the cut (see Figure 5.23**)**. The crack initiated at the top of the plate, where a sharp edge from the water jet cutting, accentuated by the ultrasonic peening of the radius, was present.

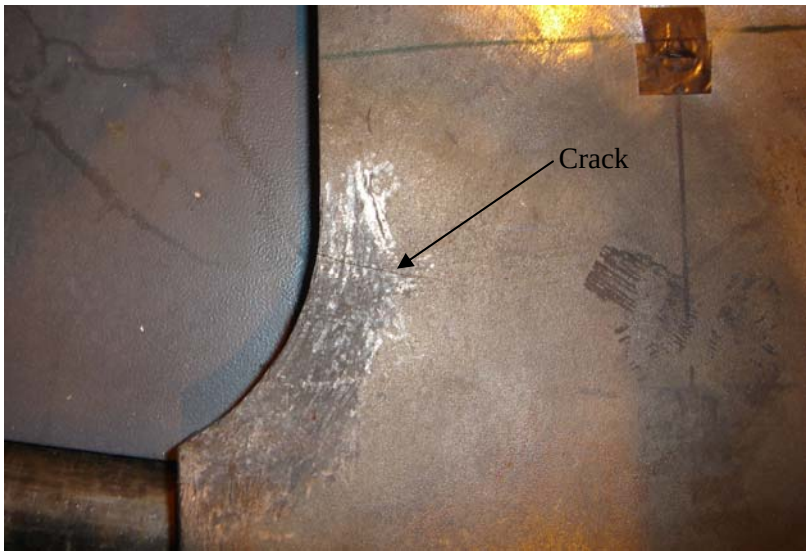

Figure 5.23 *– Failure location of L255UP21.*

The second ultrasonically peened specimen, L255UP22, failed after 2,540,000 cycles in the unreduced section where the plate was in contact with the end of one of the beam flanges (fretting fatigue).

The results of the six "dog bone" shaped tests are presented in Table 5.10. The number of cycles to failure, N, corresponds to the formation of a through-thickness crack. The stress range shown in Table 5.10, $\Delta\sigma_{init}$, is the theoretical stress range at the initiation site (or at the top of the plate for L240NT22, which did not fail). For specimen L255UP21, which failed in the transition radius of the reduced section, the stress range at the radius, $\Delta\sigma_{init}$, was determined using a nonlinear finite element model (ANSYS), ignoring any residual stresses.

Figure 5.24 shows the test results plotted in a $\Delta\sigma - N$ diagram based on the values presented in Table 5.10. For the two ultrasonically peened specimens (L255UP21 and L255UP22) the run-out test results of the treated section using the stress ranges determined with the strain gauges (approximately 255 MPa) are also shown in Figure 5.24. All test results fall above the Category A curve and it seems that even the non-treated specimens show similar fatigue resistance as is assumed for the virgin material (Category A). No conclusions about the improvement of the fatigue resistance due to ultrasonic peening can be drawn as both specimens failed away from the peened areas, without considerably surpassing the fatigue life of the untreated specimens.

Table 5.10 – *Results of "dog boned" large scale plate tests.*

Specimen Designation	$\Delta\sigma_{init}$ [MPa]	N [cycles]	Initiation Site
L240NT21	241	780,000	Top of plate in HAZ (~15 mm from weld toe)
L240NT22	234	—	No failure after 5,540,000 cycles
L255NT21	224	1,000,000	Bottom of plate in HAZ (~10 mm from weld toe)
L255NT22	226	1,140,000	Bottom of plate in HAZ (~15 mm from weld toe)
L255UP21	380	970,000	Radius of "dog bone" cut (top of plate)
L255UP22	181	2,540,000	In unreduced section at end of top flange

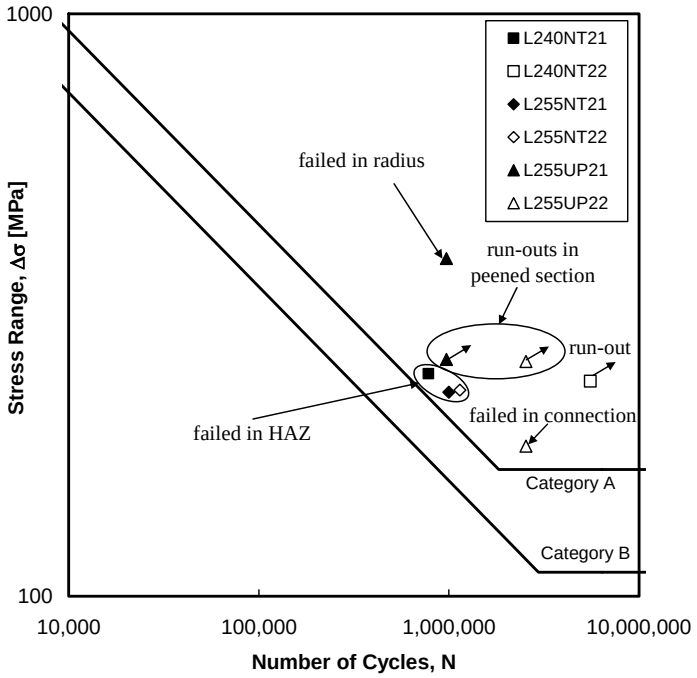

Figure 5.24 *– Results of large scale "dog bone" shaped specimens.*

5.5.4 Examination of Fracture Surfaces

L240NT21

The crack in specimen L240NT21 initiated at the top of the plate, in the HAZ, about 15 mm away from the weld toe. Figure 5.25 shows a close-up of the crack initiation site. The crack initiated at a 0.2 mm deep surface pit.

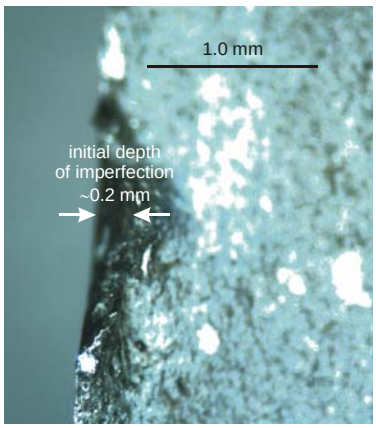

Figure 5.25 *– Crack initiation site of specimen L240NT21.*

L255NT21

The crack in specimen L255NT21 initiated at the bottom of the plate, about 10 mm away from the weld toe in the HAZ. Figure 5.26 shows a close-up of the crack initiation site. The crack initiated at 0.3 mm deep surface flaw (most likely a weld spatter mark).

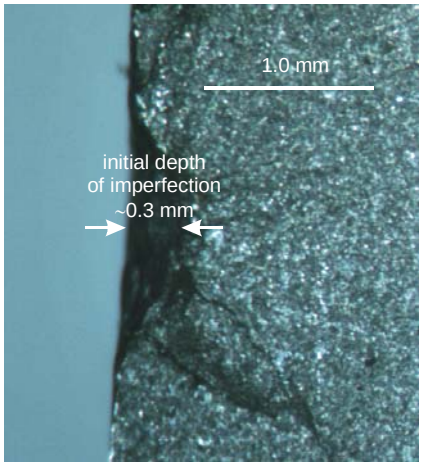

Figure 5.26 *– Crack initiation site of specimen L255NT21.*

L255NT22

The fatigue crack in specimen L255NT22 initiated at the bottom of the plate, about 15 mm from the weld toe, in the HAZ. Figure 5.27 shows a close-up of the crack initiation site. The crack again initiated at a 0.3 mm deep surface flaw. The flaw was over 15 mm long, resulting in a very small aspect ratio of less than $a/c = 0.02$. The flaw was identified as a grinding mark.

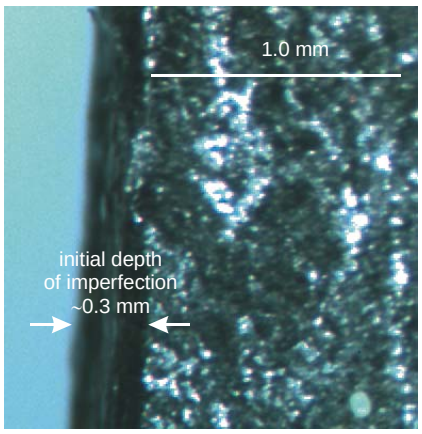

Figure 5.27 *– Crack initiation site of specimen L255NT22.*

5.5.5 Discussion

An increase in the travel speed from 3.4 mm/s to 6.0 mm/s yielded improved welds that resulted in fatigue lives close to the ones expected for virgin material. Failure of non-treated, but ground flush, repair welds occurred in the HAZ. The fatigue cracks in the non-treated specimens initiated at surface flaws. The size of these flaws has a significant effect on the initiation location, as a crack can start at the bottom of the plate, where stresses are lower (by over 10%) than at the top of the plate. Both ultrasonically peened specimens failed outside of the treated area at a number of cycles too low to draw any conclusions as to the efficiency of ultrasonic peening. It has to be noted that although L255UP22 contained an embedded inclusion large enough to lead to rejection, cracks did not initiate at the inclusion after over 2.5 million cycles and $\Delta\sigma \approx 250$ MPa. This suggests, as was observed from the ultrasonically peened specimen prepared using the initial weld procedure (L175UP1), that ultrasonic peening may be beneficial even for sub-surface flaws.

5.6 Summary and Discussion

This chapter presented the experimental program conducted to assess the performance of welded repairs with and without post weld treatment and to validate the deterministic and probabilistic approaches proposed in Chapters 6 and 7. First, small scale tests on butt welded coupons were carried out. The main objective of this part of the test program was to investigate the effectiveness of different post weld treatment methods. Initial specimens with the welds ground flush and the specimens straightened did not fail in the welds or HAZ, but in the grip locations. Therefore, a second set of specimens, where only the backing bar side was ground flush and where the deformations resulting from welding and machining were not straightened, was prepared. Two coupons were tested in the as-welded condition, two were temperature stress-relieved, two were conventionally peened,

and two specimens were ultrasonically peened. All coupons were tested in direct tension with $R = 0.1$. The nominal stress range in the second set of tests was 280 MPa for all eight specimens.

The peening intensity for the conventionally peened specimens could be determined from peening of Almen A-strips. However, the Almen method did not yield any meaningful results to determine the intensity of the ultrasonically peened specimens. This is attributed to the much higher intensity from ultrasonic peening, resulting in an elongation rather than a bending of the strips. Therefore, it is impossible to compare the intensity between conventional peening and ultrasonic peening using the Almen method.

The eight tests showed that there is no significant difference in fatigue resistance between the non-treated and the stress-relieved specimens. Conventional peening increased the fatigue resistance, but was not as effective as ultrasonic peening. In fact, ultrasonic peening resulted in at least fifty times longer lives compared to the non-peened specimens and at least ten times longer lives compared to the conventionally peened specimens.

In order to assess the effectiveness of ultrasonic peening in a realistic bridge or heavy mining equipment component, large scale tests on 35 mm steel plates, where a fictitious crack was repaired by gouging and welding, were conducted. A first set of repairs resulted in rejectable welds due to excessive slag inclusions. Nevertheless, these plates were still tested. A large scatter was observed in the test results. Some specimens expectedly showed quite poor performance. However, the last four tests, where smaller inclusions were present, showed a fatigue resistance similar to AASHTO Category C details.

An increase in travel speed yielded much improved welds. Eight large scale test specimens were prepared with this improved procedure. The first two plates were tested at a stress range of 195 MPa and both failed away from the weld repair due to fretting fatigue at the bolted connections. The cross-section in the weld repair region of the remaining six plates was reduced by water jet cutting the test specimens into a “dog bone” shape. The nominal stress range in these specimens could thus be substantially increased, while preventing failure in the bolted connections. Four specimens were tested in the non-treated condition (i.e., the welds were only ground flush). For the remaining two specimens the weld and HAZ were ultrasonically peened. Three of the four non-treated specimens failed in the HAZ due to surface flaws (approximately 0.2 to 0.3 mm deep). The fourth non-treated specimen had not failed after over 5.0 million cycles when the test was terminated due to several cracks in the reaction beam. Both ultrasonically peened specimens failed away from the weld and the HAZ at numbers of cycles that are too small to draw any conclusion about the effectiveness of ultrasonic peening.

6. DETERMINISTIC PREDICTION OF THE SMALL SCALE TEST RESULTS

6.1 Introduction

This chapter investigates different deterministic approaches for the prediction of the fatigue life of the small scale specimens presented in Chapter 5. Based on the background information presented in Chapter 2, a procedure for fatigue life calculation, using a strain based approach for crack initiation and linear elastic fracture mechanics for the crack propagation, is developed. This procedure is presented in the form of a flow chart in Figure 6.1. Although the various elements of this flow chart are explained in the following, the reader is reminded that the effect of residual stresses is important and, for this reason, their effect is discussed in detail in Section 6.2, where a crack closure model is derived to account for residual stresses.

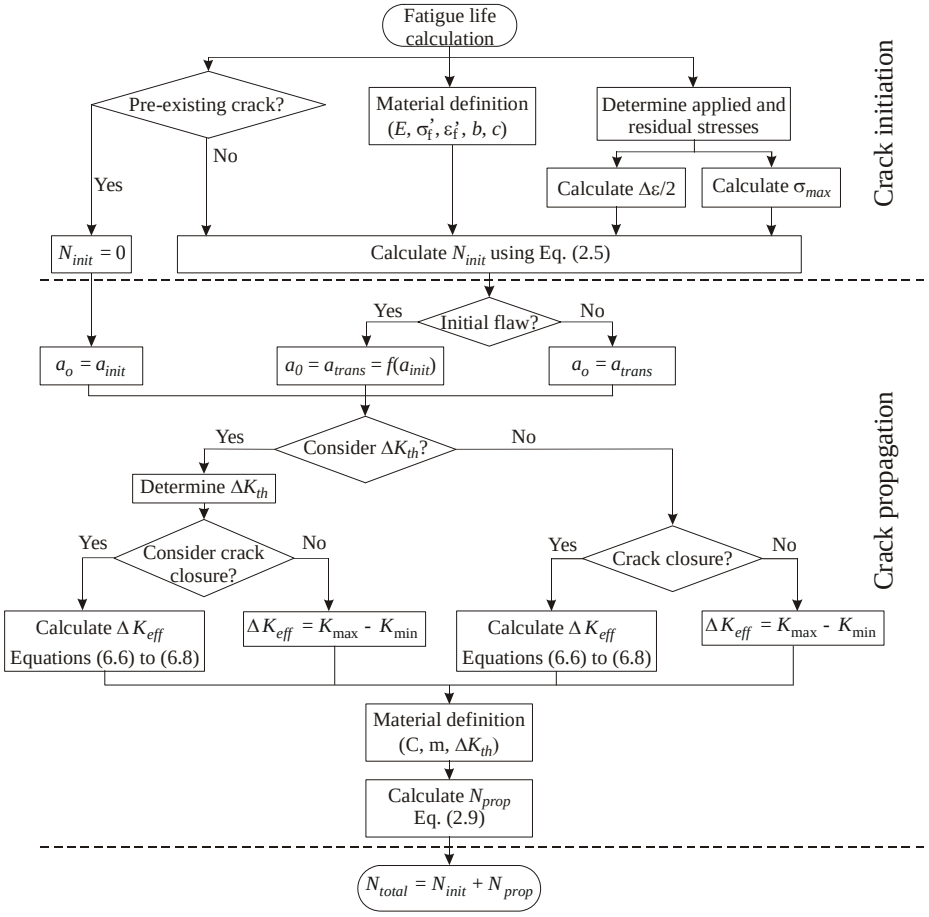

Figure 6.1 *– Flow chart for the deterministic approach.*

As illustrated in the flow chart of Figure 6.1, the initial discontinuity, the material properties, the applied loading, and the residual stresses have to be defined first. These input variables are used at different stages of the crack initiation and propagation calculations. If the initial discontinuity is a crack, then no initiation life is present and the initial crack size in the crack propagation model, a_0, is equal to the initial discontinuity size, a_{init}. If the initial discontinuity is a flaw or if there is no initial discontinuity, then the strain amplitude, $\Delta\varepsilon/2$ and the maximum stress, $\sigma_{\max}$, at the critical location have to be determined considering the flaw characteristics, the cyclic stress-strain properties, the applied loading, and the residual stresses. The obtained strains and stresses along with the fatigue initiation properties yield the crack initiation life, N_{init}, by solving equation (2.5). For details with crack initiation life the transitional crack size, a_{trans}, which is equal to a_0, has to be determined next. Four different approaches in the crack propagation stage (including or neglecting ΔK_{th}, including or neglecting crack closure, i.e., residual stresses) are then investigated. Considering the chosen approach the crack propagation life, N_{prop}, is determined with equation (2.9), taking into account the material properties, the applied loading, the residual stresses and the initial and final crack sizes, a_0 and a_f. Finally, the crack initiation and propagation lives are added to obtain the total fatigue life, N_{total}.

Depending on the starting flaw condition, whether the threshold stress intensity factor range is considered, and whether the crack closure phenomenon is taken into account, a total of 20 possible approaches can be used to calculate the total fatigue life. These different approaches are presented in Section 6.3.

In addition to the residual stresses, the stress and strain distributions resulting from the applied external force at the critical locations must be established. This is done using the finite element analysis presented in Section 6.4.

The fatigue life predictions for the 20 approaches described in Section 6.3 are presented in Section 6.5. No data from the actual tests, except for strain measurements during the static tests, are considered in Section 6.5, making the models true predictions of the test results. Section 6.6 presents a comparison between predicted and observed test results.

The eight small scale specimens with the intact weld profile are considered here. As stated in Chapter 5, where the experimental program carried out in this work is presented, only these specimens yielded test results that can be appropriately analysed.

6.2 Effect of Residual Stresses during Stable Crack Propagation

The fatigue life prediction method presented in this thesis uses the strain-based correlation approach for crack initiation presented in Chapter 2:

$$\frac{\Delta\varepsilon}{2} = \frac{\left(\sigma_f^{'}\right)^2}{\sigma_{\max} E}\left(N_{init}\right)^{2b} + \frac{\sigma_f^{'}\varepsilon_f^{'}}{\sigma_{\max}}\left(N_{init}\right)^{b+c} \tag{2.5}$$

The model for the stable crack propagation stage was also defined in Chapter 2 with the following relationship:

$$\frac{da}{dN} = C \cdot \left(\Delta K^m - \Delta K_{th}^m\right) \Rightarrow N_{prop} = \int_{a_0}^{a_f} \frac{da}{C \cdot \left(\Delta K^m - \Delta K_{th}^m\right)} \tag{2.9}$$

In contrast to equation (2.5), which accounts for the mean stress effects through $\sigma_{\max}$, equation (2.9) does not include any mean stress effects. Research, however, has demonstrated that residual stresses, which alter the mean stresses, affect the crack growth rate [Kirkhope et al. 1999a]. In order to account for residual stresses the stress intensity factor (SIF) due to residual stresses, K_{res}, is superimposed to the SIF due to the applied load, $K_{\max}$ and $K_{\min}$. This results in the following effective maximum and minimum stress intensity factors and stress ratio [Rice et al. 1988]:

$$K_{eff,\max} = K_{\max} + K_{res} \text{ and } K_{eff,\min} = K_{\min} + K_{res} \tag{6.1}$$

$$R_{eff} = \frac{K_{eff,\min}}{K_{eff,\max}} \tag{6.2}$$

The stress intensity factors can be obtained from equation (2.7), where the applied and residual stress distributions are accounted for by using their respective stress gradient correction factors, β_G [1]. When the SIFs are determined from a finite element analysis, the loadings should be superimposed, accounting for potential plasticity.

Elber [1970] demonstrated that the plastic zone that forms around a crack tip due to high localized strains can retard the propagation of a crack. The crack tip plastic zone introduces compressive residual stresses, causing the crack to remain closed even for a minimum stress intensity factor, $K_{\min}$, greater than zero (i.e., the crack is closed before all tensile load is removed). The stress intensity factor at which the crack opens upon reloading is designated as K_{op}. It is believed that the portion of the loading cycle below K_{op} has little or no influence on the fatigue crack growth [Stephens et al. 2001]. In the absence of residual stresses the effective stress intensity factor range, ΔK_{eff}, therefore becomes $K_{\max} - K_{op}$ for $K_{op} > K_{\min}$. To account for this crack closure effect a ratio, U, can be defined based on Elber's work:

$$U = \frac{\Delta K_{eff}}{\Delta K} = \frac{K_{\max} - K_{op}}{K_{\max} - K_{\min}} = \frac{\left(1 - K_{op}/K_{\max}\right)}{\left(1 - R\right)} \qquad \text{for } K_{op} > K_{\min} \tag{6.3}$$

[1] All other correction factors, β_i, are not affected by the type of loading.

where R is the applied stress ratio, $\sigma_{\min} / \sigma_{\max}$. Equation (2.9) can therefore be rewritten as:

$$\frac{da}{dN} = C \cdot \left(\Delta K_{eff}{}^{m} - \Delta K_{th}^{m}\right) \qquad \text{with } \Delta K_{eff} = U \cdot \Delta K \tag{6.4}$$

Subsequent research has revealed that a unique expression for K_{op}, and therefore U, cannot be established [Suresh 1998]. Several empirical expressions for U have been proposed. These expressions are generally material and test condition dependent [Suresh 1998]. The relationship proposed by Bremen [1989], which should result in slightly conservative fatigue life predictions, is used in the present work:

$$\begin{aligned} U &= \frac{\left(1 - 0.2/\left(1 - R\right)\right)}{\left(1 - R\right)} && \text{for } R \le 0.28 \\ U &= 1.0 && \text{for } R > 0.28 \end{aligned} \tag{6.5}$$

This relationship was chosen because it was obtained by fitting a curve to U-values determined from laboratory testing of non-treated and treated welded structural steel components subjected to a wide range of stress ratios ($-4.0 \le R \le 0.7$). Bremen [1989] demonstrated that the crack closure effect allows for the integration of residual stresses in the determination of ΔK_{eff}, resulting in the following relationships (see Appendix D):

$$\Delta K_{eff} = 0 \qquad \text{for } K_{\max} + K_{res} < 0 \text{ and all } R_{eff} \tag{6.6}$$

$$\Delta K_{eff} = \Delta K \qquad \text{for } K_{\max} + K_{res} \ge 0 \text{ and } R_{eff} > 0.28 \tag{6.7}$$

$$\Delta K_{eff} = \left(K_{\max} + K_{res}\right) \cdot \left(1 - \frac{0.2}{1 - R_{eff}}\right) \qquad \text{for } K_{\max} + K_{res} \ge 0 \text{ and } R_{eff} \le 0.28 \tag{6.8}$$

The plasticity-induced crack closure effect discussed above can further be used to assess the effect of overloads. It is well established that tensile overloads will produce crack growth retardation, whereas compressive overloads, especially in post weld treated components, will accelerate crack propagation [Stephens et al. 2001, Dubois 1994]. In order to obtain an accurate reliability-based prediction of the fatigue life of a structural component, overload cycles should be incorporated in the prediction model.

6.3 General Approaches to Fatigue Life Prediction

6.3.1 Introduction

The total fatigue life of a structural component is the sum of its crack initiation and stable propagation lives. These two components of the fatigue life are a function of the stresses, strains, and material properties at the critical location. The stresses and strains depend on

the geometry of the elements under consideration, and on initial imperfections. Therefore, one of the most important steps in calculating the fatigue life of a welded structure is to characterize the initial discontinuity. Based on the observations made on the crack initiation specimens in this and other studies [Chen et al. 2005], the most likely crack initiation site is a corner in the reduced section. However, depending on the location of a governing discontinuity, a crack could also start on the surface away from a corner or, especially for the peened specimens, from embedded weld discontinuities such as slag inclusions or porosity. Consequently, three possible initiation locations resulting in the following crack configurations are investigated in this chapter:

- Corner crack: The crack front of a corner crack is assumed to remain circular during propagation, i.e., a constant aspect ratio $a/c = 1.0$ is taken.
- Elliptical surface crack: The initial surface flaw is assumed to be located at the centre of the plate and the crack propagates symmetrically from the centre flaw. The crack aspect ratio is assumed to remain constant at $a/c = 0.5$ (approximately the mean value in Figure 2.17) throughout the entire crack propagation stage.
- Embedded elliptical crack: The initial flaw is assumed to be close to the ground surface of the weld (2.5 mm below the surface), where significant tensile residual stresses are likely to remain after peening. Again, for simplicity, a constant aspect ratio of $a/c = 0.5$ is assumed throughout the entire crack propagation stage.

Flaw and crack shapes and sizes are discussed in Section 6.3.2 and in Section 6.3.3, respectively. Another critical parameter in fatigue life calculations is the transitional crack size, a_{trans}, which corresponds to the transition from the crack initiation stage to the crack propagation stage. The definition of a_{trans} has to take into account the effect of small cracks on crack propagation. This is addressed in Section 6.3.4, where two distinct approaches to deal with the threshold stress intensity factor range, ΔK_{th}, are proposed. It is indisputable that residual stresses must be included in the crack initiation model. However, whether residual stresses play an important role in the crack propagation stage is controversial. Two different approaches to deal with residual stresses during crack propagation are proposed in Section 6.3.5. Furthermore, the expected material properties, the determination of the stress intensity factors, K_i, and the final crack size, a_f, are discussed in Sections 6.3.6, 6.3.7, and 6.3.8, respectively.

6.3.2 Initial Flaw or Crack Shape

A crack is defined here as a weld discontinuity with a sharp tip, i.e., elastic stresses are infinite at its tip. A flaw on the other hand is considered as a weld discontinuity with a rounded tip. Elastic stresses are therefore always finite at its tip. Although all the probabilistic approaches reviewed in Chapter 3 assume a crack as the governing weld imperfection, a reliability-based approach should consider the possibility of the governing imperfection being a flaw. Three limiting shapes are defined in the

deterministic models: 1) a crack, which represents the most severe type of discontinuity; 2) a spherical flaw, resulting in the least severe condition for a discontinuity; and 3) a perfect weld with no discontinuity, simulating the best case scenario. In the presence of an initial crack there is, of course, no physical crack initiation life. Conversely, in the presence of a spherical flaw or no discontinuity, there is a crack initiation life, which will be accounted for in proposed models. For analytical purposes a sphere is considered the most appropriate initial flaw shape, considering that fatigue damage is caused by the average rather than the peak strains around a flaw [Neuber 1968, Radaj & Sonsino 1998]. It is also the most convenient shape to use for the calculations since the strains and stresses are not a function of the orientation of the flaw, as would be the case for an ellipsoid, for example.

6.3.3 Initial and Transitional Flaw or Crack Size

The literature review showed that variability in initial flaw or crack sizes needs to be considered. Based on Figure 3.2, it is reasonable to assume that the size of the governing initial discontinuity in a deterministic model is somewhere between 0.1 mm and 1.0 mm. Therefore, the initial flaw or crack sizes of 0.1 mm and 1.0 mm are taken as the limiting crack sizes in the deterministic models.

As shown in Figure 2.5, the technical crack size, i.e., the crack size at the end of an initiation test, is larger than the physical crack initiation size. However, for details with initiation life (cases 2 and 3 in Section 6.3.2) it is very difficult to accurately establish the transitional crack size, a_{trans}, i.e., the crack size at the end of initiation and at the beginning of the stable propagation. For case 2 (initial flaw, but finite crack initiation life) it is assumed that a_{trans} is equal to the initial flaw size. Since the crack at the beginning of crack propagation must be at least the initial flaw size, this approach results in slightly conservative fatigue life predictions, as long as small crack behaviour (see Section 2.2.4) is not present. Adopting this simplified definition for a_{trans}, the initial crack size, a_0, in the crack propagation model (equation 2.9) is always assumed to be equal to the initial flaw size, a_{init}. For the perfect welds (i.e., where there is no discontinuity), the transitional crack size, a_{trans}, is assumed to be 0.1 mm. This value is chosen rather arbitrarily.

6.3.4 Small Crack Effect during Crack Propagation

It was shown in Chapter 2 that for small cracks the Paris equation (6.4) is not applicable and a reasonable simplification in this case is to neglect ΔK_{th} altogether. Furthermore, neglecting ΔK_{th} implicitly accounts for the presence of a technical crack size after initiation that is somewhat larger than assumed in Section 6.3.3 ($a_0 = a_{init}$). However, this approach could lead to overly pessimistic predictions. Therefore, both approaches, either accounting for or neglecting ΔK_{th}, are considered for the deterministic models.

6.3.5 Residual Stress Effect during Crack Propagation

Since the effect of residual stresses is believed to be much more significant during the crack initiation stage than in crack propagation stage (see Chapter 2), a simplifying assumption consists of neglecting residual stresses in the crack propagation equation (2.9). However, this assumption may lead to overoptimistic fatigue life predictions in the presence of tensile residual stresses, and too pessimistic fatigue life predictions in the presence of beneficial compressive residual stresses. Therefore, two models, one considering the crack closure effect presented in Section 6.2 and one neglecting crack closure, are investigated here.

6.3.6 Fatigue Material Properties

The following values for the weld material properties, as introduced in Chapter 4, are used for all deterministic models[1]:

- Crack initiation: $E = 207{,}000$ MPa
  $K' = 530$ MPa
  $n' = 0.037$
  $\sigma_f^{'} = 630$ MPa
  $b = -0.059$
  $\varepsilon_f^{'} = 0.34$
  $c = -0.63$
- Crack propagation: $C = 3.5\times10^{-13}$ (mm/cycle)$\cdot\left(\text{MPa}\sqrt{\text{mm}}\right)^{-3}$
  $\Delta K_{th} = 60$ MPa$\sqrt{\text{mm}}$ (with and without crack closure)
  $m = 3.0$

6.3.7 Stress Intensity Factors

The stress intensity factors, K_i, used in equation (2.9), are calculated using equation (2.7):

$$K_i = \beta_E \cdot \beta_S \cdot \beta_W \cdot \beta_G \cdot \sigma_i \cdot \sqrt{\pi a} \tag{2.7}$$

where σ_i is the reference stress in the uncracked condition. and:

β_E	:	crack shape correction factor (e.g. elliptical versus straight crack front)
β_S	:	free surface correction factor
β_W	:	finite width (or thickness) correction factor
β_G	:	stress gradient correction factor (accounting for non-uniform stress distribution along the anticipated crack path)

[1] It is assumed that the cracks start at the root of the weld and propagate through the heat affected zone (HAZ). Therefore, the crack growth constant for the HAZ is taken here.

For a ***circular corner crack*** in a finite plate, Newman & Raju [1983] proposed the following expression for the product $\beta_E \cdot \beta_S \cdot \beta_W$, which was simplified here for $a/c = 1.0$:

$$\beta_{ESW} = \left[0.722 + 0.526\left(\frac{a}{t}\right)^2 - 0.0764\left(\frac{a}{t}\right)^4 - 0.0637\left(\frac{a}{t}\right)^6 \right] \sqrt{\sec\left(\frac{\pi a}{2W}\sqrt{\frac{a}{t}}\right)} \qquad (6.9)$$

where t is the specimen thickness and W the specimen width in the reduced section. For the square cross-section of the small scale specimens described in Chapter 5, $t = W = 19.05$ mm. Newman and Raju [1983] limit the applicability of equation (6.9) to $a/W \leq 0.2$ (and $a/t \leq 1.0$). However, the expression is used here up to $a/W = 1.0$. This simplification is warranted in view that over 90% of the crack propagation life is consumed by the time that a/W reaches a value of 0.2.

For an ***elliptical crack*** the crack shape correction factor, β_E, can be expressed as [Anderson 2005]:

$$\beta_E = \frac{1}{\Phi_0} \qquad (6.10)$$

where Φ_0 is the elliptical integral, which is a function of the crack aspect ratio, a/c, and has to be integrated numerically over the ellipse angle from the major to the minor axis, i.e., from 0 to $\pi/2$. In order to apply the elliptical integral in a reliability based analysis, approximations have to be used. The following fourth order polynomial fit of the exact solution was derived for the present work:

$$\Phi_0 = 0.2568\left(\frac{a}{c}\right)^4 - 0.7635\left(\frac{a}{c}\right)^3 + 0.9916\left(\frac{a}{c}\right)^2 + 0.0875\left(\frac{a}{c}\right) + 1 \qquad (6.11)$$

With an R^2 value of 1.00 equation (6.11) is found to provide an excellent fit of the elliptical integral. Substituting the aspect ratio $a/c = 0.5$ as defined in Section 6.3.1, the crack shape correction factor becomes $\beta_E = 0.825$.

The free surface correction factor, β_S, is [Broek 1989]:

$$\begin{aligned} \beta_S &= 1.12 && \text{for a surface crack} \\ \beta_S &= 1.00 && \text{for an embedded crack} \end{aligned} \qquad (6.12)$$

The finite thickness correction factor, β_W, is determined with the following relationship [Broek 1989]:

$$\beta_W = \sqrt{\frac{1}{\cos\left(\frac{\pi a}{W}\right)}} \qquad (6.13)$$

where $W = 2t$ for a surface crack and $W = t$ for an embedded crack. It should be noted that $W = t$ for an embedded crack is only valid for a crack at mid-thickness. For cracks that are not centered through the thickness, the surface that gives the largest β_W should be used (an embedded crack that is very close to the surface has a β_W-value

approximately equal to the value of a surface crack). This effect, however, is neglected here. This is deemed reasonable considering that the difference in β_W between a surface and a centred embedded crack is less than 10% for crack lengths smaller than half the specimen thickness, which for non-centered embedded cracks is always larger than the failure crack size defined in the present work (see Section 6.3.8).

The expression for the stress gradient correction factor, β_G, used here for all models is [Anderson 2005]:

$$\beta_G = SCF\left(1+\frac{2A}{\pi}a+\frac{B}{2}a^2+\frac{4}{3}\frac{C}{\pi}a^3+\frac{3}{8}Da^4\right) \tag{6.14}$$

where the coefficients A through D are determined from a fourth order polynomial expression fitted through the stress distribution along the anticipated crack path in the absence of a flaw or crack, with the origin of x placed at the centre of the initial crack:

$$\sigma(x) = SCF \cdot \sigma_n\left(1+Ax+Bx^2+Cx^3+Dx^4\right) \tag{6.15}$$

In the present work, the nominal stress, σ_n, is taken as the stress at the centre of the initial flaw or crack, i.e., at $x=0$, and thus $SCF=1.0$. Furthermore, since linearly varying stresses are assumed in this work, $B=C=D=0$. The nominal stresses, σ_n, for the applied loads and the residual stresses as well as the coefficient A are defined in Section 6.5 for each investigated case.

6.3.8 Final Crack Size

As stated in Chapter 2, the final crack size is usually limited by either brittle fracture or yielding of the remaining cross-section. Since the tests are all carried out at room temperature, it is expected that the steel will have sufficient toughness to allow the crack to propagate over most of the reduced section before it becomes unstable. The transition from a corner or surface crack to a through-thickness crack increases the level of complexity of the crack growth problem. In order to avoid this transition, the crack size should not exceed the following values:

- Corner crack: The crack size is equal to the thickness, t (and width, W).
  $$a = 19.05 \text{ mm}$$
- Elliptical surface crack: The crack reaches the corners.
  $$2c = 19.05 \text{ mm} \Rightarrow a = 0.5c = 4.76 \text{ mm}$$
- Embedded elliptical crack: The crack reaches the surface closest to crack initiation location.
  $$a = 2.5 \text{ mm}$$

These values are adopted here as the failure criteria and although they do not exactly correspond to the failure criterion adopted during the tests (complete severing of cross-section), they are appropriate considering the rather small residual fatigue life remaining at that stage.

6.3.9 Summary

Twenty deterministic models are tested for the prediction of the fatigue life of the small scale specimens. All the models are based on the following common assumptions:

- Cracks initiate either at a corner, at the surface, or within the specimens. A corner crack propagates as a circular crack, i.e., $a = c$. Surface and embedded cracks are assumed to be elliptical with a constant aspect ratio of $a/c = 0.5$ throughout the entire crack propagation stage.
- The material properties are known and taken as the expected values defined in Chapter 4 for the HAZ.
- The stress intensity factors, K_i, are determined using the correction factors, β, defined in equations (6.9) to (6.15).
- The final crack size, a_f, is taken as the crack size at which it is equal to the specimen thickness, t (and width, W), for a corner crack, when it reaches the corners for a surface crack, or when it reaches the surface for an embedded crack.

Four parameters are considered with two or three characteristic values each. These are:

- Initial discontinuity: 1) crack, 2) spherical flaw, 3) no discontinuity
- Initial flaw or crack size: 1) 0.1 mm, 2) 1.0 mm
- Small crack sizes: 1) ΔK_{th} considered, 2) $\Delta K_{th} = 0$
- Residual stresses during crack propagation: 1) crack closure not considered, 2) crack closure considered, i.e., ΔK is replaced by ΔK_{eff} in equation (2.9).

The combination of all these conditions results in 20 basic approaches, which are summarized in Table 6.1. The following coding for the approach designation is adopted:

- **C** for a crack, **F** for a spherical flaw, **N** for no discontinuity
- **01** for $a_{init} = 0.1$ mm, **10** for $a_{init} = 1.0$ mm, and **00** if no discontinuity
- **L** if ΔK_{th} considered (large crack), **S** if $\Delta K_{th} = 0$ (small crack)
- **N** if crack closure not considered, **C** if crack closure and thus residual stresses considered

Table 6.1 *– Summary of the 20 proposed deterministic models.*

Approach Designation	**Shape**		***a***		ΔK_{th}		σ_{res}	
	Crack	**Flaw**	**0.1 mm**	**1.0 mm**	**> 0**	**= 0**	**No**	**Yes**
C01LN	X		X		X		X	
C01LC	X		X		X			X
C01SN	X		X			X	X	
C01SC	X		X			X		X
C10LN	X			X	X		X	
C10LC	X			X	X			X
C10SN	X			X		X	X	
C10SC	X			X		X		X
F01LN		X	X		X		X	
F01LC		X	X		X			X
F01SN		X	X			X	X	
F01SC		X	X			X		X
F10LN		X		X	X		X	
F10LC		X		X	X			X
F10SN		X		X		X	X	
F10SC		X		X		X		X
N00LN	---	---	---	---	X		X	
N00LC	---	---	---	---	X			X
N00SN	---	---	---	---		X	X	
N00SC	---	---	---	---		X		X

6.4 Finite Element Analyses

6.4.1 Introduction

The finite element software ANSYS was used to determine the local stresses and strains around weld flaws. These stresses and strains are used in equation (2.5) for the calculation of the crack initiation life.

First, the stress distribution in the entire specimen was obtained from a global model to determine the locations of stress concentration. This is presented in Section 6.4.2. Section 6.4.3 presents the refined mesh models that were generated to determine the magnitude of the stresses and strains to be used in equation (2.5). Different levels of stresses, resulting from a combination of the external force and residual stresses, were introduced as described in Section 6.4.4. Finally, the analysis results for all the investigated combinations of flaw sizes and locations, as well as applied and residual stresses are summarized in Section 6.4.5.

6.4.2 Global Finite Element Model

The stress distribution at the critical location of the specimens was determined using a finite element analysis of the entire specimen. Figure 6.2 shows the dimensions of the global finite element model. Only one quarter of a specimen needed to be modeled because of the two planes of symmetry that were assumed: one at the centre of the specimen in the longitudinal direction (negative y-plane) and one in the transverse direction at mid-length (positive x-plane). As stated in Chapter 5 the specimens were not perfectly straight prior to testing. However, due to the non-uniform thickness resulting from hand grinding of the weld the initial deformation could not be accurately measured. Therefore, the initial deformation was analytically established by matching the strains in the model to the extensometer measurements presented in Chapter 5. A parabolic curvature with a maximum deformation of 0.2 mm in the positive z-direction at mid-length of the specimen was assumed. Applying a tensile force, the curvature resulted in an increase of the stresses on the ground face of the specimen due to bending. The weld profile was modeled with an arc of a circle having an arc height of 5 mm and a projected arc length of 40 mm. Based on rough measurements this shape was deemed to most appropriately represent the actual weld profiles. No local imperfections, such as an undercut, were introduced.

A 20-node solid element (Solid95) was used. This element is capable of modeling curved shapes such as the transition radius from the grip section to the reduced test section and the weld profile. The element size was varied from 5.0 mm in the grip area to 2.0 mm in the reduced section, resulting in a model with 2009 elements. Planes of symmetry were introduced in the longitudinal (positive x-plane) and transverse directions (negative y-plane), as shown in Figure 6.2. The nodes were fixed in the thickness direction (z-direction). A uniform load of 56 kN in total (due to the symmetry of the model half the

maximum applied test load, see Chapter 5) was applied to all nodes on the vertical end area of the specimen (the negative x-plane). The nonlinear plastic material behaviour was introduced using a multi-linear isotropic hardening model[1] based on the modulus of elasticity, E, and the Ramberg-Osgood parameters, K' and n', defined in Section 4.3.6. Poisson's ratio for steel, $\upsilon = 0.3$, was used for all calculations. Figure 6.3 shows the mesh of the global finite element model.

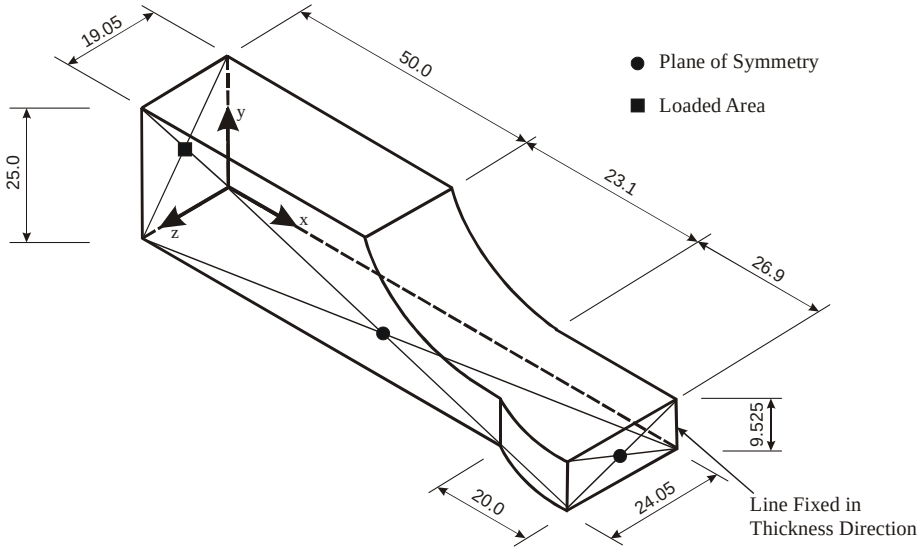

Figure 6.2 *– Dimensions and boundary conditions of the global finite element model.*

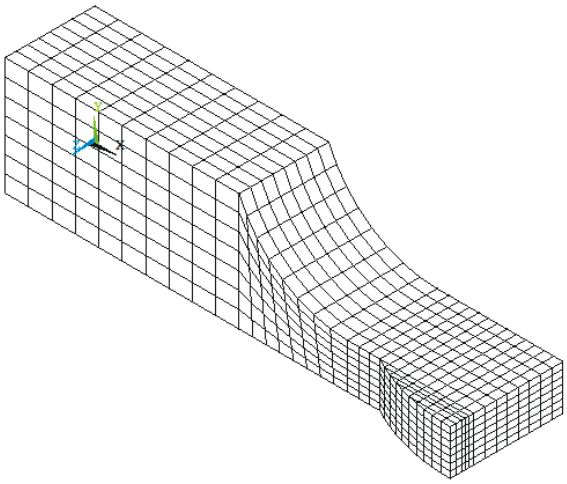

Figure 6.3 *– Global finite element model.*

[1] Since there is no strain reversal and the overall strains are rather small in the tested specimens, it is appropriate to use an isotropic hardening model. The implementation of a more complex kinematic hardening model is thus not warranted.

The longitudinal stresses obtained with this model under the maximum applied load of $P_{max} = 56$ kN are shown in Figure 6.4. The governing stresses on the ground surface at mid-length and at the toe of the weld are 400 MPa and 360 MPa, respectively. As observed in the tests, this suggests that it is more likely to have a crack initiating on the ground face than at the toe of the weld.

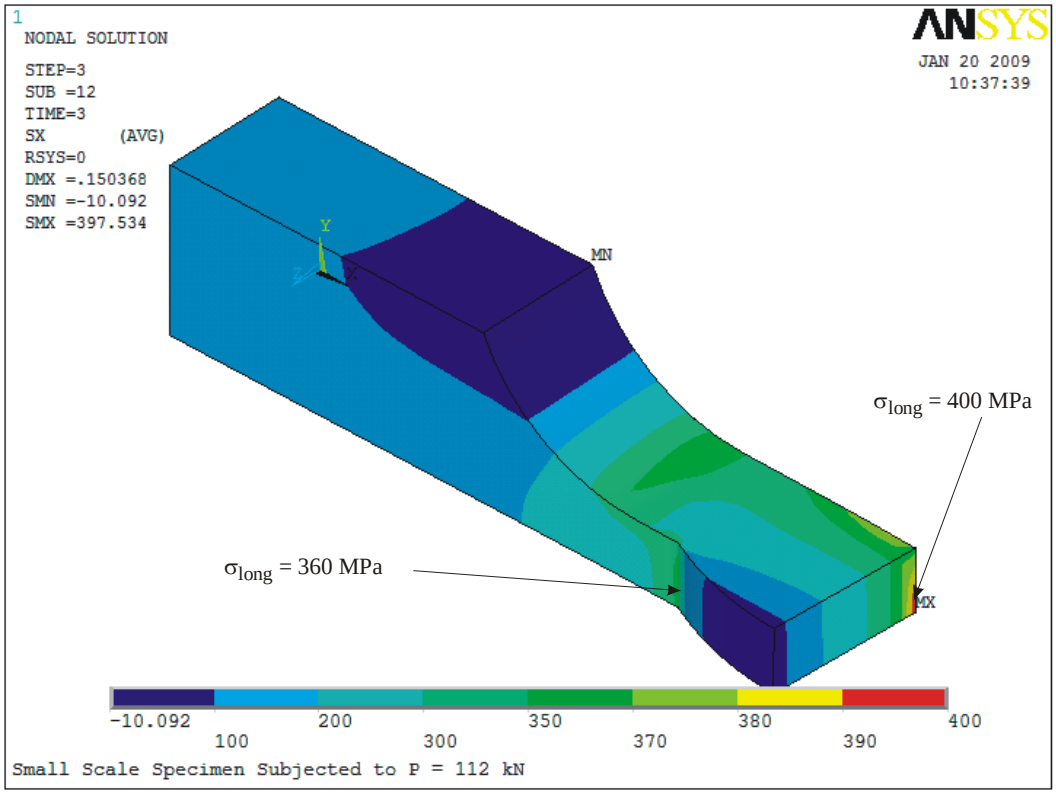

***Figure 6.4** – Longitudinal stresses under $P_{max} = 112$ kN.*

6.4.3 Local Finite Element Models

Due to the very small dimensions of the flaws (0.1 and 1.0 mm) compared to the specimen size, a refined mesh model was developed around the flaw. The objective of this refined mesh model was to determine the localized strains and stresses at the flaw (crack initiation site) in order to determine the fatigue initiation life. The complexity arising from geometrical imperfections and residual stresses, which were altered several times during the welding, grinding, and machining processes, render the determination of the exact governing strains and stresses in the test specimens impossible. Therefore, an independent local model where the applied loads are based on the global analysis was preferred to a more complex, but not necessarily more accurate, sub-model, which requires substantially more computational resources.

Figure 6.4 suggests that the ground flush face is the more likely crack initiation site than the weld toe. A flat surface geometry was thus assumed in the local model and no imperfections other than a weld flaw were introduced.

The applied stresses in the local models were based on the analysis results from the global model. The location of a typical weld flaw was assumed to be at exactly mid-length of the specimens. This allowed for a reduction of the size of the model due to symmetry. Figure 6.5 shows the boundary conditions (symmetry and load areas) of the local finite element models, which are the same as for the global model with an additional plane of symmetry on the z-plane at mid-thickness. Although the specimen is not symmetrical about the mid-thickness this plane of symmetry was introduced to further reduce the size of the model. The stress gradient due to the applied load is not large enough to have a significant effect on the stresses and strains at the critical location. Furthermore, due to the relatively large specimen thickness, the distance between two flaws on or 2.5 mm below opposite faces (top and bottom faces of the prism in Figure 6.5) is large enough not to result in an interaction between the flaws. These reasons justified a reduction of the model size.

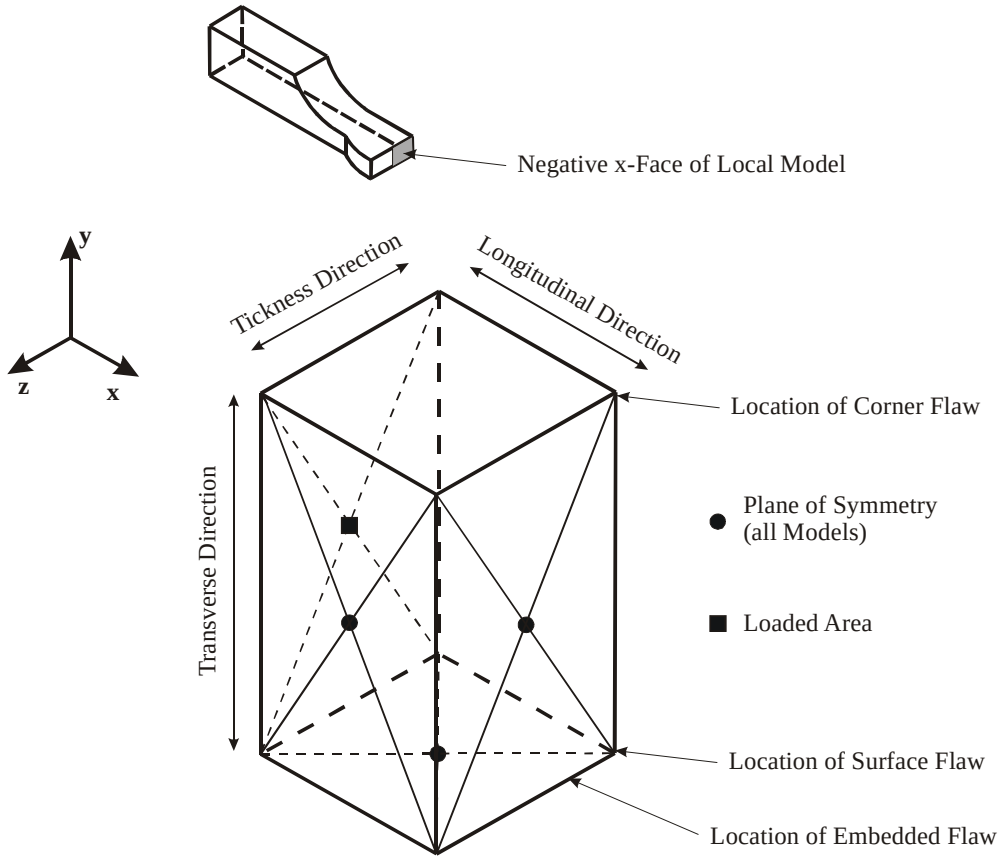

Figure 6.5 *– Schematic representation of the symmetry boundary conditions and the loaded area of the local finite element models.*

Based on Section 6.3, three initial flaw locations are considered:

- Corner flaw: The centre of the flaw is at the top of the prism (z = 0) in Figure 6.5.
- Surface flaw: The centre of the flaw is at the bottom of the prism (z = 0) in Figure 6.5.
- Embedded flaw: The flaw is 2.5 mm below the surface (z ≠ 0) at the bottom of the prism in Figure 6.5.

It is very likely that a crack in a model without a flaw (perfect weld) initiates at a corner. Thus, the boundary conditions for this case are identical to the corner flaw model.

Even with the local model, it was necessary to vary the mesh size in order to achieve computational efficiency. In a first attempt the elements were modeled by incrementally increasing the mesh size towards the flaw. The transition from the fine mesh to the coarser mesh was accomplished through multi-freedom constraints. Although the model converged during an elastic analysis, convergence was not reached during the non-linear analysis. To remedy this problem, the automatic meshing option in ANSYS was used, defining a small mesh size in the areas around the flaw and a larger mesh size in the outer areas of the model. In order to allow automatic meshing, the tetrahedral option of the 20 node solid element (Solid95) had to be specified in ANSYS, reducing the number of independent nodes per element from 20 to 9. A reference model, one without a flaw (perfect weld), was also meshed with 20 node solid elements (Solid95). However, octahedral elements could be used, keeping the number of independent nodes at 20. Different mesh sizes and configurations were investigated for each model until stable results of non-linear analyses were obtained (see Appendix E).

The adequacy of the chosen model sizes and meshes was also checked by comparing the elastic stress concentration around a centred spherical flaw resulting from a tensile surface pressure, T, to the theoretical value of $2.045T$ [Goodier 1933]. Two models, one with a 0.1 mm and one with a 1.0 mm flaw, were checked. The models were the same size as the respective local models (see Table 6.3). The flaw was introduced at the intersection of the positive x-, the negative y-, and the positive z-planes (flaw at centre of the model, which is the assumption resulting in a theoretical stress at the flaw of $2.045T$). The tensile surface pressure, T, was applied at the negative x-plane. The results of this comparison are shown in Table 6.2. Both final meshes showed elastic stress agreement within 1% of the theoretical value.

Figure 6.6 shows the local models with respect to the global model. The local finite element models for the two flaw sizes (1.0 and 0.1 mm) and two flaw locations (surface and embedded) are illustrated in Figure 6.7. The mesh for the corner crack models, which are not shown in Figure 6.7, is identical to the surface flaw models, but with the flaw at the top (see Figure 6.5). The model size, the element size around the flaws as well as the maximum element size in the outer areas, and the total number of elements for each model are summarized in Table 6.3.

Table 6.2 *– Comparison of theoretical elastic peak stresses at the flaws and stresses obtained from the chosen local FE-models.*

Flaw size	Theoretical Elastic Peak Stress	Elastic Peak Stress from Local FE-Model	Relative Difference
0.1 mm	$2.045 \cdot T$	$2.034 \cdot T$	0.54%
1.0 mm	$2.045 \cdot T$	$2.047 \cdot T$	0.10%

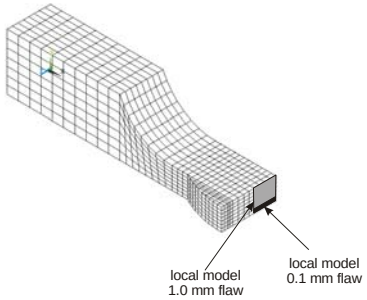

Figure 6.6 *– Location of local models in the global model.*

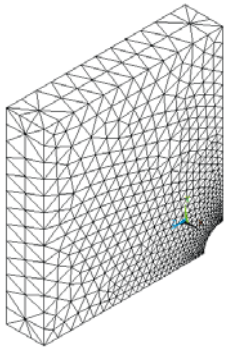

a) 1.0 mm surface flaw

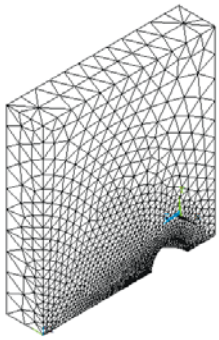

b) 1.0 mm embedded flaw

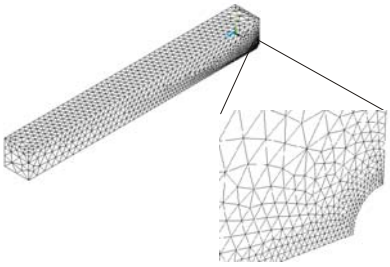

c) 0.1 mm surface flaw

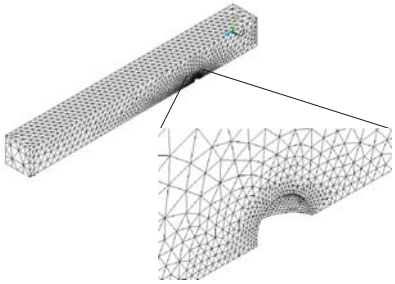

d) 0.1 mm embedded flaw

Figure 6.7 *– Local finite element models.*

Table 6.3 *– Mesh sizes and number of elements used in the five local models.*

Flaw	Model Size $B \times T \times L$ [mm]	Mesh Size [mm]		Number of	
		Around Flaw	Outer Areas	Nodes	Elements
No flaw	10.0×9.525×2.0	0.60 everywhere		5639	1088
1.0 mm surface/corner	10.0×9.525×2.0	0.10	0.80	30357	20094
1.0 mm embedded	10.0×9.525×2.0	0.10	0.80	33938	22224
0.1 mm surface/corner	1.0×9.525×1.0	0.010	0.20	42944	28159
0.1 mm embedded	1.0×9.525×1.0	0.010	0.30	48845	32279

B: Dimension in transverse direction of plate (y-dir. in Figure 6.5)
T: Thickness (z-dir. in Figure 6.5)
L: Dimension in longitudinal direction of plate (x-dir. in Figure 6.5)

The same inelastic material model as for the global model was used. Poisson's ratio for steel, $\upsilon = 0.3$, was specified in all the models.

6.4.4 Application of External Load and Residual Stresses

The specimens are subjected to stresses from an external source (the testing machine), which are superimposed to a residual stress field. These stresses are applied in the finite element models as surface pressures on the negative x-plane.

Welding residual stresses as well as residual stresses due to peening were applied to the local models. The residual stresses, which are in self-equilibrium within the global model, are applied as external loads on the negative x-plane, acting in the same direction as the stresses from the testing machine. Three different surface pressure distributions, as shown in Figure 6.8, were investigated on the 0.1 mm surface flaw model: 1) two rectangular stress blocks, one tension and one compression; 2) a single stress gradient with identical stress magnitude but opposite signs at the top and bottom of the local model; 3) two mirror-imaged stress gradients with identical stress magnitude at the top, mid-thickness and bottom of the model, having an opposite sign at mid-thickness with respect to the top and bottom.

All three distributions resulted in the same strain amplitude and in maximum stresses that were within 2% of one another (the highest stresses were obtained with the rectangular stress block (distribution 1) and the lowest with the double gradient (distribution 3)). It is therefore safe to assume that the exact residual stress gradient is not critical for the determination of the governing strains and stresses in the local model. Furthermore, any inelastic cyclic localized deformation will change the residual stress distribution around

the flaw. Based on these observations, the residual stress distribution 2 was adopted for all models, since it corresponds best to the residual stress distributions reviewed in Chapter 3. For the non-peened specimens tension was applied at the top and compression at the bottom of the model. Conversely, compression was applied at the top and tension at the bottom for the peened specimens.

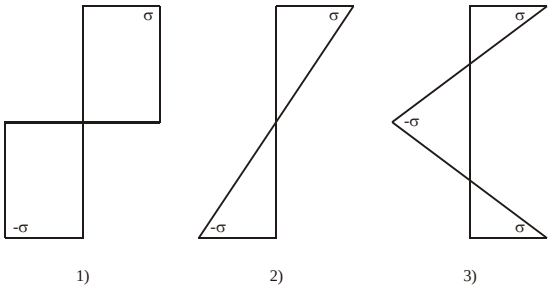

***Figure 6.8** – Investigated pressure distributions to model residual stresses.*

The first load step of the analysis consists of applying the residual stresses[1]. The stresses from the externally applied load are then introduced in the second time step, using the results from the analysis of the entire specimen (see Section 6.4.2). In the second time step, the model is fully loaded to the maximum test load (112 kN). The load is then reduced in time step 3 to the minimum test load (11.2 kN). Finally, the model is reloaded in time step 4 to the maximum load. After time steps 3 and 4, the strains in the x-direction at the critical locations are read from the output files. The difference between these strains corresponds to the governing strain range, $\Delta\varepsilon$, that the specimen is subjected to. This strain range has to be divided by 2 in order to get the strain amplitude, $\Delta\varepsilon/2$, needed in equation (2.5). In addition to $\Delta\varepsilon/2$, the maximum stress in the x-direction at the same location after time step 4, σ_{max}, is also obtained from the output files to introduce in equation (2.5). At time step 3 some models experience compressive strains, therefore changing the direction of the principal strains. Hence, using the principal strains could result in erroneous results and it is more accurate to use the longitudinal (x-direction) strains and stresses in the determination of the fatigue initiation life. At maximum load (time step 4) the x-direction strains and stresses are within 1% of the principal strains and stresses for all models.

6.4.5 Results

All small scale tests were carried out at the same load range and ratio. The maximum and minimum loads were 112 kN and 11.2 kN, respectively. The resulting longitudinal

[1] Due to the relatively short dimension of the models in the x-direction, the desired residual stresses at the critical location (flaw on positive x-plane) could be obtained by introducing these desired stresses on the negative x-plane (i.e., practically no redistribution of the stresses occurred from the negative to the positive x-plane).

stresses on the ground surface of the specimens (intersection of positive x-plane and negative z-plane in global and local models) and at mid-thickness of the specimens (intersection of positive x-plane and positvie z-plane in local model) obtained from the global model are presented in Table 6.4. It is noted that, due to the non-linear material response, the stress ratio is not the same as the load ratio.

Table 6.4 *– x-direction stresses at ground surface and mid-thickness of the specimens due to the applied test loads, P.*

Location	***P* = 112 kN**	***P* = 11.2 kN**
Ground Surface	400 MPa	30 MPa
Mid-Thickness	290 MPa	30 MPa

Because the test specimens were small it is expected that some of the initial residual stresses were relieved during the machining process and therefore will be significantly less than the yield strength of the material. From the observations made in Chapter 5 it is also expected that ultrasonic peening will introduce higher compressive residual stresses than needle peening. Therefore, each model was analysed with four different residual stress distributions, σ_{res}: 1) tensile stress of 100 MPa at the surface (intersection of positive x-plane and negative z-plane), corresponding to an expected upper bound residual stress field for the non-treated specimens; 2) no residual stress field, corresponding to an expected lower bound residual stress field for the non-treated specimens and to a reasonable stress field for the stress relieved specimens; 3) compressive stress of -100 MPa at the surface, corresponding to a lower bound stress field for the conventionally peened specimens; and 4) compressive stress of -200 MPa at the surface, corresponding to an upper bound residual stress field for the conventionally peened and lower bound stress field for the ultrasonically peened specimens.

Models without a Flaw

The governing longitudinal strain amplitudes, $\Delta\varepsilon/2$, as well as the maximum longitudinal stresses after time step 4, $\sigma_{\max}$, for each of the models without a flaw are presented in Table 6.5. The strains and stresses were obtained at the most highly stressed node in the absence of residual stresses, i.e., at the node where the positive x-, the positive y-, and the negative z-planes intersect.

Table 6.5 *– Governing longitudinal strain amplitudes, $\Delta\varepsilon/2$, and maximum stresses, σ_{max}, for model without flaw.*

σ_{res}	$\Delta\varepsilon/2$	σ_{max}
100 MPa	8.92×10^{-4}	496 MPa
0 MPa	8.92×10^{-4}	397 MPa
-100 MPa	8.92×10^{-4}	301 MPa
-200 MPa	8.92×10^{-4}	200 MPa

Models with 0.1 mm Flaw

The governing longitudinal strain amplitudes, $\Delta\varepsilon/2$, as well as the maximum longitudinal stresses, σ_{max}, for each of the models with a 0.1 mm flaw are presented in Table 6.6 for a model with a corner flaw and in Table 6.7 for a model with a surface flaw, and in Table 6.8 for a model with an embedded flaw. The strains and stresses were obtained taking an average of all the outputs of the nodes delimiting the flaw on the positive x-plane.

Table 6.6 *– Governing longitudinal strain amplitudes, $\Delta\varepsilon/2$, and maximum stresses, σ_{max}, for a model with a 0.1 mm corner flaw.*

σ_{res}	$\Delta\varepsilon/2$	σ_{max}
100 MPa	1.74×10^{-3}	537 MPa
0 MPa	1.74×10^{-3}	470 MPa
-100 MPa	1.74×10^{-3}	443 MPa
-200 MPa	1.74×10^{-3}	396 MPa

Table 6.7 *– Governing longitudinal strain amplitudes, $\Delta\varepsilon/2$, and maximum stresses, σ_{max}, for a model with a 0.1 mm surface flaw.*

σ_{res}	$\Delta\varepsilon/2$	σ_{max}
100 MPa	1.62×10^{-3}	516 MPa
0 MPa	1.62×10^{-3}	484 MPa
-100 MPa	1.62×10^{-3}	459 MPa
-200 MPa	1.62×10^{-3}	390 MPa

Table 6.8 *– Governing longitudinal strain amplitudes, $\Delta\varepsilon/2$, and maximum stresses, σ_{max}, for a model with a 0.1 mm embedded flaw.*

σ_{res}	$\Delta\varepsilon/2$	σ_{max}
100 MPa	1.48×10^{-3}	502 MPa
0 MPa	1.48×10^{-3}	487 MPa
-100 MPa	1.48×10^{-3}	471 MPa
-200 MPa	1.48×10^{-3}	450 MPa

Models with 1.0 mm Flaw

The governing longitudinal strain amplitudes, $\Delta\varepsilon/2$, as well as the maximum longitudinal stresses, σ_{max}, for each of the models with a 1.0 mm flaw are presented in Table 6.9 for a model with a corner flaw, in Table 6.10 for a model with a surface flaw, and in Table 6.11 for a model with an embedded flaw. The strains and stresses were obtained taking an average of all the outputs of the nodes delimiting the flaw on the positive x-plane.

Table 6.9 *– Governing longitudinal strain amplitudes, $\Delta\varepsilon/2$, and maximum stresses, σ_{max}, for a model with a 1.0 mm corner flaw.*

σ_{res}	$\Delta\varepsilon/2$	σ_{max}
100 MPa	2.03×10^{-3}	558 MPa
0 MPa	2.03×10^{-3}	479 MPa
-100 MPa	2.03×10^{-3}	456 MPa
-200 MPa	2.03×10^{-3}	432 MPa

Table 6.10 *– Governing longitudinal strain amplitudes, $\Delta\varepsilon/2$, and maximum stresses, σ_{max}, for a model with a 1.0 mm surface flaw.*

σ_{res}	$\Delta\varepsilon/2$	σ_{max}
100 MPa	1.84×10^{-3}	532 MPa
0 MPa	1.84×10^{-3}	491 MPa
-100 MPa	1.84×10^{-3}	472 MPa
-200 MPa	1.84×10^{-3}	435 MPa

Table 6.11 *– Governing longitudinal strain amplitudes, $\Delta\varepsilon/2$, and maximum stresses, σ_{max} , for a model with a 1.0 mm embedded flaw.*

σ_{res}	$\Delta\varepsilon/2$	σ_{max}
100 MPa	1.70×10^{-3}	521 MPa
0 MPa	1.70×10^{-3}	501 MPa
-100 MPa	1.70×10^{-3}	484 MPa
-200 MPa	1.70×10^{-3}	464 MPa

These strain amplitudes and maximum stresses are used in the fatigue life predictions carried out in the next section. A discussion and interpretation of the finite element results is presented in Chapter 7 where the predictions will be validated through probabilistic analyses.

6.5 Fatigue Life Predictions of Tested Specimens

The fatigue life of the tested specimens is predicted using the general approaches outlined in Section 6.3 and the finite element results obtained in Section 6.4. The case of a welded joint with no inclusions is first examined. Welded joints with a surface or corner flaw, as well as joints with a surface or corner crack are then investigated. The literature review in Chapter 3 showed that for non-peened welds these imperfections are the more likely initiation sites than embedded flaws. Nevertheless, due to the introduction of compressive residual stresses at the surface (and thus tensile residual stresses within) and plastic deformation of surface flaws, making them less innocuous, an embedded flaw might become the prevailing imperfection for the peened specimens. Therefore, the fatigue life for embedded flaws or cracks of peened specimens was also investigated.

In all the crack propagation calculations that include crack closure, a simplified constant residual stress field of 100 MPa (tension) through the thickness or no residual stresses are assumed for the non-peened specimens. The constant tensile residual stress field does not respect equilibrium. It was nevertheless chosen as a conservative approach because it is expected that residual stresses relax with crack growth (see Chapter 3), hence potentially eliminating compressive residual stresses within the specimens. For the peened specimens a linear residual stress distribution is assumed with the specified residual stress at the surface (-200 MPa and -100 MPa, respectively) and a tensile stress of 100 MPa at 2.525 mm below the surface (centre of embedded flaws).

The global finite element model showed that the maximum stresses due to the externally applied force first decrease from 400 MPa on the ground surface to 290 MPa at mid-thickness, and increase again to approximately 380 MPa at the weld toe. Since a linearly

varying stress is assumed through the thickness of the model, a slightly higher stress of 300 MPa is introduced at mid-thickness under maximum load in order to take into account the increase in stress from mid-thickness to the weld toe. The stress gradient coefficient A in equations (6.14) and (6.15) is therefore always equal to -0.0262 at maximum load. The stresses resulting from the minimum applied load are uniform at 30 MPa through the entire cross-section, i.e., $A = 0.0$.

A sample calculation incorporating crack closure and the threshold stress intensity factor range, ΔK_{th} , for an ultrasonically peened specimen with a 1.0 mm surface flaw (residual stress of -200 MPa surface) is shown in Appendix F. This example was chosen because it incorporates all the complexities of the calculations that are involved in fatigue life predictions.

The results of the fatigue life predictions for each model are given in Appendix G. These results are discussed in the following section.

6.6 Discussion of Analytical Results

The shortest and longest fatigue lives of the non-peened models are 14,000 cycles (C10LN-E and C10SN-E with 0 or 100 MPa peak residual stress) and 2.11 million cycles (N00LC and N00SC with no residual stress). The two non-treated specimens failed after 213,000 and 327,000 cycles (see Chapter 5). The stress-relieved specimens failed after 229,000 and 226,000 cycles. As stated in the introduction to this chapter, the test results for the non-peened (non-treated and stress-relieved) specimens lie between the two extreme predictions.

The fatigue life predictions from the peened models are between 25,000 cycles (C10LC-S with a surface residual stress of -100 MPa) and infinity (specimen with no flaw and a surface residual stress of -200 MPa). The two conventionally peened specimens failed after 493,000 and 1,240,000 cycles. The ultrasonically peened specimens did not fail at all. Again, the test results are encompassed by the chosen models.

The crack initiated in all four non-peened test specimens on the ground or the weld-toe surface. Comparing the theoretical predictions for specimens with a surface flaw (no inclusion, 0.1 mm inclusion, 1.0 mm inclusion) in the non-peened welds to the actual test results of these four tests, it is evident that all models with no inclusion overestimate the fatigue life (N_{tot} > 550,000 cycles). Likewise, all models with flaws and especially the models with cracks underestimate the fatigue life (N_{tot} < 150 ,000 cycles). The best prediction is obtained from the model with a 0.1 mm flaw and no residual stress, including crack closure and the threshold stress intensity factor range, ΔK_{th} ($N_{tot} = 142{,}000$ cycles).

The calculations for specimens with an embedded flaw show that the life of these non-peened specimens is very similar to those with a surface and corner crack. Since the probability of having a critical embedded discontinuity is smaller than having a critical

discontinuity on the surface (see Chapter 3), it is very unlikely that a crack initiates within the weld, unless the weld is peened.

Both conventionally peened specimens failed from cracks initiating at a corner. As for the non-peened specimens, models with 1.0 mm flaws underestimate the fatigue life (N_{tot} < 100,000 cycles) and the models with no flaw overestimate the fatigue life (N_{tot} > 10 million cycles). The most realistic predictions of the conventionally peened specimens are (as for the non-peened specimens) obtained with the 0.1 mm flaw model that includes crack closure and the threshold stress intensity factor range, ΔK_{th}. The predicted fatigue lives with this model are 450,000 cycles for a residual stress of -100 MPa and 1.1 million cycles for a residual stress of -200 MPa.

Fatigue run-outs, i.e., fatigue lives over 10 million cycles, are only obtained for peened models without a flaw. However, extrapolating the fatigue life predictions for the models with a 0.1 mm corner flaw and either no residual stresses, compressive residual stresses of -100, and compressive residual stresses of -200 MPa run-outs are expected for compressive residual stresses of approximately -350 MPa. This suggests that for the ultrasonically peened specimens, where the compressive residual stresses are expected to be close to the yield strength of the material (see Chapter 3), a model with a 0.1 mm flaw will result in good predictions.

Generally, it is observed that the fatigue initiation life for the models with weld flaws is short compared to the crack propagation life (generally less than 20%). However, the crack initiation life is never insignificant.

6.7 Summary

The fatigue life of the small scale specimens with the weld profile left in place, which were tested in Chapter 5, were predicted in this chapter. Several deterministic approaches and models were considered:

- perfect weld, weld with spherical flaw, and weld with a crack;
- initial crack/flaw size of 0.1 mm and 1.0 mm;
- considering the threshold stress intensity factor range, ΔK_{th}, and neglecting ΔK_{th} (small crack theory);
- considering residual stresses during the crack propagation stage through integration of the crack closure model and neglecting residual stresses during the crack propagation stage;
- applying four levels of residual stresses at the surface of the specimens: 100 MPa, 0 MPa, -100 MPa, and -200 MPa.

The fatigue life predictions were presented for perfect welds (welds with no flaws or cracks) and for welds with corner, surface, and embedded flaws or cracks. This resulted in 160 predictions for the four sets of tested specimens. The governing strain amplitudes

and maximum stresses were determined from finite element analysis. Finite element analysis results from a global model of the entire specimen were used to define the applied stresses (from the test load) in local finite element models and for the crack propagation calculations.

All test results are encompassed by the selected models. For the failed specimens it was shown that the models with no flaw result in a significant overestimation of the fatigue life. On the other hand, the models with a 1.0 mm flaw or crack significantly underestimated the fatigue life. Based on the analytical results it was found that an initial spherical flaw size of 0.1 mm and an approach accounting for crack closure and ΔK_{th} leads to the most accurate predictions of the fatigue resistance of the tested specimens. This correlates well to the inclusion sizes measured in Chapter 5, where 0.3 mm diameter inclusions were reported, which corresponds to a flaw size of 0.15 mm.

Crack initiation life was found to be substantially smaller than the propagation life for the specimens without an initial discontinuity or with an initial flaw. However, it was never negligible.

A discussion of the strain amplitudes and maximum stresses found from the refined mesh models is presented in Chapter 7, where the predictions will be validated through probabilistic analyses.

7. VALIDATION OF FATIGUE PREDICTION MODELS THROUGH PROBABILISTIC ANALYSIS

7.1 Introduction

In this chapter, the deterministic models proposed in Chapter 6 are validated through probabilistic analyses. The background information (Chapter 2) and the literature review (Chapter 3) have shown that fatigue life predictions are subject to significant uncertainties and can only be reliably predicted through probabilistic approaches. First, the two reliability solution methods, Monte Carlo Simulation and First Order Reliability Method, which are used in the present study, are outlined in Section 7.2. Several of the models proposed in Chapter 6 result in reasonable predictions of the fatigue life. However, for probabilistic fatigue life predictions to be practical, only one should be retained. The choice of the most appropriate fatigue life prediction model based on the investigation presented in Chapter 6 and some additional considerations is presented in Section 7.3. In the previous chapters probabilistic modeling of many parameters has been introduced. Section 7.4 recapitulates these models and reflects on useful modifications of the defined probabilistic distributions. Using these probabilistic distributions, results of Monte Carlo Simulations for the probabilistic fatigue life predictions of each test specimen from Chapter 6 are presented in Section 7.5. In section 7.6 a sensitivity analysis is used to select and calibrate the most influential parameters for crack initiation and propagation life prediction. It should be understood that this calibration is not very representative because of the limited amount of test results it is based on. Nevertheless, the procedure shown here is applicable to any probabilistic prediction of test results and is therefore merited to be outlined.

7.2 Reliability Methods

7.2.1 Introduction

The fatigue limit state function used in the present study can be expressed as:

$$\begin{aligned} G(\mathbf{Z}) &= N_{total}(\mathbf{Z}) - N_{\mathbf{S}}(\mathbf{Z}) = N_{init}(\mathbf{Z_{init}}) + N_{prop}(\mathbf{Z_{prop}}) - N(\mathbf{Z_S}) \\ &= \int f_{\mathbf{Z}}(\mathbf{z_{init}})\mathrm{d}\mathbf{z_{init}} + \int f_{\mathbf{Z}}(\mathbf{z_{prop}})\mathrm{d}\mathbf{z_{prop}} - \int f_{\mathbf{Z}}(\mathbf{z}_S)\mathrm{d}\mathbf{z}_S \end{aligned} \tag{7.1}$$

The first two terms in equation (7.1) correspond to the resistance, R. The last term, $N(\mathbf{Z_S})$, is a measure of the applied load (or solicitation, S), e.g. number of truck passages on a bridge. Recall from Section 2.4.2 that the limit state is violated, i.e., failure occurs, when $G(\mathbf{Z}) < 0$.

As shown in Chapter 2 both the fatigue crack initiation life, N_{init}, and the fatigue crack propagation life, N_{prop}, have to be determined numerically, making the limit state

function very complex. Direct integration of equation (7.1) is impossible and numerical methods need to be applied. Solution methods employing Monte Carlo Simulation (MCS) and First Order Reliability Method (FORM) are discussed in the following. These two methods are most commonly used in structural engineering applications [Ang & Tang 1984, Melchers 1999]. The more intuitive method, the Monte Carlo Simulation method, is described in Section 7.2.2. A brief theoretical outline of the First Order Reliability Method is then presented in Section 7.2.3. For both methods, subroutines to solve the limit state function were developed using the commercially available software MATLAB®. Some information concerning the implementation of the two methods into MATLAB and their suitability to solve the limit state function are given in Section 7.2.4. For more information about Monte Carlo Simulation and the First Order Reliability Method the reader is referred to Ang & Tang [1984], Melchers [1999], and Haldar & Mahadevan [2000].

7.2.2 Monte Carlo Simulation (MCS)

Monte Carlo Simulation (MCS) is a method in which the limit state function is solved numerous times using randomly generated values of the parameters that define the limit state function. The randomly generated parameter values are based on the probability distributions of each parameter. One solution cycle is commonly referred to as a simulation. If the number of simulations is large enough, a stable distribution of the limit state function $G(\mathbf{Z})$ is obtained. According to the central limit theorem, a normal distribution of $G(\mathbf{Z})$ can then be expected.

Figure 7.1 illustrates the random sampling process from a probabilistic distribution of a variable. A random number, u_{11}, between 0 and 1 is generated for the first random variable (the index 11 stands for first simulation and first random variable). Generally, it is assumed that the random number follows a uniform distribution. Therefore, the cumulative distribution function, CDF, is linear with $F_U(u_{11}) = u_{11}$. Setting $F_U(u_{11}) = u_{11}$ equal to the CDF of the first random variable, $F_{Z_1}(z_{11})$, a unique parameter value for z_1 is obtained, $z_{11} = F_Z^{-1}(u_{11})$. Repeating this process for each random variable yields a set of parameter values for the first simulation, $\mathbf{Z}_1$, that are introduced into the limit state function. Solving the limit state function then gives one simulation result, $G(\mathbf{Z}_1)$. The entire process is repeated as often as needed to get stable results, i.e., a stable mean value and standard deviation of $G(\mathbf{Z}) = G(\mathbf{Z}_1, \mathbf{Z}_2, ..., \mathbf{Z}_n)$. MCS therefore simulates a large number of experiments, without incurring the high cost associated with testing. The simulation process assures that the distribution of the parameter values of each random variable follows the assumed probabilistic distribution. Therefore representative sampling is carried out.

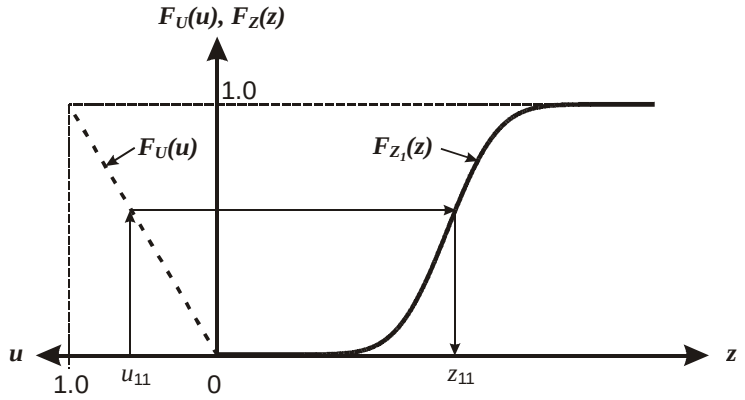

Figure 7.1 *– Procedure for random sampling of probabilistic variables in MCS.*

For complex limit state functions, a large number of simulations is needed to achieve stability. In such cases it is often beneficial to reduce the number of simulations. In a reliability problem, the region with $G(\mathbf{Z}) \leq 0$ is often the only region of interest. With an approach that guarantees results close to and smaller than $G(\mathbf{Z}) = 0$ the number of simulations can be drastically reduced. However, finding such an approach is not straight forward. Different methods of importance sampling have been developed. Most of them aim at reducing the variance of the simulation. Since the entire distribution of $N_{total}(\mathbf{Z})$ is of interest in the present work (see Section 7.2.4) and the weight of each parameter is not known a priori, importance sampling is not needed. Furthermore, in view of the modest computation time needed to run the simulations (see Section 7.2.4), importance sampling would not result in significant savings.

The crack propagation model used here can result in negative values of the term $\Delta K_{eff}{}^{m} - \Delta K_{th}{}^{m}$ in equation (2.9). Such negative values indicate that there is no crack growth and therefore the fatigue life is infinite. To be consistent with fatigue testing, where specimens that have not failed after 10 million cycles are generally treated as run-outs, the maximum number of cycles to failure in a simulation is limited to 10,000,000.

7.2.3 First Order Reliability Method (FORM)

It was shown in Chapter 2 that the probability of failure, p_f, can be expressed as a function of the safety index, β. For the basic reliability problem it was further demonstrated that $\beta = \mu_Z / \sigma_Z$. For more complex reliability problems, the mean, μ_Z, and standard deviation, σ_Z, of the limit state function are not easy to determine. FORM uses an algorithm to find μ_Z and σ_Z. The random variables, $\mathbf{Z}$, are first transformed into standard normal variables, $\mathbf{X}$, i.e., all variables have a mean, $\mu_{\mathbf{X}} = 0$, and a standard deviation, $\sigma_{\mathbf{X}} = 1.0$. With this transformation, β simply becomes the distance from the transformed origin to the failure surface.[1] For a complex problem, the failure surface is

[1] This transformation is not strictly necessary, but facilitates the computations considerably.

not a point, but a higher dimension "surface". Therefore, an infinite number of distances from the origin to the failure surface exists. Intuitively, the governing β value is the shortest of all these distances because it results in the highest probability of failure. To facilitate the search for the shortest distance, the limit state function is linearized by retaining only the zeroth and first order terms of a Taylor series expansion. Generally, all random variables are assumed to be independent and normally distributed, i.e., the first two moments (mean and variance) fully define the distribution. This is why FORM is sometimes also referred to as the First Order Second Moment (FOSM) Reliability Method.

There are different algorithms to determine β. The Rackwitz & Fiessler [1978] algorithm is considered to be one of the more suitable methods, although it does not always converge to the correct solution or converge at all [Madsen et al. 1986]. Figure 7.2 illustrates the conceptual procedure used to determine β for a two dimensional problem. After transformation of the random variables into standard normal distributions, an initial estimate of the failure point is made. Often this point, denoted $P^{(0)}$ in Figure 7.2, is the solution of the limit state function using mean values for the random variables, i.e., $x_i = 0$. Most likely, $P^{(0)}$ does not fulfill two conditions to be the actual failure point: it does not lie on the failure surface, i.e., $P^{(0)} \notin G(\mathbf{X}) = 0$, and it is not the shortest distance from the origin, i.e., it is not perpendicular to the linearized limit state function. Using the gradient vector $dG(\mathbf{X})/d\mathbf{X}$ at point $P^{(0)}$, $P^{(0)}$ can be projected onto $G(\mathbf{X}) = 0$, as is shown in Section B-B of Figure 7.2. The gradient vector $dG(\mathbf{X})/d\mathbf{X}$ is conveniently determined numerically by successively varying the value of each variable ($x_i' = x_i + \mathrm{d}x_i$, with $\mathrm{d}x_i$ being small). A new trial point, $P^{(1)}$, can now be found by taking a parallel to the $dG(\mathbf{X})/d\mathbf{X}$ vector going through the origin. $P^{(1)}$ is still not necessarily the actual failure point, but it is closer to the failure surface than $P^{(0)}$ and also closer to being the shortest distance to the origin because it is parallel to the $dG(\mathbf{X})/d\mathbf{X}$ vector. The iterative process continues with a new $dG(\mathbf{X})/d\mathbf{X}$ vector at point $P^{(1)}$ and subsequently another trial point, $P^{(2)}$. Convergence is achieved when $P^{(n-1)} = P^{(n)}$.

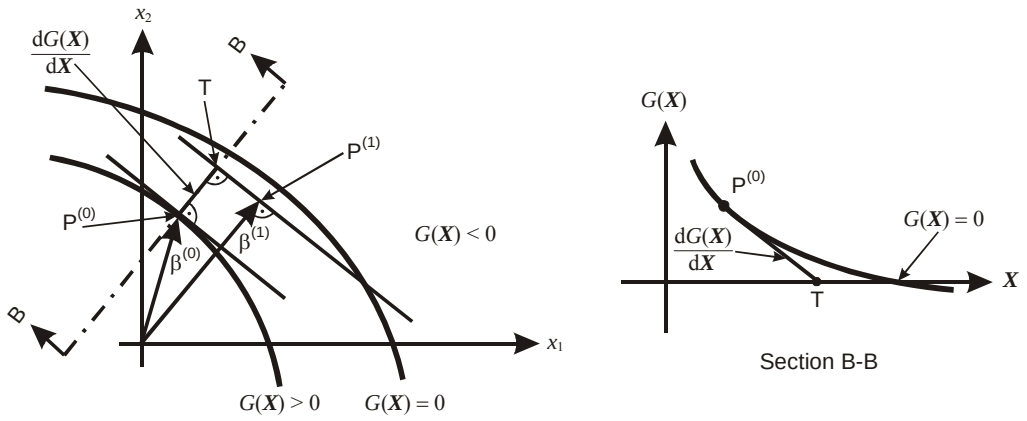

Figure 7.2 *– Concept of FORM.*

Since all random variables are normalized, the safety index can be determined after every iteration *i* by the following relationship:

$$\beta^{(i)} = \left(\mathbf{x}^{(i)T}\mathbf{x}^{(i)}\right) = \sqrt{\sum x_k^{(i)}} \tag{7.2}$$

At each iteration a direction cosine vector, $\vec{\alpha}$, is obtained by dividing the gradient vector $dG(\mathbf{X})/d\mathbf{X}$ by its magnitude. The direction cosine vector is a measure of how much the solution needs to be adapted to find a new point. The magnitude of each component of $\vec{\alpha}$ is therefore a very useful indicator of the individual weight of each random variable. A large value of the direction cosine for a variable indicates a high sensitivity of the limit state function to changes in this variable. Consequently, the variables that are most interesting to calibrate are the ones with large direction cosine values.

7.2.4 Evaluation and Implementation of MCS and FORM

MCS and FORM each have their inherent advantages and shortcomings. MCS is very easy to implement into a subroutine. It always converges to the correct solution as long as enough simulations are conducted. Furthermore, MCS does not need a transformation into standard normal variables and any probabilistic distribution can be implemented as-is. Its main disadvantage is the large number of simulations sometimes required to reach convergence, although this factor is mitigated because the method is usually programmed. FORM usually converges after a few iterations. The direction cosines provide a useful measure of importance for each variable. However, the transformation of non-normal or non-lognormal random variables into standard normal variables is not straight forward. Furthermore, due to the approximations used in the transformation process the solution to the limit state function is not exact anymore. However, the resulting error is thought to be small [Melchers 1999]. The main disadvantage of FORM is that it is not guaranteed to converge.

The goal in this chapter is to find a probabilistic distribution of cycles to failure, $N_{total}(\mathbf{Z})$, that matches as closely as possible the test results. MCS and FORM can be used to determine the probabilistic distribution of $N_{total}(\mathbf{Z})$. However, due to the complexity of the formulations, FORM often failed to converge for either the crack initiation or crack propagation life and was therefore abandoned. The calibration of the random variables in Section 7.6, which is preferably done through the direction cosines in FORM, thus had to be carried out with MCS.

Subroutines for MCS and FORM were developed using MATLAB. For MCS, 10,000 simulations required a computation time of roughly 75 seconds on a conventional laptop (1.73 GHz processor, 1024 MB RAM). The computation time for a FORM calculation that converged after nine iterations was less than a second.

7.3 Choice of Fatigue Life Prediction Model

Several fatigue life prediction models were evaluated in Chapter 6. These were:

- accounting for versus neglecting initiation life;[1]
- accounting for versus neglecting crack closure;
- accounting for versus neglecting threshold stress intensity factor range.

The calculations in Chapter 6 showed that initial flaws are likely always present. Without these initial flaws the fatigue life would be significantly longer than observed in the tests. Assuming a crack as the initial imperfection resulted in fatigue lives that – even for a small crack of 0.1 mm – were generally much shorter than observed in the tests. Therefore, an initial flaw (not a crack) should be assumed and initiation life accounted for.

The analyses in Chapter 6 also showed that the most accurate fatigue life predictions are obtained from a crack closure model – thus accounting for residual stresses – and the threshold stress intensity factor range, ΔK_{th}. Therefore crack closure and ΔK_{th} are considered in the probabilistic predictions.

The flow chart of Chapter 6 summarizing the deterministic approach to fatigue life calculation is reproduced in Figure 7.3. The parts and steps that are not retained for the probabilistic approach were removed and only the procedure used here for the probabilistic approach is shown. The procedure consists of first defining the initial flaw, the material properties, the applied loading, and the residual stresses. Then the strain amplitude, $\Delta\varepsilon/2$ and the maximum stress, $\sigma_{\max}$, at the critical location are determined considering the flaw characteristics, the cyclic stress-strain properties, the applied loading, and the residual stresses. The crack initiation life, N_{init}, is obtained from equation (2.5), using strains and stresses obtained from a finite element analysis and the fatigue initiation properties. The transitional crack size, a_{trans}, which is a function of the initial flaw size, is used as the initial crack size, a_0, in the crack propagation. The crack propagation life, N_{prop}, is determined from equation (2.9), which takes into account the material properties, the applied loading, the residual stresses and the initial and final crack sizes, a_0 and a_f. It also includes ΔK_{th} and crack closure (equations (6.6) through (6.8)). Finally, the crack initiation and propagation lives are added to obtain the total fatigue life, N_{total}.

The appropriate values for all probabilistic parameters are discussed in the next section. The stress intensity correction factors, β_i, are determined according to equations (6.9) through (6.15). Investigations of the fracture surfaces in Chapter 5 showed that the most likely crack initiation site for a non-peened specimen is on a surface (not corner) and for

[1] Three models were investigated: pre-existing crack (no crack initiation life), crack starting from a weld flaw (with crack initiation life), and detail with no flaw (with crack initiation life). The initial sizes of the cracks and flaws were the same.

a peened specimen at a corner. Therefore, a surface crack for the non-peened and a corner crack for the peened specimens were assumed.

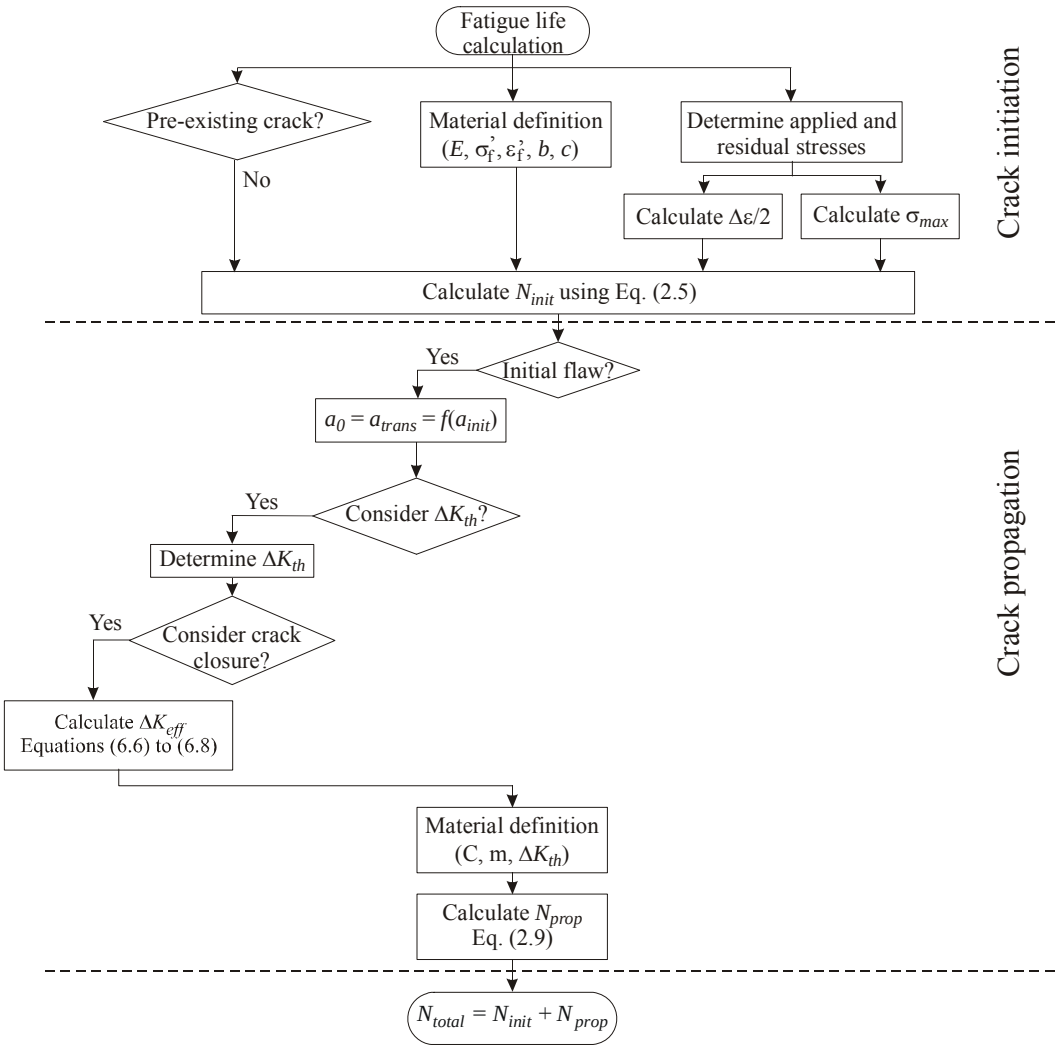

***Figure 7.3** – Flow chart of probabilistic approach.*

7.4 Probabilistic Modeling of Parameters

7.4.1 Introduction

A meaningful probabilistic prediction of fatigue life is only possible with adequate probabilistic modeling of all relevant parameters. Based on the work presented in the previous chapters, the following parameters are modeled as random variables:

- Fatigue initiation and propagation properties: E, σ_f', ε_f', C, and ΔK_{th}
- Initial flaw size and aspect ratio: a_{init} and a/c
- Transitional crack size: a_{trans}
- Final crack size: a_f
- Residual stresses (magnitude and sign): σ_{res}
- Strain amplitude and maximum stress during initiation: $\Delta\varepsilon/2$ and $\sigma_{\max}$
- Stress range during propagation: $\Delta\sigma$

With the exception of the residual stress, σ_{res}, all the parameters used in this investigation take only positive values. Furthermore, none of the parameter distributions are skewed. For these reasons it is appropriate to model E, σ_f', ε_f', C, ΔK_{th}, a_{init}, a/c, a_{trans}, a_f, $\Delta\varepsilon/2$, $\sigma_{\max}$, and $\Delta\sigma$ with a lognormal distribution, LN(μ,σ). The residual stresses, which can take positive or negative values, are represented by a normal distribution, N(μ,σ). For both the lognormal and normal distributions, μ and σ are the mean and standard deviation of the parameter, respectively.

The following presents the probabilistic models for all parameters under consideration, which will be used in the fatigue life predictions presented in Section 7.5. Modeling of some parameters was introduced in previous chapters. These models are adopted in this chapter for some of the parameters while for other parameters the models are slightly modified or redefined. The models for all parameters are summarized in section 7.4.9.

7.4.2 Fatigue Initiation and Propagation Properties

The small scale tests presented in Chapter 5 were prepared using the same weld procedure and the same base metal as the crack initiation and propagation test samples presented in Chapter 4. Therefore, the mean values found from these tests (see Chapter 4) are representative of the weld material used in this program. However, the standard deviations are increased to account for the fact that each parameter was only obtained from one series of tests. According to the literature review presented in Chapter 3, the coefficient of variation (COV) for the crack growth constant, C, can be as high as 0.6 [Cheung & Li 2003, Walbridge 2005]. The COV found from the propagation tests presented in Chapter 4 was 0.22 for the base metal, 0.12 for the weld metal, and 0.20 for the HAZ. The COV of C used in the following work was therefore taken as 0.4. Since all the specimens failed in the HAZ, the C-values for the HAZ are used for all predictions. The standard deviation for the two crack initiation properties, σ_f' and ε_f', are taken as the values proposed in Chapter 4 since no other relevant test data were found. The resulting distributions yield a COV of approximately 1.0 for the initiation life, therefore reasonably considering their variability. Based on these adjustments, the following distributions are assumed:

- σ_f': LN(630,30)
- ε_f': LN(0.34,0.07)
- C: LN(3.5×10^{-14}, 1.4×10^{-14})

The threshold stress intensity factor range, ΔK_{th}, was not determined during the crack propagation tests. The lognormal distribution, LN(60,6), proposed in Chapter 4 based on a literature review is used in the following.

7.4.3 Initial Flaw Size and Shape

The maximum measured flaw radius in the small scale specimens reported in Chapter 5 was 0.15 mm. Generally, the flaws found on the investigated fracture surfaces were 0.1 mm or smaller. Therefore a mean value for the flaw radius of 0.1 mm is representative of the expected flaw size in the small scale specimens. A standard deviation of 0.02 mm indicates that over 95% of the flaws are smaller than 0.15 mm. Although no visible flaws were detected in the two conventionally peened specimens, the indentations from the peening impacts acted as local stress raisers. According to the indentation depths reported in Chapter 3 and observed on the peened specimens, an initial surface flaw with a radius of 0.15 mm for the conventionally peened specimens and of 0.30 mm for the ultrasonically peened specimens is assumed. The same COV as for the non-peened specimens is used (COV = 0.2). The following distributions for the initial flaw size are therefore adopted here:

- non-peened: LN(0.10,0.02)
- conventionally peened: LN(0.15,0.03)
- ultrasonically peened: LN(0.30,0.06)

The aspect ratio a/c is assumed to remain constant throughout the crack propagation stage. The distribution proposed in Walbridge [2005], LN(0.5, 0.16), is used here for the non-peened specimens (surface crack). For the peened specimens a corner crack with equal crack length in both legs is assumed throughout the crack propagation stage, i.e., a/c is Det(1.0).

7.4.4 Transitional Crack Size

In the deterministic models of Chapter 6 the transitional crack size, a_{trans}, was assumed to be equal to the initial flaw size. As was explained in Chapter 2, this approach is not necessarily correct since after the initiation of a crack in a crack initiation test, some propagation life has already been consumed. Linear elastic fracture mechanics is only applicable if the initial crack size, a_0, is large enough to avoid small crack behaviour (see Chapter 2). It is therefore reasonable to assume that a_{trans} corresponds to the transition from small to large crack behaviour as defined by equation (2.10):

$$a_{trans} = a_{init} + \Delta a = \frac{a_{init}}{\left(1.12 \cdot k_t / \beta\right)^2 - 1} + a_{init} \tag{2.10}$$

wherein a_{init} is the initial flaw size, Δa is the crack extension measured from the edge of the initial flaw, σ is the applied stress, k_t is the elastic stress concentration factor at the initial flaw, and β is the product of the stress intensity correction factors.

Assuming an initial surface flaw size, a_{init}, of 0.10 mm radius as defined above for the non-peened specimens, an elastic stress concentration factor of $k_t = 2.10$ is obtained from the finite element model of Chapter 6. Equation (2.10) thus yields $a_{trans} = 0.0118$ mm. This crack size is practically equal to a_{init}.

For a surface crack in the small scale tests, an initial crack size $a_0 = 0.10$ mm yields a stress intensity factor range of $\Delta K = K_{\max} - K_{\min} = 193$ MPa$\sqrt{\text{mm}}$. This is significantly larger than ΔK_{th}, therefore assuring that in the absence of compressive residual stresses the crack propagates. Furthermore, it is practically identical to the stress intensity factor range assumed at the beginning of the propagation life of specimens investigated by Chen et al. [2005], where ΔK was taken equal to 190 MPa$\sqrt{\text{mm}}$. The initial crack size of 0.10 mm is also consistent with crack sizes proposed by Radaj & Sonsino [1998].

Based on the above observations, the initial crack size, a_0, is taken equal to the initial flaw size, a_{init}, as defined in Section 7.4.3, using the same probabilistic distributions.

7.4.5 Final Crack Size

The final crack size, $a_f = 4.76$ mm, assumed in the deterministic models of Chapter 6 for surface cracks, does not quite correspond to the crack size at failure of the specimens defined in Chapter 5 (complete severing), which tends to result in somewhat shorter predicted fatigue life. The final crack size in the deterministic models was chosen at 4.76 mm because it is the size at which a centered surface crack reaches the corners of the specimen (see Section 6.3.8). At this point the stress intensity factor formulation changes from elliptical surface crack to a through-thickness crack with an elliptical crack front. For ease of implementation of the crack propagation model into a probabilistic approach it is desirable to keep the stress intensity factor calculations for an elliptical surface crack throughout the entire propagation life. This approach, however, underestimates the crack growth rate once the crack has reached the corners. Consequently, the final crack size used in the probabilistic model has to be smaller than the specimen thickness (19.05 mm) but larger than 4.76 mm. A lognormal distribution for a_f with LN(12, 1.5) is therefore assumed. The standard deviation of 1.5 mm assures that more than 99.99% of all samples fall within the interval (4.76, 19.05).

For the peened specimens described in Chapter 6 failure was assumed at a crack length of 19.05 mm (corner crack reaches far corners), which does not quite correspond to a complete severing of the specimens. However, the examination of the fracture surfaces showed that ductile fracture, and thus a very fast crack growth rate, occurs at this stage.

Therefore, the final crack size for the peened specimens is assumed to be deterministic with $a_f = 19$ mm.

7.4.6 Residual Stresses

According to the findings presented in Chapter 6, the residual stresses for the non-peened specimens should be close to 0. The model with $\sigma_{res} = 100$ MPa (F01LC-S) resulted in a significantly shorter fatigue life prediction of 94,000 cycles, compared to the value of approximately 200,000 cycles observed in the tests. The model with no residual stresses yielded a fatigue life closer to the fatigue life observed in the tests. Therefore, the model for the non-peened specimens always assumes no residual stresses, i.e., Det(0). This is consistent with observations reported by Haibach [2006] that for small scale specimens the residual stresses due to welding are generally negligible for both the crack initiation and propagation stages.

The model for the conventionally peened specimens (F01LC-C) with $\sigma_{res} = $-100 MPa results in a fatigue life prediction of 450,000 cycles, which is roughly equal to the lower of the two test results (490,000 cycles). The model with $\sigma_{res} = $-200 MPa results in 1,130,000 cyles, which is roughly equal to the higher of the two test results (1,240,000 cycles). Thus the residual stresses are most likely somewhere between -100 and -200 MPa, including potential relaxation effects. The residual stresses due to conventional peening are modeled here with a normal distribution, N(-150, 30). The standard deviation of 30 MPa is based on findings in Walbridge [2005], who analyzed the statistical distribution of residual stresses for conventionally peened welds.

Although the parameters for the ultrasonically peened small scale specimens cannot be calibrated because they were test run-outs, it is still of interest for future reference to statistically model the expected residual stresses. Due to the apparent higher intensity of ultrasonic peening compared to conventional peening and the fact that no failures were observed in the ultrasonically peened specimens, the average residual stress at the surface has to be substantially higher than the value of $\sigma_{res} = $-150 MPa assumed for the conventional peening. Based on measurements reported by Statinikov [1997] and Kudryavtsev et al. [2005], it is expected that the residual stresses are close to the actual yield strength of the steel, which was measured to be around 450 MPa for the small scale specimens investigated here. Considering potential relaxation of the residual stresses during cyclic loading, a mean residual compressive stress value of 350 MPa is assumed in the following analysis. According to Schmidt & Bartlett [2002] the COV for the yield strength is 0.054. Therefore the following distribution is proposed for the residual stress N(-350, 20) in ultrasonically peened specimens.

For all the ultrasonically and conventionally peened specimens the specified compressive residual stress is taken at the surface and a tensile residual stress of 100 MPa is assumed 2.5 mm below the surface (see Chapter 6), i.e., $A = \left(100/\sigma_{res} - 1\right)/2.5$ (coefficient used in

the stress gradient correction factor calculation, $\beta_{G,res}$). Since no residual stresses are assumed for the non-peened specimens, no stress gradient factor, $\beta_{G,res}$, needs to be considered.

7.4.7 Strain Amplitudes and Maximum Stresses in Initiation

Assuming a spherical initial flaw, the strain amplitudes governing the crack initiation phase are only a function of the flaw size, whereas the maximum stresses are influenced by the flaw size and the residual stresses. The finite element analysis presented in Chapter 6 showed that the strain amplitude, $\Delta\varepsilon/2$, increases with increasing flaw size, a_{init}. The following relationships between $\Delta\varepsilon/2$ and a_{init} for the non-peened specimens (surface flaw) and the peened specimens (corner flaw) can be defined based on linear interpolation of the finite element results presented in Chapter 6:

$$\begin{aligned}
&\Delta\varepsilon/2 = 8.92\times10^{-4} + 7.28\times10^{-3}\, a_{init} && \text{for non-peened specimens and } a_{init} \le 0.1 \text{ mm}\\
&\Delta\varepsilon/2 = 1.62\times10^{-3} + 2.44\times10^{-4}\left(a_{init} - 0.1\right) && \text{for non-peened specimens and } a_{init} > 0.1 \text{ mm}\\
&\Delta\varepsilon/2 = 8.92\times10^{-4} + 8.48\times10^{-3}\, a_{init} && \text{for peened specimens and } a_{init} \le 0.1 \text{ mm}\\
&\Delta\varepsilon/2 = 1.74\times10^{-3} + 3.11\times10^{-4}\left(a_{init} - 0.1\right) && \text{for peened specimens and } a_{init} > 0.1 \text{ mm}
\end{aligned} \tag{7.3}$$

The strain amplitudes calculated according to equation (7.3) take into account the variability in a_{init} (see Section 7.4.3), but do not consider uncertainties due to the finite element model and the applied loads. Therefore, the strain amplitudes are modelled with a lognormal distribution with a mean value given by equation (7.3) and a COV equal to 0.05, which is based on values reported in Galambos & Ravindra [1977] for the variability due to model uncertainties in steel design.

Based on the finite element results presented in Chapter 6 the following relationships for the mean values of $\sigma_{\max}$ are defined:

$$\begin{aligned}
&\sigma_{\max} = 400 + 800 a_{init} && \text{for non-peened specimens and } a_{init} \le 0.1 \text{ mm}\\
&\sigma_{\max} = 480 + 10\left(a_{init} - 0.1\right) && \text{for non-peened specimens and } a_{init} > 0.1 \text{ mm}\\
&\sigma_{\max} = 250 + 1700 a_{init} && \text{for conv. peened specimens and } a_{init} \le 0.1 \text{ mm}\\
&\sigma_{\max} = 420 + 25\left(a_{init} - 0.1\right) && \text{for conv. peened specimens and } a_{init} > 0.1 \text{ mm}\\
&\sigma_{\max} = 100 + 2300 a_{init} && \text{for US peened specimens and } a_{init} \le 0.1 \text{ mm}
\end{aligned} \tag{7.4}$$

$$\sigma_{\max} = 330 + 75(a_{init} - 0.1) \qquad \text{for US peened specimens and } a_{init} > 0.1 \text{ mm}$$

The residual stresses defined in the previous section (0 MPa for the non-peened specimens, -150 MPa for the conventionally peened specimens, and -300 MPa for the ultrasonically peened specimens) were used in deriving equations (7.4).

The maximum stresses calculated according to equation (7.4) take into account the variability in a_{init} (see Section 7.4.3), but do not consider uncertainties due to the residual stresses, the finite element models, and the applied loads. Therefore, the maximum stresses are modelled with a lognormal distribution having a mean value according to equation (7.4) and a COV equal to 0.1. Due to the uncertainties related to residual stresses a higher COV of variation was chosen for the maximum stresses than for the strain amplitudes.

7.4.8 Stresses in Crack Propagation

The applied stresses in test specimens are obtained from the measured load and a finite element analysis of the test specimen. Due to the inherent uncertainties in finite element modeling and, to a lesser extent, in the test monitoring, the maximum and minimum applied stresses are subjected to some variability. This variability is very difficult to assess, but it can be expected that the model stresses should not be more than 5% off. It is thus assumed that for the maximum applied stress, $\sigma_{\max,app}$, 99.9% of all samples are in the interval (380, 420). Likewise, 99.9% of the samples for the minimum applied stress, $\sigma_{\min,app}$, lie in the interval (28.5, 31.5). This results in LN(400, 6) for the maximum and LN(30, 0.45) for the minimum applied stress.

The coefficient A used in the stress gradient correction factor, β_G, calculations is assumed to be deterministic for both the maximum and minimum stresses. At maximum load the stress at mid-thickness is assumed to be 300 MPa (see Chapter 6) and the resulting value of A is $A = (300/\sigma_{\max,app} - 1)/9.525$. At the minimum load the stress is constant through the thickness (see Chapter 6), i.e., $A = 0.0$.

7.4.9 Summary

Table 7.1 summarizes the statistical models of all the parameters used in the probabilistic fatigue life predictions carried out in the next section. Several of the parameters in Table 7.1 are correlated. For example, the strain amplitude, $\Delta\varepsilon/2$, the maximum stress, $\sigma_{\max}$, and the initial crack size, a_0, are a function of the initial flaw size, a_{init}. These correlations are considered in the Monte Carlo Simulations using the appropriate functions, where all the related parameters are sampled using a single random number.

Table 7.1 – *Models of all parameters used in the probabilistic fatigue life predictions.*

Stage	Parameter	μ_Z	σ_Z	Distribution	Note
General	$a_{init} = a_0$	0.10	0.02	lognormal	non-peened
		0.15	0.03	lognormal	conv. peened
		0.30	0.06	lognormal	US peened
Initiation	$\Delta\varepsilon/2$	Eq. (7.3)	COV=0.05	lognormal	
	$\sigma_{\max}$	Eq. (7.4)	COV=0.10	normal	
	E	207,000	5,000	lognormal	
	σ_f'	630	30	lognormal	
	ε_f'	0.34	0.07	lognormal	
	b	-0.059	---	deterministic	
	c	-0.63	---	deterministic	
Propa-gation	a/c	0.5	0.16	lognormal	non-peened
		1.0	---	deterministic	peened
	a_f	12	1.5	lognormal	non-peened
		19.05	---	deterministic	peened
	$\sigma_{\max,app}$	400	6.0	lognormal	
	$\sigma_{\min,app}$	30	0.045	lognormal	
	$(\sigma_{res})_{np}$	0	---	deterministic	non-peened
	$(\sigma_{res})_{cp}$	-150	30	normal	conv. peened
	$(\sigma_{res})_{up}$	-350	20	normal	US peened
	C	3.5×10^{-13}	1.4×10^{-13}	lognormal	
	m	3.0	---	deterministic	
	$\Delta K_{th,eff}$	60	6	lognormal	

7.5 Probabilistic Fatigue Life Predictions

The fatigue life of the three small scale test series reported in Chapter 5 (non-peened, conventionally peened, and ultrasonically peened) are predicted using Monte Carlo Simulation (MCS). The fatigue model proposed in Section 7.3 and the probabilistic

distributions defined in Table 7.1 are used for the MCS. For each of the three series a total of 100,000 simulations were conducted. Stable results were generally obtained after less than 50,000 simulations.

Subroutines to run the simulations were written in MatLab®. The results for the crack initiation life, N_{init}, the crack propagation life, N_{prop}, and the total life, N_{total}, were stored in ascii-files, which were then imported into Microsoft® Excel to determine the mean, standard deviation, and number of run-outs (fatigue life $\geq 10^7$ cycles) for each series. Table 7.2 summarizes the simulation results and the fraction of the total fatigue life spent in the initiation stage (N_{init}/N_{total} in %) for the non-peened and conventionally peened specimens. Over 98% of the simulations on specimens with ultrasonic peening yielded fatigue lives in excess of 10,000,000 cycles. A statistical analysis of these simulations is not meaningful since most of the predicted test results are run-outs. However, it is interesting to note that the initiation life of the ultrasonically peened specimens was always less than ten million cycles, with an average of approximately 100,000 cycles. The infinite life of these specimens is associated to the crack arrest once it has initiated.

Table 7.2 – *MCS results for the non-peened and conventionally peened series (100,000 simulations).*

Series	**Mean of N_{total} [cycles]**	**Standard Deviation of N_{total} [cycles]**	**Number of Run-Outs**	**Average N_{init}/N_{total}**
Non-Peened	200,000	133,000	8	15%
Conv. Peened	646,000	387,000	33	6%

The crack initiation life is more important for the non-peened specimens, as it makes up for 15% of the total life compared to only 6% for the conventionally peened specimens. The introduction of compressive residual stresses at the surface of the tested specimens thus has a greater effect on the propagation life than on the initiation life.

Figure 7.4 shows the probability density functions for the non-peened and the conventionally peened MCS results. Superimposed on the two curves are the likelihoods of the six test results, which were generated from the obtained MCS pdf. Also shown in Figure 7.4 are the 5th and 95th percentiles for both pdf's. A comparison between the MCS and the test results shows that all test results lie within the 90% confidence interval of the simulations. A perfect fit, however, would have all the test results evenly distributed around the mean. For the non-treated and stress relieved specimens, three test results are close to the predicted mean value. However, one specimen (S280NT12) falls at 0.95 standard deviations above the mean predicted value. A similar conclusion can be drawn

from the two conventionally peened results where the average of the two tests is 0.57 standard deviations to the right of the simulated mean. The likelihood of the test results can be maximized through calibration of the input parameters, resulting in a better fit and therefore and more accurate model. This is done in the next section.

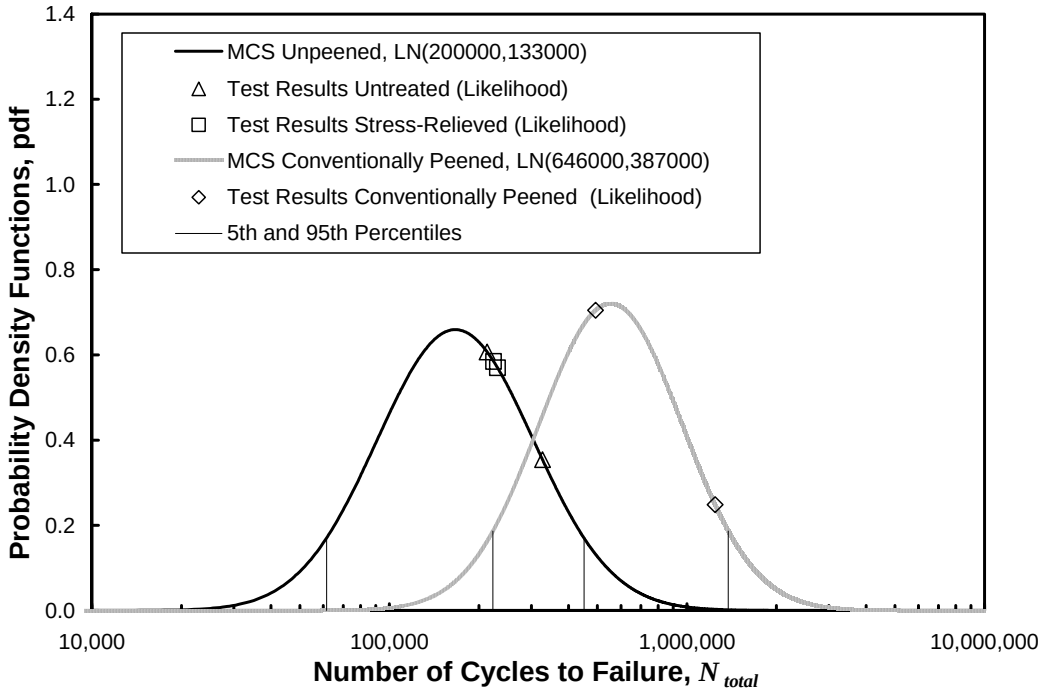

Figure 7.4 *– Probability density functions of MCS and likelihood of the test results.*

7.6 Calibration of Probabilistic Parameters

The mean values and standard deviations of the input parameters were chosen based on the literature, fatigue properties obtained from tests on crack initiation and propagation specimens, and observations from the small scale tests. A comparison of the predicted fatigue life distribution with the results of a few fatigue tests on small scale specimens indicated that the distributions may be too conservative. A better correlation between the observed and the predicted test results could be achieved by shifting the predicted pdf's so that the test results are centered around the peak of the curves through a calibration of the input parameters. It is possible that a combination of calibrated parameters might be needed to appropriately shift both curves.

Not all the parameters have the same influence on the MCS results and, presumably, it is most efficient to calibrate the parameters that have an important effect. An intuitive approach to determine the weight of every parameter is presented in the following:

1. All but one parameter (referred to as the investigated parameter in the following) are assumed to be deterministic (taken with their mean values; the investigated parameter is modeled with the probabilistic distribution defined above).
2. MCS is run for each investigated parameter.
3. The standard deviations obtained for each MCS are compared. The weight of a parameter is proportional to the standard deviation obtained from its MCS result.

Figure 7.5 and Figure 7.6 present the standard deviations of the fatigue life obtained for each investigated parameter for the non-peened and conventionally peened specimens, respectively. It is evident from the two figures that none of the crack initiation parameters have an important weight. This is not surprising since the crack initiation stage accounts only for a relatively small portion of the total life. Furthermore, the maximum and minimum applied stresses, $\sigma_{\max,app}$ and $\sigma_{\min,app}$, and the threshold stress intensity factor range, ΔK_{th}, also have only a small effect on the variability of the fatigue life. The simulations of the non-peened specimens also show that the final crack size, a_f, has a minor weight, whereas the crack aspect ratio, a/c, is important. Both series demonstrate that the initial flaw size, a_{init}, and especially the crack propagation constant, C, are of great importance. The simulations of the conventionally peened specimens further show that the residual stresses, σ_{res}, have a substantial weight.

In summary, four of the total 13 parameters have a significant effect on the outcome of the simulations. These four parameters are a_{init}, a/c, σ_{res}, and C. This is in good agreement with the findings of Walbridge [2005], who identified a/c, C, and ΔK_{th} as the major parameters in an investigation of the fatigue life of tubular joints. The smaller importance of ΔK_{th} observed in the present study is due to a combination of the smaller mean value, the smaller standard deviation, and the incorporation of a crack initiation model in the fatigue life prediction. The latter introduces a crack at the beginning of the propagation stage that is large enough that the predicted fatigue life is not significantly influenced by ΔK_{th}.

Since two of the four major parameters are only used in one of the simulations (a/c for the non-peened condition and σ_{res} for the conventionally peened condition), they are not calibrated here. Furthermore, the initial flaw size, a_{init}, is different in the two simulations and therefore not suitable for calibration. As a consequence, only the most influential parameter, C, will be calibrated in the following.

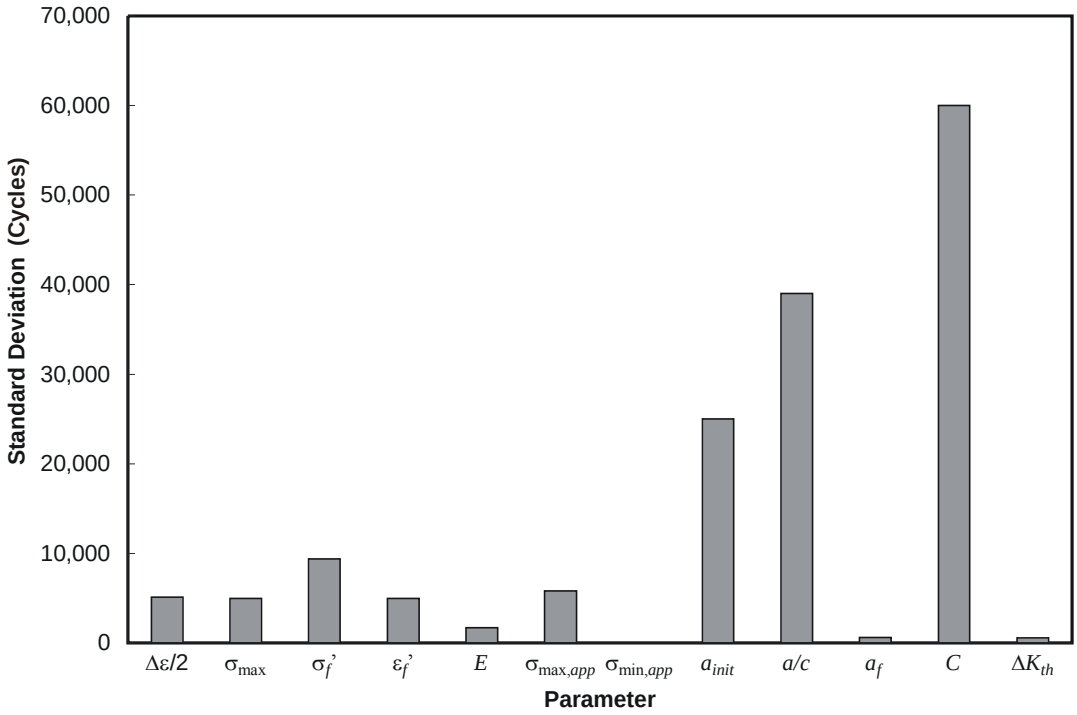

Figure 7.5 *– Standard deviations of the non-peened MCS results for the investigated parameters.*

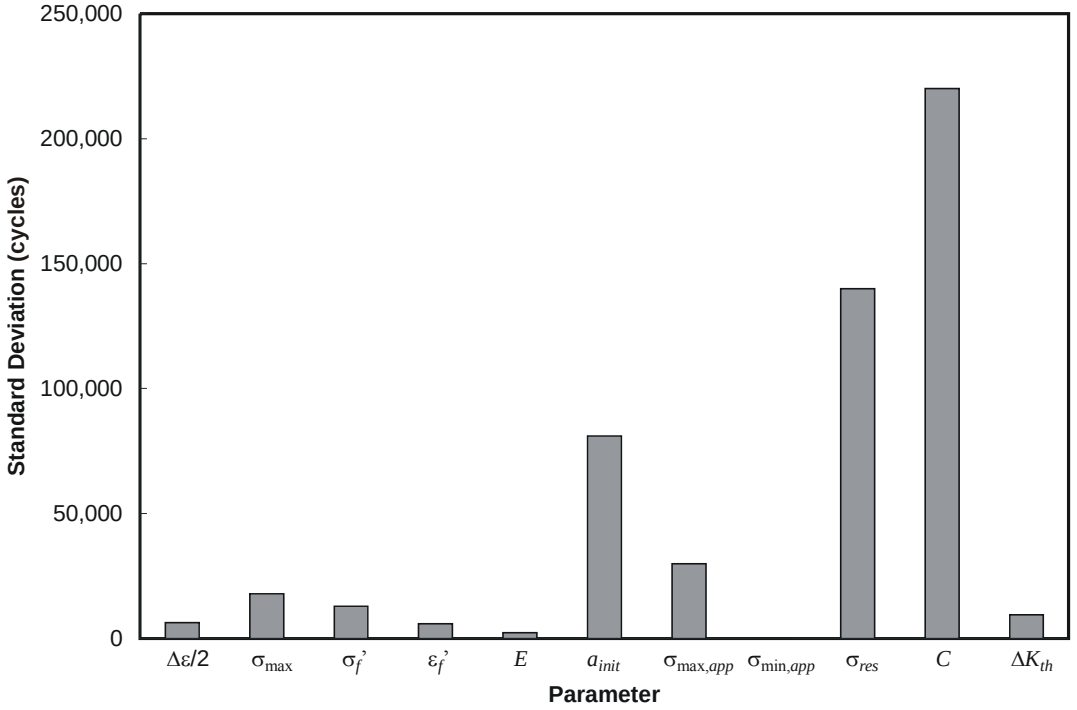

Figure 7.6 *– Standard deviations of the conventionally peened MCS results for the investigated parameters.*

An iterative procedure was used to calibrate C. The mean value of the parameter was varied between $C = 2.50 \times 10^{-13}$ and $C = 3.50 \times 10^{-13}$ (initial value). The standard deviation of C (1.40×10^{-13}) and the probabilistic distributions of all other parameters were kept as defined in Table 7.1. MCS was run for each mean value of C. The sum of the likelihoods of all six test results was determined for each C-value. The C-value resulting in the highest sum of the likelihoods (maximized likelihood) corresponds to the calibrated parameter.

Table 7.3 summarizes the simulation results of the calibration procedure. In addition to the sum of the likelihoods of the test results, the mean value and the standard deviation of the MCS are given.

Table 7.3 – *MCS results of the calibration of* C **.**

Mean Value of C	**Treatment**	**Mean of N_{total} [cycles]**	**Standard Deviation of N_{total} [cycles]**	**Sum of Likelihoods of Test Results**
3.50×10^{-13}	Non-peened Conv. Peened	200,000 646,000	132,000 387,000	3.068
2.90×10^{-13}	Non-peened Conv. Peened	244,000 818,000	164,000 520,000	3.186
2.80×10^{-13}	Non-peened Conv. Peened	254,000 853,000	170,000 547,000	3.468
2.70×10^{-13}	Non-peened Conv. Peened	265,000 897,000	171,000 603,000	3.552
2.60×10^{-13}	Non-peened Conv. Peened	277,000 943,000	185,000 629,000	3.504
2.50×10^{-13}	Non-peened Conv. Peened	291,000 997,000	207,000 695,000	3.375

The maximum likelihood is achieved with a mean value of $C = 2.70 \times 10^{-13}$. This value corresponds well to the one found for the base metal of grade 350WT steel (see Chapter 4) and to an average value of the distributions proposed by several researchers for $m = 3.0$ (see Table 3.4). Figure 7.7 shows the pdf's obtained from the calibrated MCS and the individual likelihoods of the test results.

It should be noted that during this calibration procedure, it was assumed that the standard deviation of each parameter is representative. If a parameter has a larger standard deviation than assumed here, its weight would increase and might therefore influence the outcome of the calibration.

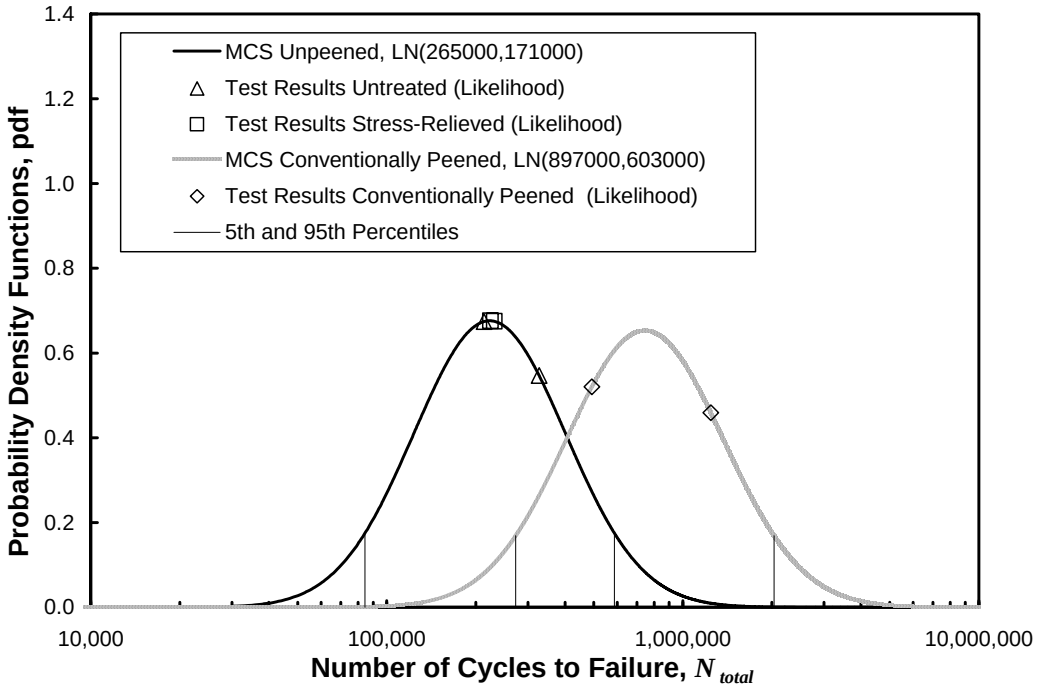

***Figure 7.7** – Probability density functions for the calibrated MCS ($C = 2.70 \times 10^{-13}$) and likelihood of the test results.*

7.7 Summary

In this chapter, the deterministic models proposed in Chapter 6 were validated through probabilistic analyses. The concepts of the most commonly used methods for reliability analyses in structural engineering, Monte Carlo Simulation (MCS) and First Order Reliability Method (FORM), were introduced. Due to frequent convergence problems with the FORM method for the crack initiation and propagation models used in the present work, only MCS was implemented.

An analysis of the prediction results using the various deterministic approaches outlined in Chapter 6 showed that a model with an initial flaw accounting for initiation life, crack closure, and ΔK_{th} was the most suitable approach for the prediction of the fatigue resistance of the small scale specimens tested in Chapter 5. The following parameters were considered as random variables:

- Fatigue initiation and propagation properties: E, $\sigma_f^{'}$, $\varepsilon_f^{'}$, C, and ΔK_{th}
- Initial flaw size and shape: a_{init} and a/c
- Transitional crack size: a_{trans}
- Final crack size: a_f
- Residual stresses: σ_{res}
- Strains and stresses during initiation: $\Delta\varepsilon/2$ and $\sigma_{\max}$

- Stress range during propagation: $\Delta\sigma$

The probabilistic models of each of these parameters were based on findings presented in previous chapters and are summarized in Table 7.1. It was shown that a_{trans}, which is by definition equal to the initial crack size a_0 in the crack propagation model, can be taken as the size of the initial flaw, a_{init}, i.e., $a_0 = a_{init}$. It should be noted that this is a simplification and does not mean that there is no initiation life.

Probabilistic predictions that adequately matched the test results of three sets of test specimens (non-peened, conventionally peened, and ultrasonically peened) were obtained with Monte Carlo Simulations. The MCS indicated that run-outs were very likely to be encountered with the ultrasonically peened test specimens. The test results of the non-peened and the conventionally peened specimens fell well within the 90% confidence interval of the simulations. However, the probabilistic predictions for both series tend to be too pessimistic. Through a calibration of the fatigue propagation constant C, which was found to be the most significant parameter in a sensitivity study, a better fit of the predictions with the test results was obtained. The calibration was carried out by maximizing the sum of the likelihoods (as determined through MCS) of the test results. The resulting mean value for C is 2.70×10^{-13} rather than 3.50×10^{-13} originally obtained from crack propagation tests. The standard deviation was not changed. Due to the limited number of test results used to calibrate C, the new C-value might not be representative and should therefore be used with caution in other probabilistic analyses.

8. GENERAL RELIABILITY-BASED APPROACH

8.1 Introduction

The validation of the prediction models carried out through probabilistic analyses in the previous chapter showed that the test results could be predicted reliably. For in-service structures the proposed approach has to be extended to include the uncertainties and variability in loading. In a general reliability-based approach of actual structures and their components an acceptable probability of failure, or target reliability, has to be defined first. This is not as simple as it appears and several factors, of which some are rather subjective, have to be accounted for. Factors affecting the definition of a target reliability are reviewed in Section 8.2. The loading side of the limit state function is discussed in Section 8.3. Section 8.4 addresses the resistance, for which the ground work was laid in the previous chapters. The proposed general reliability-based approach, which is presented in Section 8.5, is then applied to three examples in Section 8.6. Two of these examples only deal with the resistance aspect of the reliability approach, i.e., they are predictions of test results. The third one deals with a real, cracked structural component for which the remaining fatigue life will be predicted based on in-situ load measurements and the detected crack length.

8.2 Target Reliability

As has been shown in the previous chapters, the reliability of a structure can either be expressed by the probability of failure, p_f, or by the corresponding safety index, β. Historically, the use of β has prevailed in most structural engineering applications. Reliability-based codes adopted β-values on the basis of existing deterministic codes, trying to achieve similar levels of safety with the two generations of codes. This approach is intuitive considering designs according to the old codes performed well. Furthermore, the definition of an appropriate probability of failure was not evident. Although some advances in fixing β-values have been made, some ambiguity in the targeted level of safety has carried through. It is agreed that the more critical the consequence of failure, the larger β has to be, i.e., the probability of failure needs to be reduced. For example, a lower safety index can be tolerated for a structure at the serviceability limit state compared to the same structure at the ultimate limit state. Fatigue is usually considered an ultimate limit state since fatigue failures often lead to partial or complete collapse of a structure. The safety index also depends on the nature of the failure. Brittle fracture, which shows little warning, would require a higher safety index than ductile fracture. In fatigue this often translates to defining a larger safety index for structures where a crack cannot easily be detected. If the propagation of a crack can be easily detected and monitored before failure, a lower safety index is warranted.

The latest version of the National Building Code of Canada, NBCC, was calibrated with a target safety index of approximately 3.0 for the ultimate limit state and a design life of 50 years [Bartlett et al. 2003]. Section 14.12 of the *Canadian Highway Bridge Design Code*, CAN/CSA-S6 [CSA 2006] recommends target β-values for the evaluation of existing bridges ranging from 2.5 for members that can be easily inspected and show ductile behaviour of a local portion of the bridge to 4.0 for members that are difficult to inspect and where brittle failure leading to a total collapse of the bridge is expected. According to Galambos et al. [1982] representative values of β are between 2.5 and 2.9 for steel and between 2.8 and 3.2 for concrete structures, reflecting the generally more brittle behaviour of concrete structures. Due to localized and often severe failures, steel connections are designed for typical values of β close to 4.0 The joint committee on structural safety [JCSS 2001a] proposes various target reliabilities depending on the relative cost of the safety measures and the consequence of failure. For the most common design situation (normal cost and moderate consequence of failure) a safety index of 4.2 is recommended. DNV [1992] recommends $\beta = 3.09$ for redundant structures where ample warning is provided before a failure and where failure leads to less serious consequences. The highest safety index, $\beta = 4.75$, is recommended for structures with brittle failure modes and serious consequences. Eurocode 0, *Basis of Structural Design* [EC 2002], recommends values for β for a reference period of 50 years, β_{50}. Depending on the "degree of inspectability, reparability, and damage tolerance", EC [2002] proposes β_{50}-values ranging from 1.5 to 3.8 for the fatigue limit state and for moderate consequences of failure.

For the fatigue limit state a judicious selection of a safety index should be based on the risks inherent to a structural failure, considering the consequence of failure, inspection management, crack growth rates, toughness aspects, and redundancies.

8.3 Loading

8.3.1 Introduction

Fatigue cracking results from the cyclic action of live loads such as traffic loads on bridges, hoisting loads on cranes, or excavation loads on earth moving equipment. In some cases, fatigue can also be caused by climatic actions, such as wind on transmission towers or waves on offshore structures. Although live loads vary significantly, and often randomly, during the lifetime of a structure this variability is not a concern when considering the ultimate limit state because only the extreme loads, which are easier to determine than the entire loading history, are of importance. However, fatigue damage is not only caused by extreme loads but also by loads of much lower intensity. Therefore, the loading history has to be known and represented by a load spectrum. Modern design standards account for load variability over the life of structures through a calibration process. A brief outline of the methodology used to establish these loads is presented in

8.3.2. For many applications, such as in the design of mining equipment, the loads are not a priori known and the design loads for fatigue design are not published in design codes. In these cases in-situ measurements have to be carried out, which is discussed in some detail in Section 8.3.3. Section 8.3.4 proposes an approach to transform the in-situ loading history into an equivalent fatigue load.

8.3.2 Design Code Approach

According to most modern structural engineering design standards, the fatigue limit state is satisfied when:

$$\phi_F F_{sr} \geq \alpha_F f_{sr} \tag{8.1}$$

where ϕ_F is the resistance factor for fatigue, F_{sr} the fatigue resistance, α_F the load factor for fatigue, and f_{sr} the calculated stress range at the considered detail due to the fatigue loading. F_{sr} is commonly determined through $\Delta\sigma - N$ curves (see Chapter 2) as a function of the number of load cycles used for the design.

Only fatigue loading due to highway traffic is considered in the following. Other fatigue loading, e.g. rail or crane loading, is treated accordingly in the codes. The fatigue provisions of the Canadian Highway Bridge Design Code, CSA-S6-06 [CSA 2006] idealizes the loading with a single, five-axle truck placed at the centre of the governing lane. This truck is the same for the ultimate, fatigue, and serviceability limit states. The load factor for fatigue is $\alpha_F = 1.0$. As stated above, fatigue loading is not only due to the design truck, which passes the bridge very rarely over the life of the bridge, but to a larger extend to smaller trucks. To consider this, CSA-S6-06 reduces the calculated stress range by a factor of 0.52. This is equivalent to setting α_F equal to 0.52. The fatigue resistance, F_{sr}, is determined using the following relationship:

$$F_{sr} = (\gamma / N_c)^{1/3} \geq 0.5 F_{srt} \tag{8.2}$$

where γ is the fatigue constant for the considered detail and N_c is the expected number of truck passages during the design life (normally 70 years) of the bridge. Since one truck passage can cause more than one stress cycle in a component, the number of applied truck passages is multiplied by a factor between 1.0 and 5.0 depending on the structural system (e.g. simple spans or continuous spans, longitudinal or transverse members) and the span length. The fatigue limit of $0.5F_{srt}$ takes into account that if the equivalent stress range is below 50% of the constant amplitude fatigue limit, F_{srt}, no damage occurs. No resistance factor, ϕ_F, is applied in equation (8.2), i.e., $\phi_F = 1.0$. However, it is noted that the fatigue design curves are obtained by subtracting two standard deviations from the mean fatigue curves (see Chapter 2).

The Eurocodes [EC 2002, EC 2003, EC 2005] use a very similar format. The fatigue design truck is idealized by two axles. The characteristic values of the axle loads are multiplied by a factor to take into account the composition of the traffic, which can vary

from country to country. The load factor for fatigue is $\alpha_F = 1.0$. The calculated stress range, $\Delta\sigma(Q_{fat})$, is again reduced by a factor, λ. In addition to considering the generally lighter traffic that contributes to the fatigue damage this factor also takes into account design considerations that are included in the calculation of N_c such as the structural system, the span length, and the design life. Furthermore, the factor transforms the number of truck passages to a standard number of cycles of 2 million. The fatigue limit state takes the following form:

$$\Delta\sigma_{E2} = \lambda\Delta\sigma(Q_{fat}) \leq \Delta\sigma_{c,d} \tag{8.3}$$

where $\Delta\sigma_{E2}$ is the equivalent stress range at two million cycles and $\Delta\sigma_{c,d}$ is the design fatigue resistance for the detail under consideration at two million cycles. The stress range $\Delta\sigma_{c,d}$ includes a partial resistance factor that depends on the type and consequence of failure.

The main difference between CSA-S6-06 and the Eurocodes is that the latter include all the factors affecting the loading on the load, whereas CSA [2006] introduces N_c as part of the resistance. This, however, does not affect the end result since the two codes use the same approach to transform the actual loading on a bridge into the fatigue loading. The methodology of this transformation is illustrated in Figure 8.1 [after Kunz & Hirt 1991].

The first step in the procedure is to assemble and evaluate field data on representative bridges (left column of Figure 8.1). The resulting stress history for the measured truck passages, N_{meas}, needs to be transformed into a histogram of stress ranges through a counting method such as the rainflow or reservoir methods [Fisher et al. 1997]. Using a cumulative damage model with a slope of $m = 3.0$ for the $\Delta\sigma - N$ curve (e.g. Miner [1945])[1], the different stress ranges of a truck passage are transformed into an equivalent stress range for this truck, $\Delta\sigma_{e,i}$. A histogram of all $\Delta\sigma_{e,i}$ is then established, from which the equivalent stress range, $\Delta\sigma_e$, is determined using a cumulative damage model with a slope of $m = 3.0$. The equivalent stress range, $\Delta\sigma_e$, corresponds to the stress range caused by an "average" truck. In addition, the maximum and minimum stresses, $\sigma_{fat,\max}$ and $\sigma_{fat,\min}$, on the same structure due to the design fatigue load are determined (right column of Figure 8.1). The algebraic difference of these stresses yields a theoretical stress range, $\Delta\sigma_{fat,th}$. Assuming that the damage due to the expected number of truck passages during the life of the bridge, N_{actual}, where each passage causes the "average" truck stress range, $\Delta\sigma_e$, is equal to the damage due to N_{design} passages of the design truck causing $\Delta\sigma_{fat,th}$, the following coefficient is found:

[1] Although other cumulative damage models exist, some of them attempting to take into account the stress sequence, it is believed here that Miner's rule gives as reliable results as more complex models [Fatemi & Yang 1998].

$$\eta = \left(\frac{N_{actual}}{N_{design}} \right)^{1/m} \frac{\Delta\sigma_e}{\Delta\sigma_{fat,th}} \tag{8.4}$$

In CSA-S6-06 $N_{actual} = N_{design}$, whereas in the Eurocodes $N_{actual} \neq N_{design} = 2 \times 10^6$. η corresponds to the λ-factor in equation (8.3) or the factor 0.52 in CSA [2006]. In order to use the same fatigue load model for all types of bridge structures and their elements, η must be adjusted with regards to the structural system, as discussed above.

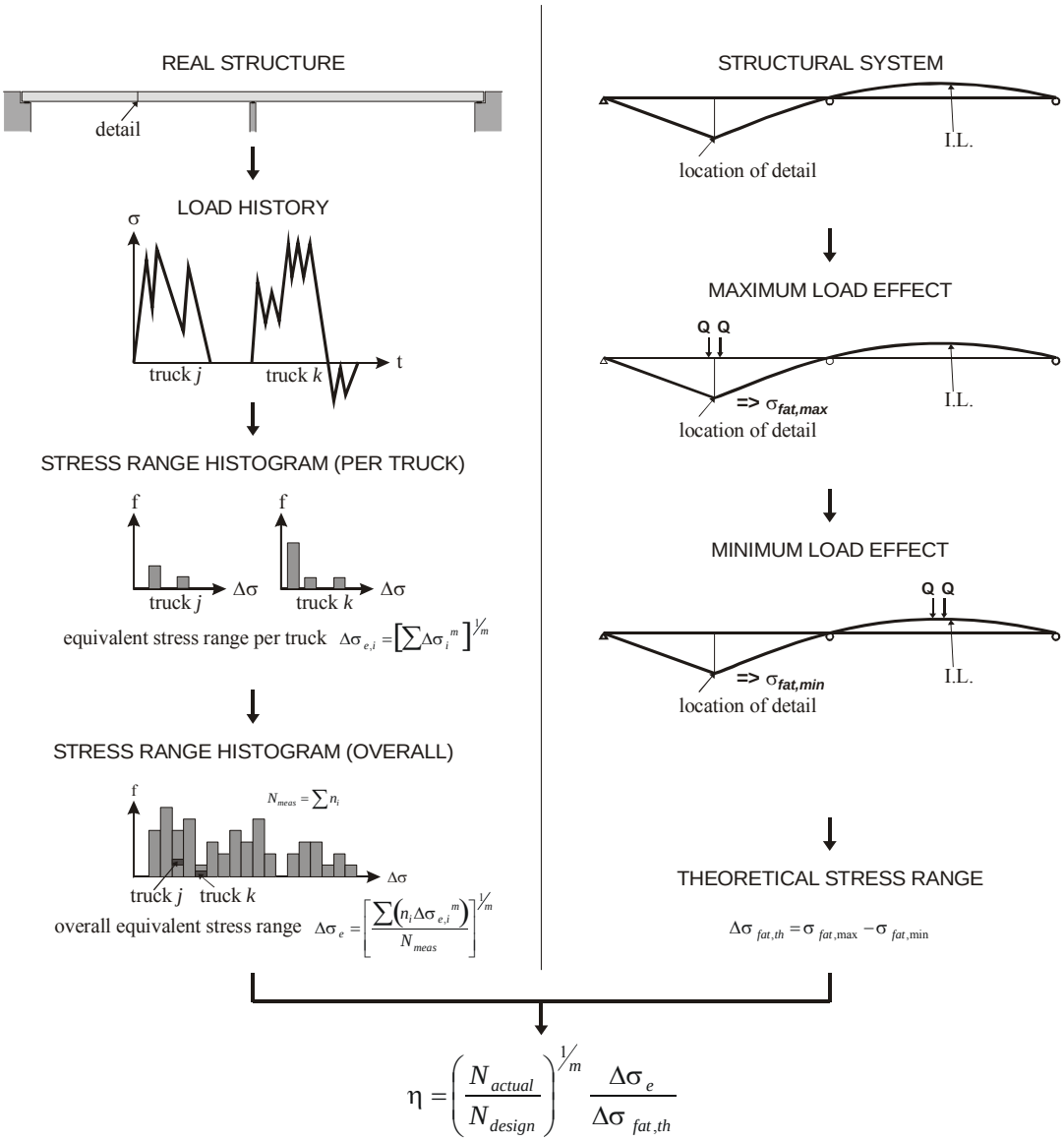

***Figure 8.1** – Methodology to transform actual loading into fatigue loading.*

Not all stress ranges cause fatigue damage in the detail. This is accounted for by neglecting all stress ranges below a certain threshold called the variable amplitude fatigue limit (VAFL). CSA [2006] defines the VAFL as half of the constant amplitude fatigue limit (CAFL), see equation (8.2). The CAFL is a function of the detail and is tabulated in the code. The VAFL in the Eurocodes is assumed to be the stress range corresponding to $N = 10^7$, which can be determined from the $\Delta\sigma - N$ curve of the considered detail.

8.3.3 Loading According to In-Situ Measurements

Much of the variability in fatigue life predictions is related to the uncertainties in the loading history. For many applications, no historical data are available and in-situ measurements need to be carried out. Field data collection can also be of interest for structures where the assessment of the remaining fatigue life is inconclusive to whether the structure has to be reinforced or even replaced. In such cases an updated load model often results in lower stresses than assumed according to code loading and thus to an extension of the calculated fatigue life.

In-situ measurements are generally time-consuming and entail high costs. Therefore, meticulous planning is imperative. Different types of in-situ monitoring can be distinguished:

- Measurements of the loading: Only the loads are directly measured and the stresses are then determined through a structural analysis. For a highway bridge, this can be accomplished by automatically or manually counting the number of truck (or axle) passages. Using measurements from a nearby weigh station, the load history can be estimated. In mining equipment calibrated load measuring devices would have to be installed on the equipment and the load history recorded. The advantage of using only load measurements is the rather small amount of data that needs to be analysed. Its main shortcoming is that even if the load history can be established with accuracy, the structural response is still subjected to significant uncertainty due to the lack of specific stress measurements.
- Measurements of strains: Strains are monitored at specific locations in the structure, but no load measurements are taken. The most convenient way to measure strains is by mounting strain gauges. The advantage of this method is that the strain (and stress) history is known at specific locations and can be readily used for the fatigue assessment. However, in order to obtain the stresses at locations other than the instrumented locations, the loading has to be determined from a structural analysis, which can introduce significant variability.
- Combination of load and strain measurements: The most favourable approach is to carry out simultaneous load and strain measurements on the structure. This is more demanding than any of the two former methods. Especially the analysis of the data can be time-consuming. However, with

diligent planning and execution, reliable results concerning the loading and the structural response are found. In addition, supplementary monitoring, such as deflection measurements, can be carried out to further enhance the knowledge of the structural response.

In a reliability-based assessment of fatigue resistance, the loading is a random variable. Two different aspects contribute to the randomness. First, the measurements are subjected to variability, depending on the amount of data collected and how representative they are. For example, the stresses in a bridge will depend on factors such as the load distribution of the truck, the position of the truck across the width of the bridge, the speed, and the interaction of the truck with the bridge. For mining equipment operating conditions are primarily affected by the operator of the equipment and the ground conditions. Second, the measurements have to be transformed into stresses at different locations in the structure, necessitating some sort of structural analysis. The real structure is idealized, introducing uncertainties pertaining to the structural response. It is therefore desirable to use the last of the three listed methods to obtain a reliable stress history for the structure and its components and details. The measurements should preferably be done first under controlled loading to obtain reference data to calibrate an analysis model of the structure. On bridges this is often done through load tests with predetermined axle loads. Static and dynamic tests should be carried out. Once the reference data are collected, in-service measurements have to be performed. The application of such a procedure is shown in Section 8.6.4, where the remaining fatigue life of a cracked boom of an excavator is investigated.

The variability in loading has to be assessed on a case by case basis. As stated above, the better the collected data the smaller the variability. Little information on statistical evaluation of bridge loading measurements was found in the literature. Table 8.1 summarizes the distribution type, the coefficient of variation (COV), and the type of loading for highway traffic loads proposed in four different sources.

Table 8.1 – *Some probabilistic distributions of loading on highway bridges.*

Reference	Distribution	COV	Loading
Bailey [1996]	Normal	0.10	Highway traffic, Ultimate Limit State
Lukic & Cremona [2001]	Gumbel	0.03	Highway traffic, Fatigue Limit State
Darchuk [2003]	Normal	0.34	Highway traffic, Fatigue Limit State
Walbridge [2005]	Normal	0.15	Highway traffic, Fatigue Limit State

8.3.4 Equivalent Strains and Stresses

The fatigue loading in most engineering applications is random and a structure is thus subjected to variable load ranges. Both the crack initiation and propagation models used in this work assume a constant load range. Theoretically, the linear elastic fracture mechanics model can be adapted to include variable load ranges by changing the maximum and minimum stresses at every crack propagation step. However, in a reliability-based approach this is hardly feasible. Therefore, the variable strains and stresses have to be transformed into equivalent constant amplitude values. An approach similar to the one used for bridge design live loads, as outlined in Section 8.3.2, seems to be most promising. This approach has the advantage of being straight forward for the crack propagation model, where the loading can be fully defined by the stress range, $\Delta\sigma$, and the stress ratio, R. Assuming the same stress ratio for all load cycles, which is a rational simplification that does not significantly affect the results, only one load related variable, $\Delta\sigma$, needs to be considered. The approach becomes more complex for the crack initiation stage, where the two load variables $\Delta\varepsilon/2$ (strain amplitude) and $\sigma_{\max}$ (maximum stress) have to be considered. An approach based on the equivalent stress range calculation carried out for the propagation stage will be proposed here for the initiation stage. Consequently, the transformation of the stress ranges in the propagation stage is first discussed in the following.

As stated above the passage of a truck can cause several load peaks. Similarly, an excavation and dumping cycle from mining equipment such as an excavator can include more than one load range. A loading event is defined here as the response of a structure to one action, such as a truck passage or an excavation and dumping cycle. Preferably, the load ranges experienced in one load event are first transformed into an equivalent load range. This facilitates the prediction of the remaining fatigue life. The number of events to failure, N_{total}, then represents the number of trucks passing on a bridge or the number of excavation and dumping cycles for mining equipment before the structure has reached the end of its life. Knowing the number of estimated loading events per time unit, $N(t)$, the remaining fatigue life, T_r, is determined by:

$$T_r = \frac{N_{total}}{N(t)} \tag{8.5}$$

The transformation of measured stress ranges into an equivalent stress range is accomplished using the method outlined in Section 8.3.2 for a bridge design load. The method is based on the hypothesis that the damage caused by the equivalent stress range, $\Delta\sigma_e$, is equal to the damage caused by the sum of all the variable stress ranges. Using the $\Delta\sigma - N$ curve approach with a constant slope m, and the Miner's linear damage assumption, the damage due to a stress range, $\Delta\sigma_i$, can be defined as:

$$d_i = \frac{1}{N_i} \tag{8.6}$$

where $N_i = A \cdot \Delta\sigma_i^{-m}$ is the number of cycles at the stress range $\Delta\sigma_i$ that the detail having a fatigue life constant A can sustain before failure occurs. Adding the individual damages, d_i, the total damage after *n* stress cycles is calculated as:

$$D = \sum d_i = \sum \frac{n_i}{N_i} = \sum \frac{n_i}{A \cdot \Delta\sigma_i^{-m}} \tag{8.7}$$

where n_i is the number of cycles at a specific stress range, $\Delta\sigma_i$. Setting the damage done due to the individual cycles, n_i, equal to the damage done by N_e cycles of the equivalent stress range, the following expression is obtained:

$$\sum \frac{n_i}{A \cdot \Delta\sigma_i^{-m}} = \frac{N_e}{A \cdot \Delta\sigma_e^{-m}}$$

from which

$$\Delta\sigma_e = \left(\frac{\sum n_i \Delta\sigma_i^m}{N_e} \right)^{1/m} \tag{8.8}$$

The first step consists of transforming the different stress ranges, $\Delta\sigma_{ij}$, of a loading event *i* into one equivalent stress range, $\Delta\sigma_{e,i}$:

$$\Delta\sigma_{e,i} = \left(\sum_j \Delta\sigma_{ij}^m \right)^{1/m} \tag{8.9}$$

The second step consists of applying equation (8.8) to get the desired equivalent stress range, $\Delta\sigma_e$, with $N_e = \sum n_i$ being the number of loading sequences.

In the fatigue life prediction approach presented in this work the crack initiation and crack propagation stages are treated separately. Consequently, the slope m of the $\Delta\sigma - N$ curves can be assumed to be equal to the slope of the Paris-Erdogan equation, which is taken as $m = 3.0$ in all the following calculations. If a different model, e.g. a strain-based fracture mechanics model as proposed by Walbridge [2008], is used to predict the fatigue life, then the slope of the $\Delta\sigma - N$ curves may no longer be 3.0.

An example of the transformation of measured stress ranges into an equivalent stress range is presented in Section 8.6.4, where the remaining fatigue life of a cracked excavator boom is predicted. For this application in-situ measurements were carried out and stress histories established.

As stated before, the fatigue crack initiation life is a function of two load dependant variables, namely, $\Delta\varepsilon/2$ and $\sigma_{\max}$. By reformulating equation (2.5) the two variables can be paired:

$$\sigma_{\max}\left(\Delta\varepsilon/2\right)=\frac{\left(\sigma_f^{'}\right)^2}{E}\left(N_{init}\right)^{2b}+\sigma_f^{'}\varepsilon_f^{'}\left(N_{init}\right)^{b+c} \tag{2.5a}$$

The relationship between $\sigma_{\max}\left(\Delta\varepsilon/2\right)$ and N_{init} is found to be approximately linear on a log-log scale. This yields the following expression:

$$\sigma_{\max}\left(\Delta\varepsilon/2\right)=A\left(N_{init}\right)^{-1/B} \tag{8.10}$$

where A and B are obtained from a regression analysis. Equation (8.10) is thus similar to the Paris-Erdogan relationship. As for the crack propagation life the equivalent stress-strain product $\left(\sigma_{\max}\left(\Delta\varepsilon/2\right)\right)_e$ is found by setting the damage due to the sum of the individual products equal to the damage due to n_{ref} cycles of the equivalent product, yielding the following relationship:

$$\left(\sigma_{\max}\left(\Delta\varepsilon/2\right)\right)_e=\left(\frac{\sum n_i\left(\sigma_{\max}\left(\Delta\varepsilon/2\right)_i\right)^B}{N_e}\right)^{1/B} \tag{8.11}$$

where n_i is the number of cycles for a specific stress-strain product, $\left(\sigma_{\max}\left(\Delta\varepsilon/2\right)\right)_i$. Since the transformation of the strains and stresses for the initiation life is not needed for any of the applications presented in Section 8.6, an example of the approach is presented in Appendix H. Appendix H also shows the derivation of equation (8.11).

8.4 Resistance

8.4.1 Introduction

The fatigue resistance of a detail is a function of the fatigue material properties, the natural stress concentration[1], the severity of an imperfection, and the failure criterion. All these factors are random in nature. Information about the fatigue parameters is often scarce. The following presents guidelines about the fatigue material properties (Section 8.4.2), the stresses and strains at a perfect detail, i.e., a detail without any flaws (Section 8.4.3), the quantification of the severity of an imperfection in a detail (Section 8.4.3), and the definition of the failure criterion (Section 8.4.5). Probabilistic models that are deemed reasonable are proposed in Sections 8.4.2 through 8.4.5. Nevertheless, due to the great variability in most of these parameters sound engineering judgment is essential in all fatigue life predictions and no final recipe to model the uncertainties can be provided.

[1] A natural stress concentration is considered here as the stress concentration due to the geometry of the detail, but not accounting for any imperfections.

8.4.2 Fatigue Material Properties

The fatigue material properties for both the initiation and propagation lives have been discussed in detail in the previous chapters. It has been shown that the crack propagation properties are not significantly affected by the steel grade, especially considering the calibration of the crack growth rate constant C presented in Chapter 7. However, there seems to be an appreciable difference between the crack initiation properties of the base metal and the weld metal, especially at low strain amplitudes (see Figure 4.25). Based on these observations, the characteristic values presented in Table 8.2 are proposed for any structural steel and weld metal having a yield strength between 250 and 600 MPa. The probabilistic and deterministic values for the crack initiation stage were obtained from the tests on 350WT steel and the corresponding weld metal analyzed in Chapter 4. The mean value for C was adopted from the calibration procedure presented in Chapter 7, which is a reasonable average for C -values reported in the literature. The standard deviations are as defined in Chapter 7.

Table 8.2 – *Characteristic values of material properties.*

Crack Stage	Parameter	Distribution	
		Base Metal	**Weld/HAZ**
Initiation	E [MPa]	LN(205,000, 5,000)	LN(205,000, 5,000)
	$\sigma_f^{'}$ [MPa]	LN(540,20)	LN(630,30)
	b [-]	Det(-0.072)	Det(-0.059)
	$\varepsilon_f^{'}$ [MPa]	LN(0.092,0.02)	LN(0.34,0.07)
	c [-]	Det(-0.43)	Det(-0.63)
Propagation	C [1)]	LN(2.70×10^{-13}, 1.40×10^{-13})	
	m [-]	Det(3.0)	
	ΔK_{th} [$\mathrm{MPa}\sqrt{\mathrm{mm}}$]	LN(60, 6)	

[1)] for da/dN in [mm/cycle] and ΔK in [$\mathrm{MPa}\sqrt{\mathrm{mm}}$]

8.4.3 Detail with no Imperfections

Fabricated steel structures often contain initial imperfections. The strain and stress fields at the critical location are strongly influenced by such imperfections and thus need to be included in the proposed fatigue assessment approach. However, characterizing and modeling imperfections is generally very difficult and time consuming. Therefore,

simplifications have to be made. In any case, the detail of interest should be modeled as accurately as possible ignoring any imperfections and residual stresses. The stress concentration due to the detail geometry such as the weld profile, the presence of a hole, or cross-sectional changes has to be included in the model. To achieve the required analysis accuracy, a global and a local model may be required. The resulting strains and stresses correspond to a perfect case scenario concerning the fatigue initiation life of the detail. Depending on the severity of potential imperfections and the magnitude of the residual stresses, a different fatigue initiation life would be observed.

8.4.4 Severity of Imperfections and Residual Stresses

The strain amplitudes obtained from the model with no initial imperfections constitute a best case, resulting in an upper bound estimate of the fatigue initiation life. In some applications where very strict quality control is implemented the "perfect" model might correspond to a realistic estimate of the crack initiation life. In other cases, where quality control is more relaxed, cracks might have formed during the fabrication process and no initiation life is present.[1] Furthermore, welded details often contain natural stress concentrations that are high enough to render the crack initiation life small. For such cases, or when no detrimental initial imperfections are expected, it might be warranted to use the results of the "perfect" model to determine the crack initiation life. However, for details where a significant portion (roughly 15% and more) of the fatigue life is spent in the initiation stage and where initial imperfections are expected, a finite element model including the imperfections must be investigated.

Large welded and untreated details contain high tensile residual stresses that, together with the applied load, result in maximum stresses under cyclic loading that can exceed the monotonic yield strength of the material. Welded details where heat input is minimized or where stresses are relieved due to heat treatment, cutting or machining may have maximum tensile residual stresses below the yield strength. As observed during the peening carried out in Chapter 5 and from the probabilistic analysis in Chapter 7, conventional peening seems to introduce moderate compressive residual stresses (roughly half the yield strength) at the surface that penetrate less than 1 mm into the material, whereas ultrasonic peening introduces compressive residual stresses close to the monotonic yield strength, which penetrate up to 2 mm into the material. Table 8.3 proposes magnitudes of the residual stresses to use in the fatigue initiation calculations for different applications.

[1] It is noted that standards require more stringent quality control for welds in cyclically loaded structures than for welds in predominately statically loaded structures.

Table 8.3 – *Residual stresses, σ_{res}, to determine $\sigma_{\max}$ for crack initiation calculations.*

Application	σ_{res}
Welded, untreated large scale details	σ_y
Welded details with small heat input Welded, untreated small scale details	$\frac{1}{3}\sigma_y$ to $\frac{2}{3}\sigma_y$
Stress relieved details	0
Conventionally peened details	$-\frac{1}{3}\sigma_y$ to $-\frac{2}{3}\sigma_y$
Ultrasonically peened details	$-\frac{2}{3}\sigma_y$ to $-\sigma_y$

These residual stresses are superimposed to the stresses due to the external loading. Since the material response under cyclic loading is nonlinear, the two stresses cannot be added algebraically. The following procedure is proposed to determine the combined effect of the two stress fields:

1. Determine the strain due to the residual stress from Hooke's law: $\varepsilon_{res} = \sigma_{res} / E$;
2. Determine the strain due to the external loading from the cyclic stress-strain curve: $\varepsilon_{ext} = f(\sigma_{ext})$;
3. Add the two strains to obtain the total strain, $\varepsilon_{tot} = \varepsilon_{res} + \varepsilon_{ext}$, and determine the resulting total stress from the cyclic stress-strain curve.

8.4.5 Failure Criterion

The failure criterion for the experimental part of the small scale tests was defined as the complete severing of the specimens. Since this failure criterion was not practical for the analytical computations, the failure criterion was taken as the crack length corresponding to a certain stage in the crack propagation. For most structures the definition of the appropriate failure criterion involves other considerations, such as critical crack size (toughness), yielding of the remaining cross-section under ultimate design loads, or leakage, which corresponds to transformation of a surface crack to a through-thickness crack. To illustrate these different failure criteria the three examples presented in Section 8.6 will each use a different definition of the final crack length:

- Fatigue repair with hole-drilling and expansion: yielding of the remaining cross-section under the maximum test load;
- Fatigue life of welded non-load-carrying cruciform specimen: formation of through-thickness crack (leak before break criterion);

- Fatigue life of cracked boom: critical crack size, i.e., onset of unstable crack growth at lowest service temperature.

8.5 General Reliability-Based Approach to Predict Fatigue Performance

Based on the preceding work a general reliability-based approach to predict the fatigue performance of structures and their components is proposed. The procedure comprises of the following steps:

1. Identify the critical detail;
2. Set the target safety index (probability of failure);
3. Establish the loading history of the structure;
4. Find the strain and stress spectrum from the load history and structural analysis of the detail;
5. Determine the equivalent strain amplitudes and maximum stresses at the detail with no imperfections or alternatively accounting for imperfections (in the latter case the second part of step 6 is omitted);
6. Estimate residual stresses and the severity of initial flaws to find the strain amplitude and maximum stress used in the crack initiation calculations;
7. Define the variability of the equivalent strains and stresses of the actual detail;
8. Define probabilistic material properties;
9. Define probabilistic distributions of initial crack size and shape, transitional crack size, and final crack size;
10. Determine the stress intensity factor range as a function of crack geometry and stress distribution;
11. Run Monte Carlo Simulation of crack initiation (if necessary) and crack propagation until satisfactory convergence of results is achieved; the initial crack size in the crack propagation calculations is equal to the larger of the initial flaw size or the transitional crack size.

The proposed procedure is applied to three details in the next section.

8.6 Sample Applications

8.6.1 Introduction

Three applications are presented to illustrate the proposed procedure for a reliability-based fatigue life prediction. The applications were chosen to cover a wide range of possible scenarios. The first two examples deal with the fatigue life of laboratory test specimens. They are used to critically assess the performance of the proposed crack

initiation and propagation models. The fatigue life of one of the examples, fatigue repair method of hole-drilling and expansion (Section 8.6.2), is predominantly governed by crack initiation. In the other set of analysed tests, welded non load carrying cruciform specimens (Section 8.6.3), the crack initiation life is negligible. The third example, fatigue life prediction of a cracked boom (Section 8.6.4), is a practical application of a heavy mining equipment detail. For this case it is assumed that a crack was detected and the remaining fatigue life in the presence of this crack is predicted, i.e., the crack initiation life does not need to be considered.

8.6.2 Fatigue Repair with Hole-Drilling and Expansion

Description

Wang [2010] tested flat plates containing a saw-cut edge "crack" terminated by a hole to simulate the repair of a fatigue crack by hole drilling. The specimen geometry is shown in Figure 8.2. The plates were 100 mm wide and 19 mm thick and made of grade CSA-G40.21 350WT steel. The stop hole diameter was 22.2 mm and the cut "crack" 8 mm. The specimens were tested in a universal hydraulic testing machine. They were fully gripped at both ends, preventing end rotation. The free distance between the two grips was 300 mm.

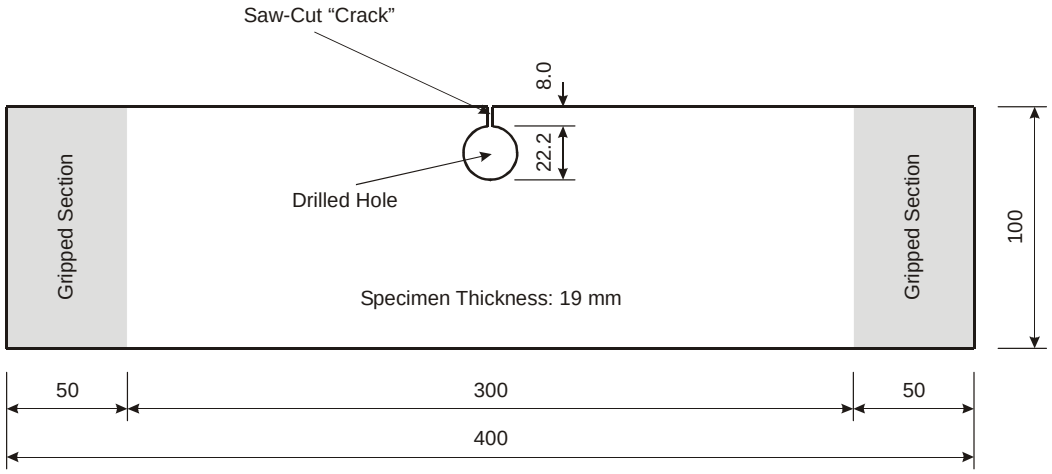

***Figure 8.2** – Specimen with hole-drilling repair tested by Wang [2010], in mm.*

Two repair methods were applied, namely, hole-drilling and hole-drilling with subsequent cold expansion of the hole. For both repair investigations the hole was drilled and expanded before the saw-cut "crack" was introduced. The cold expansion was carried out by pulling a tapered pin through the hole prior to cutting the crack. The shape of the pin was varied to investigate the effect of the expansion ratio, ER (ratio of pin to hole diameter).

The specimens were tested at nominal gross section stress ranges, $\Delta\sigma_g$, between 80 MPa and 160 MPa. Only the results from the four specimens tested at $\Delta\sigma_g = 114$ MPa are considered here. These specimens were selected because both the unexpanded and the expanded specimens had a finite fatigue life. All cracks initiated at the edge of the stop hole as the extension of the "crack", where the strains and stresses are highest. The test results are summarized in Table 8.4. Two different pin sizes were used for the expanded specimens, resulting in expansion ratios of 1.025 and 1.05 as shown in Table 8.4.

Table 8.4 – *Test results of hole-drilling repaired specimens tested by Wang [2010].*

Specimen	$\Delta\sigma_g$	Expansion (*ER*)	Fatigue Life
H1	114 MPa	No	219,000
H6	114 MPa	No	169,000
E3	114 MPa	Yes (1.025)	704,000
E10	114 MPa	Yes (1.050)	1,250,000

Finite Element Model

Wang [2010] developed a model of the plate and the pin with the finite element program ABAQUS®. Deformable 8-node brick elements were used to model the plate. The pin was modeled with collapsed rigid 8-node wedge elements. The finite element mesh of the plate and the pin as used by Wang [2010] is shown in Figure 8.3. The cyclic stress-strain properties for grade 350WT steel, as presented in Chapter 4, were used for the material properties. The results of the finite element analysis as reported by Wang [2010] are adopted for the following work.

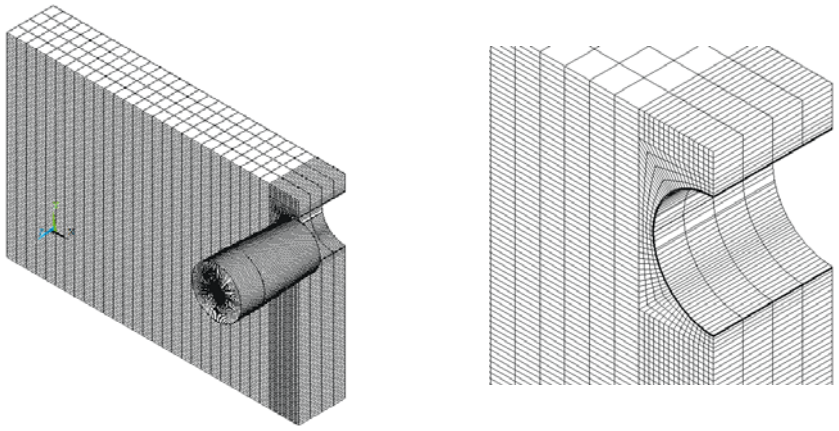

a) overview b) hole detail

Figure 8.3 *– Finite element mesh of hole-drilling repaired plate and the pin.*

Loading and Resulting Strains and Stresses

A constant amplitude nominal gross section stress range of 114 MPa was applied to the specimens, with $\sigma_{\min} = 2$ MPa. Ignoring any residual stresses from drilling, cutting, and expansion, the resulting strain-amplitude was $\Delta\varepsilon/2 = 2.03\times10^{-3}$ and the maximum stress $\sigma_{\max} = 255$ MPa. Wang [2010] assumed in one of the investigated cases that compressive residual stresses of 200 MPa around the hole were introduced by the drilling process. These compressive residual stresses were introduced into the finite element model prior to the application of the load. They were estimated based on results reported in the literature for cut and machined surfaces and reduced by 55% to account for relaxation during cyclic loading.

Residual Stresses, Severity of Fatigue Detail, and Crack Characteristics

The two non-expanded specimens are analysed using the proposed compressive residual stresses of 90 MPa (45% of 200 MPa) as mean values. In order to consider the expected large variability in these residual stresses, a coefficient of variation, COV, of 0.2 is assumed, giving a lognormal distribution LN(90, 18). The two expansion ratios, ER, used in the tests resulted in total compressive residual stresses of 114 MPa for specimen E3 ($ER = 1.025$) and 138 MPa for specimen E10 ($ER = 1.050$). The maximum stress as determined from the finite element model at the edge of the hole, ignoring residual stresses, is still elastic (255 MPa), allowing for a simple subtraction of the residual stresses from this stress. The mean values of the maximum stresses used in the crack initiation predictions become $\sigma_{\max} = 165$ MPa for the unexpanded specimens and $\sigma_{\max} = 141$ MPa and 117 MPa for E3 and E10, respectively. No additional variance is introduced for uncertainties in the load model. Since the compressive residual stresses decrease rapidly with increasing distance from the hole, they are ignored in the crack propagation stage.

Although the drilling and expansion processes may introduce small surface flaws, it is assumed that these flaws are not severe, i.e., the strains and stresses obtained above are used in the crack initiation calculations. To take uncertainties into account, the lognormal distributions given in Table 8.5 are assumed.

The crack is treated as an edge crack and the following deterministic geometry factors are used:

$$\beta_E = 1.0$$
$$\beta_S = 1.12$$
$$\beta_W = \sqrt{\frac{1}{\cos\left(\frac{\pi a}{2W}\right)}},\ W = 100 \text{ mm}$$
$$\beta_G = 1.0 \text{ (uniform gross section stress)}$$

The initial crack size for the crack propagation stage, $a_0 = a_{trans}$, is determined according to equation (2.10). A finite element model of the plate with the hole and the cut "crack" yielded a stress concentration factor at the hole of $k_t = 7.0$, resulting in $a_{trans} = 32.9$ mm. This crack length is assumed as the deterministic value of a_0 for all calculations. The final crack size, a_f, is taken as the crack length when yielding of the remaining cross-section under the maximum applied gross section stress, $\sigma_{app,\max}$, occurs. Introducing $\sigma_{app,\max} = 116$ MPa and the nominal yield strength $F_y = 350$ MPa, a LN(67, 7) distribution is assumed for a_f. The mean final crack length of approximately 70 mm corresponds well to the average observed crack length when the tests were stopped.

The applied gross section stresses, $\sigma_{app,\max} = 116$ MPa and $\sigma_{app,\min} = 2$ MPa, are introduced into the calculations of $K_{\max}$ and $K_{\min}$. Due to uncertainties pertaining to the load cell measurements and fluctuations in the testing machine response, $\sigma_{app,\max}$ is treated as a random variable, LN(114,5). Because $\sigma_{app,\min}$ is small, it is assumed to be deterministic. All statistical distributions for the load and crack characteristics are summarized in Table 8.5.

Table 8.5 – *Assumed statistical distributions for the load and crack characteristics.*

Crack Stage	Parameter	Distribution
Initiation	$\Delta\varepsilon/2$ [-]	LN(2.03×10^{-3}, 2×10^{-4})
	$\sigma_{\max}$ [MPa], Non-Expanded	LN(165,18)
	$\sigma_{\max}$ [MPa], Expanded, $ER = 1.025$	LN(141,18)
	$\sigma_{\max}$ [MPa], Expanded, $ER = 1.050$	LN(117,18)
Propagation	$\sigma_{app,\max}$ [MPa]	LN(116,5)
	$\sigma_{app,\min}$ [MPa]	Det(2.0)
	a_0 [mm]	Det(30.9)
	a_f [mm]	LN(67,7)

Crack Initiation Properties

The tests were carried out on non-welded plates. Therefore the initiation properties for the base metal are used.

Monte Carlo Simulation (MCS)

The results of the MCS for the three specimen types are shown in Figure 8.4. A total of 100,000 simulations were run for each series. Stable results were obtained after roughly 50,000 simulations. The resulting probabilistic distributions are:

- Unexpanded: LN(3.97×10^5, 3.24×10^5)
- Expanded with $ER = 1.025$ (E3): LN(7.99×10^5, 8.49×10^5)
- Expanded with $ER = 1.050$ (E10): LN(1.97×10^6, 2.11×10^6)

The percentage of the crack initiation life increases from 86% for the unexpanded specimens to 93% for E3 to 97% for E10. This confirms that for a detail with a small severity such as a hole the crack initiation stage is dominant. The crack propagation stage becomes negligible when the severity of the fatigue detail is further reduced by introducing compressive residual stresses at the governing location.

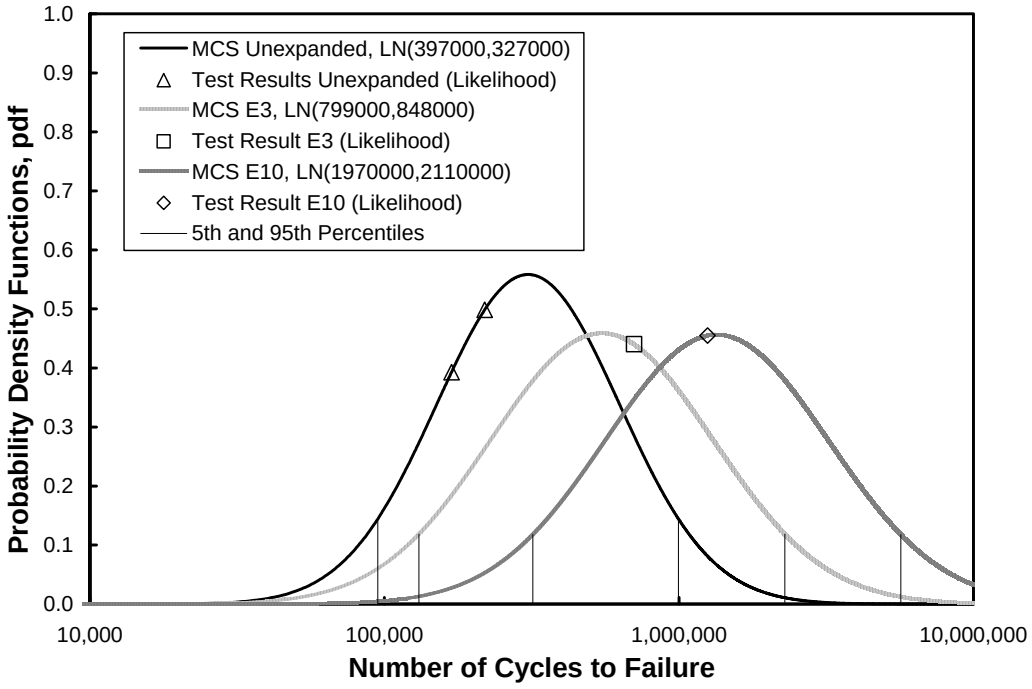

Figure 8.4 *– MCS results of Wang [2010] tests.*

Discussion

All test results lie well within the 90% confidence interval of the simulations. The prediction for the unexpanded specimens tends to be too optimistic (H1 is at the 20th and H6 at the 30th percentile). The other two predictions yield mean fatigue lives very close to the test results (E3 is at the 60th and E10 at the 50th percentile). The overestimation of the unexpanded results is most likely due to the assumed compressive residual stresses from

drilling. As stated earlier, these residual stresses are highly variable and could be anywhere from high tension to high compression depending on the drilling conditions. Using an approach where the residual stresses from drilling are neglected, but a less conservative relaxation of the residual stresses from the expansion is assumed, a better fit might be obtained.

The standard deviation of the Wang [2010] test result predictions increases with an increase in mean fatigue life. The higher standard deviation is primarily a reflection of the flattening out of the crack initiation curve (see Chapter 4) with increasing life, therefore increasing the variability due to changes in loading. Furthermore, the standard deviation of the maximum stress, σ_{max}, was kept constant for all simulations. With the maximum stress decreasing for the expanded specimens, the effect of the standard deviation becomes more pronounced.

8.6.3 Fatigue Life of Welded Non-Load-Carrying Cruciform Specimens

Description

Friedland et al. [1982] tested non-load-carrying cruciform specimens. The test specimens simulated a local cut through the flange or web of a stiffened girder. The specimen geometry is shown in Figure 8.5. The main plate was 25 mm wide, 10 mm thick, and 330 mm long. Two 7 mm thick, 25 mm wide, and 50 mm long plates were attached at mid-length to the main plate with 7 mm fillet welds using the shielded metal arc welding (SMAW) process. All plates were of grade ASTM A588 steel, which is a weathering steel. The specimens were tested at the University of Maryland at room temperature.

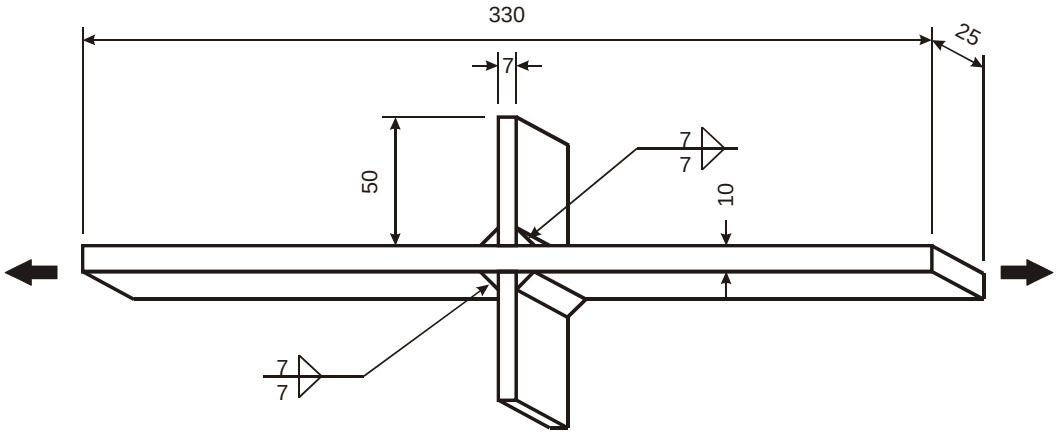

Figure 8.5 *– Non-load-carrying cruciform specimen tested by Friedland et al. [1982].*

Different stages of weathering were investigated. Only the control tests with no weathering are considered here. Axial load was applied to the main plate, the attachments being free. The specimens were tested at nominal gross section stress ranges of 90, 138, 207, and 290 MPa. Five specimens were tested at each stress range. The minimum stress was kept at 3 MPa in all tests. Since some of the specimens at 90 MPa did not fail, they are not investigated any further here. All specimens at the other three stress ranges had finite fatigue lives. The test results are summarized in Table 8.6.

All cracks initiated in the main plate at one or more locations along the toe of a weld. The crack first propagated into the main plate at an angle corresponding approximately to the normal of the principal stresses. The cracks then gradually changed direction until they became perpendicular to the load axis before failure took place at an average net section stress almost equal to the tensile strength of the main plate. The mean regression and design (mean minus two standard deviations) lines of the 15 test results are:

Mean test regression line: $\text{Log}(N_{mean}) = 12.06 - 2.84\log(\Delta\sigma)$

Design line: $\text{Log}(N_{design}) = 11.80 - 2.84\log(\Delta\sigma)$

Table 8.6 – *Test results of cruciform specimens tested by Friedland et al. [1982].*

Stress Range Δσ	**Fatigue Life for Replicate Test Specimens (in Cycles)**				
	1	**2**	**3**	**4**	**5**
138 MPa	634,000	993,000	1,480,000	1,400,000	573,000
207 MPa	259,000	315,000	304,000	307,000	204,000
290 MPa	127,000	113,000	144,000	85,000	114,000

Chen et al. [2005] deterministically predicted the test results using an energy-based approach for the initiation life and a linear elastic fracture mechanics approach without considering crack closure and the threshold stress intensity factor range for the propagation life. No residual stresses and no weld flaws were assumed. The mean regression line for the predicted fatigue life for the three stress ranges is described as follows:

Mean predicted regression line: $\text{Log}(N_{predicted}) = 15.88 - 4.42\log(\Delta\sigma)$

It is evident from the mean predicted regression line of the Chen et al. [2005] results that the slope of the $\Delta\sigma - N$ curve is too shallow compared to the test results. This is most likely due to the assumptions that no residual stresses and initial flaws are present. Since crack initiation becomes predominant at lower stress ranges, the fatigue life is overestimated in this region. Conversely, the prediction at the highest stress range,

$\Delta\sigma = 290$ MPa, is quite accurate. For this stress range the initiation life is less significant than at the lower stress ranges and the effects of residual stresses and initial flaws play a secondary role.

Finite Element Model

The cruciform specimens were analysed with a two dimensional finite element model using ANSYS. An undercut with a radius of 0.2 mm was introduced into the model. This value corresponds to the mean undercut size proposed by Walbridge [2005]. Chen et al. [2005] analysed the specimens ignoring any potential undercut with 4-node plane strain elements using the finite element program ABAQUS. A reference model also using 4-node plane strain elements (Plane42) and the mesh proposed by Chen et al. [2005] was developed first on ANSYS. The results from this model corresponded very well to the Chen et al. [2005] results. A model with the undercut was then generated using 8-node plane strain elements (Plane82) and ANSYS' automatic mesh generator. The 8-node elements were preferred to the 4-node elements since they better represent the curved shape of the undercut. The maximum element size at the undercut was limited to 0.032 mm and increased to 0.25 mm at the edges of the model. The limitation of 0.032 mm at the undercut corresponds to the ratio of the mesh to flaw size used to model the flaws of the small scale specimens in Chapter 6. The finite element model is shown in Figure 8.6. The cyclic stress-strain parameters of the weld metal (see Table 8.2) were used for all elements.

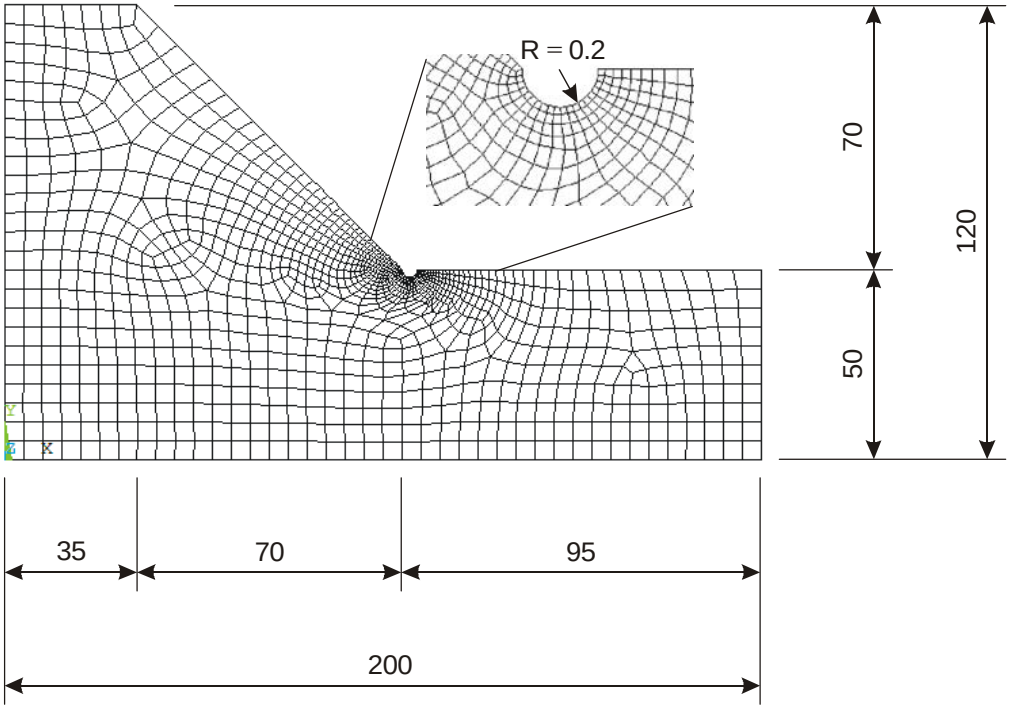

Figure 8.6 *– Finite element model of a cruciform specimen with potential undercut.*

Loading and Resulting Strains and Stresses

In order to get the cyclic response from the finite element model, the specimen was loaded to the maximum applied stress (141, 210, and 293 MPa, corresponding to the peak stress for each test conditions of the test program) in time step 1 then unloaded in time step 2 to the minimum applied stress (3 MPa for all specimens), and finally reloaded to the peak stress levels in time step 3. No residual stresses were introduced into the finite element model. The strain amplitudes used in the crack initiation life calculations were taken as half the difference between the maximum principal strains after time steps 3 and 2. The maximum principal stress distribution was plotted after time step 3 as is illustrated in Figure 8.7**.** The direction of the principal stresses correspond well with the angle of the crack path as reported by Friedland et al. [1982].

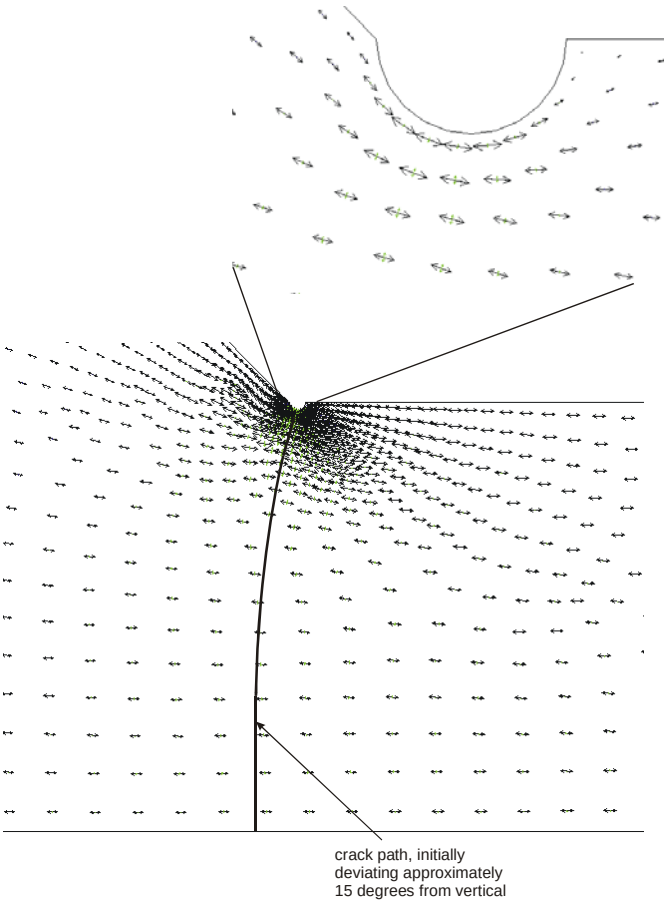

Figure 8.7 *– Principal stresses.*

The governing strain amplitudes, $\Delta\varepsilon/2$, and maximum stresses, $\sigma_{\max,0}$, taking into account the undercut, but ignoring residual stresses, are summarized in Table 8.7. As stated earlier, the strain amplitudes are not be affected by residual stresses.

Table 8.7 – *Strain amplitudes and maximum stresses for cruciform specimens.*

Nominal Stress Range $\Delta\sigma$ [MPa]	Strain Amplitude $\Delta\varepsilon/2$ [-]	Max. Stress $\sigma_{max,0}$ [MPa]
138	1.81×10^{-3}	445
207	2.45×10^{-3}	453
290	4.18×10^{-3}	472

The specimens were cut from a bigger assembly, therefore releasing part of the residual stresses. However, due to the restraint from the attached stiffener, the residual stresses are, contrary to the small scale specimens tested in Chapter 5, most likely not negligible. A tensile residual stress of 100 MPa is assumed at the toe of the welds. Using the procedure outlined at the end of Section 8.4.3, the maximum stresses, $\sigma_{\max}$, slightly increase to 447 MPa for $\Delta\sigma = 138$ MPa, to 455 MPa for $\Delta\sigma = 207$ MPa, and to 473 MPa for $\Delta\sigma = 290$ MPa. Since there are fillet welds on both sides of the main plates, the tensile residual stresses for the crack propagation stage were assumed to be 100 MPa on both faces of the main plate, and -100 MPa at mid-thickness. Furthermore, a fourth order polynomial distribution satisfying equilibrium was assumed. The probabilistic values are modeled with a normal distribution having a mean value of 100 MPa and a standard deviation of 20 MPa on both faces of the main plate. The stress gradient correction factors for the residual stresses are presented in the following.

Severity of Fatigue Detail and Crack Characteristics

Although no measurements are reported in Friedland et al. [1982] it is assumed that the weld toe undercut introduced in the finite element model is a realistic representation of an initial flaw. Therefore, no changes need to be made to the strains and stresses obtained from the finite element analysis. To take into account uncertainties due to the starting flaw geometry, the statistical distributions for the load effects given in Table 8.8 are used.

Once a fatigue crack has initiated, it is treated as a semi-elliptical surface crack, at one location only. The initial crack size, $a_0 = a_{trans}$, is determined according to equation (2.10). The finite element analysis indicates that the stress concentration factor at the undercut is $k_t = 4.86$, yielding $a_{trans} = 0.206$ mm. As for the small scale tests investigated in the previous chapters, this crack size is practically equal to a_{init} and it is therefore assumed that a_{trans} is equal to a_{init}, i.e., $a_0 = a_{init}$ in all cases. The final crack size is taken as the main plate thickness (leak before break), $a_f = 10$ mm. The crack is assumed to be elliptical and its aspect ratio, a/c, is assumed to remain constant throughout the crack propagation stage. The statistical distributions of the crack properties are summarized in Table 8.8. The standard deviations for a_0 and a/c are obtained based on work from Walbridge [2005].

The following geometry factors are used in the calculation of the stress intensity factor (see also equations (6.10) to (6.14)):

$$\beta_E = \frac{1}{\Phi_0},$$

$$\Phi_0 = 0.2568\left(\frac{a}{c}\right)^4 - 0.7635\left(\frac{a}{c}\right)^3 + 0.9916\left(\frac{a}{c}\right)^2 + 0.0875\left(\frac{a}{c}\right) + 1$$

$$\beta_S = 1.12$$

$$\beta_W = \sqrt{\frac{1}{\cos\left(\frac{\pi a}{2t}\right)}},\ t = 10 \text{ mm}$$

$$\beta_G = SCF\left(1 + \frac{2A}{\pi}a + \frac{B}{2}a^2 + \frac{4}{3}\frac{C}{\pi}a^3 + \frac{3}{8}Da^4\right)$$

Table 8.8 – *Statistical distributions of load effects and crack properties.*

Parameter	**$\Delta\sigma$ = 138 MPa**	**$\Delta\sigma$ = 207 MPa**	**$\Delta\sigma$ = 290 MPa**
Crack Initiation			
$\Delta\varepsilon/2$ [-]	LN(1.81×10^{-3} 9×10^{-5})	LN(2.45×10^{-3}, 1.3×10^{-4})	LN(4.18×10^{-3}, 2.1×10^{-4})
$\sigma_{\max}$ [MPa]	N(447,5)	N(455,5)	N(473,5)
Crack Propagation			
$\sigma_{app,\max}$ [MPa]	N(141,2)	N(210,3)	N(293,4)
$\sigma_{app,\min}$ [MPa]	Det(3)	Det(3)	Det(3)
σ_{res} [MPa]	N(100,20)	N(100,20)	N(100,20)
a_0 [mm]	LN(0.2,0.05)	LN(0.2,0.05)	LN(0.2,0.05)
a_f [mm]	Det(10)	Det(10)	Det(10)
a/c [-]	LN(0.5,0.16)	LN(0.5,0.16)	LN(0.5,0.16)

The stress concentration factor, SCF, and the constants A through D for the applied loads were determined from the stress distribution obtained from the finite element analysis without the undercut (see Chen et al. [2005]). Since the load response was mostly elastic even for the high stress range, the same stress gradient factor was used for $\sigma_{app,\max}$ and $\sigma_{app,\min}$, irrespective of the stress range. The factors for the residual stresses are based on a fourth order polynomial with the specified tensile residual stress at both faces of the main plate and the same specified residual stress, but compressive, at mid-

thickness. The resulting deterministic values for all the coefficients in the expression for the stress gradient correction factor are given in Table 8.9.

Crack Initiation Properties

The cracks clearly initiated at the toe of the fillet weld. Therefore, the initiation properties for the weld/HAZ presented in Table 8.2 are used.

Table 8.9 – *Constants used to determine the stress gradient geometry factors,* β_G.

Stress Field	*SCF*	*A*	*B*	*C*	*D*
Applied Loads	1.91	-1.68	1.00	-0.251	0.0220
Residual Stresses	1.00	0.20	-0.42	0.080	-0.0040

Monte Carlo Simulation

The results of the MCS for the three test series are shown in Figure 8.8. A total of 100,000 simulations were run for each series. Stable results were obtained after roughly 50,000 simulations. The resulting probabilistic distributions are:

- $\Delta\sigma = 138$ MPa: LN(8.54×10^5, 5.31×10^5)
- $\Delta\sigma = 207$ MPa: LN(2.55×10^5, 1.55×10^5)
- $\Delta\sigma = 290$ MPa: LN(1.01×10^5, 6.16×10^4)

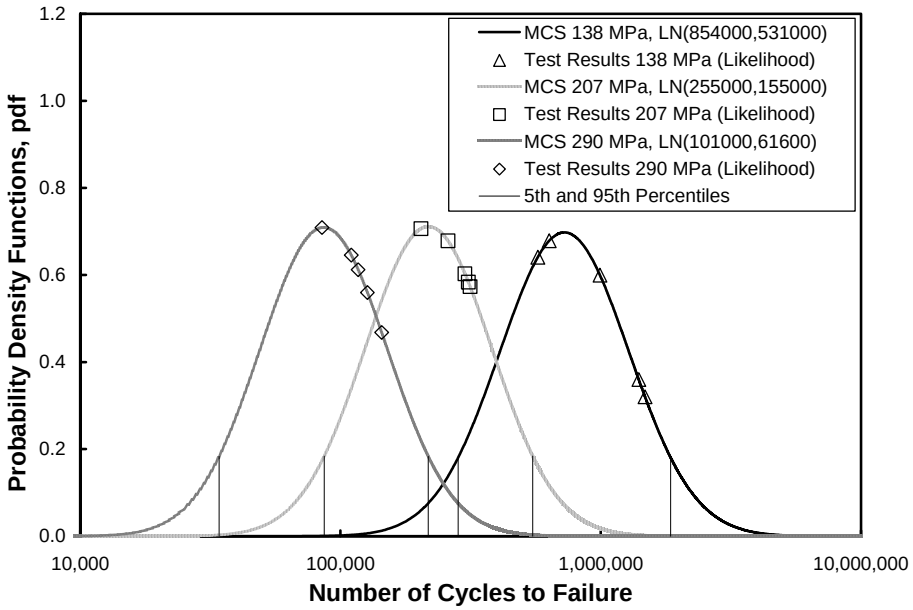

Figure 8.8 *– MCS results of Friedland et al. [1982] tests.*

The fraction of the total fatigue life expended in the crack initiation phase is negligible for all three series (less than 3%). This confirms that for a detail with a severe discontinuity (untreated weld toe undercut) the total fatigue life is essentially equal to the propagation life.

Discussion

All test results lie well within the 90% confidence interval of the simulations. In fact, the test results for $\Delta\sigma = 138$ MPa lie between the 40th and the 90th percentiles, the test results for $\Delta\sigma = 207$ MPa between the 45th and the 75th percentiles, and the test results for $\Delta\sigma = 290$ MPa between the 50th and the 75th percentiles. Generally, the predictions tend to be conservative. There might be several reasons why shorter lives are predicted, the most likely candidates being an overestimation of the severity of the undercut or the tensile residual stresses.

The mean and design $\Delta\sigma - N$ curves can be plotted using the MCS results for the three stress ranges used in the Friedland et al. [1982] test program. Figure 8.9 shows the two curves.[1] Also shown are the mean and design curves obtained from the test results [Friedland et al. 1982] and the mean curve obtained in a deterministic prediction by Chen et al. [2005].

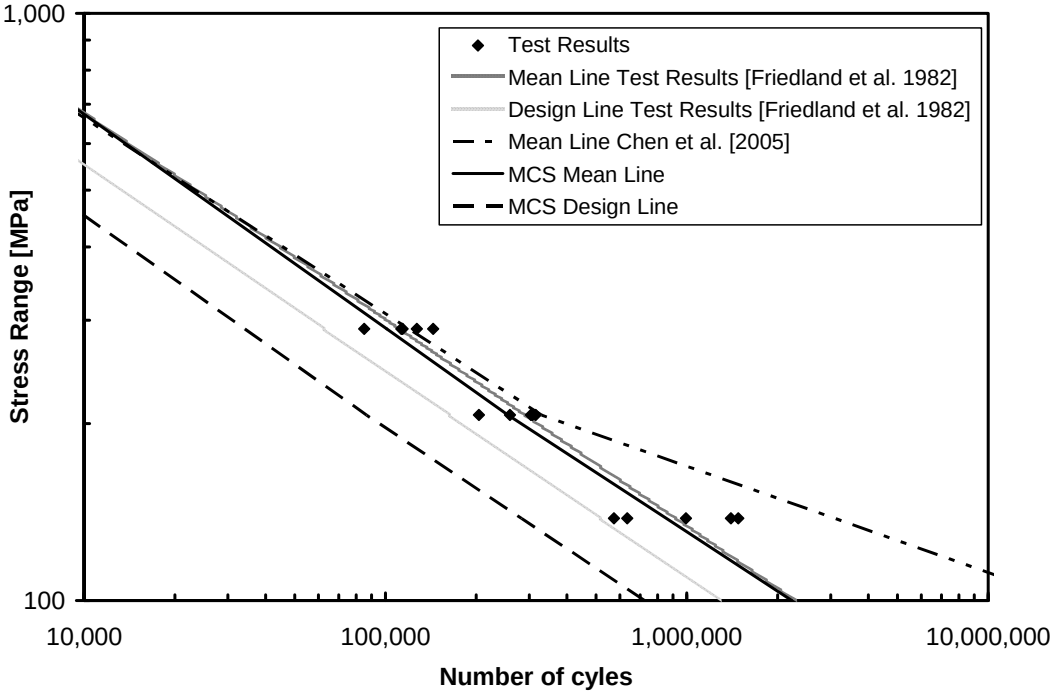

***Figure 8.9** – Fatigue curves for Friedland et al. [1982] tests.*

[1] A linear interpolation between the three stress ranges was assumed.

The mean probabilistic predictions result in a more consistent fit of the test data than the Chen et al. [2005] predictions, which assumed no undercut, no threshold stress intensity factor, and no crack closure. The MCS mean line shows excellent agreement with the mean line for the test results. However, it is important to note that the MCS design line is significantly lower than the test results design line. This is a reflection of the larger variability in the simulations than in the test results, which are all from the same source. The probabilistic analysis of the test results most likely underestimates the variability in material properties and imperfections, which would be present in test specimens from different sources. This illustrates that establishing design curves from just one source of test data may result in design curves that are too optimistic.

8.6.4 Fatigue Life Prediction of an Excavator Boom

Description

Yin et al. [2006] investigated the remaining fatigue life of a cracked boom of an excavator. Deterministic predictions as a function of the detected crack size were made. The predictions were summarized in charts showing the remaining service days as a function of the crack location and crack length. Measurements were taken on the excavator, both under controlled and in-service loading. The boom consisted of two box girders joined together near their extremities. Each box girder was stiffened with perforated diaphragms. Based on the stress distribution along the boom, the box girders were divided into four load effect zones. In each zone the most probable fatigue crack location was identified. An overview of the boom with the zones and crack locations is shown in Figure 8.10.

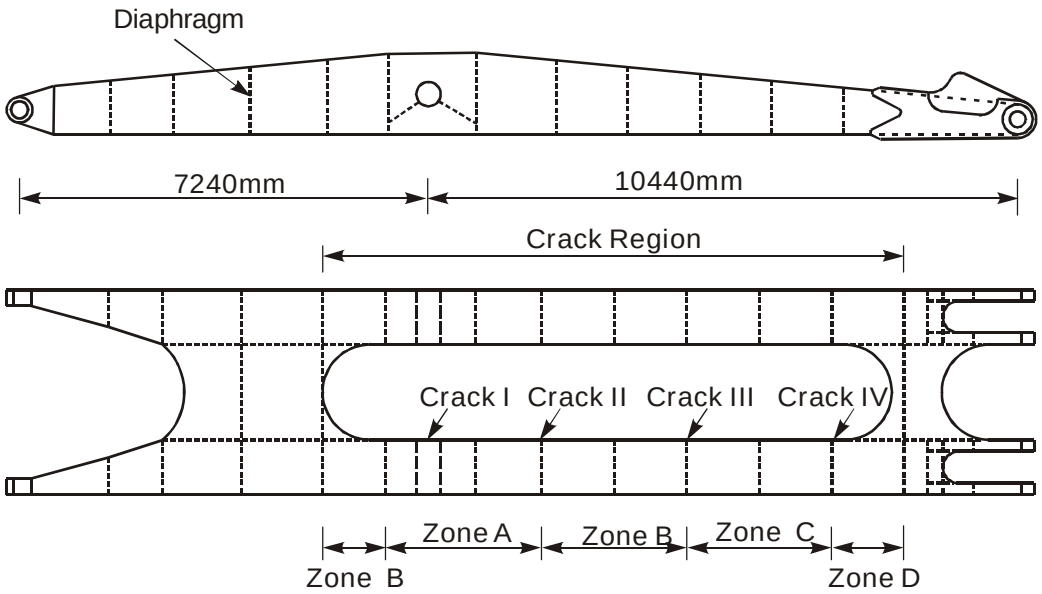

Figure 8.10 *– Investigated boom of an excavator.*

The box girders consisted of a 1038×37 mm bottom and a 1038×22 mm top flange held by two 16 mm thick webs. The total height varied from approximately 900 mm to 1400 mm. A typical cross-section of one box girder is shown in Figure 8.11.

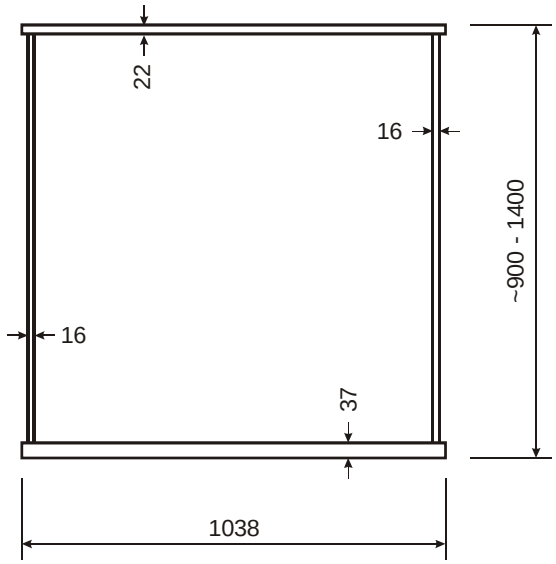

Figure 8.11 *– Typical cross-section of a box girder.*

Field Measurements

The boom was instrumented to collect strain and displacement data used to validate a finite element model and determine the strain history in the boom during normal operation. A total of 32 strain gauges were placed on the flanges and webs of both girders in two sections with regions of little stress concentration. Two cable transducers were mounted to determine the position of the boom at any given time.

Data were collected during a controlled field test. The position of the shovel under no load and under full load was monitored with a camera and corroborated to the cable transducer measurements. The position of the shovel was then correlated to the strain measurements. This correlation was used to determine the stresses during two 24 hour in-service measurement periods within one week. The collected strain data indicated that the loading sequences and magnitude were very similar for the two periods. Furthermore the data showed that both box girders were stressed similarly, confirming that no significant out-of-plane or torsion effects were present.

Governing Crack Location

With the help of the field measurements Yin et al. [2006] developed a detailed finite element model of the boom. A very good match between the measured and calculated stresses was obtained. From the output of the detailed finite element model it was

determined that the most likely place for crack initiation was at one of the corners of the bottom flange to web connection in Zone A (Crack I). This is consistent with field observations indicating that cracks in the boom often start at the toe of the diaphragm to flange weld at the high stress location identified in the finite element model, propagating into the web and forming a through-thickness crack with a tip in the flange and a tip in the web. Therefore only this location is further investigated here.

Equivalent Stress Range

Yin et al. [2006] used the rainflow counting method to determine the stress spectrum from a transformation of the collected data during one of the two one-day measurement periods. The resulting stress spectrum at Crack I location is shown in Figure 8.12.

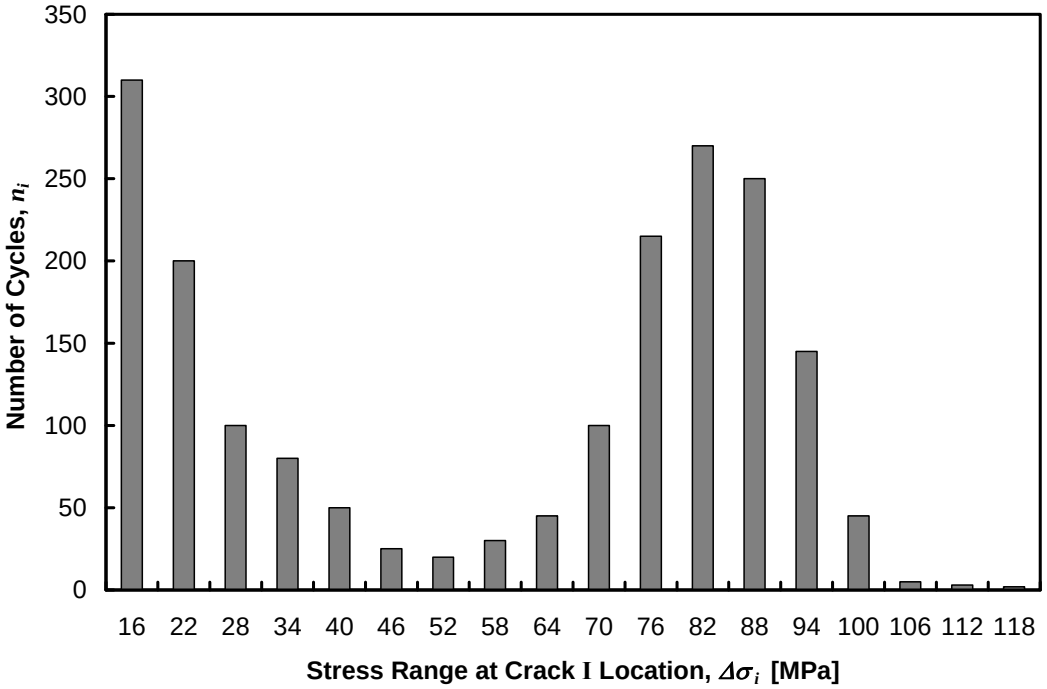

Figure 8.12 *– Stress range spectrum at Crack I location.*

The total number of recorded stress cycles is $N_e = 1900$. Using a slope of $m = 3.0$ for all stress ranges in Figure 8.12 the sum of the individual damages is $\Sigma n_i \Delta\sigma_i^m = 652 \times 10^6$. The equivalent stress range, $\Delta\sigma_e$, becomes (equation (8.8)):

$$\Delta\sigma_e = \left(\frac{\sum n_i \Delta\sigma_i^{3.0}}{N_e} \right)^{1/3.0} = 70 \text{ MPa}$$

Reliability Index

The limit state function can be formulated as $G(\mathbf{Z}) = N(\mathbf{Z_R}) - N(\mathbf{Z_S})$, where $N(\mathbf{Z_R})$ is the calculated crack propagation (resistance) and $N(\mathbf{Z_S})$ is the number of stress cycles applied to the boom before it has to be repaired (solicitation). The goal is to determine $N(\mathbf{Z_S})$ for a target reliability index. Assuming that $N(\mathbf{Z_R})$ follows a lognormal distribution with mean μ_R and standard deviation σ_R and that $N(\mathbf{Z_S})$ is deterministic (all variability is included in $N(\mathbf{Z_R})$), the reliability index can be estimated as:

$$\beta = \frac{\mu_G}{\sigma_G} = \frac{\mu_{R,normal} - N_S}{\sigma_{R,normal}} \tag{8.12}$$

where the mean and standard deviation of the lognormal distribution of $N(\mathbf{Z_R})$, μ_R and σ_R, are transformed into normal distributions, $\mu_{R,normal}$ and $\sigma_{R,normal}$, using the procedure outlined in Appendix A. Equation (8.12) can be rewritten to find a closed form solution for the deterministic number of cycles until the boom has to be repaired, N_S:

$$N_S = \mu_{R,normal} - \beta \cdot \sigma_{R,normal} \tag{8.13}$$

Failure of the boom would most likely not lead to any loss of life since commonly only two persons are involved in loading a truck, namely the truck and excavator operators. Both are protected in their cabins and the risk of them getting hurt is rather small. Furthermore, the excavator operator should be aware of the cracks (they were detected) and would most likely keep an eye on their propagation. These two arguments suggest that a rather low target safety index can be accepted. However, if a boom failure occurs, the excavator is immediately out of service and a repair is much more involved than on a cracked, but not severed, boom. This will lead to a significant loss of production time and revenue. For these reasons, an "average" safety index, $\beta = 3.0$, as proposed in Section 8.2 is used in the following calculations.

Crack Characteristics and Stress Intensity Factor Calculations

Fatigue cracks initiate at the toe of a diaphragm to flange (web) weld. The state of stress at this location is very complex and the use of the geometry correction factors, β_i, does no longer give satisfying results. Yin et al. [2006] therefore used finite element analysis results to determine the stress intensity factors, K_i, based on the equivalent stress range, $\Delta\sigma_e$, discussed earlier. Closed form solutions for K_i were derived based on the ratio of the crack length in the flange to the crack length in the web. An analysis of different crack lengths in the flange and web showed that the fastest crack propagation, and thus the most conservative results, is obtained when both cracks are of equal length. The following simplified expression for K_i (in $\text{MPa}\sqrt{\text{mm}}$) at Crack I location is used for the fatigue calculations:

$$K_i = A_0 + A_1 a = 670 + 4.6a \tag{8.14}$$

where a is the crack length in the flange (equal to half of the total crack length). This expression for K_i includes uncertainties due to the loading ($\Delta\sigma_e$), the finite element model, and the regression analysis. Therefore both constants, A_0 and A_1, are modelled with a normal distribution having a COV = 0.1, i.e., $A_0 = \text{N}(670, 67)$, $A_1 = \text{N}(4.6, 0.46)$.

The stress ratio, R, is, according to Yin et al. [2005], approximately 0.5, not considering any residual stresses. Since the crack propagates along the toe of the weld, it is in a tensile residual stress field, which increases the effective stress ratio, R_{eff}. Therefore, the crack closure phenomenon is negligible ($R_{eff} > 0.28$). The crack propagation model becomes:

$$N_{total} = \int_{a_0}^{a_f} \frac{da}{C \cdot \left(\Delta K^m - \Delta K_{th}^m\right)} \tag{2.9}$$

where $\Delta K = K_{\max} - K_{\min}$, and $K_{\max}$ and $K_{\min}$ are directly determined from equation (8.14).

The initial crack size, a_0, corresponds to the detected crack length. Since the inspection is commonly done just visually, some variability in a_0 has to be considered. This is done by taking a lognormal distribution with a standard deviation of 5 mm irrespective of the inspected crack size.

The excavator operates in Northern Alberta, where temperatures in winter are often below
–40°C. It is therefore prudent to limit the maximum stress intensity factor to the critical crack size at very cold temperatures. According to Yin et al. [2006] the toughness of grade 350WT steel at $-50°\text{C}$ is approximately 3,000 $\text{MPa}\sqrt{\text{mm}}$. The corresponding critical crack length is approximately $a_f = 220$ mm. At this crack size the net section stress is less than 200 MPa, confirming that brittle fracture occurs before yielding of the remaining cross-section. The uncertainty in toughness and thus in a_f is considered with a lognormal distribution for a_f, LN(220, 22).

Monte Carlo Simulation

MCS of the remaining fatigue life, N_R, for four different initial crack sizes, $a_0 = 50$, 100, 150, 200 mm, were run. The probability density functions of these simulations are shown in Figure 8.13. A total of 50,000 simulations were run for each series. Stable results were obtained after roughly 10,000 simulations. The resulting probabilistic distributions are:

- $a_0 = 50$ mm: LN(4.63×10^5, 2.72×10^5)
- $a_0 = 100$ mm: LN(2.25×10^5, 1.33×10^5)
- $a_0 = 150$ mm: LN(9.63×10^4, 6.16×10^4)
- $a_0 = 200$ mm: LN(2.31×10^4, 2.58×10^4)

The observed reduction in N_R with increasing a_0 can also be illustrated by plotting the reliability index, β, as a function of the number of cycles until the boom has to be repaired, N_S. This is presented in Figure 8.14 according to equation (8.13). For a given target reliability the number of cycles until failure reduces significantly with increasing a_0. For example for $\beta = 3.0$, N_S is 61,000 cycles for $a_0 = 50$ mm, but drops to 1,000 cycles for $a_0 = 200$ mm.

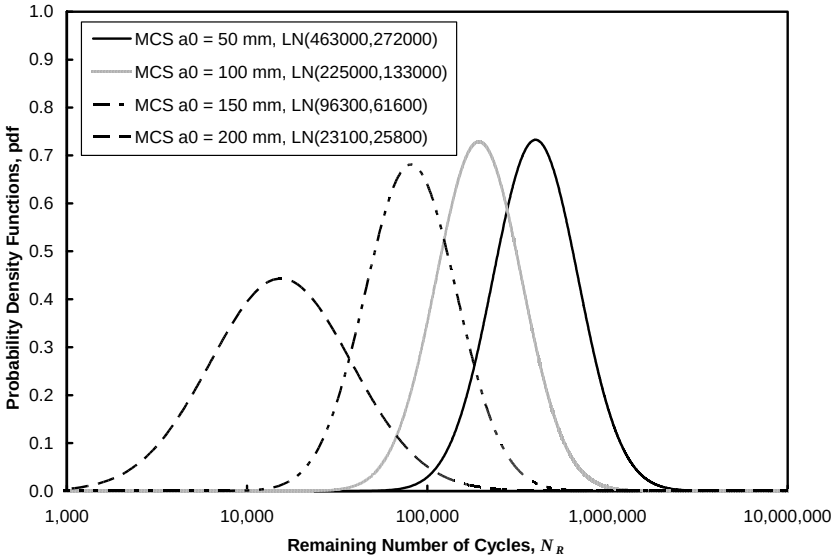

Figure 8.13 *– MCS results for the cracked boom.*

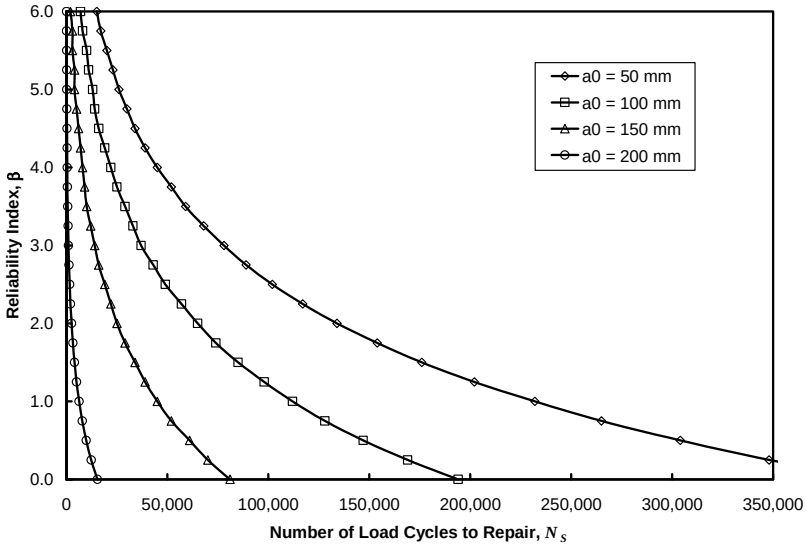

Figure 8.14 *– Reliability index, β, as a function of the number of cycles to required repair, N_S, for different initial crack sizes, a_0.*

The number of cycles to failure is not a particularly useful measure of the remaining fatigue life of mining equipment. It is more appropriate to express the remaining life in operating hours or days. The observed number of stress cycles per day based on the field measurements by Yin et al. [2006] is approximately 1,900 (see Figure 8.12). However, this value was obtained from measurements during two days only and variability in the number of stress cycles must be accounted for. It is assumed that the number of load cycles is a reasonable estimate of the mean value and that the excavators operate at a steady rate, i.e., that the standard deviation is rather small. Therefore a normal distribution, N(1900,20), is assumed for the number of stress cycles per day, N_{day}. The limit state function, in days, becomes:

$$G(\mathbf{Z}) = \frac{N(\mathbf{Z_R}) - N_S}{N_{day}(z_{day})} \tag{8.15}$$

Since N_S is no longer a stand alone term, no closed form solution exists for N_S for a specific target reliability index, β. The number of safe operating days has to be determined through iteration. A first estimate of N_S has to be made and MCS run to determine the number of simulations with $G(\mathbf{Z}) < 0$. The probability of failure, p_f, is the number of simulations with $G(\mathbf{Z}) < 0$ divided by the total number of simulations. The reliability index can be determined from the resulting probability of failure as the inverse of the normalized cumulative distribution function. If β is larger than the target reliability, N_S is increased in the next iteration (and vice versa for β smaller than the target reliability) until the target reliability converges. The number of remaining days of operation is finally obtained by dividing the converged N_S by the mean value of N_{day} (1,900). Due to the additional variability in N_{day}, N_S for a given β will be smaller than the values presented in Figure 8.14. The results of these iterations for a target reliability $\beta = 3.0$ and four initial crack sizes varying from 50 mm to 200 mm are summarized in Table 8.10.

Table 8.10 – *Remaining operation days for $\beta = 3.0$ and different initial crack sizes, a_0.*

a_0	Remaining Operating Days
50 mm	43
100 mm	20
150 mm	5
200 mm	<< 1

Discussion

Yin et al. [2006] developed charts where the remaining fatigue life in days as a function of the crack length in the flange and in the web. The calculations were based on a deterministic approach with the failure criterion being yield of the remaining cross-section. In order to account for the uncertainty in the crack propagation calculations, Yin et al. [2006] reduced the calculated fatigue life by a safety factor that depended on the crack length. Since the remaining days determined by Yin et al. [2006] were not based on the same failure criterion as defined in the present work, the results cannot be compared. However, it is possible to evaluate the safety factors used by Yin et al. [2006] with the safety margin obtained by dividing the mean lives in Figure 8.13 with the remaining days of operation presented in Table 8.10 multiplied by 1,900 cycles per day. The safety margins found in the present study are compared in Table 8.11 to the safety factors proposed by Yin et al. [2006].

Table 8.11 – *Comparison of safety margins.*

a_0	Safety Factor according to Yin et al. [2006]	Safety Margin Found in Present Study
50 mm	1.35	5.72
100 mm	1.45	5.92
150 mm	1.55	9.63
200 mm	1.64	>> 10

It is evident that the arbitrary safety factors used by Yin et al. [2006] correspond to a reliability index that is significantly lower than $\beta = 3.0$. However, Yin et al. [2006] correctly anticipated that the safety factor has to increase with increasing crack length.

8.7 Summary

A general reliability-based approach to predict the fatigue performance of structural components was proposed. The proposed approach is applicable to any detail subjected to cyclic loading, whether the detail is new, has been in service for some time or has undergone repair.

The difficulty in defining an appropriate target reliability was discussed in Section 8.2. Information from the literature was used to show that the reliability index, β, is a function of several factors, some of which are complex to evaluate. Based on this review it was concluded that β can be taken as rather low, i.e., around 2.0, for redundant structures, where the consequence of failure is small and the components will be

inspected. For non-redundant structures with severe consequence of failure the reliability index should be set to at least 4.0. A reasonable "average" reliability index for many structures is around 3.0 for structural components and materials that will allow cracks to grow to sizes large enough to be detected and monitored before failure.

In Section 8.3, fatigue loading was examined from a probabilistic point of view. The background to the fatigue provisions in North American and European codes was reviewed. Similar procedures were employed in these codes to transform general load measurements into fatigue loading. The fatigue loads adopted in these design codes are based on simplifying assumptions, which may result in large uncertainty, often not suitable for a reliability-based management of fatigue failures. Depending on the desired level of accuracy, field measurements may need to be carried out to better assess the loading on a structure. Sound planning of such measurements (what should be measured where and how for how long) is essential to obtain a maximum of information at reasonable cost. The field measurements can be transformed into fatigue loading and equivalent strains and stresses using a procedure similar to that employed by code writers. The procedure is illustrated in Figure 8.1 and mathematically represented by equations (8.5) through (8.11).

The probabilistic nature of the fatigue resistance was assessed in Section 8.4. The groundwork for this was laid in the previous chapters. Fatigue material properties for different steel grades are proposed in Table 8.2. Since it is often too cumbersome to include initial imperfections in a finite element model, it was suggested to first conduct an analysis of a detail without any flaws and residual stresses. The obtained results are appropriate to use in fatigue initiation life calculations for details, where natural stress concentrations are high or where no initial imperfections are expected. For cases with initial imperfections and where a significant fraction of the total fatigue life is spent in the initiation stage and for cases where no data for local strains and stresses can be found elsewhere or reasonably estimated, a local model containing a flaw and possibly residual stresses has to be investigated.

A general reliability-based approach to predict fatigue performance was proposed in Section 8.5. Eleven steps were identified. In particular cases, it might not be necessary to apply some of these steps, as e.g. when the procedure is used to predict the results of fatigue tests.

The proposed general reliability-based approach was applied to three examples in Section 8.6. The first two examples demonstrated the prediction of test results. Although the two examples were of very different nature, one primarily consisting of crack initiation life and the other primarily of crack propagation life, the test results were predicted accurately. The resulting probabilistic distributions of the fatigue lives can be used to establish $\Delta\sigma - N$ design curves adequately incorporating the variability of all parameters. The third example predicted the remaining fatigue life of a cracked box girder. The example demonstrated that much more reliable recommendations can be

made using a reliability-based approach compared to a deterministic approach, where the uncertainty needs to be accounted for through somewhat arbitrarily defined global safety factors.

In conclusion, the examples demonstrated that the proposed reliability-based approach can be a very powerful tool for the management of fatigue failures. Both, the crack initiation and propagation stages can be adequately modelled, as long as reasonable data and assumptions concerning the loading and resistance are considered.

9. SUMMARY, CONCLUSIONS, AND RECOMMENDATIONS

9.1 Summary

The fatigue performance of structural steel is a function of several factors, such as the loading and service conditions, the material properties, the detail configuration, and initial imperfections. Since these factors are often subjected to considerable variability, reliability-based approaches must be used to properly account for the uncertainties.

Due to the large variability observed in fatigue resistance, it is best determined through testing. However, fatigue testing is time consuming and expensive. Furthermore, actual structural components are often too large to be tested in a laboratory. Therefore, alternative approaches such as fracture mechanics, need to be applied.

Several investigations based on probabilistic approaches for fatigue life prediction have been carried out in the past few years, especially in the offshore and nuclear industries. These investigations have generally assumed that a fatigue crack is present, thus focusing only on the crack propagation stage. However, many structural components contain flaws that do not have a sharp tip and a significant portion of the fatigue life of the structural component is spent initiating a crack. The potential of crack initiation therefore needs to be included in a reliability-based approach.

This work focused on the development of a reliability-based approach to manage fatigue failures accounting for crack initiation, crack propagation, and final fracture and incorporating the post weld treatment method of ultrasonic peening. A statistical analysis of the fatigue material properties of the base and weld metal was conducted. The probabilistic properties of the base metal, CSA G40.21 Grade 350WT [CSA 2004], were established based on tests carried out earlier at the University of Alberta and elsewhere, whereas tests were conducted within this program to establish the fatigue material properties for a matching weld metal.

Small and large scale fatigue tests on structural components were carried out. Small scale welded tests were used to assess the effectiveness of post weld treatment using stress-relieving, conventional peening, and ultrasonic peening. The large scale tests were carried out to assess the suitability of a ground flush weld repair and the effectiveness of ultrasonic peening on large plates.

The test results from the small scale tests were predicted with deterministic approaches. Finite element models were developed to assess the effect of spherical flaws and residual stresses on the strain and stress distribution. Several approaches to describe the crack initiation and propagation lives were investigated. The approaches considered different flaw or crack sizes and locations, different magnitudes of residual stresses, absence or presence of the threshold stress intensity factor range, and absence or presence of crack closure. From this investigation, the most suitable approach was determined and

validated through a reliability-based analysis, resulting in a probabilistic prediction of each test series. A sensitivity study of each probabilistic parameter was carried out and the most influential parameter, the crack growth constant C, calibrated by maximizing the likelihood of each test result.

Based on these findings, a general reliability-based approach to manage fatigue failures, including the uncertainty in loading, was presented in Chapter 8. The general reliability-based approach was applied to three examples. Two examples included the prediction of test results from a detail with a rather low stress concentration, i.e., primarily affected by crack initiation, and from a detail with a severe fatigue detail, i.e., primarily affected by crack propagation. The third example consisted of predicting the remaining fatigue life of a cracked box girder subjected to in-service, i.e., variable, loading.

The application examples showed that the proposed approach reliably predicts fatigue test results and can be used to estimate the remaining fatigue life of in-service components as a function of the desired probability of failure. It is imperative that accurate probabilistic models for initial flaw or crack sizes, shapes, and locations, as well as residual stresses, loading conditions, and material properties be used. Most of these models have been developed as part of this work. In some cases, such as for initial flaws, more information is required to characterize their geometry and distribution or to characterize their effect on local stresses and strains.

Several simplifying assumptions were made to keep the scope focused. The most important ones are:

- Only mode I loading was considered. This mode governs crack behaviour in the propagation stage [Broek 1989].
- The location of cracks or flaws was assumed to be known a priori and interaction between multiple flaws or cracks was ignored.
- Initial weld flaws were assumed to be spherical or circular.
- The stress sequence was not considered in the probabilistic approach.
- The transitional crack size, a_{trans}, was determined by comparing short to long crack behaviour according to Dowling [1979], equation (2.10). Using this relationship it was concluded that $a_{trans} = a_{init}$.

9.2 Conclusions

The following conclusions can be drawn from the work described above:

1. Probabilistic fatigue life prediction is best modelled with a strain-based approach for the crack initiation life and a linear fracture mechanics approach, including the threshold stress intensity factor range and crack closure, for the crack propagation life.

2. For common structural steel grades, crack propagation properties are generally not noticeably affected by the steel grade or type of metal (base or weld). However, crack initiation properties used in a strain-based approach show significant scatter depending on the steel grade and whether we are dealing with the base or weld metal.

3. Simulated fatigue crack repairs by gouging and re-welding on 35 mm thick flat plates showed that components prepared with sound weld procedures and diligent workmanship possess a fatigue resistance comparable to the base metal.

4. The weld procedure proposed for field repair was found to lead to excessively large slag inclusions, which results in a large reduction in the fatigue resistance of the detail.

5. Small scale tests showed that ultrasonic peening results in a significant increase in fatigue resistance of welded details and is clearly superior to conventional peening.

6. The results of large scale tests on welded repairs were inconclusive with respect to the effectiveness of ultrasonic peening since all the large scale specimens failed at relatively similar number of cycles, with most failures outside the weld zone. However, it seems that ultrasonic peening prolonged the fatigue life of such specimens as well, even in the presence of an initial embedded flaw.

7. The use of Almen strips to quantify ultrasonic peening intensity was found to be ineffective.

8. Initial flaws increase the strain amplitude and maximum stresses and, therefore, decrease the fatigue initiation life. Tensile residual stresses further increase the maximum stresses, but do not affect the strain amplitude. Due to the flattening of the stress–strain curve, the effect of tensile residual stresses on the maximum stress diminishes with an increase in overall stresses.

9. Monte Carlo Simulation (MCS) can be easily implemented in a probabilistic fatigue life prediction of a component. Parameters can be calibrated through a sensitivity study.

10. A sensitivity analysis of non-treated and post weld treated small scale specimens showed that the initial imperfection size and shape, as well as the crack propagation constant, C , have the greatest effect on fatigue life.

11. Fatigue design curves that are based on a small number of tests from limited sources may not have a representative variability, leading to an overly optimistic design curve.

12. The variability in loading needs to be incorporated in a reliability-based approach. Most realistic results are obtained through in-situ measurements on the investigated

structure or a structure, where a similar response is expected. Strain measurements on equipment under controlled conditions (i.e., where the loads and dynamics are known) and under representative field conditions should be carried out. Alternatively, loads obtained from design codes can be used where such exist.

13. A reliability-based analysis allows for the prediction of the remaining fatigue life of a structure for a target safety index, β. The safety index should be determined considering the consequence of failure, inspection management, crack growth rates, toughness aspects, and redundancies. Monte Carlo Simulation can be used to solve the limit state function.

14. For welded details, the total fatigue life is primarily governed by crack propagation. Therefore, it is generally not necessary to exactly determine the actual strain and stress fields at the governing location. Approximations that simplify the shape of flaws and the distribution of residual stresses are therefore adequate for the fatigue life prediction of welded details. For non-welded details, the fatigue life is mostly made up by crack initiation. In such cases, an accurate account of the strains and stresses at the crack initiation location is critical.

9.3 Recommendations

Based on the summary and conclusions the following recommendations can be made for future research:

1. The initial flaw size is one of the most important factors influencing the fatigue life of a structure. A more comprehensive investigation is needed to characterize the size and shape of weld flaws and flaws due to mechanical damage.

2. Residual stresses are influential for details with a significant crack initiation life and/or when a crack closure model is used. The residual stress field resulting from welding and mechanical treatments (cutting, machining, peening, etc.) was only estimated in the present work and has to be further investigated. Also, the effect of relaxation and redistribution of residual stresses during cyclic loading should be further investigated.

3. As opposed to the crack propagation properties, the crack initiation properties needed for the strain-based approach seem to be significantly affected by the type and grade of steel. More research is needed to define appropriate crack initiation properties for commonly used steel grades, including weld metal.

4. The analysis of the small scale test results showed that a calibration of the most relevant parameters is opportune in order to obtain best-fit predictions. However, only six test results could be used for this calibration and the results are to be treated

with caution. A systematic analysis and parametric calibration of other test results, where the initial conditions (imperfections, loads, and material properties) are well known, is necessary in order to obtain more accurate probabilistic models for all parameters.

5. Ultrasonic peening vastly improves the fatigue resistance of welded details. Unfortunately, no accepted method to control the intensity of ultrasonic peening exists. In order to optimize the application of ultrasonic peening, a method for quality control needs to be developed.

6. More large scale tests have to be carried out to quantify the effect of ultrasonic peening, especially investigating the effect of peening time per unit area and the required extent of peening to optimize its effectiveness.

7. Compression overloads of a peened detail relax the introduced compressive residual stresses and thus offset at least partially the beneficial effect of peening. The proposed crack initiation and propagation models do not incorporate overloads. A more general approach accounting for overloads (compressive or tensile) needs to be implemented for structures susceptible to unforeseen overloads.

8. The present study ignored interaction between adjacent flaws. The potential interaction effect of two or more flaws needs to be investigated and if relevant incorporated in the general reliability based approach.

9. The crack propagation model assumed mode I loading (tensile). However, some structural components are subjected to other loading modes. Especially the effect of mode III loading (tearing), which might be present in some structures due to e.g. out-of-plane distortions, needs to be investigated.

LIST OF REFERENCES

[AASHTO 2007] AASHTO: *AASHTO LRFD Bridge Design Specifications.* SI Units, 4th Edition, American Association of State Highway and Transportation Officials, Washington, D.C., USA, 2007.

[AASHTO/AWS 2008] AASHTO/AWS: *Bridge Welding Code.* AASHTO/AWS D1.5M/D1.5:2008, American Association of State Highway and Transportation Officials, Washington, D.C. / American Welding Society, Miami, USA, 2008.

[Agerskov & Nielsen 1999] AGERSKOV, H.; NIELSEN, J. A.: *Fatigue in Steel Highway Bridges under Random Loading.* Journal of Structural Engineering, Vol. 125, 1999, pp. 152 – 162.

[Albrecht & Lenwari 2007] ALBRECHT, P.; LENWARI A.: *Fatigue-Proofing Cover Plates.* Journal of Bridge Engineering, Vol. 12, 2007, pp. 275 – 283.

[Albrecht & Rubeiz 1990] ALBRECHT, P.; RUBEIZ, C. G.: *Variable Amplitude Load Fatigue, Task A - Literature Review, Volume III – Variable Amplitude Fatigue Behavior.* Report No. FHWA/RD-87/061, Federal Highway Administration, U.S. Department of Transportation, Washington, D.C., USA, 1990.

[Albrecht & Yamada 1977] ALBRECHT, P.; YAMADA, K.: *Rapid Calculation of Stress Intensity Factors.* Journal of the Structural Division, ASCE, Vol. 103, ST2, 1977, pp. 377 – 389.

[Almen & Black 1963] ALMEN, J. O.; BLACK, P. H.: *Residual Stresses and Fatigue in Metals.* McGraw-Hill Book Company Inc., New York, USA, 1963.

[Anderson 2005] ANDERSON, T. L.: *Fracture Mechanics: Fundamentals and Applications.* 3rd Edition, CRC Press, Boca Raton, USA, 2005.

[Ang & Cornell 1974] ANG, A. H.-S.; CORNELL, A. M.: *Reliability Bases of Structural Safety and Design.* Journal of the Structural Division, Vol. 100, ST9, 1974, pp. 1755 – 1769.

[Ang & Tang 1984] Ang, A. H.-S.; Tang, W. H.: Probability Concepts in Engineering Planning and Design, Vol. II: Decision, Risk, and Reliability. John Wiley & Sons, New York, USA, 1984.

[Aoki et al. 1986] AOKI, T.; NAKANO, K.; FUKUHARA, H.; OKADA, A.; KOBAYASHI, S.; KIMURA, K.; INAGAKI, M.: *Fatigue Life and Corrosion Fatigue Life Prediction of Welded Joints of Structural Steel Containing Planar Defects.* Transactions of the Iron and Steel Institute of Japan, Vol. 26, No. 11, 1986, pp. 977 – 984.

[ASCE 1982] ASCE Committee on Fatigue and Fracture Reliability: *Fatigue Reliability: Introduction.* Journal of the Structural Division, Vol. 108, ST1, 1982, pp. 3 – 23.

[ASM 1996] ASM Handbook Volume 19: *Fatigue and Fracture.* ASM International, Online Edition, Materials Park, USA, 1996.

[ASME 2004] ASME: Boiler and Pressure Vessel Code Section XI – Rules for Inservice Inspection of Nuclear Power Plant Components. American Society of Mechanical Engineers, New York, USA, 2004.

[ASTM 2000] ASTM Designation E 647 – 00: *Standard Test Method for Measurement of Fatigue Crack Growth Rates.* American Society for Testing and Materials, Philadelphia, USA, 2000.

[ASTM 2004a] ASTM Designation B 581 – 04: *Automated Controlled Shot Peening of Metallic Articles Prior to Nickel, Autocatalytic Nickel, or Chromium Plating, or as Final Finish.* American Society for Testing and Materials, Philadelphia, USA, 2004.

[ASTM 2004b] ASTM Designation E 606 – 04: *Standard Practice for Strain-Controlled Fatigue Testing.* American Society for Testing and Materials, Philadelphia, USA, 2004.

[ASTM 2005] ASTM Designation A 370 – 05: *Standard Test Methods and Definitions for Mechanical Testing of Steel Products.* American Society for Testing and Materials, Philadelphia, USA, 2005.

[AWS 2000] AWS B4.0M:2000: *Standard Methods for Mechanical Testing of Welds.* American Welding Society, Miami, USA, 2000.

[AWS 2005] AWS A5.20/A5.20M:2005: *Specification for Carbon Steel Electrodes for Flux Cored Arc Welding.* American Welding Society, Miami, USA, 2005.

[AWS 2008] AWS D1.1/D1.1M:2006: *Structural Welding Code – Steel.* American Welding Society, Miami, USA, 2008.

[Bailey 1996] BAILEY, S. F.: *Basic Principles and Load Models for the Structural Safety Evaluation of Existing Road Bridges.* Ph.D. Thesis No. 1467, Swiss Federal Institute of Technology, Lausanne, Switzerland, 1996.

[Ball & Lowry 1998] BALL, D. L.; LOWRY, D. R.: *Experimental Investigation on the Effects of Cold Expansion of Fastener Holes.* Fatigue & Fracture of Engineering Materials & Structures, Vol. 21, 1998, pp. 17 – 34.

[Banks-Sills 1991] BANKS-SILLS, L.: *Application of the Finite Element Method to Linear Elastic Fracture Mechanics.* Applied Mechanics Reviews, Vol. 44, No. 10, 1991, pp. 447 – 461.

[Banz & Nussbaumer 2001] BANZ, A.; NUSSBAUMER, A.: *Fiabilité des ponts métalliques vis à vis de l'état limite combiné fatigue et rupture (Reliability of Steel Bridges Under the Combined Limit State of Fatigue and Fracture).* Report 446, ICOM Steel Structures Institute, Swiss Federal Institute of Technology, Lausanne, Switzerland, 2001.

[Barsom 1971] BARSOM, J. M.: *Fatigue-Crack Propagation in Steels of Various Yield Strength.* Transaction of the ASME, Vol. 93, 1971, pp. 1190 – 1196.

[Barsom 1987] BARSOM, M.: *Fracture Mechanics Retrospective: Early Classic Papers (1913 – 1965).* American Society for Testing and Materials, Baltimore, USA, 1987.

[Barsom & Rolfe 1999] BARSOM, M.; ROLFE, S. T.: *Fracture and Fatigue Control in Structures: Applications of Fracture Mechanics*. 3rd Edition, American Society for Testing and Materials, West Conshohocken, USA, 1999.

[Bartlett et al. 2003] Bartlett, F.M.; Hong, H.P.; Zhou, W.: Load Factor Calibration for the Proposed 2005 Edition of the National Building Code of Canada: Companion-Action Load Combinations. Canadian Journal of Civil Engineering, Vol. 30, No. 2, 2003, pp. 440 – 448.

[Basquin 1910] BASQUIN, O. H.: *The Exponential Law of Endurance Tests.* Proceedings of the American Society for Testing and Materials, Vol. 10, 1910, pp. 625-630.

[Bathias 1999] BATHIAS, C.: *There Is no Infinite Fatigue Life in Metallic Materials.* Fatigue and Fracture of Engineering Materials and Structures, Vol. 22, 1999, pp. 559 – 565.

[Bignonnet et al. 1987] Bignonnet, A.; Lieurade, H. P.; Picouet, L., CASTEX, L.: *Shot Peening Of Welded Joints And Residual Stress Relaxation During Fatigue.* Third International Conference on Shot Peening, 1987, pp.585 – 594.

[Blatt et al. 1994] BLATT, D.; JOHN, R.; COKER, D.: *Stress Intensity Factor and Compliance Solutions for a Single Edge Notched Specimen with Clamped Ends.* Engineering Fracture Mechanics, Vol. 47, 1994, pp. 521 – 532.

[Blodgett & Nagy 2004] BLODGETT, M . P.; NAGY, P. B.: *Eddy Current Assessment of Near-Surface Residual Stress in Shot-Peened Nickel-Base Superalloys.* Journal of Nondestructive Evaluation, Vol. 23, 2004, pp. 107 – 123.

[Bokalrud & Karlsen 1982] Bokalrud, T.; Karlsen, A.: *Probabilistic Fracture Mechanics Evaluation of Fatigue Failure from Weld Defects in Butt Welded Joints.* Conference on Fitness for Purpose Validation of Welded Constructions, Vol. 1, The Welding Institute, Cambridge, U.K., 1982.

[Boller & Seeger 1987] BOLLER, C.; SEEGER, T.: *Materials Data for Cyclic Loading, Part B: Low-Alloy Steels.* Elsevier, Amsterdam, 1987.

[Bremen 1989] BREMEN, U.: Amélioration du comportement à la fatigue d'assemblages soudés: étude et modélisation de l'effet de contraintes résiduelles. Ph.D. Thesis No. 787, Swiss Federal Institute of Technology, Lausanne, Switzerland, 1989.

[Bright &.Smith 2004] BRIGHT, S. R.; SMITH, J. W.: *Fatigue Performance of Laser-Welded Steel Bridge Decks.* Structural Engineer, Vol. 82, Issue 21, 2004, pp. 31 – 39.

[Broek 1989] BROEK, D.: *The Practical Use of Fracture Mechanics.* 2nd Printing, Kluwer Academic Publishers, Dordrecht, The Netherlands, 1989.

[Brown et al. 2006] BROWN, T. B.; DAUDA, T. A.; TRUMAN, C. E.; SMITH, D. J.; MEMHARD, D.; PFEIFFER, W.: *Predictions and Measurements of Residual Stress in Repair Weld in Plates.* International Journal of Pressure Vessels and Piping, Vol. 83, 2006, pp. 809 – 818.

[Brozzetti et al. 1991] BROZZETTI, J.; SEDLACEK, G.; HENSEN, W.: *Fondements des règles de l'Eurocode 3 en vue de se garantir du risque de rupture fragile (Bases of the Rules in Eurocode 3 Concerning the Risk of Brittle Fracture).* Construction Métallique, Vol. 28, No. 1, 1991, pp. 15 – 28.

[Brückner & Munz 1982] BRUCKNER, A.; MUNZ, D.: *Curve Fitting to Defect Size Distributions for the Calculation of Failure Probabilities.* Nuclear Engineering and Design, Vol. 74, 1982, pp. 75 – 78.

[Brühwiler & Kunz 1993] BRÜHWILER, E.; KUNZ P.: *Remaining Service Life of a Riveted Railway Bridge.* In: Remaining Structural Capacity. Proceedings of IABSE-Colloquium (Copenhagen, Denmark), International Association for Bridge and Structural Engineering, Zurich, Switzerland, 1993, pp. 375 – 383.

[BSI 2005] BS 7910: Guide to Methods for Assessing the Acceptability of Flaws in Metallic Structures. British Standard Institute, London, UK, 2005.

[CEN 2005] EN 1993-1-1, EUROCODE 3: *Design of Steel Structures – General Rules and Rules for Buildings.* European Committee for Standardization CEN, Brussels, Belgium, 2005.

[Chen et al. 2005] CHEN, H.; GRONDIN, G. Y.; DRIVER, R. G.: *Fatigue Resistance of High Performance Steel.* Structural Engineering Report No. 258, Department of Civil Engineering, University of Alberta, Edmonton, Canada, 2005.

[Cheng & Finnie 1993] CHENG W.; FINNIE, I.: Measurement of Residual Stress Distributions near the Toe of an Attachment Welded on a Plate Using the Crack Compliance Method. Engineering Fracture Mechanics, Vol. 46, 1993, pp. 79 – 91.

[Cheng et al. 2003] CHENG, X.; FISHER, J. W.; PRASK, H. J.; GNÄUPEL-HEROLD, T.; YEN, B. T.; ROY, S.: *Residual Stress Modification by Post-Weld Treatment and its Beneficial Effect on Fatigue Strength of Welded Structures.* International Journal of Fatigue, Vol. 25, 2003, pp. 1259 – 1269.

[Cheung & Li 2003] CHEUNG, M. S.; LI, W. C.: *Probabilistic Fatigue and Fracture Analyses of Steel Bridges.* Structural Safety, Vol. 23, 2003, pp. 245 – 262.

[Colombi et al. 2003] COLOMBI, P.; BASSETTI, A.; NUSSBAUMER, A.: *Analysis of Cracked Steel Members Reinforced by Pre-Stress Composite Patch.* Fatigue and Fracture of Engineering Materials and Structures, Vol. 26, 2003, pp. 59 – 66.

[Connor & Fisher 2006] CONNOR, R. J.; FISHER, J. W.: *Identifying Effective and Ineffective Retrofits for Distortion Fatigue Cracking in Steel Bridges Using Field Instrumentation.* Journal of Bridge Engineering, Vol. 11, 2006, pp. 745 – 752.

[Cornell 1969] CORNELL, C. A.: *A Probability-Based Structural Code.* Journal of the American Concrete Institute, Vol. 66, No. 12, 1969, pp. 974 – 985.

[CSA 1994] CAN/CSA N285.4-94: *Periodic Inspection of CANDU Nuclear Power Plant Components.* Canadian Standards Association, Toronto, Canada, 1994.

[CSA 2001] CAN/CSA S16-01: *Limit States Design of Steel Structures.* Canadian Standards Association, Toronto, Canada, 2001.

[CSA 2003] CSA W59-03: *Welded Steel Construction (Metal Arc Welding).* Canadian Standards Association, Mississauga, Canada, 2003.

[CSA 2004] CAN/CSA G40.21-04: *Structural Quality Steel.* Canadian Standards Association International, Mississauga, Canada, 2004.

[CSA 2006] CAN/CSA S6-06: *Canadian Highway Bridge Design Code.* Canadian Standards Association International, Toronto, Canada, 2006.

[Darchuk 2003] DARCHUK, O. I.: *Application of the Probabilistic Mechanics of Fatigue Fracture to the Evaluation of the Reliability of Welded Structures.* Materials Science, Vol. 39, 2003, pp. 481 – 491.

[Davidson 2004] DAVIDSON, D. L.: *Characterizing Small Fatigue Cracks in Metallic Alloys.* Metallurgical and Materials Transactions A: Physical Metallurgy and Materials Science, Vol. 35, 2004, pp. 7 – 14.

[DNV 1992] DNV 30.6: *Structural Reliability Analysis of Marine Structures.* Det Norske Veritas, Classification Notes No. 30.6, Høvik, Norway, 1992.

[Dowling 1979] DOWLING, N. E.: *Notched Member Fatigue Life Predictions Combining Crack Initiation and Propagation.* Fatigue of Engineering Materials and Structures, Vol. 2, 1979, pp. 129 – 138.

[Dowling 1982] DOWLING, N. E.: *A Discussion of Methods for Estimating Fatigue Life.* Proceedings of the SAE Fatigue Conference, Dearborn, Michigan, Society of Automotive Engineers, 1982, pp. 161 – 174.

[Dowling 1999] DOWLING, N. E.: *Mechanical Behavior of Materials: Engineering Methods for Deformation, Fracture, and Fatigue.* 2nd Edition, Prentice Hall, Upper Saddle River, USA, 1999.

[Dowse & Richards 1971] DOWSE, K. R.; RICHARDS, C. E.: *Fatigue Crack Propagation Through Weld Heat Affected Zones.* Metallurgical Transactions, Vol. 2, 1971, pp. 599 – 603.

[Dubois 1994] DUBOIS, V.: *Fatigue de détails soudés traités sous sollicitations d'amplitude variable (Fatigue of Treated Welded Details under Variable Amplitude Loading).* Ph.D. Thesis No. 1260, Swiss Federal Institute of Technology, Lausanne, Switzerland, 1994.

[DVS 1993] DEUTSCHER VERBAND FUER SCHWEISSTECHNIK, E.V.: *Guidance for use of the Catalogue of acceptance criteria EN 25817 / ISO 5817 (Collection*

of radiographs). Deutscher Verlag für Schweisstechnik DVS GmbH, Düsseldorf, Germany, 1993.

[EC 2002] EN 1990: *Eurocode 0 – Basis of Structural Design.* European Committee for Standardization, Brussels, Belgium, 2002.

[EC 2003] EN 1991-2: *Eurocode 1 – Actions on Structures, Part 2 – Traffic Loads on Bridges.* European Committee for Standardization, Brussels, Belgium, 2003.

[EC 2005] EN 1993-1-9: *Eurocode 3 – Design of Steel Structures, Part 1-9 – Fatigue.* European Committee for Standardization, Brussels, Belgium, 2005.

[ECCS 1985] ECCS: *Recommendations for the Fatigue Design of Steel Structures.* Publication No. 43, European Convention for Constructional Steelwork, Brussels, Belgium, 1985.

[Elber 1970] ELBER, W: *Fatigue Crack Closure under Cyclic Tension*. Engineering Fracture Mechanics, Vol. 2, 1970, pp. 37 – 45.

[Elber 1971] ELBER, W: *The Significance of Fatigue Crack Closure.* ASTM Special Technical Publication 486: Damage Tolerance in Aircraft Structures, American Society for Testing and Materials, Philadelphia, USA, 1971, pp. 230 – 242.

[Ellyin 1997] ELLYIN, F.: *Fatigue Damage, Crack Growth and Life Prediction.* Chapman & Hall, London, UK, 1997.

[EN 1992] EN 25817: *Arc Welded Joints in Steel – Guidance on Quality Levels for Imperfections.* European Committee for Standardization, Brussels, Belgium, 1992.

[Engesvik & Moan 1983] ENGESVIK, K. M.; MOAN, T.: *Probabilistic Analysis of the Uncertainty in the Fatigue Capacity of Welded Joints*. Engineering Fracture Mechanics, Vol. 18, 1983, pp. 743 – 762.

[Faber et al. 2005] FABER, M. H.; STRAUB, D.; CHAKRABARTI, P.; ABU-ODEH, I.; de la O RAMIREZ, J. d. D: *Fatigue Analysis and Risk Based Inspection Planning for Life Extension of Fixed Offshore Platforms.* Proceedings of the 24th International Conference on Offshore Mechanics and Arctic Engineering – OMAE, Vol. 1, 2005, pp. 511 – 519.

[Fatemi & Yang 1998] FATEIM, A.; YANG, L.: *Cumulative Fatigue Damage and Life Prediction Theories - Survey of the State of the Art.* International Journal of Fatigue, Vol. 20, 1998, pp. 9 – 34.

[Fathallah et al. 2004] FATHALLAH, R.; LAAMOURI, A.; SIDHOM, H; BRAHAM, C.: *High Cycle Fatigue Behavior Prediction of Shot-Peened Parts.* International Journal of Fatigue, Vol. 26, 2004, pp. 1053 – 1067.

[Fisher 1984] FISHER, J. W.: *Fatigue and Fracture in Steel Bridges: Case Studies.* John Wiley & Sons, New York, USA, 1984.

[Fisher et al. 1997] FISHER, J. W.; KULAK, G. L.; SMITH, I. F. C.: *A Fatigue Primer for Structural Engineers.* ATLSS Report No. 97-11, Lehigh University, Bethlehem, USA, 1997.

[Forsyth 1952] FORSYTH, P. J. E.: *Some Metallographic Observations on the Fatigue of Metals.* Journal of the Institute of Metals, Vol. 80, pp. 181 – 186.

[Forsyth 1953] FORSYTH, P. J. E.: *Exudation of Material from Slip Bands at the Surface of Fatigued Crystals of an Aluminium-Copper Alloy.* Nature, Vol. 171, pp. 172 – 173.

[Friedland et al. 1982] FRIEDLAND, I. M.; ALBRECHT, P.; IRWIN, G. R.: *Fatigue of Two-Year Weathered A588 Stiffeners and Attachments.* Journal of the Structural Division, Vol. 108, 1982, pp. 125 – 144.

[Fuchs 1984] FUCHS, H. O.: *Defects and Virtues of the Almen Intensity Scale.* Proceedings of ICSP-2 in Chicago, International Scientific Committee for Shot Peening, 1984, pp. 74 – 78.

[Galambos & Ravindra 1977] GALAMBOS, T. V.; RAVINDRA, M. K.: *The Basis for Load and Resistance Factor Design Criteria of Steel Buildings Structures.* Canadian Journal of Civil Engineering, Vol. 4, No. 3, 1977, pp. 178 – 189.

[Galambos & Ravindra 1978] GALAMBOS, T. V.; RAVINDRA, M. K.: *Properties of Steel for Use in LRFD.* Journal of the Structural Division, Vol. 104, 1978, pp. 1459 – 1468.

[Galambos et al. 1982] GALAMBOS, T. V.; ELLINGWOOD, B.; MacGREGOR, J. G.; CORNELL, C. A.: *Probability Based Load Criteria: Assessment of Current Design Practice.* Journal of the Structural Division, Vol. 108, 1982, pp. 959 – 977.

[Galtier & Statnikov 2004] GALTIER, A.; STATNIKOV, E. S.: *The Influence of Ultrasonic Impact Treatemtent on Fatigue Behaviour of Wedled Joints in High-Strength Steel.* Welding in the World, Vol. 48, 2004, pp. 61 – 66.

[Garbatov & Guedes Soares 2004] GARBATOV, Y.; GUEDES SOARES, C.: *Influence of Steel Strength on the Fatigue Reliability of Welded Structural Components.* International Journal of Fatigue, Vol. 26, 2004, pp. 753 – 762.

[Goodier 1933] GOODIER, J. N.: *Concentration of Stress around Spherical and Cylindrical Inclusions and Flaws.* Transactions of Applied Mechanics, Vol. 1, 1933, pp. 39 – 44.

[Gourd 1995] GOURD, L. M.: *Principles of Welding Technology.* 3rd Edition, Edward Arnold (a Member of the Hodder Headline Group), London, UK, 1995.

[Gregory et al. 1989] GREGORY, E. N.; SLATER, G; WOODLEY, C. C.: *Welded Repair of Cracks in Steel Bridge Members.* National Cooperative Highway Research Program Reprot 321, Transportation Research Board, Washington, D.C., 1989.

[Griffith 1920] GRIFFITH, A. A.: *The Phenomena of Rupture and Flow in Solids.* Philosophical Transactions, Series A, Vol. 221, 1920, pp. 163 – 198.

[Guagliano 2001] GUAGLIANO, M.: *Relating Almen Intensity to Residual Stresses Induced by Shot Peening: A Numerical Approach.* Journal of Materials Processing Technology, Vol. 110, No. 3, 2001, pp. 277 – 286.

[Günther et al. 2005] GÜNTHER, H.-P.; KUHLMANN, U.; DÜRR, A.: *Rehabilitation of Welded Joints by Ultrasonic Impact Treatment (UIT).* In: Structures and Extreme Events, IABSE Symposium Report, Vol. 90, 2005, pp. 358 – 359.

[Gurney 1979a] GURNEY, T. R.: *An Analysis of some Fatigue Crack Propagation Data for Steels Subjected to Pulsating Tension Loading.* Welding Research International, Vol. 9, No. 4, 1979, pp. 45 – 59.

[Gurney 1979b] GURNEY, T. R.: *Fatigue of Welded Structures.* 2nd Edition, Cambridge University Press, Cambridge, UK, 1979.

[Haagensen & Fredborg 2003] HAAGENSEN, P. J.; FREDBORG, A.: *Fatigue Life Extension of Structural Details of a Floating Production Unit by Weld Improvement Methods.* Proceedings of the 22nd International Conference on Offshore Mechanics and Arctic Engineering – OMAE, Vol. 3, 2003, pp. 11 – 15.

[Haagensen & Maddox 2002] Haagensen, P .J.; Maddox, S. J.: *IIW Recommendations on the Post Weld Improvement of Steel and Aluminum Structures.* International Institute of Welding, Doc. XIII-1815-00, Revised 2002.

[Haagensen et al. 1987] Haagensen, P. J.; Dragen A.; Slind T.; Orjasaeter O.: *Prediction of the Improvement in Fatigue Life of Welded Joints Due to Grinding, TIG Dressing, Weld Shape Control and Shot Peening.* Proceedings 3rd International Conference on Steel in Marine Structures (SIMS 87), Paper TS35, Elsevier Publishers, Amsterdam, 1987. pp. 689 – 698.

[Haagensen et al. 1998] HAAGENSEN, P. J.; STATNIKOV, E. S.; LOPEZ-MARTINEZ, L.: *Introductory Fatigue Tests on Welded Joints in High Strength Steel and Aluminium Improved by Various Methods Including Ultrasonic Impact Treatment (UIT).* International Institute of Welding, Doc. XIII-1748-98, 1998.

[Haibach 2006] HAIBACH, E.: *Betriebsfestigkeit – Verfahren und Daten zur Bauteilberechnung (Fatigue Resistance – Procedure and Data for Component Design).* 3rd Ed., Springer-Verlag, Berlin, Germany, 2006.

[Haldar & Mahadevan 2000] HALDAR, A.; MAHADEVAN, S.: *Probability, Reliability, and Statistical Methods in Engineering Design.* John Wiley & Sons, New York, USA, 2000.

[Harlow 2005] HARLOW, D. G.: *Probability versus Statistical Modeling: Examples from Fatigue Life Prediction.* International Journal of Reliability, Quality and Safety Engineering, Vol. 12, No. 6, 2005, pp. 535 – 550.

[Harris 1995] HARRIS, D. O.: *Probabilistic Fracture Mechanics.* In: Probabilistic Structural Mechanics Handbook. C. Sundararajan (Editor), Chapman & Hall, New York, USA, 1995, pp. 106 – 145.

[Hassan & Bowman 1998] HASSAN, A. F.; BOWMAN, M. D.: *Fatigue Crack Repair of Steel Beams with Tapered Cover Plate Details.* Journal of Structural Engineering, Vol. 122, No. 11, 1996, pp. 1337 – 1346.

[HSE 1999] Health and Safety Executive: *Review of Probabilistic Inspection Analysis Methods.* Offshore Technology Report 1999/061, Aker Offshore Partner, Sandsli, Norway, 1999.

[Huo et al. 2000] HUO, L.; WANG, D.; ZHANG, Y.; CHEN, J.: *Investigation on Improving Fatigue Properties of Welded Joints by Ultrasonic Peening Method.* Key Engineering Materials, Vols. 183 – 187, 2000, pp. 1315 – 1320.

[Huo et al. 2005] HUO, L.; WANG, D.; ZHANG, Y.: *Investigation of the Fatigue Behaviour of the Welded Joints Treated by TIG Dressing and Ultrasonic Peening under Variable-Amplitude Load.* International Journal of Fatigue, Vol. 27, 2005, pp. 95 – 101.

[IABSE 2005] IABSE: *Use and Application of High-Performance Steels for Steel Structures.* Structural Engineering Documents 8, International Association for Bridge and Structural Engineering, Zurich, Switzerland, 2005.

[IIW 2002] IIW: *Causes and Repairing Methods of Fatigue Damaged Bridges.* International Institute of Welding, IIW-XIII-WG5, Villepinte, France, 2002.

Retrieved April 25, 2006, from http://iiw-wg5.cv.titech.ac.jp/

[Ikeda et al. 1978] IKEDA, K.; DENOH, S.; GODAI, T.; OGAWA, T.: *Improvement of Fatigue Strength of Fillet Welded Joints in 780 N/mm^2 High Strength Steel.* Welding Research International, Vol. 8, No. 1, 1978, pp. 16 – 26.

[Irwin 1956] IRWIN, G. R.: *Onset of Fast Crack Propagation in High Strength Steel and Aluminum Alloys.* Sagamore Research Proceedings, Vol. 2, 1956, pp. 289 – 305.

[Jang et al. 2004] JANG, C. D.; SONG, H. C.; JO, Y. C.: *Fatigue Life Assessment of Fillet Welded Joint Considering the Relaxation and Redistribution of Residual Stresses.* Proceedings of the 23rd International Conference on Offshore Mechanics and Arctic Engineering – OMAE, Vol. 2, 2004, pp. 319 – 323.

[JCSS 2001a] Joint Committee on Structural Safety: *Probabilistic Model Code, Part 1 – Basis of Design.* Federal Institute of Technology, Zurich, Switzerland, 2001.

Retrieved August 4, 2006, from http://www.jcss.ethz.ch

[JCSS 2001b] Joint Committee on Structural Safety: *Probabilistic Model Code, Part 3 – Resistance Models.* Federal Institute of Technology, Zurich, Switzerland, 2001.

Retrieved August 4, 2006, from http://www.jcss.ethz.ch

[Jeffus 1999] JEFFUS, L.: *Repairing Damaged Rail Sections.* Practical Welding Today, Vol. 3, No. 2 (March/April), 1999, pp. 34 – 38.

[Kelly & Dexter 1997] KELLY, B. A.; DEXTER, R. J.: *Restored Fatigue Life with Repair Welds.* Proceedings of the 7th International Offshore and Polar Engineering Conference, Vol. 4, 1997, pp. 572 – 577.

[Kirkhope et al. 1999a] KIRKHOPE, K. J.; BELL, R.; CARON, L.; BASU, R. I.; MA, K.-T.: *Weld Detail Fatigue Improvement Techniques. Part 1: Review.* Marine Structures, Vol. 12, No. 6, 1999, pp. 447 – 474.

[Kirkhope et al. 1999b] KIRKHOPE, K. J.; BELL, R.; CARON, L.; BASU, R. I.; MA, K.-T.: *Weld Detail Fatigue Improvement Techniques. Part 2: Application to Ship Structures.* Marine Structures, Vol. 12, No. 7, 1999, pp. 477 – 496.

[Kitsunai & Yoshihisa 1991] Kitsunai, Y. and Yoshihisa, E.: *Fatigue Crack Growth Behavior in Welded Joints of High-Strength Steel under Low Temperatures.* JSME International Journal, Series I: Solid Mechanics, Strength of Materials, Vol. 34, No 3, 1991, pp. 339 – 346.

[Klippstein 1987] KLIPPSTEIN, K. H.: *Variable Amplitude Load Fatigue, Task A – Literature Review, Volume III – Supplementary Information on Constant Amplitude Fatigue Behavior.* Report No. DTFH61-86-C-00036-III, U.S. Department of Transportation, Federal Highway Administration, Washington, D.C., USA, 1987.

[Kountouris & Baker 1990] KOUNTOURIS, I. S.; BAKER, M. J.: *The Occurrence of Defects in Welded Joints.* Proceedings of the International Offshore Mechanics and Arctic Engineering Symposium, Vol. 3, 1990, pp. 539 – 546.

[Kudryavtsev et al. 1995] KUDRYAVTSEV, Y.; MIKHEEV, P. P.; KORSHUN, V. F.: *Effect of Plastic Strains and Residual Stresses, Caused by Ultrasound Shock Treatment, on Fatigue Strength of Welded Joints.* The Paton Welding Journal, Vol. 7, 1995, pp. 667 – 671.

[Kudryavtsev et al. 2004] KUDRYAVTSEV, Y.; KLEIMAN, J.; LOBANOV, L.; KNYSH, V.; PROKOPENKO, G.: *Fatigue Life Improvement of Welded Elements by Ultrasonic Peening.* International Institute of Welding, Doc. XIII-2010-04, 2004.

[Kudryavtsev et al. 2005] KUDRYAVTSEV, Y.; KLEIMAN, J.; LUGOVSKOY, A.; LOBANOV, L.; KNYSH, V.; VOITENKO, O.; PROKOPENKO, G.: *Rehabilitation and Repair of Welded Elements and Structures by Ultrasonic Peening.* International Institute of Welding, Doc. XIII-2076-05, 2005.

[Kudryavtsev et al. 2006] KUDRYAVTSEV, Y.; KLEIMAN, J.; LUGOVSKOY, A.; PROKOPENKO, G.: *Fatigue Life Improvement of Tubular Welded Joints by Ultrasonic Peening.* International Institute of Welding, Doc. XIII-2117-06, 2006.

[Kuhlmann et al. 2006] KUHLMANN, U.; DÜRR, A.; GÜNTHER, H.-P.: *Verbesserung der Ermüdungsfestigkeit höherfester Baustähle durch Anwendung der UIT-Nachbehandlung (Improvement of the Fatigue Resistance of Higher Strength*

Steels through the Application of UIT Post Weld Treatment). Stahlbau, Vol. 75, 2006, pp. 930 – 938.

[Kulak & Grondin 2002] KULAK, G. L.; GRONDIN, G. Y.: *Limits State Design in Structural Steel.* 7th Edition, Canadian Institute of Steel Construction, Willowdale, Canada, 2002.

[Kulak et al. 2001] KULAK, G. L.; FISHER, J. W.; STRUIK, J. H. A.: *Guide to Design Criteria for Bolted and Riveted Joints.* 2nd Edition, American Institute of Steel Construction, INC, Chicago, USA, 2001.

[Kunz 1992] KUNZ, P.: *Probabilistisches Verfahren zur Beurteilung der Ermüdungssicherheit bestehender Brücken aus Stahl (Probabilistic Procedure for the Evaluation of the Fatigue Safety of Existing Steel Bridges).* Ph.D. Thesis No. 1023, Swiss Federal Institute of Technology, Lausanne, Switzerland, 1992.

[Kunz & Hirt 1991] KUNZ, P.; HIRT, M. A.: *Grundlagen und Annahmen für den Nachweis der Ermüdungssicherheit in den Tragwerksnormen des SIA (Bases and Assumptions for the Verification of the Fatigue Safety of the SIA (Swiss) Structural Codes).* Publication D 076, Swiss Society of Engineers and Architects SIA, Zurich, Switzerland, 1991.

[Kunz & Hirt 1993] KUNZ, P.; HIRT, M. A.: *Reliability Analysis of Steel Railway Bridges under Fatigue Loading.* Proceedings of IABSE-Colloquium "Remaining Structural Capacity" (Copenhagen, Denmark), International Association for Bridge and Structural Engineering, Zurich, Switzerland, 1993, pp. 53 – 60.

[Lawrence 1981] LAWRENCE, F. V.: *The Predicted Influence of Weld Residual Stresses on Fatigue Crack Initiation.* Industrial Diamond Review, 1981, pp. 105 – 117.

[Lihavainen et al. 2003] LIHAVAINEN, V.-M.; MARQUIS, G.; STATNIKOV, E.: *Fatigue Strength of a Longitudinal Attachment Improved by Ultrasonic Treatment.* International Institute of Welding, Doc. XIII-1990-03, 2003.

[Lixing et al. 2004] LIXING, H.; DONGPO, W; WENXIAN, W.; YUFENG, Z.: *Ultrasonic Peening and Low Transformation Temperature Electrodes Used fro Improving the Fatigue Strength of Welded Joints.* Welding in the World, Vol. 48, No. 3/4, 2004, pp. 26 – 31.

[Lobanov & Garf 1998] LOBANOV, L. M.; GARF, E. F.: *Estimation of Life of Metal Tubular Structure Connections at Ultrasonic Peening Treatment of Welded Joint Zone.* Journal of Constructional Steel Research, Vol. 46:1-3, 1998, Paper No. 353.

[Lopez Martinez & Korsgren 1993] Lopez Martinez, L.; KorsgRen, P.: *Characterization of Initial Defect Distribution and Weld Geometry in Welded Fatigue Test Specimens.* Proceedings of "Fatigue under Spectrum Loading and in Corrosive Environments," A. F. Blom (Editor), EMAS, Warley, U.K., 1993, pp. 3 – 21.

[Lotsberg et al. 2000] LOTSBERG, I.; SIGURDSSON, G.; WOLD, P. T.: *Probabilistic Inspection Planning of the Åsgard A FPSO Hull Structure with Respect to*

Fatigue. Journal of Offshore Mechanics and Arctic Engineering, Vol. 122, 2000, pp. 134 – 140.

[Lovejoy 2003] LOVEJOY, S. C.: *Determining Appropriate Fatigue Inspection Intervals for Steel Bridge Members.* Journal of Bridge Engineering, Vol. 8, No. 2, 2003, pp. 66 – 72.

[Lukic 1999] Lukic, M.: *Evaluation de maintenances probabilistes des assemblages soudés vis-à-vis de la fatigue et de la rupture – application aux ponts mixtes (Evaluation of Probabilistic Maintenance of Welded Connections concerning Fatigue and Fracture – Application to Composite Bridges).* Ph.D. Thesis, Ecole Nationale des Ponts et Chaussés, Paris, France, 1999.

[Lukic & Cremona 2001] Lukic, M.; Cremona, C.: *Probabilistic Assessment of Welded Joints versus Fatigue and Fracture.* Journal of Structural Engineering, Vol. 127, No. 2, 2001, pp. 211 – 218.

[Maarschalkerwaart 1989] van MAARSCHALKERWAART, H. M. C. M.: *Evaluation of Existing Structures.* In: Fatigue Aspects in Structural Design. Proceedings of the International Symposium on the Occasion of the Retirement of Prof. ir. J. de Back, University Press, Delft, 1989, pp. 97 – 118.

[Maddox 1973] MADDOX, S. J.: *Some Further Fatigue Crack Propagation Results Relevant to Welded Joints in Steel.* Welding Research International, Vol. 3, No. 1, 1973, pp. 72 – 99.

[Maddox 1974] MADDOX, S. J.: *Fatigue Crack Propagation Data Obtained from Parent Plate, Weld Metal and HAZ in Structural Steels.* Welding Research International, Vol. 4, No. 1, 1974, pp. 36 – 60.

[Maddox 1991] MADDOX, S. J.: *Fatigue Strength of Welded Structures.* 2nd Edition, Woodhead Publishing Ltd, Cambridge, UK, 1991.

[Madsen et al. 1986] MADSEN, H. O.; KRENK, S.; LIND, N. C.: *Methods of Structural Safety*. Prentice Hall Inc., Englewood Cliffs, USA, 1986.

[Manson 1971] MANSON, S. S. (Ed.): *Metal Fatigue Damage – Mechanism, Detection, Avoidance, and Repair*. ASTM Special Technical Publication 495, American Society for Testing and Materials, Philadelphia, USA, 1971.

[Melchers 1999] MELCHERS, R. E.: *Structural Reliability Analysis and Prediction.* 2nd Edition, John Wiley and Sons, New York, USA, 1999.

[MIL 1989] Military Specification MIL-S-13165C: *Shot Peening of Metal Parts.* US Department of Defense, Washington D.C., USA, 1989.

[Miner 1945] Miner, M. A.: *Cumulative Damage in Fatigue.* Journal of Applied Mechanics, Vol. 12, No. 3, 1945, pp. A159 – A164.

[Moan & Song 2000] Moan, T.; Song, R.: *Implications of Inspection Updating on System Fatigue Reliability of Offshore Structures.* Journal of Offshore Mechanics and Arctic Engineering, Vol. 122, No. 3, 2000, pp. 173 – 180.

[Morrow & Socie 1981] MORROW, J.; SOCIE, D. F.: *Evolution of Fatigue Crack Initiation Life Prediction Methods.* In: Material, Experimentation and Design in Fatigue – Proceedings of Fatigue ’81. Sherratt and J. B. Sturgeon (Editors), Westbury House, Guildford, UK, 1981, pp. 3 – 21.

[Nachman 1999] NACHMAN, G.: *Shot Peening – Past, Present and Future.* Proceedings of ICSP-7 in Warsaw, International Scientific Committee for Shot Peening, 1999, pp. 1 – 4.

[Nelson 1984] NELSON, W.: *Fitting of Fatigue Curves with Nonconstant Standard Deviation to Data with Runouts.* Journal of Testing and Evaluation, Vol. 12, No. 2, 1984, pp. 69 – 77.

[Neuber 1968] NEUBER, H: *A Physically Nonlinear Notch and Crack Model.* Journal of the Mechanics and Physics of Solids, Vol. 16, 1968, pp. 289 – 294.

[Newman & Raju 1983] NEWMAN, J. C., Jr.; RAJU, I. S.: *Stress-Intensity Factor Equations for Cracks in Three-Dimensional Finite Bodies.* ASTM Special Technical Publication 791, Fracture Mechanics: 14th Symposium (Los Angeles), Volume I: Theory and Analysis, 1983, pp. 238 – 265.

[Nitschke & Wohlfahrt 2001] NITSCHKE-PAGEL, T.; WOHLFAHRT, H.: *Eigenspannungsabbau in zügig und zyklisch beanspruchten Schweissverbindungen (Residual Stresses in Welded Connections Subjected to Cyclic Tension).* Zeitschrift für Metallkunde, Vol. 92, 2001, pp. 860 – 866.

[Nitschke et al. 2007] NITSCHKE-PAGEL, T.; WOHLFAHRT, H.; DILGER, K.: *Application of the Local Fatigue Strength Concept for the Evaluation of Post Weld Treatments.* Welding in the World, Vol. 51, Nov. 2007, pp. 65 – 75.

[Nowak & Lind 1995] NOWAK, A. S.; LIND, N. C.: *Probability-Based Design Codes.* In: Probabilistic Structural Mechanics Handbook. C. Sundararajan (Editor), Chapman & Hall, New York, USA, 1995, pp. 331 – 351.

[Nussbaumer & Imhof 2001] NUSSBAUMER, A.; IMHOF, D.: *On the Practical Use of Weld Improvement Methods.* Progress in Structural Engineering and Materials, Vol. 3, No. 1, 2001, p. 95 – 105.

[Ohta et al. 1986] OHTA, A.; SOYA, I.; NISHIJMA, S; KOSUGE, M.: *Statistical Evaluation of Fatigue Crack Propagation Properties Including Threshold Stress Intensity Factor.* Engineering Fracture Mechanics, Vol. 24, No. 6, 1986, pp. 789 – 802.

[Owen et al. 1989] OWEN, C. R.; BUCCI, R. J.; KEGARISE, R. J.: *Aluminum Quality Breakthrough for Aircraft Structural Reliability.* Journal of Aircraft, Vol. 26, 1989, pp. 178 – 184.

[Pardi et al. 2005] PARDI, L.; ONOUFRIOU, T.; SHETTY, N.; SOARES, C. G.: *Application of Risk and Reliability to the Management of Bridges.* Proceedings of the 5th International Conference on Bridge Management, 2005, pp. 587 – 593.

[Paris & Erdogan 1963] PARIS, P.; ERDOGAN, F.: *A Critical Analysis of Crack Propagation Laws.* Transactions of the ASME, Vol. 85, 1963, pp. 528 – 534.

[Pedersen 2004] PEDERSEN, P: *Design Study of Hole Positions and Hole Shapes for Crack Tip Stress Releasing.* Structural and Multidisciplinary Optimization, Vol. 28, 2004, pp. 243 – 251.

[Pense et al. 1984] PENSE, A. W.; DIAS, R.; FISHER, J. W.: *Examination and Repair of Bridge Structures.* Welding Journal, Vol. 63, 1984, pp. 19 – 25.

[Perez-Guerrero & Liu 2005] PEREZ-GUERRERO, F.; LIU, S.: *Maintenance and Repair Welding in the Open Sea.* Welding Journal, Vol. 84, 2005, pp. 54 – 59.

[Porter Goff et al. 1988] Porter Goff, R. F. D.; Free, J. A.; Tsiagbe, W. Z.: *Residual Stresses in Welded Tubular Nodes.* In: Fatigue of Offshore Structures. W. D. Dover & G. Glinka (Editors), 1988, pp. 285 – 295.

Prokopenko & Kuz'mich 1994] PROKOPENKO, G. I.; KUZ'MICH, G. I.: *Accumulation of Plastic Strain in Metals under Multiple Impulse Loading of Various Frequencies.* Physics of Metals (English Translation of Metallofizika), Vol. 13, 1994, pp. 464 – 475.

[Rackwitz & Fiessler 1978] RACKWITZ, R., FIESSLER, B.: *Structural Reliability under Combined Random Load Sequences.* Computers & Structures, Vol. 9, 1978, pp. 489 – 494.

[Radaj 1990] RADAJ, D.: *Design and Analysis of Fatigue Resistant Welded Structures.* Abington Publishing, Cambridge, UK, 1990

[Radaj & Sonsino 1998] RADAJ, D.; SONSINO, C. M.: *Fatigue Assessment of Welded Joints by Local Approaches.* Abington Publishing, Cambridge, UK, 1998.

[Raju & Newman 1979] RAJU. I. S.; NEWMAN, J. C., Jr.: *Stress-Intensity Factors for a Wide Range of Semi-elliptical Surface Cracks in Finite-Thickness Plates.* Engineering Fracture Mechanics, Vol. 11, 1979, pp. 817 – 829.

[Raussi & Tiainen 1980] RAUSSI, J.; TIAINEN, O. J. A..: *The Effect of Inspection an Repair on the Size Distributions of the Weld Imperfections in Nuclear Power Plant Pipes.* Nuclear Engineering and Design, Vol. 60, 1980, pp. 395 – 399.

[Rezai et al. 2005] Rezai, A.; Moore, M.; Green, T.; Washer, G.: *Laboratory and Field Testing of Automated Ultrasonic Testing (AUT) Systems for Steel Highway Bridges.* Publication No. FHWA-HRT-04-124, Federal Highway Administration, U.S. Department of Transportation, McLean, USA, 2005.

[Rice 1968] RICE, J. R.: *A Path Independent Integral and the Approximate Analysis of Strain Concentration by Notches and Cracks.* Paper No. 68-AMP-31, Transactions of the ASME, Journal of Applied Mechanics, Vol. 35, 1968, pp. 379 – 386.

[Rice et al. 1988] RICE, R. C.; LEIS, B. N.; NELSON, D. V. (Editors): *Fatigue Design Handbook.* 2nd Edition, Society of Automotive Engineers, Warrendale, USA, 1988.

[Righiniotis & Chryssanthopoulos 2003] Righiniotis, T. D.; Chryssanthopoulos, M. K.: *Probabilistic Fatigue Analysis under Constant Amplitude Loading.* Journal of Constructional Steel Research, Vol. 59, 2003, pp. 867 – 886.

[Rodriguez-Sanchez et al. 2004] RODRIGUEZ-SANCHEZ, J. E.; DOVER, W. D.; BRENNAN, F. P.: *Application of Short Repairs for Fatigue Life Extension.* International Journal of Fatigue, Vol. 26, 2004, pp. 413 – 420.

[Roeder et al. 2005] ROEDER, C. W.; MACRAE, G.; LELAND, A.; ROSPO, A.: *Extending the Fatigue Life of Riveted Coped Stringer Connections.* Journal of Bridge Engineering, Vol. 10, No. 1, 2005, pp. 69 – 76.

[Rolfe et. al. 1989] ROLFE, S. T.; SOREM, W. A.; WELLMAN, G. W.: *Fracture Control in the Transition-Temperature Region of Structural Steels.* Journal of Constructional Steel Research, Vol. 12, 1989, pp. 171 – 195.

[Roy et al. 2003] ROY, S.; FISHER, J. W.; YEN, B. T.: *Fatigue Resistance of Welded Details Enhanced by Ultrasonic Impact Treatment (UIT).* International Journal of Fatigue, Vol. 25, 2003, pp. 1239 – 1247.

[SAE 2002] SAE Standard J1099: *Technical Report on Low Cycle Fatigue Properties: Ferrous and Non-Ferrous Materials.* Society of Automotive Engineers, Warrendale, USA, 2002.

[SAE 2006] SAE Standard J442: *Test Strip, Holder, and Gage for Shot Peening.* Society of Automotive Engineers, Warrendale, USA, 2006.

[Schmidt & Bartlett 2002] SCHMIDT, B. J.; BARTLETT, F. M.: *Review of Resistance Factor for Steel: Data Collection.* Canadian Journal of Civil Engineering, Vol. 29, 2002, pp. 98 – 108.

[Schumacher 2003] SCHUMACHER, A.: *Fatigue Behaviour of Welded Circular Hollow Section Joints in Bridges.* Ph.D. Thesis No. 2727, Swiss Federal Institute of Technology, Lausanne, Switzerland, 2003.

[Sedlacek et al. 1992] SEDLACEK, G.; HENSEN, W.; BILD, J.; LANGENBERG, P.: *Verfahren zur Ermittlung der Sicherheit von alten Stahlbrücken unter Verwendung neuester Erkenntnisse der Werkstofftechnik (Procedure to Assess the Safety of Old Steel Bridges Using the Latest Findings in Material Behaviour).* Bauingenieur, Vol. 67, Heft 3, 1992, pp. 129 – 136.

[Shetty & Baker 1990] Shetty, N. K.; Baker, M. J.: *Fatigue Reliability of Tubular Joints in Offshore Structures: Reliability Analysis.* Proceedings of the 9th International Conference on Offshore Mechanics and Artic Engineering – OMAE, Vol. 2, 1990, pp. 33 – 40.

[SIA 2003] SIA 260:2003: *Basis of Structural Design.* Swiss Society of Engineers and Architects (SIA), Zurich, Switzerland, 2003.

[Simonen 1995] SIMONEN, F. A.: *Nondestructive Examination Reliability.* In: Probabilistic Structural Mechanics Handbook. C. Sundararajan (Editor), Chapman & Hall, New York, USA, 1995, pp. 238 – 260.

[Sire et al. 1992] SIRE, R. A.; KOKARAKIS, J. E.; WELLS, C. H.; TAYLOR, R. K.: *A Probabilistic Structure Life Prediction System for Container Ship Repair and Inspection.* International Journal of Pressure Vessels and Piping, Vol. 50, 1992, pp. 297 – 315.

[Smith & Hirt 1989] SMITH, I. F. C.; HIRT, M. A.: *Fatigue-Resistant Steel Bridges.* Journal of Constructional Steel Research, Vol. 12, 1989, pp. 197 – 214.

[Smith & Smith 1982] SMITH, I. F. C.; SMITH, R. A.: *Defects and Crack Development in Fillet Welded Joints.* Fatigue of Engineering Materials and Structures, Vol. 5, 1982, pp. 151 – 165.

[Smith et al. 1970] SMITH, K. N.; WATSON, P.; TOPPER, T. H.: *A Stress-Strain Function for the Fatigue of Materials.* Journal of Materials, Vol. 5, No 4, 1970, pp. 767 – 778.

[Socie et al. 1979] SOCIE, D. F.; MORROW, J.; CHEN, W.-C.: *A Procedure for Estimating the Total Fatigue Life of Notched and Cracked Members.* Engineering Fracture Mechanics, Vol. 11, No. 4, 1979, pp. 851 – 859.

[Stacey et al. 2000] Stacey, A.; Barthelemy, J.-Y.; Leggatt, R. H.; Ainsworth, R. A.: *Incorporation of Residual Stresses into the SINTAP Defect Assessment Procedure.* Engineering Fracture Mechanics, Vol. 67, 2000, pp. 573 – 611.

[Statnikov 1997] STATNIKOV, S.: *Applications of Operational Ultrasonic Impact Treatment (UIT) Technologies in Production of Welded Joints.* International Institute of Welding, Doc. XIII-1667-97, 1997.

[Statnikov 1999] STATNIKOV, S.: *Guide for Application of Ultrasonic Impact Treatment Improving Fatigue Life of Welded Structures.* International Institute of Welding, Doc. XIII-1757-99, 1999.

[Stephens et al. 2001] STEPHENS, R. I.; FATEMI, A.; STEPHENS, R. R.; FUCHS, H. O.: *Metal Fatigue in Engineering.* 2nd Edition, John Wiley and Sons, New York, USA, 2001.

[Stranghöner et al. 1998] Stranghöner, N.; Sedlacek, G; Stötzel, G.; DahL, W.; Langenberg, P.: *The Choice of Steel Material for Steel Bridges to Avoid Brittle Fracture.* Journal of Constructional Steel Research, Vol. 46, No. 1-3, Paper No. 45, 1998, p. 56.

[Straub & Faber 2004] Straub, D.; Faber, M. H.: *System Effects in Generic Risk Based Inspection Planning.* Journal of Offshore Mechanics and Arctic Engineering, Vol. 126, 2004, pp. 265 – 271.

[Sundararajan 1995] Sundararajan, C. R. (Ed.): *Probabilistic Structural Mechanics Handbook.* Chapman & Hall, New York, USA, 1995.

[Suresh 1998] SURESH, S.: *Fatigue of Materials.* 2nd Edition, Cambridge University Press, Cambridge, UK, 1998.

[Taheri et al. 2003] TAHERI, F.; TRASK, D.; PEGG, N.: *Experimental and Analytical Investigation of Fatigue Characteristics of 350WT Steel under Constant and Variable Amplitude Loadings.* Marine Structures, Vol. 16, 2003, pp. 69 – 91.

[Takamori & Fisher 2000] TAKAMORI, H.; FISHER, J. W.: *Tests of Large Girders Treated to Enhance Fatigue Strength.* Transportation Research Record 1696, Vol. 1, 2000, pp. 93 – 99.

[Tanaka & Akiniwa 2002] TANAKA, K.; AKINIWA, Y.: *Fatigue Crack Propagation Behaviour Derived from S-N Data in very high Cycle Regime.* Fatigue and Fracture of Engineering Materials and Structures, Vol. 25, 2002, pp. 775 – 784.

[Tavernelli & Coffin 1962] TAVERNELLI, J. F.; COFFIN, L. F., JR.: *Experimental Support for Generalized Equation Predicting Low Cycle Fatigue (incl. Discussion by S. S. Manson).* Transactions ASME, Journal of Basic Engineering, Vol. 84, 1962, pp. 533 – 541.

[Ummenhofer & Weich 2007] UMMENHOFER, T.; WEICH, I.: *Steigerung der Ermüdungsfestigkeit von Schweissverbindungen höherfester Stähle – Wirksamkeit hochfrequenter Hämmerverfahren (Increase of the Fatigue Strength of Welded Joints Made of High Strength Steel – Efficiency of High Frequent Hammer Peening Methods).* VDI-Berichte Nr. 1970, 2007, pp. 261 – 267.

[Vandenberg 2005] VANDENBERG, M.: *Equipment Repair Company Benefits from Unique Wire Feeder/Inverter.* Heavy Equipment Guide, July, 2005, pp. 18 – 19.

[Vårdal et al. 1999] VÅRDAL, O. T.; MOAN, T.; HELLEVIG, N.-C.: *Comparison between Observed and Predicted Characteristics of Fatigue Cracks in North Sea Jackets.* Proceedings of the Annual Offshore Technology Conference, Vol. 3, 1999, 243 – 252.

[Vo & Balkey 1995] VO, T. V.; BALKEY, K. R.: *Risk-Based Inspection and Maintenance.* In: Probabilistic Structural Mechanics Handbook. C. Sundararajan (Editor), Chapman & Hall, New York, USA, 1995, pp. 388 – 415.

[Walbridge 2005] WALBRIDGE, S.: *A Probabilistic Study of Fatigue in Post-Weld Treated Tubular Bridge Structures.* Ph.D. Thesis No. 3330, Swiss Federal Institute of Technology, Lausanne, Switzerland, 2005.

[Walbridge 2008] WALBRIDGE, S.: *Fatigue Analysis of Post-Weld Fatigue Improvement Treatments Using a Strain-Based Fracture Mechanics Model.* Engineering Fracture Mechanics, Vol. 75, 2008, pp. 5057 – 5071

[Wang 2010] WANG, Y.: *Fatigue Repair Technique Investigation – Hole Drilling and Expansion Method.* PhD Thesis, Department of Civil Engineering, University of Alberta, Edmonton, Canada, 2010 (to be published).

[Wei & Shih 1974] WEI, R. P.; SHIH, T. T.: *Delay in Fatigue Crack Growth.* International Journal of Fracture, Vol. 10, No. 1, 1974, pp. 77 – 85.

[Weisstein 2003] Weisstein, E. W: *Normal Sum Distribution.* Math World - A Wolfram Web Resource, Wolfram Research Inc., Champaign, USA, 2003.
Retrieved August 03, 2006, from
http://mathworld.wolfram.com/NormalSumDistribution.html

[Wirsching 1995] WIRSCHING, P. H.: *Probabilistic Fatigue Analysis.* In: Probabilistic Structural Mechanics Handbook. C. Sundararajan (Editor), Chapman & Hall, New York, USA, 1995, pp. 146 – 165.

[Wright 1996] WRIGHT, W.: *Post-Weld Treatment of a Welded Bridge Girder by Ultrasonic Impact Treatment.* Internal Research Report, Federal Highway Administration, Turner-Fairbank Highway Research Center, McLean, USA, 1996.

[Yamada & Nagatsu 1989] YAMADA, K.; NAGATSU, S.: *Evaluation of Scatter in Fatigue Life of Welded Details Using Fracture Mechanics.* Structural Engineering / Earthquake Engineering, Vol. 6, 1989, pp. 13s – 21s.

[Yin et al. 2006] YIN, Y.; GRONDIN, G. Y.; ELWI, A. E: *Fatigue Crack Behaviour in Mine Excavator.* Structural Engineering Report No. 265, Department of Civil Engineering, University of Alberta, Edmonton, Canada, 2006.

[Zhang & Mahadevan 2001] ZHANG, R.; MAHADEVAN, S.: *Fatigue Reliability Analysis Using Nondestructive Inspection.* Journal of Structural Engineering, Vol. 127, No. 8, 2001, pp. 957 – 965.

[Zhao et al. 1994a] Zhao, Z.; Haldar, A.; Breen, F.: *Fatigue-Reliability Evaluation of Steel Bridges.* Journal of Structural Engineering, Vol. 120, No. 5, 1994, pp. 1608 – 1623.

[Zhao et al. 1994b] Zhao, Z.; Haldar, A.; Breen, F.: *Fatigue-Reliability Updating through Inspections of Steel Bridges.* Journal of Structural Engineering, Vol. 120, No. 5, 1994, pp. 1624 – 1642.

[Zhuang & Halford 2001] ZHUANG W. Z.; HALFORD, G. R.: *Investigation of Residual Stress Relaxation under Cyclic Load.* International Journal of Fatigue, Vol. 23, 2001, pp. S31 – S37.

APPENDIX A

Probability Density Functions

PROBABILITY DENSITY FUNCTIONS

The probability density functions (pdf), $f_X(x)$, and cumulative distribution functions, $F_X(x)$, used in the present work are:

- Exponential: Exp(λ)

$$f_X(x) = \frac{1}{\lambda} \cdot \mathrm{e}^{-x/\lambda}$$
$$F_X(x) = 1 - \mathrm{e}^{-x/\lambda} \tag{A.1}$$

- Normal: N(μ, σ)

$$f_X(x) = \frac{1}{\sqrt{2\pi}\sigma} \cdot \mathrm{e}^{-\frac{1}{2}\cdot\left(\frac{x-\mu}{\sigma}\right)^2}$$
$$F_X(x) = \int_{-\infty}^{x} \frac{1}{\sqrt{2\pi}\sigma} \cdot \mathrm{e}^{-\frac{1}{2}\cdot\left(\frac{y-\mu}{\sigma}\right)^2} dy \qquad \text{(no closed form sol.)} \tag{A.2}$$

- Lognormal: LN(α, β)

$$f_X(x) = \frac{1}{\sqrt{2\pi}x\varepsilon} \cdot \mathrm{e}^{-\frac{1}{2}\cdot\left(\frac{\ln x-\lambda}{\varepsilon}\right)^2}$$
$$F_X(x) = \int_{-\infty}^{x} \frac{1}{\sqrt{2\pi}y\varepsilon} \cdot \mathrm{e}^{-\frac{1}{2}\cdot\left(\frac{\ln y-\lambda}{\varepsilon}\right)^2} dy \qquad \text{(no closed form sol.)} \tag{A.3}$$

where $\lambda = E[\ln(X)]$ and $\varepsilon^2 = Var[\ln(X)]$

The lognormal distribution can be expressed as a normal distribution by putting

$$x = \ln(x)$$
$$\mu = \ln(\alpha) - \frac{1}{2}\ln\left(1 + \left(\frac{\beta}{\alpha}\right)^2\right) = \ln(\alpha) - \frac{1}{2}\sigma^2$$
$$\sigma = \sqrt{\ln\left(1 + \left(\frac{\beta}{\alpha}\right)^2\right)}$$

in equation (A.2), where $\alpha = E[X]$ (mean value) and $\beta = \sqrt{Var[X]}$ (standard deviation). The parameters of the lognormal distribution as used in the present work always refer to α, β (mean values and standard deviation) and not λ, ε.

- Weibull: W(θ, τ)

$$f_X(x) = \frac{\tau}{x} \cdot \left(\frac{x}{\theta}\right)^{\tau} \cdot \mathrm{e}^{-\left(\frac{x}{\theta}\right)^{\tau}}$$

$$F_X(x) = 1 - \mathrm{e}^{-\left(\frac{x}{\theta}\right)^{\tau}} \qquad \text{(A.4)}$$

APPENDIX B

Gouging and Welding Procedure Specification

GOUGING AND WELDING PROCEDURE SPECIFICATION

Gouging Procedure

The gouging in the splice plates of the large scale specimens was done by one welder according to the following procedure:

Electrode:	Arcair® DC Copperclad Pointed Electrode 4.7 x 305 mm carbon / graphite electrode with copper coating
Voltage:	~9.0 V
Amperage:	~300 A
Air Pressure:	~275 kPa (~40 psi)

Welding Procedure Specification

Initial Welding Procedure

The welding of the specimens described in Chapter 4 (pad for chemical analysis, welded plates), of the welded plates for the small scale tests and the first six repair welds for the large scale tests presented in Chapter 5 was performed by one welder using the flux cored arc welding (FCAW) process and the following procedure:

Position:	Flat
Electrode:	Stein-Megafil® 713R (seamless rutile flux cored wire with rapidly solidifying slag) AWS 5.20 [2005]: E491T1
Diameter:	1.2 mm (0.045 in.)
Voltage:	~30 V
Wire feed speed:	~190 mm/s (~450 ipm), resulting in a current of ~300 A
Electrode extension:	~25 mm
Current and Polarity:	DCEP
Transfer	Spray
Travel speed:	~3.4 mm/s (~8 ipm), with stringer beads (no weaving)
Shielding Gas:	25% CO2 – 75% Ar (flow rate ~15 L/min)
Preheat Temp.	Min. 20°C (all plates < 40 mm)
Interpass Temp.	Min. 20°C Max. 230°C
Cooling Rate	Slow cool
Cleaning	Brushing and if needed grinding

Improved Welding Procedure Specification

Since the large scale weld repairs contained severe slag inclusions, a modified welding procedure had to be developed. In order to be able to apply the weld material properties determined in Chapter 3, where the initial welding procedure was used, care was taken not to change any fundamental parameters. The rather simple, but often effective method of lowering the heat input by increasing the travel speed from 3.4 mm/s to approximately 6 mm/s (14 ipm) was tried first. In addition, slight weaving was done in order to be able to fill the groove. Ultrasonic inspection and subsequent cutting of a trial weld profile at several sections showed that no significant inclusions were present. Therefore, all the remaining repair welds were done with exactly the same settings as in the initial procedure, but with a higher travel speed of approximately 6 mm/s (14 ipm) and slight weaving. The higher travel speed resulted in a lesser deposited volume of weld metal in each pass and the number of passes had to be increased as well (from five to seven passes on each the top and bottom side of the plates). All welds were done by the same welder as the initial welds.

APPENDIX C

Load History of Cracked Reaction Beam

LOAD HISTORY OF CRACKED REACTION BEAM

The load history the cracked and replaced reaction beam was subjected to is summarized in Table C.1.

Table C.1 – *Load history of cracked reaction beam.*

Specimen	P_{min} [kN]	P_{max} [kN]	N	Start	End
L175NT1	20	400	190,000	12.03.08	27.03.08
L145NTT	20	335	60,000	03.04.08	03.04.08
L145NT1	20	335	880,000	21.04.08	26.04.08
L145NT2	20	335	5,360,000	28.04.08	30.05.08
L175UP1	20	400	1,130,000	30.05.08	04.06.08
L175NT2	20	400	270,000	05.06.08	09.06.08
L195NT11	20	450	1,580,000	10.06.08	17.06.08
L195NT12	20	450	1,500,000	20.06.08	26.06.08
L240NT21	20	400	820,000	15.07.08	22.07.08
L240NT22	20	400	5,540,000	23.07.08	06.11.08

The first cracks in the support region were detected after about 500,000 cycles in L240NT21. The diagonal crack under the North actuator was first detected after 3.60 million cycles in L240NT22.

Figure C.1 and Figure C.2 show the diagonal and a typical crack between the supports. All cracks started in the flange to web fillet welds. The diagonal crack under the actuator only propagated into the web. The cracks in the support region propagated into the flange and the web. They self-arrested in the flange, but in spite of compressive stresses due to the applied loads could only be stopped by drilling a hole at the crack tip in the web.

Figure C.1 *– Diagonal crack in reaction beam under North actuator.*

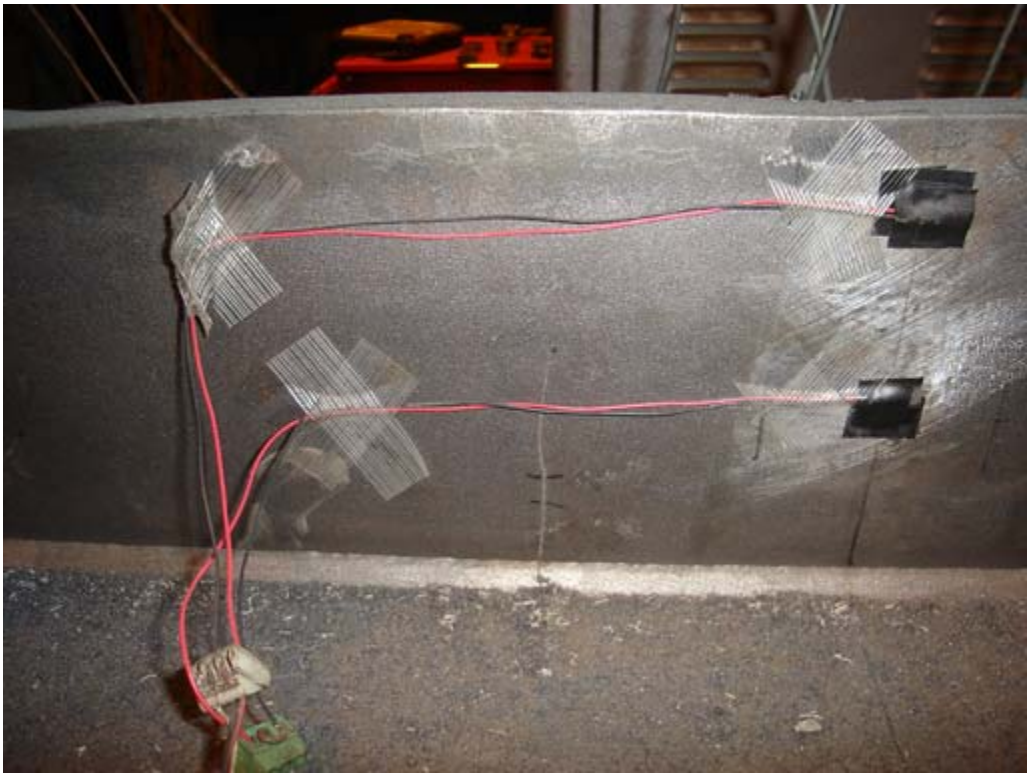

Figure C.2 *–Typical crack in reaction beam between the two supports.*

APPENDIX D

Crack Closure

INTEGRATION OF CRACK CLOSURE EFFECT AND RESIDUAL STRESSES IN STABLE FATIGUE CRACK PROPAGATION MODEL

The stable fatigue crack propagation stage is modeled in the present work by the following relationship [Ohta et al. 1986]:

$$\frac{da}{dN} = C \cdot \left(\Delta K_{eff}{}^{m} - \Delta K_{th}^{m} \right) \tag{2.9}$$

where da/dN is the crack propagation rate (increase in crack size da per load cycle dN), C and m are empirically established material constants, ΔK_{eff} is the effective stress intensity factor range, accounting for crack closure and residual stresses, and ΔK_{th} is the threshold stress intensity factor range.

In order to determine ΔK_{eff}, let's define the total stress intensity factor, K_{tot}, accounting for crack closure and residual stresses as follows:

$$K_{tot} = K + K_{pl} + K_{res} \tag{D.1}$$

where K is the SIF corresponding to the applied stress, σ, and K_{pl} and K_{res} are the SIF corresponding to crack closure and residual stress distribution, respectively. In order that $K_{tot} = 0$ at an applied stress level of $\sigma = \sigma_{op}$, where σ_{op} is the crack opening stress with the corresponding stress intensity factor K_{op}, and assuming no residual stresses, i.e. $K_{res} = 0$, the following must be true:

$$K_{tot} = K_{op} + K_{pl} + 0 = 0 \;\Rightarrow\; K_{op} = -K_{pl} \tag{D.2}$$

Recall Elber's crack closure ratio, U:

$$U = \frac{\Delta K_{eff}}{\Delta K} = \frac{K_{\max} - K_{op}}{K_{\max} - K_{\min}} = \frac{\left(1 - K_{op}/K_{\max}\right)}{\left(1 - R\right)} \tag{6.3}$$

and Bremen's empirical relationship for U:

$$\begin{aligned} U &= \frac{\left(1 - 0.2/\left(1 - R\right)\right)}{\left(1 - R\right)} && \text{for } R \le 0.28 \\ U &= 1.0 && \text{for } R > 0.28 \end{aligned} \tag{6.5}$$

where R is the stress ratio due to the applied stresses, $\sigma_{\min}$ and $\sigma_{\max}$.

Substituting equation (D.2) in (6.3) yields:

$$U = \frac{\left(1 + K_{pl} / K_{\max}\right)}{\left(1 - R\right)} \tag{D.3}$$

For $R \le 0.28$, K_{pl} can be determined by setting the first expression of equation (6.5) equal to equation (D.3):

$$\frac{\left(1 - 0.2/\left(1 - R\right)\right)}{\left(1 - R\right)} = \frac{\left(1 + K_{pl} / K_{\max}\right)}{\left(1 - R\right)}$$

$$\Rightarrow K_{pl} = -\frac{0.2}{1 - R} \cdot K_{\max} \tag{D.4}$$

and K_{op} and ΔK_{eff} become:

$$K_{op} = -K_{pl} = \frac{0.2}{1 - R} \cdot K_{\max} \tag{D.5}$$

$$\Delta K_{eff} = K_{\max} - K_{op} = K_{\max} - \frac{0.2}{1 - R} \cdot K_{\max} = K_{\max} \cdot \left(1 - \frac{0.2}{1 - R}\right) \tag{D.6}$$

Similarly, for $R > 0.28$, K_{pl} can be determined by setting the second expression of equation (6.5) equal to equation (D.3):

$$1.0 = \frac{\left(1 + K_{pl} / K_{\max}\right)}{\left(1 - R\right)}$$

$$\Rightarrow K_{pl} = -R \cdot K_{\max} = -K_{\min} \tag{D.7}$$

and K_{op} and ΔK_{eff} become:

$$K_{op} = -K_{pl} = K_{\min} \tag{D.8}$$

$$\Delta K_{eff} = K_{\max} - K_{op} = K_{\max} - K_{\min} = \Delta K \tag{D.9}$$

Equation (D.9) shows that no crack closure effect is present for $R > 0.28$, which corresponds, as would be expected, to the definition of $U = 1.0$ for $R > 0.28$.

The above derivations can now be expanded to account for residual stresses by replacing $K_{\min}$ with $\left(K_{\min} + K_{res}\right)$, $K_{\max}$ with $\left(K_{\max} + K_{res}\right)$, and subsequently R with $R_{eff} = \left(K_{\min} + K_{res}\right) / \left(K_{\max} + K_{res}\right)$, and adjusting ΔK_{eff} for the effect of residual stresses:

$$\Delta K_{eff} = \left(K_{\max} + K_{res}\right) - K_{op} \qquad \text{for} \tag{D.10}$$

$$K_{op} > (K_{\min} + K_{res})$$

$$\Delta K_{eff} = (K_{\max} + K_{res}) - (K_{\min} + K_{res}) = \Delta K$$

for

$$K_{op} \le (K_{\min} + K_{res}) \tag{D.11}$$

Of course there will be no crack propagation for effective compressive stresses:

$$\Delta K_{eff} = 0 \qquad \text{for } K_{\max} + K_{res} < 0 \tag{D.12}$$

Recalling from equation (D.1) that in the presence of residual stresses $K_{op} = -(K_{pl} + K_{res})$, equation (D.3) becomes:

$$U = \frac{\left(1 + (K_{pl} + K_{res}) / (K_{\max} + K_{res})\right)}{(1 - R_{eff})} \tag{D.13}$$

Let's again first consider the case when $R_{eff} \le 0.28$. Equalling the first expression of equation (6.5), which is adapted to account for residual stresses by replacing R with R_{eff}, with equation (D.13) results in:

$$\frac{\left(1 - 0.2/(1 - R_{eff})\right)}{(1 - R_{eff})} = \frac{\left(1 + (K_{pl} + K_{res}) / (K_{\max} + K_{res})\right)}{(1 - R_{eff})}$$

$$\Rightarrow K_{pl} = -\frac{0.2}{1 - R_{eff}} \cdot (K_{\max} + K_{res}) - K_{res} \tag{D.14}$$

and K_{op} becomes:

$$K_{op} = -(K_{pl} + K_{res}) = \frac{0.2}{1 - R_{eff}} \cdot (K_{\max} + K_{res}) \tag{D.15}$$

ΔK_{eff} can now be determined for $K_{op} > (K_{\min} + K_{res})$ as:

$$\begin{aligned} \Delta K_{eff} &= (K_{\max} + K_{res}) - K_{op} \\ &= (K_{\max} + K_{res}) - \left(\frac{0.2}{1 - R_{eff}} \cdot (K_{\max} + K_{res}) \right) \\ &= (K_{\max} + K_{res}) \cdot \left(1 - \frac{0.2}{1 - R_{eff}} \right) \end{aligned} \tag{D.16}$$

Note that for no residual stresses ($K_{res} = 0$), equation (D.16) reduces to equation (D.6).

For $R > 0.28$, K_{pl} can be determined by setting the second expression of equation (6.5) equal to equation (D.13):

$$K_{pl} = -R_{eff} \cdot (K_{\max} + K_{res}) - K_{res} = -(K_{\min} + 2K_{res}) \tag{D.17}$$

and K_{op} and ΔK_{eff} become:

$$K_{op} = -(K_{pl} + K_{res}) = (K_{\min} + 2K_{res}) - K_{res} = K_{\min} + K_{res} \tag{D.18}$$

$$\Delta K_{eff} = (K_{\max} + K_{res}) - K_{op} = (K_{\max} + K_{res}) - (K_{\min} + K_{res}) = \Delta K \tag{D.19}$$

Grouping the above relationships, ΔK_{eff} is determined as follows:

- $\Delta K_{eff} = 0$ for $K_{\max} + K_{res} < 0$
- $\Delta K_{eff} = \Delta K$ for $K_{\max} + K_{res} \geq 0$ and $K_{op} \leq (K_{\min} + K_{res})$ and all R_{eff} or $K_{op} > (K_{\min} + K_{res})$ and $R_{eff} > 0.28$
- $\Delta K_{eff} = (K_{\max} + K_{res}) \cdot \left(1 - \frac{0.2}{1 - R_{eff}}\right)$ for $K_{\max} + K_{res} \geq 0$ and $K_{op} > (K_{\min} + K_{res})$ and $R_{eff} \leq 0.28$

where $K_{op} = \frac{0.2}{1 - R_{eff}} \cdot (K_{\max} + K_{res})$ for $R_{eff} \leq 0.28$

$K_{op} = K_{\min} + K_{res}$ for $R_{eff} > 0.28$

Since $K_{op} = K_{\min} + K_{res}$ for $R_{eff} > 0.28$, the third condition in $\Delta K_{eff} = \Delta K$ ($K_{op} > K_{\min} + K_{res}$ and $R_{eff} > 0.28$) can never occur. Furthermore the condition $K_{op} \leq (K_{\min} + K_{res})$ for $R_{eff} \leq 0.28$ is only satisfied in the interval $0.2764 < R_{eff} \leq 0.28$, i.e. for $R_{eff} < 0.2764$, K_{op} is always greater than $(K_{\min} + K_{res})$. Using $\Delta K_{eff} = (K_{\max} + K_{res}) \cdot (1 - 0.2/(1 - R_{eff}))$ instead of $\Delta K_{eff} = \Delta K$ in the interval $0.2764 < R_{eff} \leq 0.28$ results in a negligible inaccuracy. Therefore the following simplified relationships can be used:

- $\Delta K_{eff} = 0$ for $K_{\max} + K_{res} < 0$
- $\Delta K_{eff} = \Delta K$ for $K_{\max} + K_{res} \geq 0$ and $R_{eff} > 0.28$
- $\Delta K_{eff} = (K_{\max} + K_{res}) \cdot \left(1 - \frac{0.2}{1 - R_{eff}}\right)$ for $K_{\max} + K_{res} \geq 0$ and $R_{eff} \leq 0.28$

Having determined ΔK_{eff} and knowing the material properties C, m, and ΔK_{th} from tests, equation (2.9) can now be integrated from an initial crack size, a_0, to a final crack size, a_f, to get the stable crack propagation life.

APPENDIX E

Mesh Refinement Study

MESH REFINEMENT STUDY

This appendix presents the results of the mesh refinement studies that were carried out to find the optimum mesh for the local models presented in Chapter 6. For each of the seven models (no flaw, 0.1 mm surface flaw, 0.1 mm corner flaw, 0.1 mm embedded flaw, 1.0 mm surface flaw, 1.0 mm corner flaw, and 1.0 mm embedded flaw) the following tables show the investigated mesh configurations and sizes and the resulting principal strain at the critical location (see Chapter 6). The strains were obtained from non-linear analyses of the models subjected to the maximum applied stress of 400 MPa. The models that reached convergence are shown in bold.

Table E.1 *– Mesh refinement for the model with no flaw (model size (in mm): 10.0×9.525×2.0).*

Element Size [mm]	Number of		Principal Strain	Relative Difference
	Nodes	Elements		
2.00	228	25	2.29×10^{-3}	---
1.50	656	98	2.33×10^{-3}	1.75%
1.00	1262	200	2.35×10^{-3}	0.86%
0.80	2622	468	2.36×10^{-3}	0.43%
0.70	3476	630	2.36×10^{-3}	0.00%
0.60	**5639**	**1088**	$\mathbf{2.36\times10^{-3}}$	**0.00%**
0.50	8169	1600	2.36×10^{-3}	0.00%

Table E.2 *– Mesh refinement for the model with a 0.1 mm surface flaw (model size (in mm): 1.0×9.525×1.0).*

Element Size [mm]		**Number of**		**Principal Strain**	**Relative Difference**
Around Flaw	**Outer Areas**	**Nodes**	**Elements**		
0.020	1.00	5253	3040	4.86×10^{-3}	---
0.015	0.50	13394	8313	4.97×10^{-3}	2.26%
0.012	0.30	21322	13539	5.00×10^{-3}	0.60%
0.010	0.30	33691	21573	5.02×10^{-3}	0.04%
0.010	**0.20**	**42944**	**28159**	$\mathbf{5.02\times10^{-3}}$	**0.00%**
0.009	0.15	58664	40079	5.02×10^{-3}	0.00%

Table E.3 *– Mesh refinement for the model with a 0.1 mm corner flaw (model size (in mm): 1.0×9.525×1.0).*

Element Size [mm]		**Number of**		**Principal Strain**	**Relative Difference**
Around Flaw	**Outer Areas**	**Nodes**	**Elements**		
0.020	1.00	5253	3040	7.46×10^{-3}	---
0.015	0.50	13394	8313	7.63×10^{-3}	2.28%
0.012	0.30	21322	13539	7.72×10^{-3}	1.18%
0.010	0.30	33691	21573	7.75×10^{-3}	0.39%
0.010	**0.20**	**42944**	**28159**	$\mathbf{7.76\times10^{-3}}$	**0.13%**
0.009	0.15	58664	40079	7.76×10^{-3}	0.00%

Table E.4 *– Mesh refinement for the model with a 0.1 mm embedded flaw (model size (in mm): 1.0×9.525×1.0).*

Element Size [mm]		**Number of**		**Principal Strain**	**Relative Difference**
Around Flaw	**Outer Areas**	**Nodes**	**Elements**		
0.020	1.00	6174	3506	4.05×10^{-3}	
0.015	0.50	12005	7131	4.07×10^{-3}	0.49%
0.012	0.50	25845	14783	4.08×10^{-3}	0.25%
0.012	0.30	35148	20054	4.09×10^{-3}	0.25%
0.010	**0.30**	**48845**	**32279**	$\mathbf{4.10\times10^{-3}}$	0.25%
0.009	0.20	65047	48932	4.10×10^{-3}	0.00%

Table E.5 *– Mesh refinement for the model with a 1.0 mm surface flaw (model size (in mm): 10.0×9.525×2.0).*

Element Size [mm]		**Number of**		**Principal Strain**	**Relative Difference**
Around Flaw	**Outer Areas**	**Nodes**	**Elements**		
0.20	2.00	1320	657	6.80×10^{-3}	---
0.15	1.50	3002	1657	7.00×10^{-3}	2.94%
0.12	1.20	8979	5525	7.08×10^{-3}	1.14%
0.10	1.00	18630	12841	7.10×10^{-3}	0.28%
0.10	**0.80**	**30357**	**20094**	$\mathbf{7.11\times10^{-3}}$	**0.14%**
0.09	0.70	45622	32178	7.11×10^{-3}	0.00%

Table E.6 *– Mesh refinement for the model with a 1.0 mm corner flaw (model size (in mm): 10.0×9.525×2.0).*

Element Size [mm]		Number of		Principal Strain	Relative Difference
Around Flaw	Outer Areas	Nodes	Elements		
0.20	2.00	1320	657	1.41×10^{-2}	---
0.15	1.50	3002	1657	1.46×10^{-2}	3.55%
0.12	1.20	8979	5525	1.47×10^{-2}	0.68%
0.10	1.00	18630	12841	1.48×10^{-2}	0.68%
0.10	**0.80**	**30357**	**20094**	$\mathbf{1.48\times10^{-2}}$	**0.00%**
0.09	0.70	45622	32178	1.48×10^{-2}	0.00%

Table E.7 *– Mesh refinement for the model with a 1.0 mm embedded flaw (model size (in mm): 10.0×9.525×2.0).*

Element Size [mm]		Number of		Principal Strain	Relative Difference
Around Flaw	Outer Areas	Nodes	Elements		
0.20	2.00	2880	1624	5.93×10^{-3}	---
0.15	1.50	5651	3350	6.37×10^{-3}	7.42%
0.12	1.20	10028	6145	6.43×10^{-3}	0.94%
0.10	1.00	22552	13982	6.44×10^{-3}	0.16%
0.10	**0.80**	**33938**	**22224**	$\mathbf{6.44\times10^{-3}}$	**0.00%**
0.09	0.70	44533	31087	6.44×10^{-3}	0.00%

APPENDIX F

Sample Fatigue Life Calculation

SAMPLE FATIGUE LIFE CALCULATION

A sample fatigue life calculation procedure is presented in this Appendix as an illustration of the calculations used for the predictions presented in Chapters 6, 7, and 8. The specimen used for this illustration consists of an ultrasonically peened test specimen with a 1.0 mm surface flaw (residual stress of -200 MPa at critical location), incorporating crack closure and the threshold stress intensity factor range, ΔK_{th}. Equations (2.5) and (2.9) are used to determine the crack initiation and propagation lives, respectively:

$$\frac{\Delta\varepsilon}{2} = \frac{\left(\sigma_f^{'}\right)^2}{\sigma_{\max} E}\left(N_{init}\right)^{2b} + \frac{\sigma_f^{'}\varepsilon_f^{'}}{\sigma_{\max}}\left(N_{init}\right)^{b+c} \tag{2.5}$$

$$\frac{da}{dN} = C\cdot\left(\Delta K_{eff}^{m} - \Delta K_{th,eff}^{m}\right) \Leftrightarrow N_{prop} = \int_{a_0}^{a_f} \frac{da}{C\cdot\left(\Delta K_{eff}^{m} - \Delta K_{th}^{m}\right)} \tag{2.9}$$

with $\Delta K_{eff} = 0$ for $K_{\max} + K_{res} < 0$ and all R_{eff}

$\Delta K_{eff} = \Delta K$ for $K_{\max} + K_{res} \geq 0$ and $R_{eff} > 0.28$

$\Delta K_{eff} = \left(K_{\max} + K_{res}\right)\cdot\left(1 - \frac{0.2}{1 - R_{eff}}\right)$ for $K_{\max} + K_{res} \geq 0$ and $R_{eff} \leq 0.28$

All parameters in equations (2.5) and (2.9) are obtained from Chapter 6:

$\frac{\Delta\varepsilon}{2} = 1.84\times10^{-3}$

$\sigma_{\max} = 435$ MPa

$E = 207{,}000$ MPa

$\sigma_f^{'} = 630$ MPa

$b = -0.059$

$\varepsilon_f^{'} = 0.34$

$c = -0.63$

$a_0 = 1.0$ mm

$a_f = 4.763$ mm (crack reaches corners of reduced section)

$C = 3.50\times10^{-13}$ (mm/cycle)$\cdot\left(\text{MPa}\sqrt{\text{mm}}\right)^{-3}$

$m = 3.0$

$\Delta K_{th} = 60\ \text{MPa}\sqrt{\text{mm}}$

$K_i = \beta_E \beta_S \beta_W \beta_G \sigma_i \sqrt{\pi a}$ *i* standing for *min*, *max*, and *res*

stress due to external (MTS) load: $\sigma_{\max,app}$ = 400 MPa (top)

200MPa (bottom)

$\sigma_{\min,app}$ = 30 MPa (top and bottom)

residual stress: σ_{res} = -200 MPa (top)

100 MPa (at 2.525)

$$\beta_E = 0.825$$

$$\beta_S = 1.12$$

$$\beta_W = \sqrt{\frac{1}{\cos\left(\frac{\pi a}{2 \cdot 19.05}\right)}}$$

$$\beta_{G,i} = 1 + \frac{2A_i}{\pi} a$$

stress due to external (MTS) load: $A_{\max} = \frac{200/400 - 1}{19.05} = -0.0262$

$A_{\min} = \frac{30/30 - 1}{19.05} = 0.0$

residual stress: $A_{res} = \frac{100/(-200) - 1}{2.525} = -0.594$

Crack Initiation Life

Substituting the crack initiation parameters into equation (2.5) and solving numerically results in:

$N_{init} = 22{,}725$ cycles

Back-substituting to verify the numerical solution, we obtain:

$$\frac{\Delta\varepsilon}{2} = \frac{(\sigma_f')^2}{\sigma_{\max} E}(N_{init})^{2b} + \frac{\sigma_f' \varepsilon_f'}{\sigma_{\max}}(N_{init})^{b+c}$$

$$= \frac{(630)^2}{435 \cdot 207{,}000}(22{,}725)^{2\cdot(-0.059)} + \frac{625 \cdot 0.34}{435}(22{,}725)^{(-0.059)+(-0.63)} = 1.840\times10^{-3}$$

Crack Propagation Life

The crack propagation life is obtained by solving equation (2.9) numerically. For all the calculations presented in this research program the crack size increment was set to:

$$\Delta a = \frac{a_f - a_0}{1000}$$

which results in $\Delta a = (4.763 - 1.0)/1000 = 0.003763$ mm.

The crack size at the beginning of the increment is $a = a_0 = 1.0$ mm. At the end of the increment a is equal to $a_0 + \Delta a = 1.003763$ mm. The average crack size in increment 1 is therefore $a_{av} = 1.0018815$ mm. With this average crack size the following results are obtained:

$$\beta_W = \sqrt{\frac{1}{\cos\left(\frac{\pi \cdot 1.0018815}{2 \cdot 19.05}\right)}} = 1.00171$$

$$\beta_{G,\max} = 1 + \frac{2(-0.0262)}{\pi} 1.0018815 = 0.9833$$

$$\beta_{G,\min} = 1.0$$

$$\beta_{G,res} = 1 + \frac{2(-0.594)}{\pi} 1.0018815 = 0.6211$$

$$\beta_{\max} = 0.825 \cdot 1.12 \cdot 1.00171 \cdot 0.9833 = 0.910$$

$$\beta_{\min} = 0.825 \cdot 1.12 \cdot 1.00171 \cdot 1.0 = 0.926$$

$$\beta_{\max} = 0.825 \cdot 1.12 \cdot 1.00171 \cdot 0.6211 = 0.575$$

$$K_{\max} = 0.910 \cdot 400 \cdot \sqrt{\pi \cdot 1.0018815} = 645.8 \text{ MPa}\sqrt{\text{mm}}$$

$$K_{\min} = 0.926 \cdot 30 \cdot \sqrt{\pi \cdot 1.0018815} = 49.3 \text{ MPa}\sqrt{\text{mm}}$$

$$K_{res} = 0.575 \cdot (-200) \cdot \sqrt{\pi \cdot 1.0018815} = -204.0 \text{ MPa}\sqrt{\text{mm}}$$

$$K_{\max,eff} = 645.8 + (-204.0) = 441.8 \text{ MPa}\sqrt{\text{mm}} \qquad > 0$$

$$K_{\min,eff} = 49.3 + (-204.0) = -154.7 \text{ MPa}\sqrt{\text{mm}}$$

$$R_{eff} = \frac{-154.7}{441.8} = -0.35 \qquad < 0.28$$

$$\Rightarrow \Delta K_{eff} = (K_{\max} + K_{res}) \cdot \left(1 - \frac{0.2}{1 - R_{eff}}\right) = 376 \text{ MPa}\sqrt{\text{mm}}$$

$$\frac{da}{dN} = C\left(\Delta K_{eff}^{\,m} - \Delta K_{th}^{\,m}\right) = 3.50 \times 10^{-13}\left(376^{3.0} - 60^{3.0}\right) = 1.85 \times 10^{-5}$$

$$\Delta N_1 = \Delta a \frac{dN}{da} = 0.003763 \frac{1}{1.85 \times 10^{-5}} = 203 \text{ cycles}$$

It takes 203 cycles for the crack to propagate from 1.0 mm to 1.003763 mm (increment 1). The next increment (from a crack size of 1.003763 mm to 1.007526 mm) results in $\Delta N_2 = 201$ cycles, i.e. the total number of cycles for the crack to grow from 1.0 mm to

1.007526 mm is 404. Carrying out these calculations for the remaining 998 increments and adding up all the ΔN_i results in the total number of cycles to failure:

$$N_{prop} = 35{,}752 \text{ cycles}$$

It is interesting to note that for the last 100 increments $\Delta N_i = 6$ cycles, demonstrating that once the crack has reached the corners of the reduced section the fatigue life has been exhausted.

Total Fatigue Life

Adding the crack initiation and propagation lives gives the total fatigue life:

$$N = 22{,}700 + 35{,}800 = 58{,}500 \text{ cycles}$$

APPENDIX G

Deterministic Predictions of Test Results

DETERMINISTIC PREDICTIONS OF TEST RESULTS

G.1 Introduction

The results of all deterministic predictions of the small scale tests are presented in this appendix.

The material properties used in the predictions are (see Section 6.3.6):

- $E = 207{,}000$ MPa
- $\sigma_f^{'} = 630$ MPa
- $b = -0.059$
- $\varepsilon_f^{'} = 0.34$
- $c = -0.63$
- $m = 3.0$
- $C = 3.5 \times 10^{-13}$ (for ΔK in MPa$\sqrt{\text{mm}}$ and da/dN in mm/cycle)
- $\Delta K_{th} = 60$ MPa$\sqrt{\text{mm}}$

Recall the approach designation from Section 6.3.9:

- N = perfect weld, C = crack, F = flaw
- 00 = no inclusion, 01 = 0.1 mm inclusion, 10 = 1.0 mm inclusion
- L = ΔK_{th} included (large crack), S = ΔK_{th} neglected (small crack)
- N = crack closure neglected (no residual stresses in crack propagation), C = crack closure included (residual stresses in crack propagation)
- In order to distinguish between corner, surface, and embedded flaw or crack the letter C, S, and E are added at the end of the designation.

G.2 Non-Peened Weld with no Inclusions

The following parameters were investigated for the non-peened specimens with perfect welds (with no inclusions):

- residual stresses at top of plate of $\sigma_{res} = 100$ MPa and 0 MPa
- with and without ΔK_{th}
- with and without crack closure

A corner crack with a starting crack size of $a_0 = 0.1$ mm was assumed for all crack propagation calculations. The results of the crack initiation and propagation life calculations and the total fatigue life for each approach defined in Section 6.3 are summarized in Table G.1 through Table G.4. The approach designations defined in Table 6.1 are used in the tables. Each table shows the results for both residual stress distributions.

Table G.1 – *Fatigue lives for model with no flaw: approach including ΔK_{th} and neglecting crack closure.*

Approach Designation	σ_{res}	N_{init}	N_{prop}	N
N00LN	100 MPa	393,000	163,000	554,000
	0 MPa	1,840,000	163,000	2,000,000

Table G.2 *– Fatigue lives for model with no flaw: approach including ΔK_{th} and crack closure.*

Approach Designation	σ_{res}	N_{init}	N_{prop}	N
N00LC	100 MPa	393,000	168,000	562,000
	0 MPa	1,840,000	269,000	2,110,000

Table G.3 *– Fatigue lives for model with no flaw: approach neglecting ΔK_{th} and crack closure.*

Approach Designation	σ_{res}	N_{init}	N_{prop}	N
N00SN	100 MPa	393,000	160,000	553,000
	0 MPa	1,840,000	160,000	2,000,000

Table G.4 *– Fatigue lives for model with no flaw: approach neglecting ΔK_{th} and including crack closure.*

Approach Designation	σ_{res}	N_{init}	N_{prop}	N
N00SC	100 MPa	393,000	165,000	558,000
	0 MPa	1,840,000	261,000	2,110,000

G.3 Non-Peened Corner Flaw or Crack

The following parameters were investigated for the specimens with a non-peened corner flaw or crack:

- residual stresses at top of specimen of $\sigma_{res} = 100$ MPa and 0 MPa
- crack and flaw
- initial crack/flaw size of 0.1 mm and 1.0 mm
- with and without ΔK_{th}
- with and without crack closure

The results of the crack initiation and propagation life calculations and the total fatigue life for each approach defined in Section 6.3 are summarized in Table G.5 through Table G.8. The approach designations defined in Table 6.1 are used in the tables. The last character, C, in the designation stands for corner crack or flaw. Each table shows the results for both residual stress distributions.

Table G.5 *– Fatigue lives of corner cracks and flaws: approach including ΔK_{th} and neglecting crack closure.*

Approach Designation	σ_{res}	N_{init}	N_{prop}	N
C01LN-C	100 MPa	---	163,000	163,000
	0 MPa	---	163,000	163,000
C10LN-C	100 MPa	---	42,000	42,000
	0 MPa	---	42,000	42,000
F01LN-C	100 MPa	13,000	163,000	176,000
	0 MPa	20,000	163,000	183,000
F10LN-C	100 MPa	7,000	42,000	49,000
	0 MPa	11,000	42,000	53,000

Table G.6 *– Fatigue lives of corner cracks and flaws: approach including ΔK_{th} and crack closure.*

Approach Designation	σ_{res}	N_{init}	N_{prop}	N
C01LC-C	100 MPa	---	168,000	168,000
	0 MPa	---	269,000	269,000
C10LC-C	100 MPa	---	42,000	42,000
	0 MPa	---	68,000	68,000
F01LC-C	100 MPa	13,000	168,000	181,000
	0 MPa	20,000	269,000	289,000
F10LC-C	100 MPa	7,000	42,000	49,000
	0 MPa	11,000	68,000	79,000

Table G.7 *– Fatigue lives of corner cracks and flaws: approach neglecting ΔK_{th} and crack closure.*

Approach Designation	σ_{res}	N_{init}	N_{prop}	N
C01SN-C	100 MPa	---	160,000	160,000
	0 MPa	---	160,000	160,000
C10SN-C	100 MPa	---	42,000	42,000
	0 MPa	---	42,000	42,000
F01SN-C	100 MPa	13,000	160,000	173,000
	0 MPa	20,000	160,000	180,000
F10SN-C	100 MPa	7,000	42,000	49,000
	0 MPa	11,000	42,000	53,000

Table G.8 *– Fatigue lives of corner cracks and flaws: approach neglecting ΔK_{th} and including crack closure.*

Approach Designation	σ_{res}	N_{init}	N_{prop}	N
C01SC-C	100 MPa	---	165,000	165,000
	0 MPa	---	261,000	261,000
C10SC-C	100 MPa	---	42,000	42,000
	0 MPa	---	67,000	67,000
F01SC-C	100 MPa	13,000	165,000	178,000
	0 MPa	20,000	261,000	281,000
F10SC-C	100 MPa	7,000	42,000	49,000
	0 MPa	11,000	67,000	78,000

G.4 Non-Peened Surface Flaw or Crack

The following parameters were investigated for the specimens with a non-peened surface flaw or crack:

- residual stresses at top of plate of $\sigma_{res} = 100$ MPa and 0 MPa
- crack and flaw
- initial crack/flaw size of 0.1 mm and 1.0 mm
- with and without ΔK_{th}
- with and without crack closure

The results of the crack initiation and propagation life calculations and the total fatigue life for each approach defined in Section 6.3, are summarized in Table G.9 through Table G.12. The approach designations defined in Table 6.1 are also used in the tables. The last character, S, in the designation stands for surface crack or flaw. Each table shows the results for both residual stress distributions.

Table G.9 *– Fatigue lives of surface cracks and flaws: approach including ΔK_{th} and neglecting crack closure.*

Approach Designation	σ_{res}	N_{init}	N_{prop}	N
C01LN-S	100 MPa	---	72,000	72,000
	0 MPa	---	72,000	72,000
C10LN-S	100 MPa	---	15,000	15,000
	0 MPa	---	15,000	15,000
F01LN-S	100 MPa	19,000	72,000	91,000
	0 MPa	23,000	72,000	95,000
F10LN-S	100 MPa	11,000	15,000	26,000
	0 MPa	14,000	15,000	29,000

Table G.10 *– Fatigue lives of surface cracks and flaws: approach including ΔK_{th} and crack closure.*

Approach Designation	σ_{res}	N_{init}	N_{prop}	N
C01LC-S	100 MPa	---	75,000	75,000
	0 MPa	---	119,000	119,000
C10LC-S	100 MPa	---	16,000	16,000
	0 MPa	---	25,000	25,000
F01LC-S	100 MPa	19,000	75,000	94,000
	0 MPa	23,000	119,000	142,000
F10LC-S	100 MPa	11,000	16,000	27,000
	0 MPa	14,000	25,000	39,000

Table G.11 *– Fatigue lives of surface cracks and flaws: approach neglecting ΔK_{th} and crack closure.*

Approach Designation	σ_{res}	N_{init}	N_{prop}	N
C01SN-S	100 MPa	---	72,000	72,000
	0 MPa	---	72,000	72,000
C10SN-S	100 MPa	---	15,000	15,000
	0 MPa	---	15,000	15,000
F01SN-S	100 MPa	19,000	72,000	91,000
	0 MPa	23,000	72,000	95,000
F10SN-S	100 MPa	11,000	15,000	26,000
	0 MPa	14,000	15,000	29,000

Table G.12 *– Fatigue lives of surface cracks and flaws: approach neglecting ΔK_{th} and including crack closure.*

Approach Designation	σ_{res}	N_{init}	N_{prop}	N
C01SC-S	100 MPa	---	74,000	74,000
	0 MPa	---	118,000	118,000
C10SC-S	100 MPa	---	16,000	16,000
	0 MPa	---	25,000	25,000
F01SC-S	100 MPa	19,000	74,000	93,000
	0 MPa	23,000	118,000	141,000
F10SC-S	100 MPa	11,000	16,000	27,000
	0 MPa	14,000	25,000	39,000

G.5 Embedded Flaw or Crack

The following parameters were investigated for the welds with an embedded crack or flaw:

- residual stresses at top of plate of $\sigma_{res} = 100$ MPa and 0 MPa
- crack and flaw
- initial crack/flaw size of 0.1 mm and 1.0 mm
- with and without ΔK_{th}
- with and without crack closure

The results of the crack initiation and propagation live calculations and the total fatigue life for each approach defined in Section 6.3 are summarized in Table G.13 through Table G.16. The approach designations defined in Table 6.1 are also used in the tables. The last character, E, in the designation stands for embedded crack or flaw. Each table shows the results for both residual stress distributions.

Table G.13 *– Fatigue lives of embedded cracks and flaws: approach including* ΔK_{th} *and neglecting crack closure.*

Approach Designation	σ_{res}	N_{init}	N_{prop}	N
C01LN-E	100 MPa	---	112,000	112,000
	0 MPa	---	112,000	112,000
C10LN-E	100 MPa	---	14,000	14,000
	0 MPa	---	14,000	14,000
F01LN-E	100 MPa	28,000	112,000	140,000
	0 MPa	32,000	112,000	144,000
F10LN-E	100 MPa	15,000	14,000	29,000
	0 MPa	17,000	14,000	31,000

Table G.14 *– Fatigue lives of embedded cracks and flaws: approach including ΔK_{th} and crack closure.*

Approach Designation	σ_{res}	N_{init}	N_{prop}	N
C01LC-E	100 MPa	---	113,000	113,000
	0 MPa	---	184,000	184,000
C10LC-E	100 MPa	---	15,000	15,000
	0 MPa	---	24,000	24,000
F01LC-E	100 MPa	28,000	113,000	141,000
	0 MPa	32,000	184,000	216,000
F10LC-E	100 MPa	15,000	15,000	30,000
	0 MPa	17,000	24,000	41,000

Table G.15 *– Fatigue lives of embedded cracks and flaws: approach neglecting ΔK_{th} and crack closure.*

Approach Designation	σ_{res}	N_{init}	N_{prop}	N
C01SN-E	100 MPa	---	110,000	110,000
	0 MPa	---	110,000	110,000
C10SN-E	100 MPa	---	14,000	14,000
	0 MPa	---	14,000	14,000
F01SN-E	100 MPa	28,000	110,000	138,000
	0 MPa	32,000	110,000	142,000
F10SN-E	100 MPa	15,000	14,000	29,000
	0 MPa	17,000	14,000	31,000

Table G.16 *– Fatigue lives of embedded cracks and flaws: approach neglecting ΔK_{th} and including crack closure.*

Approach Designation	σ_{res}	N_{init}	N_{prop}	N
C01SC-E	100 MPa	---	111,000	111,000
	0 MPa	---	179,000	179,000
C10SC-E	100 MPa	---	15,000	15,000
	0 MPa	---	24,000	24,000
F01SC-E	100 MPa	28,000	111,000	139,000
	0 MPa	32,000	179,000	211,000
F10SC-E	100 MPa	15,000	15,000	30,000
	0 MPa	17,000	24,000	41,000

G.6 Peened Specimens

The following parameters were investigated for the peened specimens:

- residual stresses at top of plate of σ_{res} = -100 MPa and -200 MPa
- crack and flaw
- initial crack/flaw size of 0.0 mm (perfect weld), 0.1 mm and 1.0 mm
- with and without ΔK_{th}
- with and without crack closure

The results of the crack initiation and propagation life calculations and the total fatigue life for each approach defined in Section 6.3 are summarized in Table G.17 through Table G.20. The approach designations defined in Table 6.1 are also used in the tables. Each table shows the results for both residual stresses. Not shown are all surface and corner cracks neglecting crack closure, since they result in the same fatigue lives as the non-peened models.

Table G.17 *– Fatigue lives of peened specimens: approach including* ΔK_{th} *and neglecting crack closure.*

Approach Designation	σ_{res}	N_{init}	N_{prop}	N
N00LN	-100 MPa	16,150,000	163,000	16,300,000
	-200 MPa	∞	163,000	∞
F01LN-C	-100 MPa	25,000	163,000	188,000
	-200 MPa	39,000	163,000	202,000
F10LN-C	-100 MPa	13,000	42,000	55,000
	-200 MPa	16,000	42,000	58,000
F01LN-S	-100 MPa	28,000	72,000	100,000
	-200 MPa	56,000	72,000	128,000
F10LN-S	-100 MPa	16,000	15,000	31,000
	-200 MPa	21,000	15,000	36,000

Table G.18 *– Fatigue lives of peened specimens: approach including ΔK_{th} and crack closure.*

Approach Designation	σ_{res}	N_{init}	N_{prop}	N
N00LC	-100 MPa	16,150,000	424,000	16,600,000
	-200 MPa	∞	1,130,000	∞
C01LC-C	-100 MPa	---	424,000	424,000
	-200 MPa	---	1,130,000	1,130,000
C10LC-C	-100 MPa	---	62,000	62,000
	-200 MPa	---	84,000	84,000
C01LC-S	-100 MPa	---	191,000	191,000
	-200 MPa	---	466,000	466,000
C10LC-S	-100 MPa	---	25,000	25,000
	-200 MPa	---	36,000	36,000
F01LC-C	-100 MPa	25,000	424,000	449,000
	-200 MPa	39,000	1,130,000	1,170,000
F10LC-C	-100 MPa	13,000	62,000	75,000
	-200 MPa	16,000	84,000	100,000
F01LC-S	-100 MPa	28,000	191,000	219,000
	-200 MPa	56,000	466,000	522,000
F10LC-S	-100 MPa	16,000	25,000	41,000
	-200 MPa	21,000	36,000	57,000

Table G.19 *– Fatigue lives of peened surface and corner cracks and flaws: approach neglecting* ΔK_{th} *and crack closure.*

Approach Designation	σ_{res}	N_{init}	N_{prop}	N
N00SN	-100 MPa	16,150,000	160,000	16,300,000
	-200 MPa	∞	160,000	∞
F01SN-C	-100 MPa	25,000	160,000	185,000
	-200 MPa	39,000	160,000	199,000
F10SN-C	-100 MPa	13,000	42,000	55,000
	-200 MPa	16,000	42,000	58,000
F01SN-S	-100 MPa	28,000	72,000	100,000
	-200 MPa	56,000	72,000	128,000
F10SN-S	-100 MPa	16,000	15,000	31,000
	-200 MPa	21,000	15,000	36,000

Table G.20 *– Fatigue lives of peened surface and corner cracks and flaws: approach neglecting* ΔK_{th} *and including crack closure.*

Approach Designation	σ_{res}	N_{init}	N_{prop}	N
N00SC	-100 MPa	16,150,000	396,000	16,500,000
	-200 MPa	∞	893,000	∞
C01SC-C	-100 MPa	---	396,000	396,000
	-200 MPa	---	893,000	893,000
C10SC-C	-100 MPa	---	61,000	61,000
	-200 MPa	---	84,000	84,000
C01SC-S	-100 MPa	---	185,000	185,000
	-200 MPa	---	422,000	422,000
C10SC-S	-100 MPa	---	25,000	25,000
	-200 MPa	---	36,000	36,000
F01SC-C	-100 MPa	25,000	396,000	421,000
	-200 MPa	39,000	893,000	932,000
F10SC-C	-100 MPa	13,000	61,000	74,000
	-200 MPa	16,000	84,000	100,000
F01SC-S	-100 MPa	28,000	185,000	213,000
	-200 MPa	56,000	422,000	478,000
F10SC-S	-100 MPa	16,000	25,000	41,000
	-200 MPa	21,000	36,000	57,000

APPENDIX H

Equivalent Strains and Stresses

EQUIVALENT STRAINS AND STRESSES

H.1 Derivation of Equation (8.11)

In order to use the proposed crack initiation model for variable amplitude loading, the individual strain and stress cycles must be transformed into an equivalent product of maximum stress and strain amplitude, $\left(\Delta\sigma_{\max}\left(\Delta\varepsilon/2\right)\right)_e$. The first step in this transformation is to establish a plot of arbitrarily chosen $\left(\Delta\sigma_{\max}\left(\Delta\varepsilon/2\right)\right)_i$-products as a function of N_{init}, covering the practical range of N_{init}. The plotted products can be approximated by a linear relationship on a log-log scale, resulting in:

$$\sigma_{\max}\left(\Delta\varepsilon/2\right) = A\left(N_{init}\right)^{-1/B} \tag{H.1}$$

where $A = 10^a$ and $B = -1/b$ with a and b are the intercept and slope obtained from the linear regression analysis on the log-log plot. Rearranging equation (H.1), the number of initiation cycles for an arbitrary product $\left(\Delta\sigma_{\max}\left(\Delta\varepsilon/2\right)\right)_i$ is found to be (for simplicity the index *init* is omitted):

$$N_i = \left(\frac{A}{\left(\Delta\sigma_{\max}\left(\Delta\varepsilon/2\right)\right)_i}\right)^B \tag{H.2}$$

The damage done due to one load cycle is:

$$d_i = \frac{1}{N_i} = \left(\frac{\left(\Delta\sigma_{\max}\left(\Delta\varepsilon/2\right)\right)_i}{A}\right)^B \tag{H.3}$$

The damage resulting from n_{ref} cycles of the equivalent product, $\left(\Delta\sigma_{\max}\left(\Delta\varepsilon/2\right)\right)_e$, is:

$$D_e = \frac{n_{ref}}{N_e} = n_{ref}\left(\frac{\left(\Delta\sigma_{\max}\left(\Delta\varepsilon/2\right)\right)_e}{A}\right)^B \tag{H.4}$$

Setting the damage due to the sum of the individual products equal to the damage due to n_{ref} cycles of the equivalent product yields the following relationship:

$$\sum_{i=1}^{n}\left(\frac{\left(\Delta\sigma_{\max}\left(\Delta\varepsilon/2\right)\right)_i}{A}\right)^B = n_{ref}\left(\frac{\left(\Delta\sigma_{\max}\left(\Delta\varepsilon/2\right)\right)_e}{A}\right)^B \tag{H.5}$$

Solving equation (H.5) for $\left(\Delta\sigma_{\max}\left(\Delta\varepsilon/2\right)\right)_e$ results in:

$$\left(\Delta\sigma_{max}\left(\Delta\varepsilon/2\right)\right)_e = \left(\frac{\sum_{i=1}^{n}\left(\left(\Delta\sigma_{max}\left(\Delta\varepsilon/2\right)\right)_i\right)^B}{n_{ref}}\right)^{1/B} \tag{H.6}$$

(8.11)

H.2 Application Example

Results from the finite element model developed in Section 8.6.3 for the cruciform specimens with a weld toe undercut are used here to illustrate the transformation process used to find an equivalent stress-strain product, $\left(\Delta\sigma_{\max}\left(\Delta\varepsilon/2\right)\right)_e$. Four load ranges, all resulting in strain amplitudes and maximum stresses yielding crack initiation lives smaller than 10 million cycles, are applied. The mean crack initiation properties found in Chapter 4 for the weld metal are used. No residual stresses are assumed. The strain amplitudes, maximum stresses, the stress-strain products, and resulting initiation lives are summarized in Table H.1 for each of the four applied nominal stress ranges.

Table H.1 – *Fatigue initiation parameters for application example.*

$\Delta\sigma_{nom}$ [MPa]	$\Delta\varepsilon/2$	$\sigma_{\max}$ [MPa]	$\Delta\sigma_{\max}\left(\Delta\varepsilon/2\right)$ [MPa]	N_{init}
150	8.87×10^{-4}	366	0.3246	3,600,000
180	1.06×10^{-3}	398	0.4231	530,000
207	1.23×10^{-3}	420	0.5187	160,000
290	1.84×10^{-3}	476	0.8773	16,000

The four N_{init} versus $\Delta\sigma_{\max}\left(\Delta\varepsilon/2\right)$ points are plotted on a log-log scale in Figure H.1. The resulting regression line with its equation and coefficient of determination, r^2, is also shown.

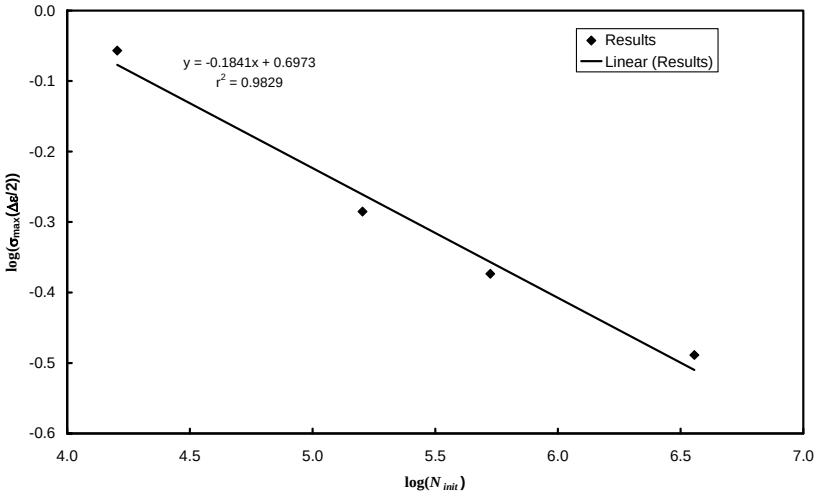

Figure H.1 *–Plot of N_{init} versus $\Delta\sigma_{\max}\left(\Delta\varepsilon/2\right)$ relationship.*

From the regression analysis: $a = 0.6973$ and $b = -0.1841$ and thus $A = 10^{0.6973} = 4.98$ and $B = -1/b = 5.43$. Using equation (8.11) the equivalent stress-strain product, $(\Delta\sigma_{\max}(\Delta\varepsilon/2))_e$ can now be determined. Table H.2 shows the calculations to find $(\Delta\sigma_{\max}(\Delta\varepsilon/2))_e$, once assuming $n_{ref} = 1$, i.e. the stress-strain products belong to one sequence, and once for $n_{ref} = 4$, i.e. the stress-strain products are from four load sequences.

Table H.2 – *Equivalent stress-strain product for application example.*

$\Delta\sigma_{nom}$ [MPa]	$\Delta\sigma_{\max}(\Delta\varepsilon/2)$ [MPa]	$(\Delta\sigma_{\max}(\Delta\varepsilon/2))^B$	$(\Delta\sigma_{\max}(\Delta\varepsilon/2))_e$ [MPa]
150	0.3246	0.0022	one sequence:
180	0.4231	0.0093	0.890
207	0.5187	0.0282	four sequences:
290	0.8773	0.4908	0.690
	$\Sigma =$	0.5306	

Table H.2 shows that the smaller stress-strain products contribute much less to the fatigue damage, and thus to the equivalent product, than the higher products. Furthermore, the equivalent product for four sequences is smaller than the equivalent product for one sequence, but due to the exponent B not proportionally to the number of sequences. Four to six stress-strain products are normally sufficient to conduct a regression analysis.